SIMULATIONS OF SIMILAR AND DISSIMILAR WELD JOINT FAILURES AND BEARINGS FOR FATIGUE ANALYSES

by

Jaewon Lee

A dissertation submitted in partial fulfillment
of the requirements for the degree of
Doctor of Philosophy
(Mechanical Engineering)
in The University of Michigan
2011

Doctoral Committee:

Professor Jwo Pan, Chair
Professor Gregory M. Hulbert
Professor Richard A. Scott
Associate Professor Gustavo J. Parra-Montesinos

Dedication

To my family.

Acknowledgements

I wish to express my sincere appreciation and gratitude to my advisor, Professor Jwo Pan, for his constant advice, support and unlimited patience throughout my study. His guidance was essential to the completion of this dissertation. I would also like to thank my doctoral committee, Professor Richard Scott, Professor Gregory Hulbert and Professor Gustavo Parra-Montesisnos.

I would like to thank Dr. Kamran Asim for the experimental results in chapter 2 which would not have been possible without his contributions. I would like to thank Teresa Franklin not only for the experimental results regarding ultrasonic weld specimens in chapter 3 but also for her help in general. I would like to thank Dr. Yung-li Lee of Chrysler for his technical, academic and financial support which led to chapters 4, 5 and 6. The quality and the impact of this dissertation have only elevated by his continued support assistance. I would like to thank Dr. Kyoosil Choi for his mental support and advice during my PhD candidacy.

I would like to thank my friends Dr. Seungjun Lee and Dr. Jaewook Lee for their company and technical consultations, Sungkwon Hong for his help in numerical analyses, Dr. Kyungchan Chae for his help in advanced computing, Yusuf Ali and Catherine Amodeo for his and her help in finite element methods and Esq. Sunjung Park for her encouragements. I would like to thank my former office mates Dr. Van-Xuan Tran and

MSE David Hsu. I would like to thank and express well wishes to Kulthilda Sripichai, Seunghoon Hong and Katherine Avery.

Finally, I would like to thank my grandparents, parents, brother, sister-in-law, Jiho and the rest of my family for their support and encouragement which has made this dissertation possible.

Table of Contents

List of Figures

List of Tables

Chapter 1
Introduction

The automotive industry is faced with the challenge of increasing vehicle fuel economy in response to changes in federal regulations and to address environmental concerns. Reducing the weight of automobiles and lowering the friction in wheel bearings are two means by which vehicle fuel consumption can be lowered. Regarding weight, the trend is to replace traditional carbon steel with light metals and their alloys such as high strength low alloy steel or magnesium. Regarding friction, developments in wheel bearing design and materials stride to lowering the friction coefficient while increasing the fatigue lives of bearings.

This dissertation consists of two parts. In Chapters 2 and 3, the failure modes of laser and ultrasonic welds in lap-shear specimens are covered. In Chapters 4, 5 and 6, analytical solutions to calculate the load exerted by the rolling elements in roller bearings are proposed and fatigue lives are estimated.

Chapter 2 represents a paper for modeling of failure mode of laser welds in lap-shear specimens of HSLA steel sheets. Chapter 3 represents a paper for modeling of failure mode of ultrasonic welds in lap-shear specimens of magnesium to steel sheets. Chapter 4 represents a paper for the calculation of load and fatigue life in roller bearings. Chapter 5 represents a paper for the geometric effects on contact pressure distribution and

fatigue lives of roller bearings. Chapter 6 represents a paper for the calculation of load and contact pressure in cylindrical roller bearings with interference.

In Chapter 2, failure mode of laser welds in lap-shear specimens of high strength low alloy (HSLA) steel sheets is investigated in this chapter. The experiments for laser welds in lap-shear specimens under quasi-static loading conditions are briefly reviewed. The experimental results showed that the laser welds failed in a ductile necking/shear failure mode and the ductile failure was initiated at a distance away from the crack tip near the boundary of the base metal and heat affected zone. In order to understand the failure mode of these welds, finite element analyses under plane strain conditions were conducted to identify the effects of the different plastic behaviors of the base metal, heat affected zone, and weld zone as well as the weld geometry on the ductile failure. The results of the reference finite element analysis based on the homogenous material model show that the failure mode is most likely to be a middle surface shear failure mode in the weld. The results of the finite element analysis based on the multi-zone non-homogeneous material models show that the higher effective stress-plastic strain curves of the weld and heat affected zones and the geometry of the weld protrusion result in the necking/shear failure mode in the load carrying sheet. The results of another finite element analysis based on the non-homogeneous material model and the Gurson yield function for porous materials indicate that the consideration of void nucleation and growth is necessary to identify the ductile failure initiation site that matches well with the experimental observations. Finally, the results of this chapter indicate that the failure mode of the welds should be examined carefully and the necking/shear failure mode

needs to be considered for development of failure or separation criteria for welds under more complex loading conditions.

In Chapter 3, failure mode of ultrasonic welds in lap-shear specimens of magnesium and steel sheets is investigated in this paper. The experiments for ultrasonic welds in dog-bone shaped lap-shear specimens under quasi-static loading conditions are briefly reviewed first. The experimental results show that the ultrasonic welds failed in a shear failure mode initiated from the pre-existing crack tip and the corner of the indentation created by the sonotrode tool tip. In order to understand the failure mode of the ultrasonic welds, finite element analyses under plane strain and plane stress conditions are conducted to identify the effects of the weld geometry and the material property variation on the failure mode. The results of the finite element analyses based on two-zone and multi-zone material models show that the weld indentation triggers different plastic flow patterns in the load carrying sheet. Also, finite element analyses are conducted to obtain the J integral solutions for the pre-existing crack and a kinked crack with a small kink length. The results of the finite element analyses indicate that the J integral solution for the kinked crack is much higher than that for the interface crack. This suggests that the interface strength between the magnesium and steel sheets is quite high and the critical J needed to grow the crack along the interface is not met. Therefore, the crack kinks out of the interface to grow into the magnesium sheet where the critical J to grow the crack is met. Finally, the results of this investigation indicate that the failure mode of the welds should be examined carefully and the failure mode needs to be considered for development of failure or separation criteria for welds under more complex loading conditions.

In Chapter 4, a closed-form load distribution solution for calculation of the loads exerted by the rolling elements on the outer raceway in cylindrical or spherical roller bearings under radial loading is proposed in this chapter. The loads exerted by the rolling elements are obtained based on an assumption that the maximum contact pressure profiles of multiple rolling elements collectively resemble the contact pressure profile of the corresponding continuous cylinder. Based on this assumption, an analytical load distribution solution which gives the loads exerted by the rolling elements on the outer raceway is derived based on the non-conforming contact solution of Hertz and the conforming contact solution of Persson. These loads can be calculated from the analytical solution with the total applied load and the normalized contact pressure profile of the corresponding continuous body. Two-dimensional and three-dimensional finite element analyses were conducted to validate the proposed analytical solutions. The maximum load of the rolling elements calculated from the analytical solution is within 3% and 10% of the result from the two-dimensional and three-dimensional finite element analyses, respectively. A method to estimate the fatigue lives of bearings based on the analytical solution is summarized to present a simple procedure to compare the fatigue performance of the bearings with different designs.

In Chapter 5, a special case in which the analytical solution proposed in Chapter 4 cannot be applied due to unique boundary conditions is discussed with the cam follower roller bearing as an example. Effects of roller diameter and number on the contact pressures, subsurface stresses and the fatigue lives of cam roller follower bearings are investigated in this chapter. Finite element analyses under plane strain conditions were conducted to identify the effects of the diameter and number of the rolling elements and

the thickness of the outer ring. A kinematic analysis under pure rolling conditions and the results of the finite element analyses show that the fatigue lives of the stationary inner pin should be shorter than those of the rotating outer ring, and the results are in agreement with the observations of the failure mode of cam follower roller bearings. The fatigue life of the inner pin generally increases as the roller diameter increases. But, reducing the number of rollers to accommodate larger rollers does not necessarily increase the fatigue life. The inevitable decrease of the thickness of the outer ring due to the increase of the roller diameter results in the increase of compliance for the outer ring. This increase of compliance leads to excessive deformation of the outer ring and consequently more load must be carried by smaller number of rolling elements. For cam roller follower bearings, a parametric study based on the finite element analyses should be conducted to obtain the optimum geometry which gives the lowest maximum subsurface Mises stress and contact pressure which results in the longest fatigue life.

In Chapter 6, a closed-form solution to calculate the loads exerted by the rolling elements in cylindrical roller bearings with consideration of interference fit of rollers is proposed in this chapter. The non-conforming Hertz solution and the conforming Persson solution are first briefly reviewed. The interference loads by the rolling elements due to the interference are derived and then approximated for a given set of geometric parameters of bearings. With the solution for the interference load, the loads exerted by the rolling elements on the outer raceway are obtained when the total load is less than the separation load where a rolling element possibly start to lose contact with the cylinders. These loads of the rolling elements can be calculated by a closed-form equation with the total applied load, the number of rolling elements, the angular locations of the rolling

elements, the equivalent elastic modulus, the interference, the outer raceway diameter and the thickness of the outer cylinder as the input parameters. Two-dimensional finite element analyses were conducted to verify the applicability of the closed-form solution. Finite element models with different diameters of the outer and inner cylinders, diameters of the rolling element, number of rolling elements, and the thickness of the outer cylinder were considered for the validation. The results of the finite element analyses show that the maximum contact pressures of the rolling elements obtained from the closed-form solution are within 1% of those of the finite element analyses when the total load is less than the separation load.

Chapter 2
Modeling of failure mode of laser welds in lap-shear specimens of HSLA steel sheets

Introduction

Laser welding has been widely used in the industry because of its advantages such as narrow heat affected zone, low distortion and relatively high welding speed. A lap joint is a common weld joint by laser welding due to its relatively less restricted tolerance requirement. Due to the geometry of the lap joint, natural crack or notch tips are present at the edges of the weld bead. Fatigue cracks are usually initiated from the natural crack or notch tips of lap joints. Laser welded components with lap joints are often subjected to cyclic loading conditions. Many researchers investigated the fatigue lives of laser welded lap joints.

Hsu and Albright [1] combined a static stress analysis with the Neuber's rule and established a model to calculate the fatigue life from the local stress and strain near the main notches of laser welded lap joints. Wang and Ewing [2] conducted experiments to examine the fatigue strengths of resistance spot welds and laser welds under lap-shear loading conditions. Flavenot et al. [3] performed fatigue tests on laser welded lap joints with various welding parameters such as the weld bead geometry, the gap between the upper and lower sheets and the input energy of laser. Wang [4] correlated the experimental fatigue lives with the values of the *J* integral from finite element computations.

Ono et al. [5] investigated the fatigue strength of laser welded lap joints and correlated the fatigue lives to the maximum stress intensity factor ranges. Terasaki et al. [6] examined the fatigue lives of laser welded lap joints and correlated the experimental results by the stress intensity factor solutions. Kaitanov et al. [7] showed that the fatigue strength of laser welded lap joints depends on the weld width. Cho et al. [8] examined the fatigue strength of laser welded lap joints with consideration of residual stresses obtained from thermo-mechanical finite element analyses. Sonsino et al. [9] examined laser welded tube-tube specimens by multiaxial fatigue theories. Sripichai et al. [10] investigated the fatigue lives of laser welded lap joints of high strength low alloy steel based on closed-form analytical and computational stress intensity factor solutions.

Many investigations on the fatigue lives of laser welded lap joints have been conducted. However, limited research has been conducted to examine the strength and failure mode of laser welded joints. Ono et al. [5] correlated the static strength of laser welded lap joints to the tensile strength and hardness values of the welds. Kaitanov et al. [7] found that the weld width and pattern significantly affect the static strength of laser welded lap joints. Recently, Chien et al. [11] examined the shear failure of laser welded aluminum blanks under uniaxial and biaxial straining conditions. Taban et al. [12] investigated the static and fatigue strength of laser welded butt joints of 12% Cr stainless steel plates by experiments. Casavola et al. [13] examined the static strength of laser welded butt joints of titanium sheets as well as their fatigue strength. They conducted a two-dimensional elastic plane strain finite element analysis to understand the stress concentration near the weld. Asim et al. [14] recently conducted an experimental

investigation of the failure mechanism and strength of laser welds in lap-shear specimens of high strength low alloy steel.

In this investigation, finite element analyses were conducted to understand the effects of the different material plastic behaviors of the base metal, heat affected zone and weld zone as well as the weld geometry on the failure mode of laser welds in lap-shear specimens of HSLA steel under quasi-static loading conditions. Two-dimensional plane strain finite element analyses with homogeneous material properties and non-homogeneous material properties in the weld zone, heat affected zone and base metal are first carried out. Since the experimental results of Asim et al. [14] indicate that the failure of the laser welds is of a ductile nature, another finite element analysis is carried out based on the Gurson yield function [15], [16] with consideration of void nucleation and growth. The results of the finite element analyses are then compared with the experimental observations. Finally, conclusions are made.

Experimental results

Lap-shear specimen

The lap-shear specimens used in Sripichai et al. [10] were also used in Asim et al. [14]. These specimens were made by using 95 mm by 27 mm HSLA steel sheets with a thickness of 0.93 mm. The specimens were welded using a 6 kW CO_2 laser with a weld speed of 8 m/min and were then machined into a dog-bone shaped profile using a CNC milling machine. The central part of the specimen has a reduced width. The width and length of the uniform straight part of the section with the reduced width are 8 mm and 13.5 mm, respectively. Figs. 2.1(a) and 2.1(b) show top and bottom views of a laser

welded lap-shear specimen. The weld zone is very narrow and its average width is about 1 mm. Two doublers of 55 mm by 27 mm were used to align the fixture to avoid the initial realignment of the specimen due to the non-aligned grips under lap-shear loading conditions. Fig. 2.1(c) shows a schematic of a lap-shear specimen. As shown in the figure, the specimen has a width W, sheet thickness t and overall length L for the upper and lower sheets. The specimen has a reduced width b for the central portion, an overlap length V and a width d for the laser weld zone which is indicated as the shaded area in the figure. The dimensions of the specimens are W = 27 mm, t = 0.93 mm, L = 95 mm, b = 8.0 mm, V = 30 mm and r = 10 mm.

Quasi-static test

Quasi-static tests of lap-shear specimens as schematically shown in Fig. 2.1(c) were carried out under displacement controlled conditions. These tests were conducted using an automated MTS testing machine at a constant cross-head speed of 1 mm/min. Fig. 2.2 shows a representative load-displacement curve obtained from one quasi-static test. The average maximum (or failure) load and the average maximum displacement obtained from three quasi-static tests are about 3 kN and 2.1 mm, respectively. The load-displacement curves obtained from the finite element analyses are also plotted in Fig. 2.2 and will be discussed later. During the tests, the weld nugget rotated as the applied displacement increased. The angle of rotation continued to increase and a final value of 50˚ with respect to the line of loading was measured for a completely failed specimen. The nugget rotation is the consequence of the non-uniform plastic deformation through the thickness of the load carrying sheet near the weld nugget.

Fig. 2.3(a) shows a micrograph of the cross section near a weld just prior to failure. Two arrows in the figure show the line of loading. A magnified view of the crack formation near the inner surface of the lower left sheet at a distance to the crack tip is shown as an insert. Also, the nugget rotation has caused the relatively rigid round protrusion to penetrate the nearby softer base metal and the heat affected zone of the left lower sheet in a buckling action which will be discussed later. Fig. 2.3(a) also shows the necking of the upper right and lower left sheet near the weld. The necking, which took place along with the weld nugget rotation, reduced the thickness of both load carrying sheets noticeably. Fig. 2.3(b) shows a micrograph of the cross section near a weld that has been completely failed after the quasi-static test. As shown, the lower left sheet was completely separated to failure at a distance away from the left crack tip. The combination of the necking and the buckling of the left lower sheet appear to be the main mechanism to fail the weld.

Weld microstructure

Fig. 2.4 shows a micrograph for the cross section near a weld in a lap-shear specimen. Three regions can be identified based on their distinct grain structures. The fusion zone of the weld is characterized by its columnar dendrites and non-equiaxed coarse grains with fine pearlite and low carbon bainite [17]. These were formed due to the localized heat from the high energy laser beam followed by a rapid cooling of the molten metal. A less coarse grain structure in the narrow heat affected zones (HAZs) is visible between the fusion zone and the base metal. The narrow HAZs span about 50 μm on both sides of the fusion zone. The base metal has a fine and randomly oriented grain structure.

Hardness measurement

Micro-hardness tests were carried out to obtain the Vickers hardness values for the upper sheet, middle surface and lower sheet across the weld width. The hardness values are fairly consistent in the thickness direction for the upper sheet, middle surface and lower sheet. Shown in Fig. 2.5 are the results of the hardness values across the weld. The hardness value for the base metal is around 150HV. The hardness value sharply increases in the heat affected zone and reaches the highest value of near 240HV at the center of the weld zone. Fig. 2.5 also shows the assumed hardness distributions for the middle surface of the weld, which are used to estimate the tensile stress-plastic strain curves of the different material sections in the 3-zone and 6-zone finite element analyses that will be discussed later.

Material stress-strain curve

The tensile stress-strain curve of the base metal is fitted by an elastic power-law strain hardening relation based on the experimental tensile stress-strain curve as

$$\begin{aligned} \sigma &= E\varepsilon \quad \text{for} \quad \sigma \le \sigma_0 \\ \sigma &= K\varepsilon^n \quad \text{for} \quad \sigma > \sigma_0 \end{aligned} \tag{2.1}$$

where σ represents the tensile stress, E represents the elastic modulus, ε is the tensile strain and σ_0 is the initial yield stress. K represents the strength coefficient and n represents the hardening exponent. σ_0, K, n and E are determined for the base metal as 315 MPa, 617 MPa, 0.18 and 200 GPa, respectively. Fig. 2.6 shows the tensile stress-plastic strain curve of the base metal based on the stress-strain relation in Eq. (2.1).

Since it is difficult to determine the tensile stress-plastic strain curves of the weld and heat affected zones, the tensile stress-plastic strain curves for the weld and heat affected zones have been estimated by scaling the tensile stress of the base metal proportional to the corresponding hardness values measured by the indentation tests for a given plastic strain. The values of the Vickers hardness and the scaled initial yield stress are listed in Table 2.1(a) for the 3-zone finite element model and Table 2.1(b) for the 6-zone finite element model. Fig. 2.6 shows the tensile stresses as functions of the plastic strain for the base metal, heat affected zone and weld zone used in the 3-zone finite element model. The tensile stress-plastic strain curves for the 6-zone finite element model are scaled up by the hardness values for a given plastic strain in a similar fashion. These tensile stress-plastic strain curves were used as the effective stress-plastic strain curves in the finite element analyses. The deformation histories of the material elements in the lap-shear specimen are obtained from the finite element analyses and are used to examine the failure mode of the laser welds that will be presented in the following section.

Finite element simulations

Finite element model

In addition to the different plastic behaviors of the base metal, heat affected zone and weld zone, the geometry of the weld appears to affect the failure mode significantly [14]. Finite element analyses based on the initial weld geometry as shown in Fig. 2.4 are carried out in this study to identify the influences of the plastic behaviors of the heat affected and weld zones as well as the weld geometry on the failure mode of the welds in

lap-shear specimens. Since the weld zone dimensions have minimal discrepancy along the welding direction due to the high consistency achieved by the laser welding process, two-dimensional plane strain finite element models are used to simulate the elastic-plastic behavior in the middle portion of the lap-shear specimen. Fig. 2.7(a) shows a two-dimensional finite element model of a lap-shear specimen where the shaded region represents the weld zone. The Cartesian coordinate X-Y system is also shown in the figure. As shown in Fig. 2.7(a), the middle plane of the left end of the model is fixed and the displacement of the middle plane of the right end of the model is applied in the X direction. Fig. 2.7(b) shows a close-up view of the finite element mesh near the weld. First-order, isoparametric, plane strain, quadrilateral, reduced integration elements (CPE4R) are used in this model. The minimum element size is 0.014 mm. The elastic modulus is taken as 200 GPa and the Poisson's ratio is taken as 0.3. The Mises yield function is adopted to describe the elastic-plastic behavior of the material with the tensile stress-plastic strain curve used as the effective stress-plastic strain curve. The yield surface evolution is assumed to follow the isotropic hardening rule. It should be mentioned that the residual stresses near the weld are not considered due to lack of quantitative information. Computations were performed using the commercial finite element code ABAQUS v6.8 [18].

Homogeneous material model

In order to understand the effect of the material stress-strain curves on the failure mode, a reference finite element analysis was first conducted by assuming a homogeneous material behavior throughout the model using the material properties of the base metal. It should be noted that the material plastic behavior can be nearly the same as

the base metal as for aluminum ultrasonic spot welds [19]. The results of the parametric study presented here can give some insight on the failure mode of the ultrasonic spot welds under lap-shear loading conditions. The results from the homogeneous model will be compared with those of more realistic multi-zone finite element models where the higher effective stress-plastic strain curves of the heat affected and weld zones are considered. It will be shown later that the existence of the heat affected and weld zones with higher effective stress-plastic strain curves significantly affects the patterns of plastic deformation, failure mode and the location of failure of the lap-shear specimen.

The load-displacement curve of the lap-shear specimen from the finite element analysis based on the homogeneous material model is shown in Fig. 2.2. The load-displacement curve from the finite element analysis is reasonably in agreement with but a bit lower than the experimental results. Figs. 2.8(a)-(d) show the deformed shapes of a lap-shear specimen from the finite element analysis based on the homogeneous material model at the applied displacements of 0.5, 1.0, 1.5 and 2 mm, respectively. The rotation of the non-load carrying sheets due to the rotation of the weld zone increases as the displacement increases. Similar rotational behavior has been observed in simulations of lap-shear specimens with resistance spot welds in Radaj et al. [20] and Nielson [21].

Fig. 2.9(a) shows the equivalent plastic strain distributions near the two crack tips at the applied displacement of 0.1 mm. The plastic zones are large near the tips in two directions due to the mixed mode loading conditions and the constraint conditions imposed by the geometry of the lap-shear specimen [22]. As the displacement increases, both type A and B plastic zones as marked in Fig. 2.9(a) grow. Due to the proximity of the two crack tips, the type A plastic zones originating from both crack tips link up and

evolve into the dominant plastic strain deformation mode of the weld as shown in Fig. 2.9(b) at the applied displacement of 2.0 mm. The type B plastic zone near the left crack tip grows to the edge of the weld protrusion on the bottom surface of the lower left sheet. However, the type B plastic zone near the right crack tip does not grow to the other side of the sheet surface. Necking develops for both the lower left and upper right load carrying sheets due to non-uniform plastic deformation near the tips. Thus, for the homogeneous material model, the failure mode of the lap-shear specimen can be most likely to be a middle surface shear failure mode in the weld due to the large plastic deformation between the two tips. This is possible only when the heat affected and weld zones have the same stress-strain behavior as the base metal. However, the experimental results clearly indicate that the failure occurs in a ductile necking/shear mode in the lower left load carrying sheet. This implies that the homogeneous material assumption is not suitable to explain the observed failure mode and that a non-homogeneous material model with consideration of more realistic stress-strain curves for the heat affected and weld zones should be considered.

3-zone non-homogeneous material model

In order to understand the effect of the higher effective stress-plastic strain curves of the heat affected and weld zones, the tensile stress-plastic strain curves as shown in Fig. 2.6 for the heat affected and weld zones have been incorporated in the finite element model as shown in Fig. 2.10(a). The different stress-plastic strain curves are adopted in the finite element analysis in order to account for the different hardness values in the base metal, heat affected zone and weld zone. The size, shape and location of the heat affected and weld zones were designed to match the distinct grain structures based on the

micrograph of the cross section near a weld in a lap-shear specimen as shown in Fig. 2.4 and again in Fig. 2.10(b). Based on the grain size and shape in the micrograph, the heat affected zone appears to extend from the crack tip into both base metal and weld zone with an average width of 50 μm along the middle surface. Therefore, in the 3-zone finite element model, the heat affected zone is assumed to extend into both base metal and weld zone with the width of 50 μm along the middle surface. Thus, the total width of the heat affected zone along the middle surface in the finite element model is taken to be 100 μm. Based on the micrographs shown in Figs. 2.4 and 2.10(b) and other cross sections of the welds, the average weld width is 800 μm measured from one crack tip to the other. Therefore, the weld width along the middle surface between the two crack tips in the finite element model is taken to be 800 μm. The weld and heat affected zones are expanded in the lower sheet due to the protrusion in the finite element model as shown in Fig. 2.10(a). The values of the scaled initial yield stresses and the assumed hardness values for the base metal, heat affected zone and the weld zone are listed in Table 2.1(a).

The deformed shapes of the specimen from the finite element analysis based on the 3-zone model at the applied displacements of 0.5, 1.0, 1.5 and 2.0 mm, respectively, are depicted in Figs. 2.11(a)-(d). The rotation of the non-load bearing sheets is visible. When compared with the results based on the homogeneous material model, the rotation of the non-load bearing sheets for the 3-zone model is slightly larger at a given displacement. When the displacement at the right end is at 2.0 mm, the angle of the rotation for the homogeneous model is 35˚ (Fig. 2.8(d)) while that angle is 40˚ (Fig. 2.11(d)) for the 3-zone model. In order to accommodate the imposed displacement boundary condition to the specimen, the material along the middle surface of the weld

deforms significantly for the homogeneous model. However, when the heat affected and weld zones have the higher stress-strain curves for the 3-zone model, the material along the middle surface of the weld is more rigid compared to the base metal and therefore has less plastic deformation along the middle surface of the weld compared to that of the homogeneous material model. Consequently, as the applied displacement increases, the material outside of the weld in the two load carrying sheets must deform more and the rotation of the non-load carrying sheets must be larger than that of the homogenous model in order to accommodate the imposed displacement boundary condition.

Figs. 2.12(a) and 2.12(b) show the equivalent plastic strain distributions near a weld for the 3-zone model at the displacements of 0.1 mm and 2.0 mm, respectively. Type A plastic zones ahead of the tips, yet small compared to type B plastic zones, are still visible at the small displacement of 0.1 mm. The higher effective stress-plastic strain curves of the heat affected and weld zones in the 3-zone model prevent type A plastic zones ahead of the two crack tips from growing and linking with each other. The type B plastic zones near the two tips are the dominant plastic deformation mode as shown in Fig. 2.12(a) for the 3-zone model at the displacement of 0.1 mm. When the displacement continues to increase to 2.0 mm, the type B plastic zones grow significantly and the necking of the two load carrying sheets becomes apparent as shown in Fig. 2.12(b). Also shown in Fig. 2.12(b), plastic deformation concentrates in the base metal near the boundary of the base metal and the heat affected zone for both load carrying sheets. The abrupt change in the effective stress-plastic strain relations along the boundary of the base metal and the heat affected zone confines most of the plastic strain to occur on the base metal side of the boundary. Fig. 2.12(c) shows a magnified view of the step-like

crack tip profile, the effective plastic strain distribution near the left crack tip, and the outer surface buckling and contact near the round protrusion of the lower left sheet. Fig. 2.12(d) shows a magnified view of the step-like crack tip profile and the effective plastic strain distribution near the right crack tip. The computational results shown in Figs. 2.12(a)-(d) indicate that the 3-zone model can simulate the ductile shear/necking failure mode observed in the experiment but the step-like crack tip profile does not match well with that of the micrograph as shown in Fig. 2.3(a).

Based on the computational results of the 3-zone model, the following two important observations can be made. First, the incorporation of the higher effective stress-plastic strain curves for the heat affected and weld zones drastically changes the macroscopic plastic flow pattern of the lap-shear specimen. While the results of the homogeneous model imply that the middle surface shear failure could occur between the two crack tips in the weld, the results of the 3-zone non-homogenous model indicate that the necking/shear failure can occur on the base metal side of the boundary of the base metal and the heat affected zone in the load carrying sheets.

Second, the bending of the load carrying sheets causes the rotation of the weld zone or vice versa as shown schematically in Figs. 2.13(a) and 2.13(b) at a small and large applied displacements, respectively. In these figures, T represents tension and C represents compression while the two arrows indicate the line of loading. The weld zone rotation induces tensile stresses on the upper portion of the lower left and the lower portion of the upper right load carrying sheets while the lower portion of the lower left and the upper portion of the upper right load carrying sheets experience compressive stresses. Since the material on the outer surface near the round protrusion of the lower

left load carrying sheet is under compression, the material begins to buckle as the round protrusion pushes in as shown in Fig. 2.13(b). The outer surface buckling creates an artificial notch or crack when the notch or crack surfaces contact each other near the left end of the round protrusion. The imposed displacement boundary condition soon begins to open up the notch or crack which contributes to the final shear failure. Based on these two observations, the necking/shear failure is most likely to occur on the side of the base metal of the lower left sheet where the plastic deformation of the upper portion of the lower left sheet can be linked up with that of the outer surface notch or crack near the weld protrusion.

6-zone non-homogeneous material model

In order to create a more realistic model than the 3-zone non-homogeneous model, the heat affected zone and the adjacent region of the weld zone as shown in Fig. 2.4 are sectioned into four distinct zones with four different effective stress-plastic strain curves. Fig. 2.14 shows a schematic of the 6-zone finite element model with different material sections. The scaled initial yield stresses and the assumed hardness values of the base metal, heat affected zones (HAZ 1 and HAZ 2) and weld zones (Weld 1, Weld 2 and Weld 3) for the 6-zone model are listed in Table 2.1(b). The initial yield stresses for HAZ 1, HAZ 2, Weld 1 and Weld 2 are scaled as $1.1\,\sigma_0^B$, $1.2\,\sigma_0^B$, $1.3\,\sigma_0^B$ and $1.43\,\sigma_0^B$ according to the trends of the experimental hardness values. Here, σ_0^B is the yield stress of the base metal. A parametric study has been performed to lower the hardening exponent as the initial yield stress or the hardness values increases. However, the

computational results indicate that the quantitative and qualitative results of the computations do not change significantly.

Figs. 2.15(a) and 2.15(b) show the distributions of the equivalent plastic strain near a weld from the finite element analysis at the applied displacements of 0.1 mm and 2.0 mm, respectively. Similar to the results of the 3-zone model, type A plastic zones ahead of the crack tips are clearly smaller than type B plastic zones due to the higher effective stress-plastic strain curve of the weld zone at the displacement of 0.1 mm. Similar to the results of the 3-zone model, type B plastic zones near the crack tips are the dominant plastic deformation mode at the displacement of 0.1 mm. As the displacement increases to 2.0 mm, type B plastic zones grow significantly, necking develops in both load carrying sheets, and plastic deformation concentrates on the base metal side of the boundary of the base metal and heat affected zone near both crack tips. However, unlike the results of the 3-zone model where the plastic strain is abruptly larger on the base metal side of the boundary of the base metal and the heat affected zone, the plastic strain is more uniformly distributed in the base metal and the heat affected zones which have lower effective stress-plastic strain curves. This allows for a smooth deformation mode and thus the crack tip profile resembles the deformed crack tip profile observed in the experiment.

The deformed mesh near a weld in a lap-shear specimen at the applied displacement of 2.4 mm is shown in Fig. 2.16(a). It should be noted that no failure criterion is selected for the finite element analysis and therefore the computation can continue to run at larger displacements than where the specimens actually failed during experiments. Similar to the result of the 3-zone model, the rotation of the weld zone is

observed and the concentrated plastic deformation between the crack tips is prevented due to the higher effective stress-plastic strain curves of the weld zone. The plastic deformation near the boundary of the base metal and heat affected zone close to the two crack tips becomes very large. The outer surface notch due to buckling can also be observed. This matches the micrograph of a weld in a lap-shear specimen before failure at the applied displacement of 1.95 mm as shown in Fig. 2.3(a) and again in Fig. 2.16(b). Although Figs. 2.16(a) and 2.16(b) correspond to different displacements, the general trend of the necking and the outer surface buckling of the lower left sheet can still be qualitatively correlated.

Failure prediction using Gurson's yield function

Gurson's yield function

Gurson [15] developed a yield function for porous materials, where the matrices are modeled by the Mises yield function, to account for the loss of stress carrying capacity due to microvoid nucleation and growth. The Gurson yield function Φ is expressed as [15], [16]

$$\Phi = \left(\frac{\Sigma_e}{\sigma_M} \right)^2 + 2q_1 f \cosh\left(q_2 \frac{3\Sigma_m}{2\sigma_M} \right) - 1 - q_3 f^2 = 0 \qquad (2.2)$$

where Σ_e is the macroscopic tensile effective stress based on the Mises yield function, Σ_m is the macroscopic mean stress, σ_M is the matrix flow stress, and f is the void volume fraction. Here, q_1, q_2 and q_3 are the fitting parameters which were first introduced by Tvergaard [23]. Chien et al. [24] obtained the fitting parameters for the Gurson yield function based on the Hill quadratic yield function for aluminum and steel

sheets with the anisotropy parameter R equal to 0.8 and 1.6, respectively. The fitting parameters are almost the same for both aluminum and steel sheets with $R = 0.8$ and $R = 1.6$. Although the Mises yield function ($R = 1$) is used for the macroscopic tensile effective stress Σ_e in the Gurson yield function in this investigation, the values of $q_1 = 1.45$, $q_2 = 0.95$ and $q_3 = 1.6$ for steel sheets obtained by Chien et al. [24] are taken in the finite element analysis.

The increase of void volume fraction arises from the nucleation of new voids and from the growth of the existing voids. For the increase rate of void volume fraction due to nucleation, we adopt the plastic strain controlled nucleation model suggested by Gurson [15] based on the experimental data in Gurland [25]. The increase rate of void volume fraction due to growth can be obtained from the plastic incompressibility of the matrix material. Thus the increase rate of void volume fraction can be expresses as

$$\dot{f} = \dot{f}_{nucleation} + \dot{f}_{growth} = A\dot{\varepsilon}_M^p + (1-f)\dot{\eta}_{.k}^{k\,p} \tag{2.3}$$

where the first term on the right-hand side of the equation represents the plastic strain controlled void nucleation rate and the second term represents the void growth rate. Here, $\dot{\varepsilon}_M^p$ is the matrix equivalent plastic strain rate, $\dot{\eta}_{.k}^{k\,p}$ represents the macroscopic dilatational plastic strain rate and A is expressed as

$$A = \frac{f_N}{s\sqrt{2\pi}} \exp\left[-\frac{1}{2}\left(\frac{\varepsilon_M^p - \varepsilon_N}{s} \right)^2 \right] \text{ for } \dot{\varepsilon}_M^p > 0 \tag{2.4}$$

Here, f_N is the volume fraction of void nucleating particles for the plastic strain controlled nucleation model, s is the standard deviation and ε_N is the mean value of the normal distribution for the plastic strain controlled nucleation model. In the finite

element analysis, the tensile stress-plastic strain curves for different zones of the 6-zone model are used as the matrix tensile stress-plastic strain curves. Without experimental data available for this HSLA steel, the void nucleation material parameters $f_N = 0.0085$, $\varepsilon_N = 0.2$ and $s = 0.04$ are assumed for all the material elements in the base metal, heat affected zone and weld zone in order to obtain some qualitative results on the void volume fraction distribution [26]. Other sets of void nucleation parameters were also chosen and the computational results in general have the same qualitative results as discussed in the following section.

Failure prediction

The failure of the laser weld in the lap-shear specimen is investigated by a finite element analysis with consideration of void nucleation and growth in all zones for the 6-zone model. Figs. 2.17(a) and 2.17(b) show the distributions of the equivalent plastic strain and the void volume fraction from the finite element analysis at the applied displacement of 1.2 mm, respectively. In the early stage of the deformation, the void volume fractions are very high for the elements near the two crack tips due to the large plastic strains near the tips. However, as the displacement increases, the higher stress-strain curves in the heat affected and weld zones near the crack tips suppress the increase of the plastic strains and, consequently, the void nucleation and growth in these zones, similar to the suppressing of the growth of type A plastic zones ahead of the tips. The void volume fractions of the material elements near the boundary of the base metal and the heat affected zone become larger than those near the crack tips due to the expansion of the type B plastic zones at the later stage of the deformation as shown in Fig. 2.17(a).

As shown in Fig. 2.17(b), the material elements with the larger void volume fractions are located near the left crack tip in the lower left load carrying sheet. This suggests that the initiation of ductile fracture due to void nucleation and growth should be observed near this location in failed specimens.

In fact, crack formation in a nearly failed specimen was observed near this location as shown in Fig. 2.3(a). Fig. 2.18(a) shows a SEM picture of a dimpled fracture surface due to void nucleation and growth on the upper portion of the fracture surface of the lower left sheet. Fig. 2.18(c) shows a SEM picture of a cleavage fracture surface on the lower portion of the fracture surface of the lower left sheet. The cleavage fracture surface corresponds to the final separation of the weld joint due to the loss of the load carrying capacity [14]. Fig. 2.18(b) shows a SEM picture of the middle portion of the fracture surface that represents the transition region from the dimpled fracture surface to the cleavage fracture surface. The crack formation location shown in Fig. 2.3(a) and the dimpled fracture surface on the upper portion of the fracture surface shown in Fig. 2.18(a) correlate very well with the results of the finite element analysis shown in Fig. 2.17(b).

Discussions

Based on the experimental observations of Asim et al. [14], several geometric features may affect the failure mode of the lap-shear specimen. The first geometric feature is the round protrusion. Its role as an additional constraint has been discussed in the previous section. The second geometric feature is the gap between the two sheets being welded together. The round protrusion is thought to be a byproduct of a gapless weld. Examination of the micrographs of many cross sections of lap-shear specimens

have led to the conclusion that if a gap exists between the two sheets, the round protrusion becomes shallow or even results in a concave surface due to the molten metal being distributed into the gap. Detailed discussions of the failure mode of the laser welds with gaps can be found in Asim et al. [14]. Note that the gap can create extra moment to the weld zone [14], [27] and, in turn, can reduce the failure strength of a lap-shear specimen.

The third geometric feature is the weld width. Here, the effects of the normalized weld width d/t on the plastic deformation mode are investigated for idealized welds (without protrusion and gap) based on the homogeneous material model. Figs. 2.19(a)-(e) show the deformed shapes and plastic strain distributions at the same displacement of 1.4 mm for the normalized weld widths of 0.7, 1.0, 1.1, 1.2 and 1.5 based on the homogeneous material model. Fig. 2.19(f) shows the angles of rotation for the non-load carrying sheet as a function of normalized weld width for the five cases. As shown in the figure, the angle of rotation of the non-load carrying sheet is maximum for the case of $d/t = 1.1$. For $d/t = 0.7$, 1 and 1.1, as the normalized weld width increases, the necking near the top surface of the lower left sheet and the bottom surface of the upper right sheet increases, the angle of rotation of the non-load carrying sheet increases, and the shear plastic deformation between the two crack tips becomes less intense. For $d/t = 1.1$, 1.2 and 1.5, as the normalized weld width increases, the necking near the top surface of the lower left sheet and the bottom surface of the upper right sheet decreases, the angle of rotation of the non-load carrying sheet decreases, and the shear plastic deformation between the two crack tips disappears. The critical normalized weld width for the transition of the shear plastic deformation mode between the two crack tips to the

necking/shear mode near the tips is near d/t =1.1 based on the homogeneous material model.

Conclusions

In this investigation, the experiments for laser welds in lap-shear specimens under quasi-static loading conditions are briefly reviewed first. The experimental results showed that the laser welds failed in a ductile necking/shear failure mode and the ductile failure was initiated at a distance away from the crack tip near the boundary of the base metal and heat affected zone. Two-dimensional plane strain finite element analyses were then carried out to understand the failure mode of laser welds in lap-shear specimens under quasi-static loading conditions. The results of the reference finite element analysis based on the homogeneous material model suggest a possible middle surface shear failure mode in the weld, which does not match with the experimental results. Therefore, the multi-zone models are developed to take into account the higher hardness values and the higher stress-strain curves of the heat affected and weld zones. The results of the finite element analyses based on the multi-zone non-homogeneous material models show that the higher effective stress-plastic strain curves of the weld and heat affected zones and the geometry of the weld protrusion can result in the necking/shear failure mode in the load carrying sheet. The results of the finite element analyses closely match with the experimental observations. Although lap-shear specimens are used to investigate the strength of the weld under shear dominant loading conditions, the load carrying sheets near the weld are subjected to dominant tensile deformation due to large plastic deformation. Note that Lin et al. [28] recognized the fact that the large plastic

deformation near a spot weld in a lap-shear sheet specimen gives dominant tensile deformation mode at the critical locations near the weld.

A two-dimensional plane strain finite element analysis of the lap-shear specimen with consideration of void nucleation and growth was also conducted. Initially, the material elements located near the two crack tips exhibit a high rate of void nucleation and growth. As the applied displacement increases, the plastic strains of the material elements of the base metal near the heat affected zone begin to exceed the plastic strains of the material elements near the crack tips due to the higher stress-strain behavior of the material elements in the heat affected zone. The location of the large void volume fraction gradually shifts from the material elements near the two crack tips to the material elements in the base metal near the heat affected zone. With the absence of the round protrusion, the void volume fraction is thought to be equal in the base metal regions for both the lower left and the upper right load carrying sheets due to symmetry. However, the round protrusion imposes additional geometric constraint to the lower left sheet and thus the computational results show that the void volume fractions are larger for the material elements on the base metal side of the boundary of the base metal and the heat affected zone. The location of the material elements with the larger void volume fraction matches well with that of the crack formation as observed in the experiment. With the adoption of the Gurson yield function, the location of the initiation of ductile fracture can be clearly correlated with the experimental observation as in the investigation of the ductile fracture mode of gas metal arc welds (GMAW) of HSLA steel sheets in Amodeo et al. [30]. It should be emphasized that the conclusions of this investigation are applicable to the laser welds in lap-shear specimens under quasi-static loading conditions.

Finally, the results of this investigation for laser welds, the research work of Lin et al. [28], [29] for resistance spot welds, and the research work of Amodeo et al. [30] for gas metal arc welds indicate that the failure mode of the welds in automotive structures should be examined carefully and the necking/shear failure mode needs to be considered for development of failure or separation criteria for welds under more complex loading conditions for crash simulations.

References

[1] Hsu C, Albright CE. Fatigue analysis of laser welded lap joints. Eng Fract Mech 1991; 39: 575-580.

[2] Wang PC, Ewing KM. A comparison of fatigue strengths: Laser beam vs. resistance spot welds. Welding J 1991; 70: 43-7.

[3] Flavenot JF, Deville JP, Diboine A, Cantello M, Gobbi SL. Fatigue resistance of laser welded lap joints of steel sheets. Welding in the World 1993; 31: 358-61.

[4] Wang PC. Fracture mechanics parameter for the fatigue resistance of laser welds. Int J Fatigue 1995; 17: 25-34.

[5] Ono M, Kabasawa M, Omura M. Static and fatigue strength of laser-welded lap joints in thin steel sheet. Welding Int 1997; 11: 462-7.

[6] Terasaki T, Sobue T, Kitamura T. Study of fatigue strength of laser welded lap joint. Q J Japan Welding Society 2001; 19: 507-12.

[7] Kaitanov AY, Ozersky AD, Zabelin AM, Kislov VS. Static and fatigue strengths of laser welded overlap joints with controlled penetration. Proc. SPIE 2002; 4644: 116-26.

[8] Cho SK, Yang YS, Son KJ, Kim JY. Fatigue strength in laser welding of the lap joint. Finite Elem Anal Des 2004; 40: 1059-70.

[9] Sonsino CM, Kueppers M, Eibl M, Zhang G. Fatigue strength of laser beam welded thin steel structures under multiaxial loading. Int J Fatigue 2006; 28: 657-62.

[10] Sripichai K, Asim K, Jo WH, Pan J, Li M. Fatigue behavior of laser welds in lap-shear specimens of high strength low alloy (HSLA) steels. SAE Technical Paper No. 2009-01-0028. Warrendale (PA): Society of Automotive Engineers; 2009.

[11] Chien WY, Pan J, Friedman PA. Failure prediction of aluminum laser-welded blanks. Int J Damage Mech 2003: 12: 193-223.

[12] Taban E, Deleu E, Dhooge A, Kaluc E. Laser welding of modified 12% Cr stainless steel: Strength, fatigue, toughness, microstructure and corrosion properties. Mater Des 2009; 30: 1193-200.

[13] Casavola C, Pappalettere C, Tattoli F. Experimental and numerical study of static and fatigue properties of titanium alloy welded joints. Mech Mater 2009; 41: 231-43.

[14] Asim K, Lee J, Pan J. Failure mechanism of laser welds in lap-shear specimens of high strength low alloy (HSLA) steel sheets. to be submitted for publication. 2011.

[15] Gurson AL. Continuum theory of ductile rupture by void nucleation and growth: Part 1 – yield criteria and flow rules for porous ductile media. J Eng Mat Tech 1977; 99: 2-15.

[16] Tvergaard V, Needleman A. Analysis of the cup-cone fracture in a round tensile bar. Acta Metallurgica 1984; 32: 157-69.

[17] Anand D, Chen DL, Bhole SD, Andreychuk P, Boudreau G. Fatigue behavior of tailor (laser)-welded blanks for automotive applications. Mater Sci Eng: A 2006; 420: 199-207.

[18] ABAQUS v6.7 User Manual. Providence, RI: SIMULIA; 2007.

[19] Jahn R, Cooper R, Wilkosz D. The effect of anvil geometry and welding energy on microstructures in ultrasonic spot welds of AA6111-T4. Metallurgical and Materials Transactions: A 2007; 38A: 570-83.

[20] Radaj D, Zheng Z, Möhrmann W. Local stress parameters at the weld spot of various specimens. Eng Fract Mech 1990; 37: 933-51.

[21] Nielson KL. 3D modelling of plug failure in resistance spot welded shear-lab specimens (DP600-steel). Int J Fract 2008; 153: 125-39.

[22] Dong P, Pan J. Plane-strain mixed-mode near-tip fields in elastic perfectly plastic solids under small-scale yielding conditions. Int J Fract 1990; 45: 243-62.

[23] Tvergaard V. Influence of voids on shear band instabilities under plane strain conditions. Int J Fract 1981; 17: 389-407.

[24] Chien WY, Pan J, Tang SC. Modified anisotropic Gurson yield criterion for porous ductile sheet metals. J Eng Mat Tech 2001; 123: 409-16.

[25] Gurland J. Observations on fracture of cementite particles in a spheroidized 1.05% c steel deformed at room temperature. Acta Metallurgica 1972; 20: 735-41.

[26] Chen Z, Worswick MJ, Keith Pilkey A, Lloyd DJ. Damage percolation during stretch flange forming of aluminum alloy sheet. J Mech Phys Solids 2005; 53: 2692-717.

[27] Tran VX, Pan J. Effects of weld geometry and sheet thickness on stress intensity factor solutions for spot and spot friction welds in lap-shear specimens of similar and dissimilar sheet materials. 2010; to appear in Eng Fract Mech

[28] Lin PC, Lin SH, Pan J. Modeling of failure near spot welds in lap-shear specimens based on a plane stress rigid inclusion analysis. Eng Fract Mech 2006; 73: 2229-49.

[29] Lin S-H, Pan J, Wu S, Tyan T, Wung P. Spot weld failure loads under combined mode loading conditions. SAE Technical Paper No. 2001-01-0428. Warrendale (PA): Society of Automotive Engineers; 2001.

[30] Amodeo CA, Lee J, Pan J. presented at the SAE 2010 World Congress, Detroit, Michigan, April 13-15, 2010; manuscript to be submitted for publication. 2010.

Table 2.1 The hardness values from indentation tests and the scaled initial yield stresses for the base metal, heat affected and weld zones for (a) the 3-zone model and (b) the 6-zone model.

(a) 3-zone model

	Base metal	Heat-affected zone	Weld
Vickers hardness	150	190	230
Yield stress σ_0 (MPa)	315	400	484

(b) 6-zone model

	Base metal	HAZ 1	HAZ 2	Weld 1	Weld 2	Weld 3
Vickers hardness	150	166	182	198	214	230
Yield stress σ_0 (MPa)	315	349	382	416	450	484

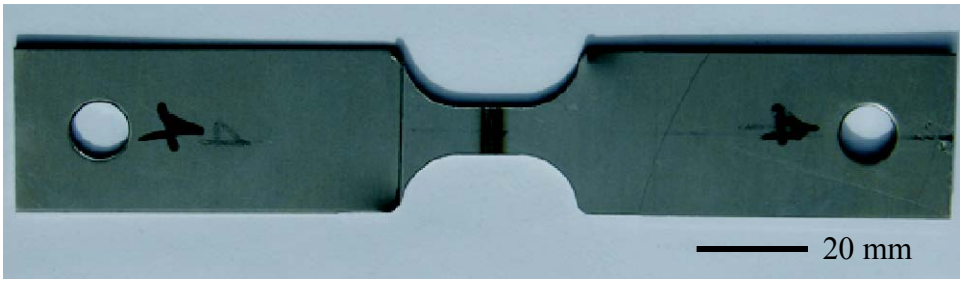

(a)

(b)

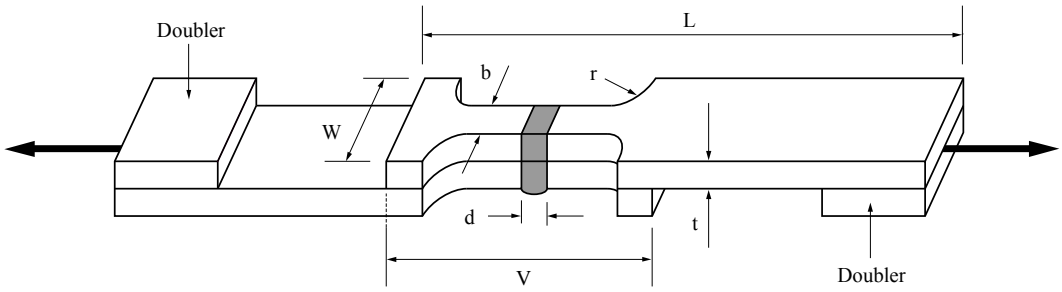

(c)

Fig. 2.1 (a) Top view, (b) bottom view and (c) a schematic of a lap-shear specimen.

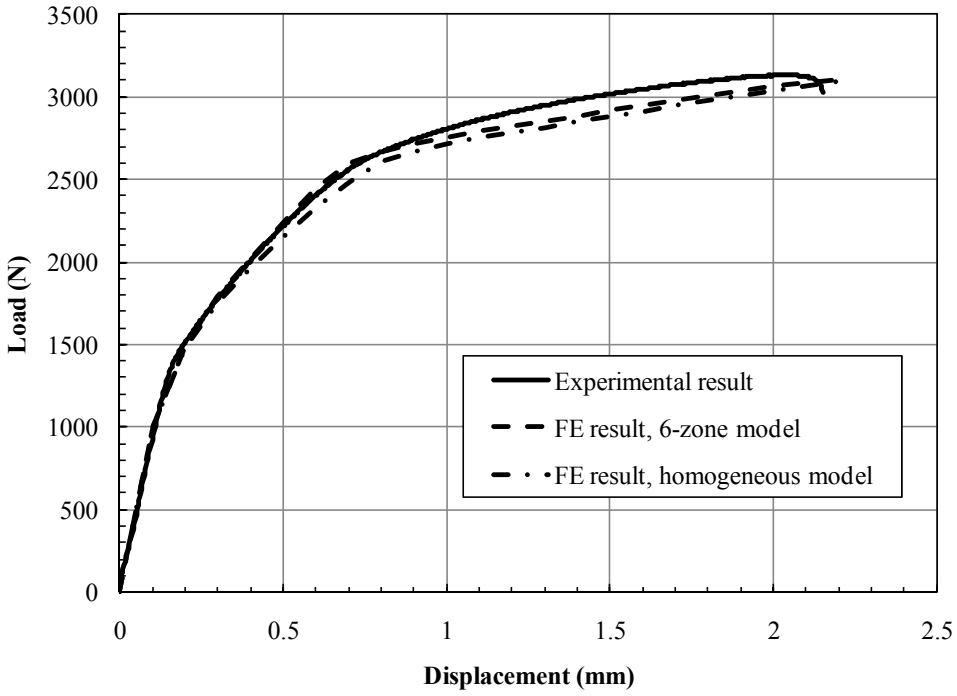

Fig. 2.2 The load-displacement curves of a lap-shear specimen from the experiment and the finite element analyses based on the homogeneous and 6-zone material model.

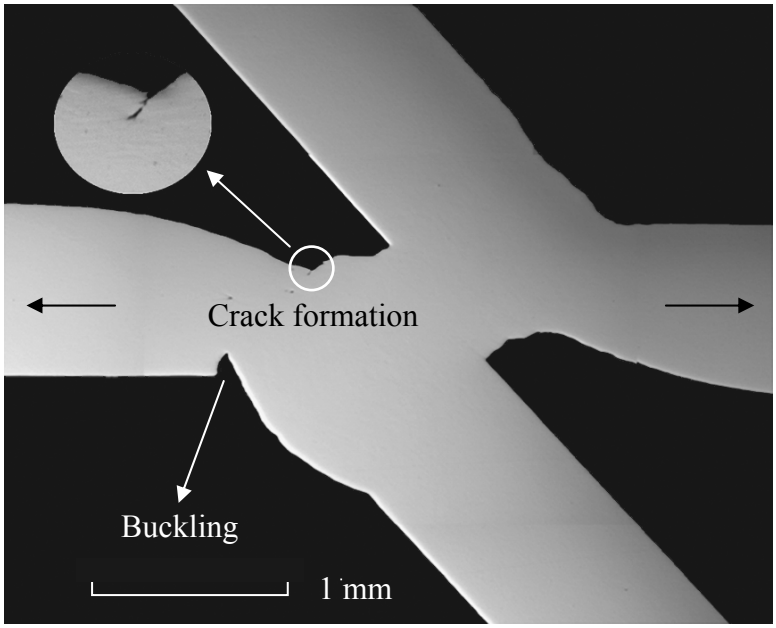

(a)

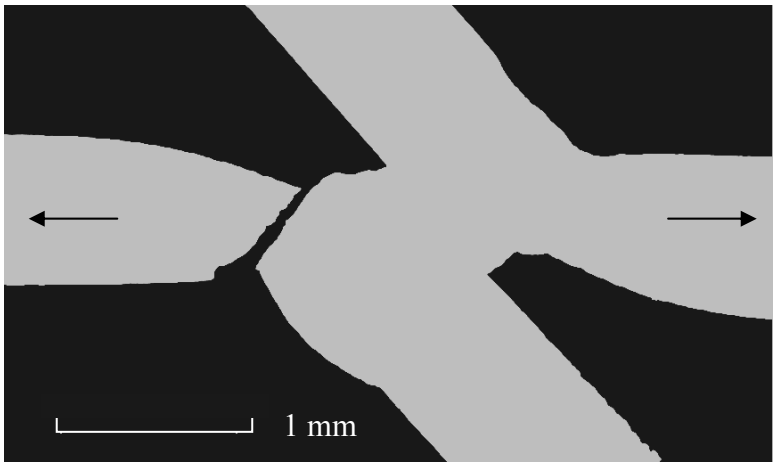

(b)

Fig. 2.3 A micrograph of the cross section near the weld from (a) a specimen just prior to failure and (b) a failed specimen.

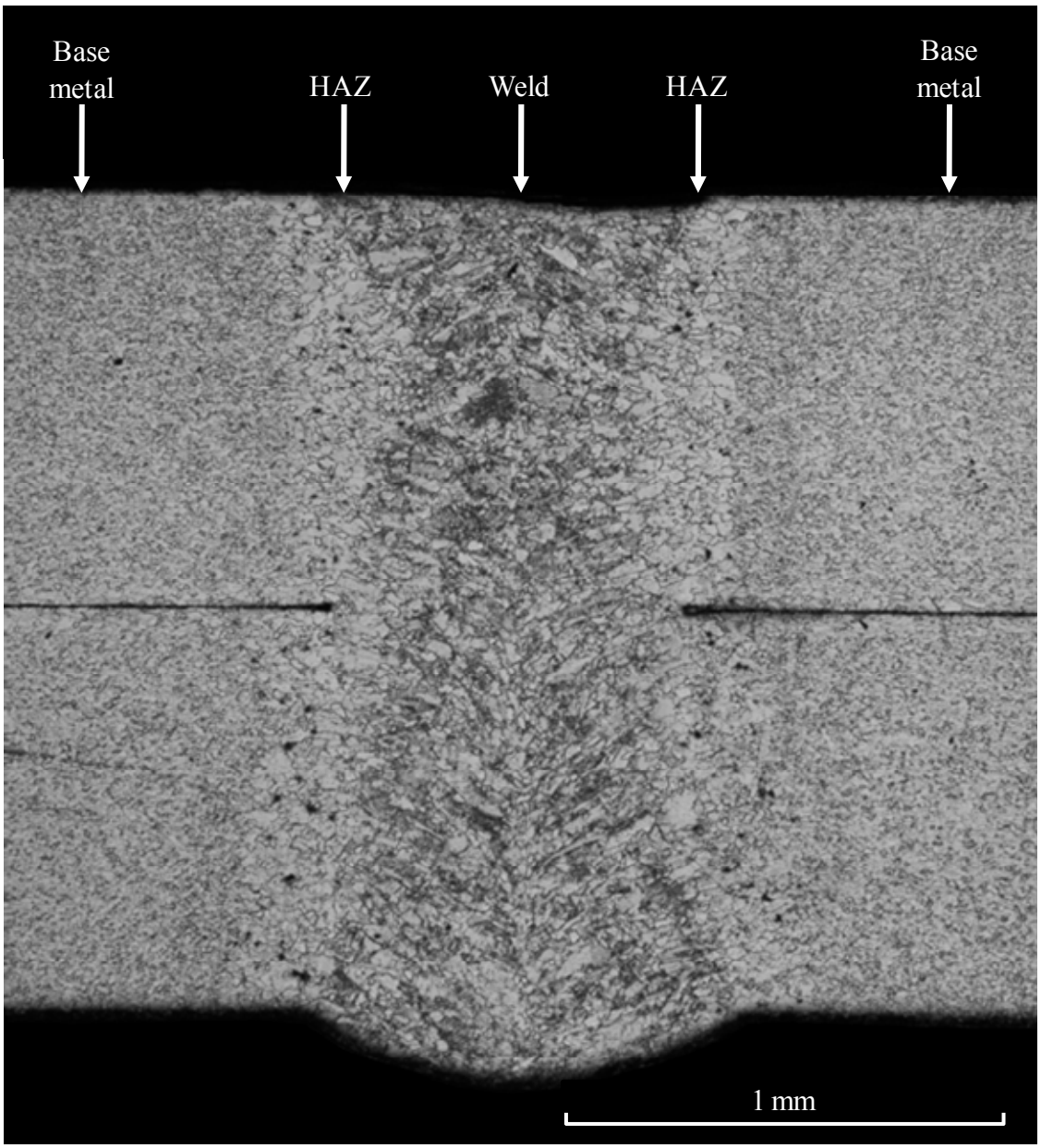

Fig. 2.4 A micrograph of the cross section of a laser weld in a lap-shear specimen.

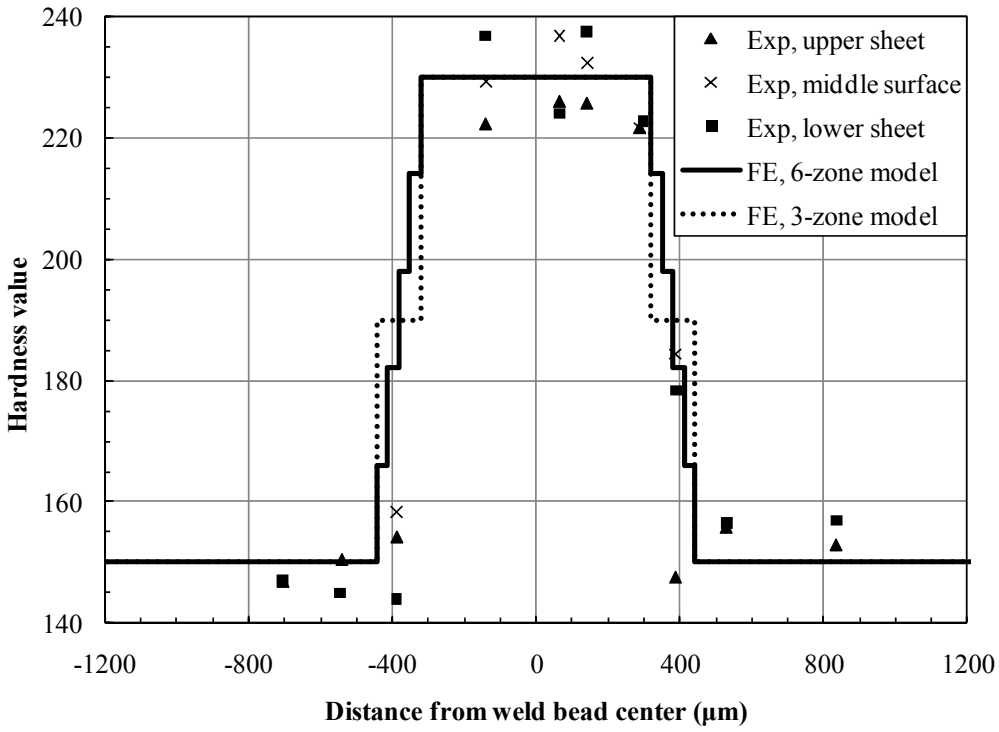

Fig. 2.5 The Vickers hardness values across the weld width obtained from the indentation tests and the assumed hardness values across the weld along the middle surface used in the 3-zone and 6-zone finite element analyses.

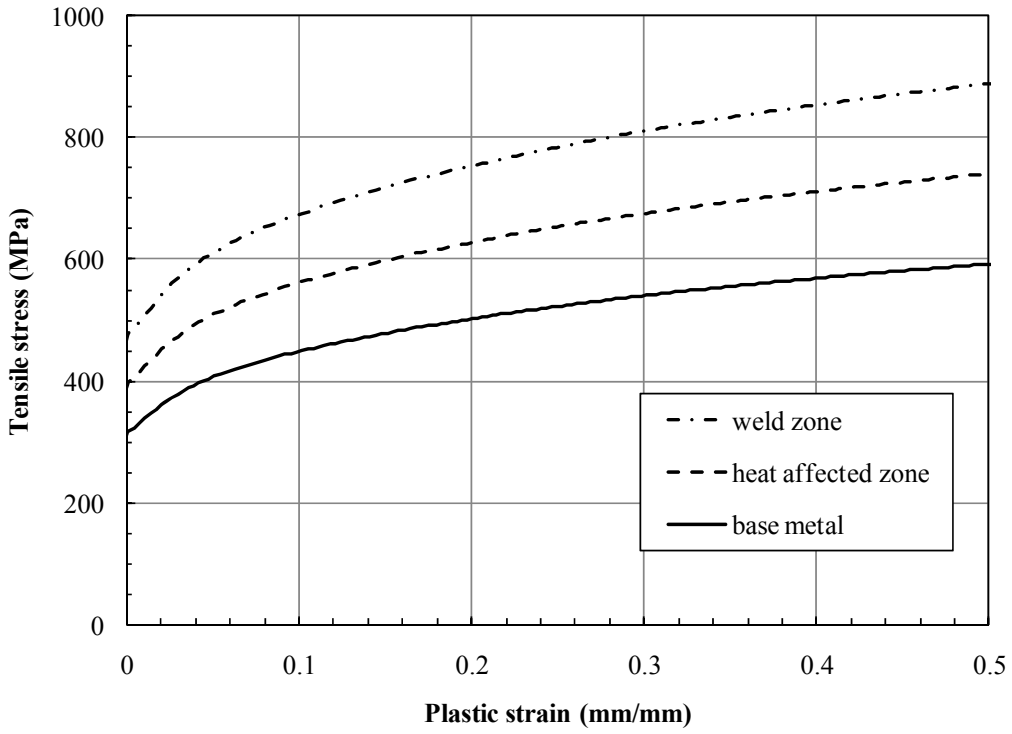

Fig. 2.6 The tensile stresses as functions of the plastic strain for the weld metal, heat affected zone and the base metal used in the 3-zone finite element analysis.

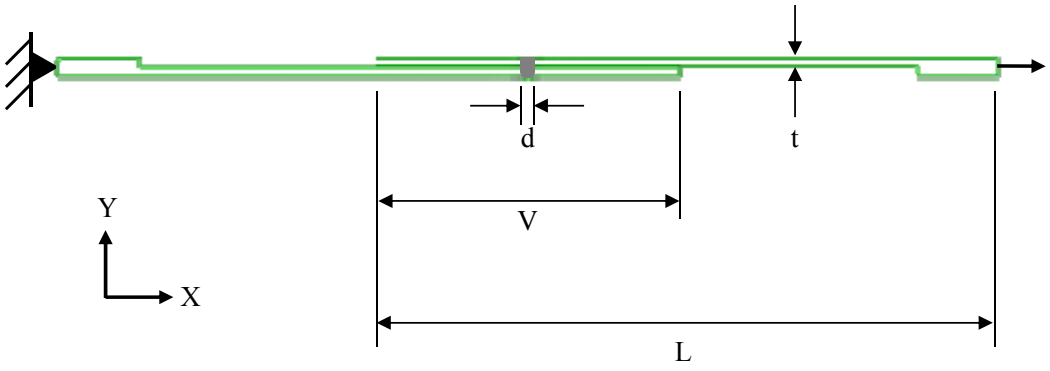

(a)

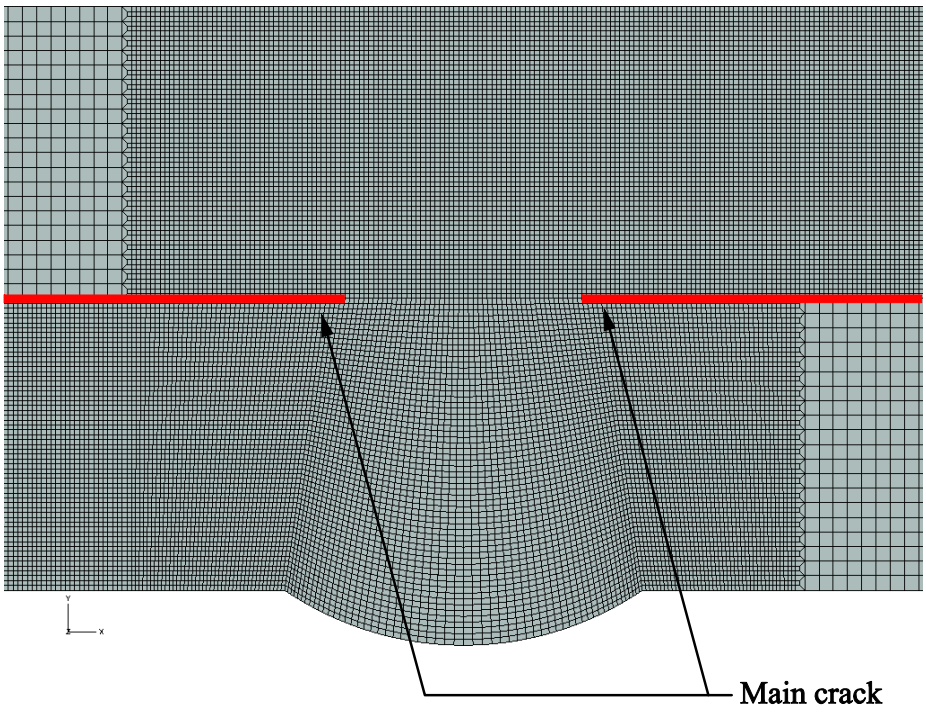

(b)

Fig. 2.7 (a) A schematic of a two-dimensional finite element model of a lap-shear specimen and the boundary conditions and (b) a close-up view of the finite element mesh near the weld.

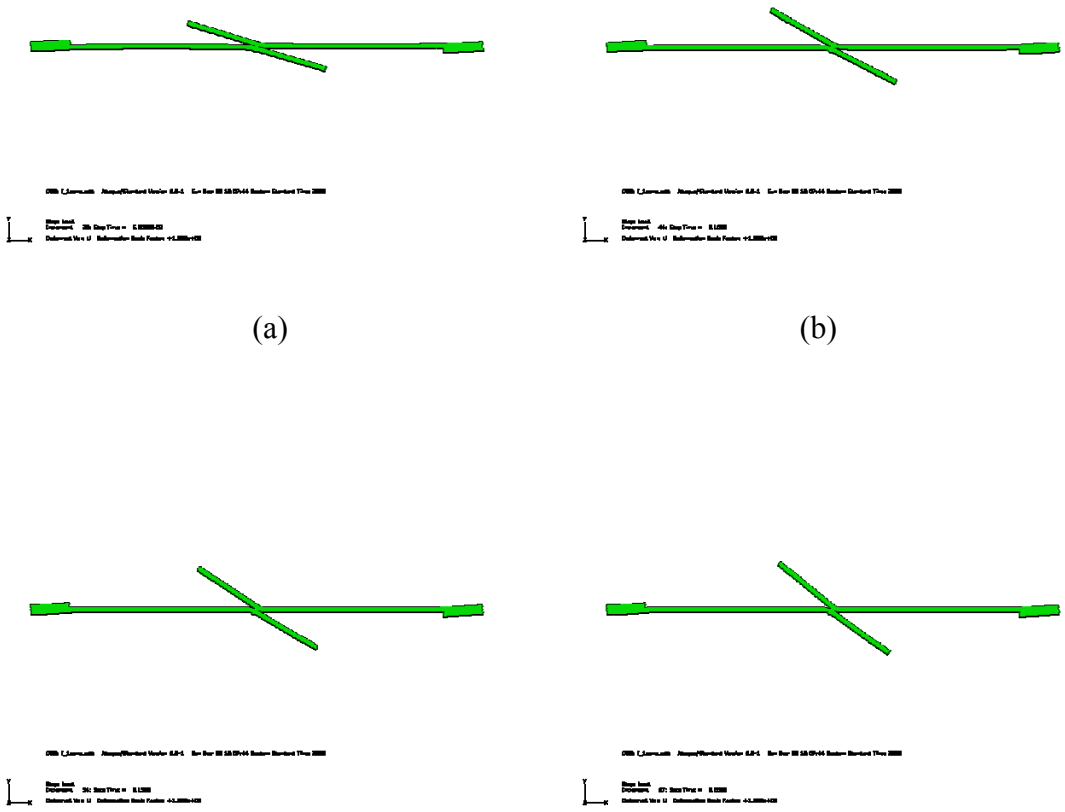

(a) (b)

(c) (d)

Fig. 2.8 Deformed shapes of a lap-shear specimen from the finite element analysis based on the homogeneous material model at the applied displacements of (a) 0.5 mm, (b) 1.0 mm, (c) 1.5mm and (d) 2.0 mm.

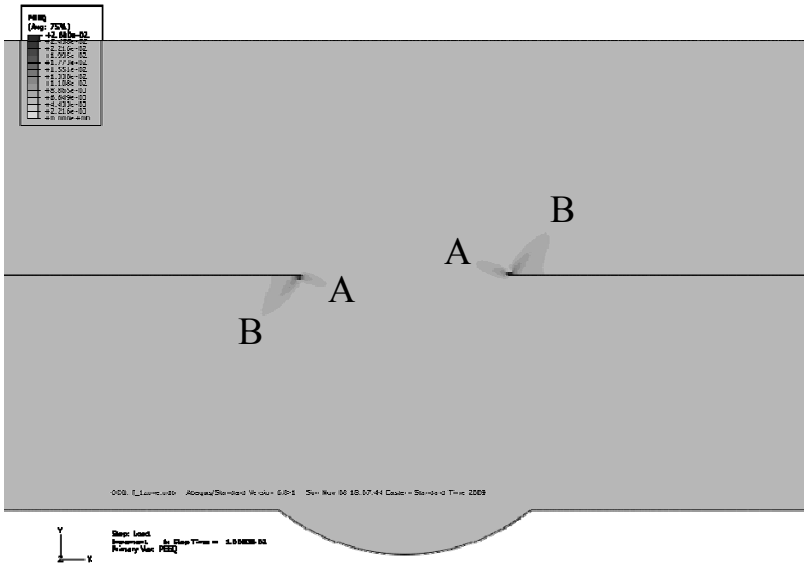

(a)

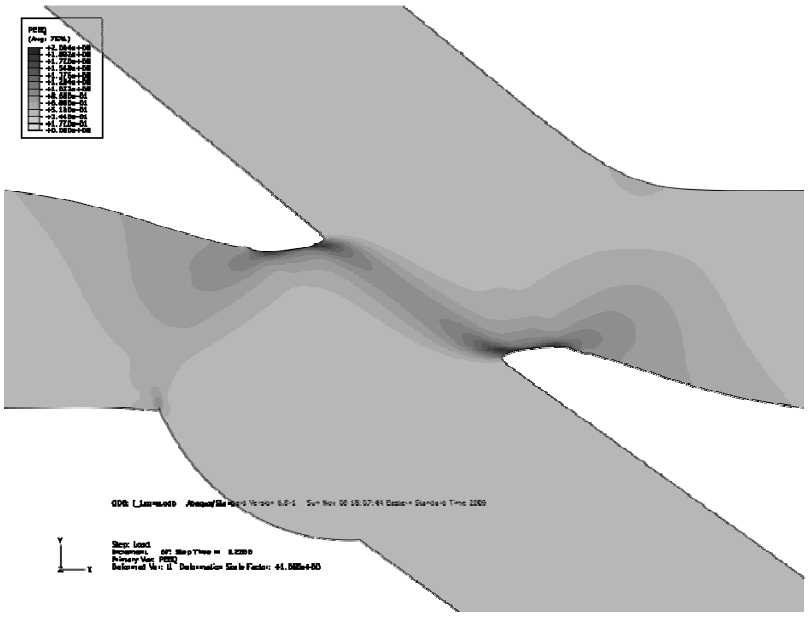

(b)

Fig. 2.9 Equivalent plastic strain distributions for the homogeneous model at the applied displacements of (a) 0.1 mm and (b) 2.0 mm. Fig. 2.9(a) shows type A and type B plastic zones.

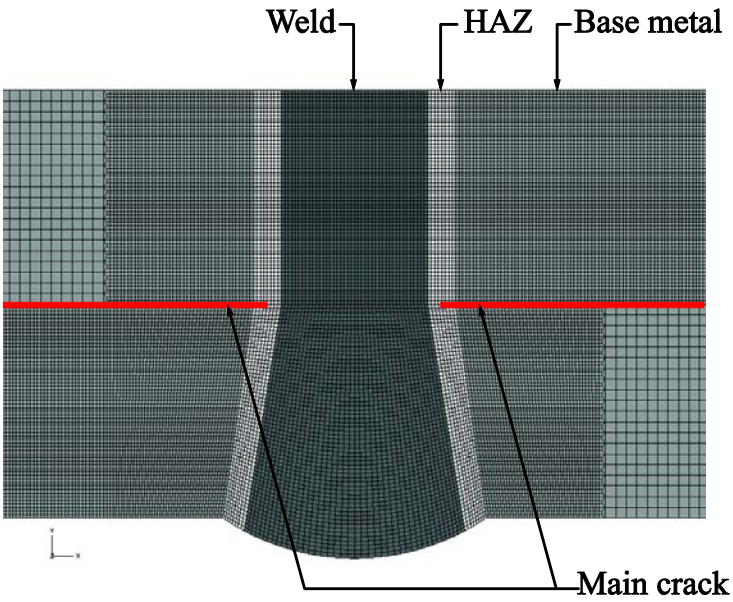

(a)

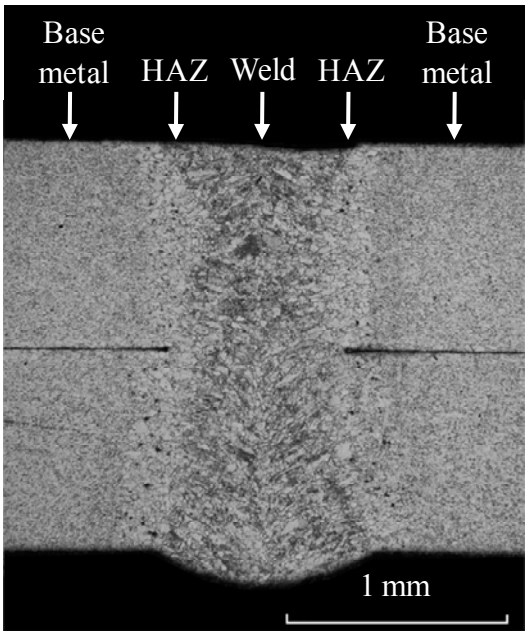

(b)

Fig. 2.10 (a) A schematic of the 3-zone finite element model with different material sections and (b) the corresponding micrograph of the cross section near a weld in a lap-shear specimen.

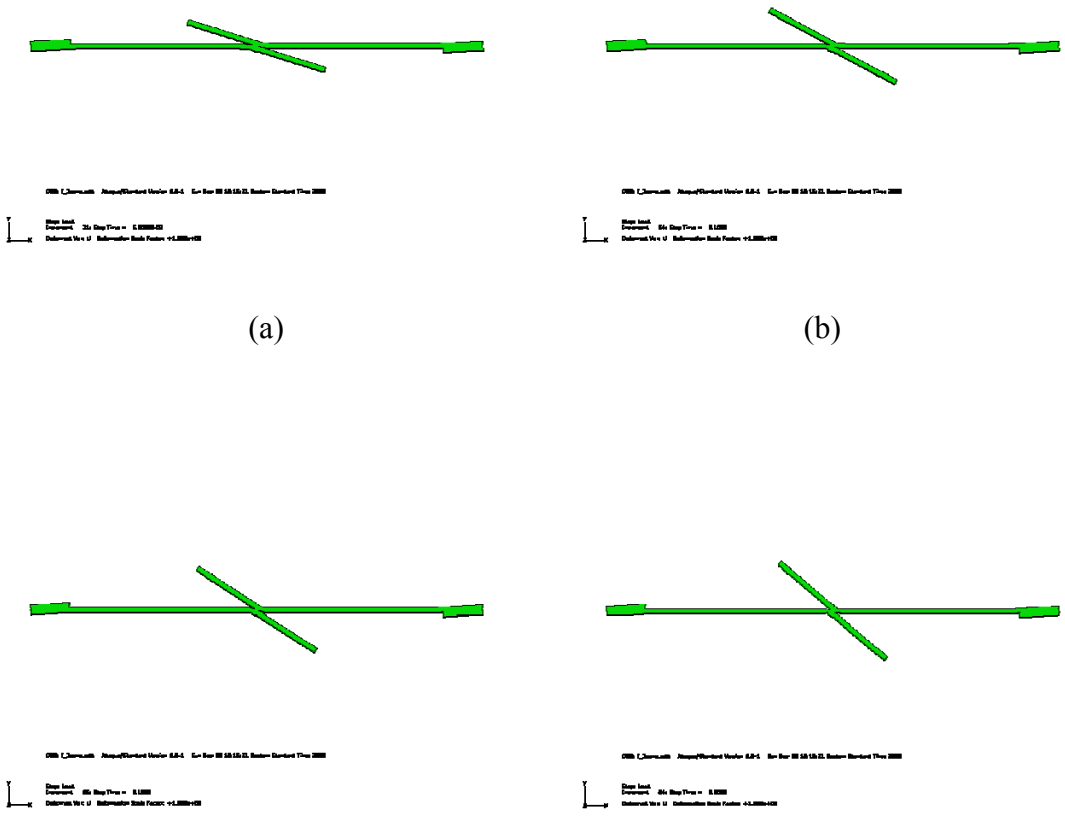

(a) (b)

(c) (d)

Fig. 2.11 Deformed shapes of a lap-shear specimen from the finite element analysis based on the 3-zone material model at the applied displacements of (a) 0.5 mm, (b) 1.0 mm, (c) 1.5mm and (d) 2.0 mm.

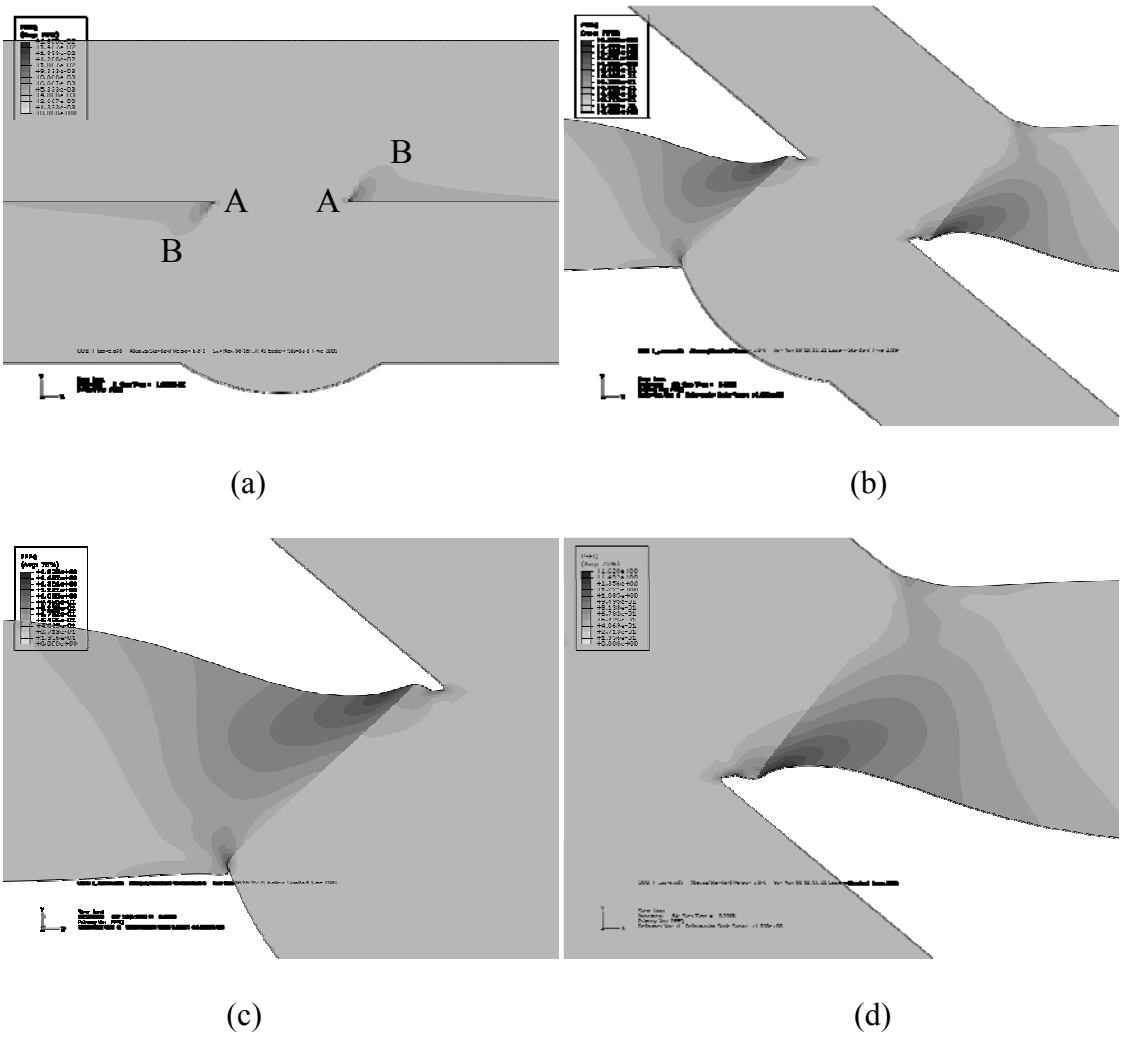

Fig. 2.12 Equivalent plastic strain distributions near a weld from the finite element analysis for the 3-zone model at the applied displacements of (a) 0.1 mm and (b) 2.0 mm. Close-up views of the deformed shapes and equivalent plastic strain distributions near (c) the left crack tip and (d) the right crack tip at the applied displacement of 2.0 mm.

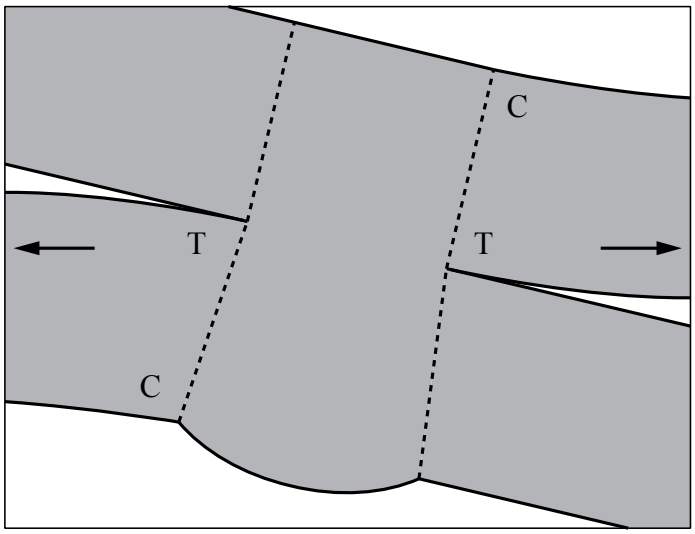

(a)

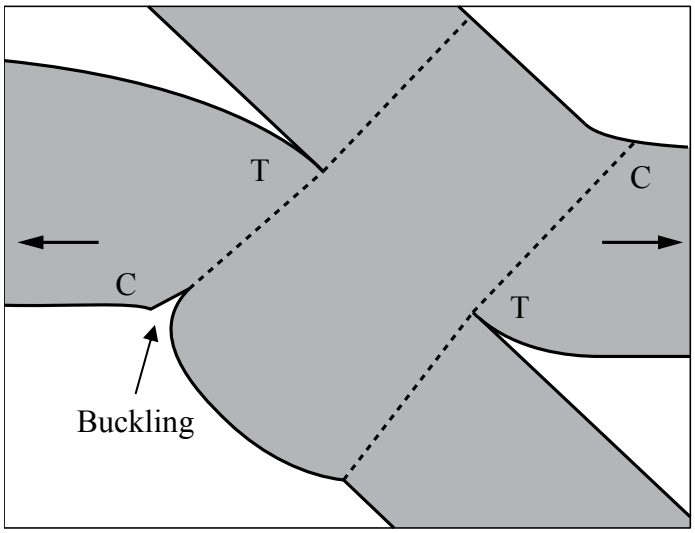

(b)

Fig. 2.13 Schematics of the tensile and compressive stress regions (a) before and (b) after the outer surface buckling of the lower left load carrying sheet.

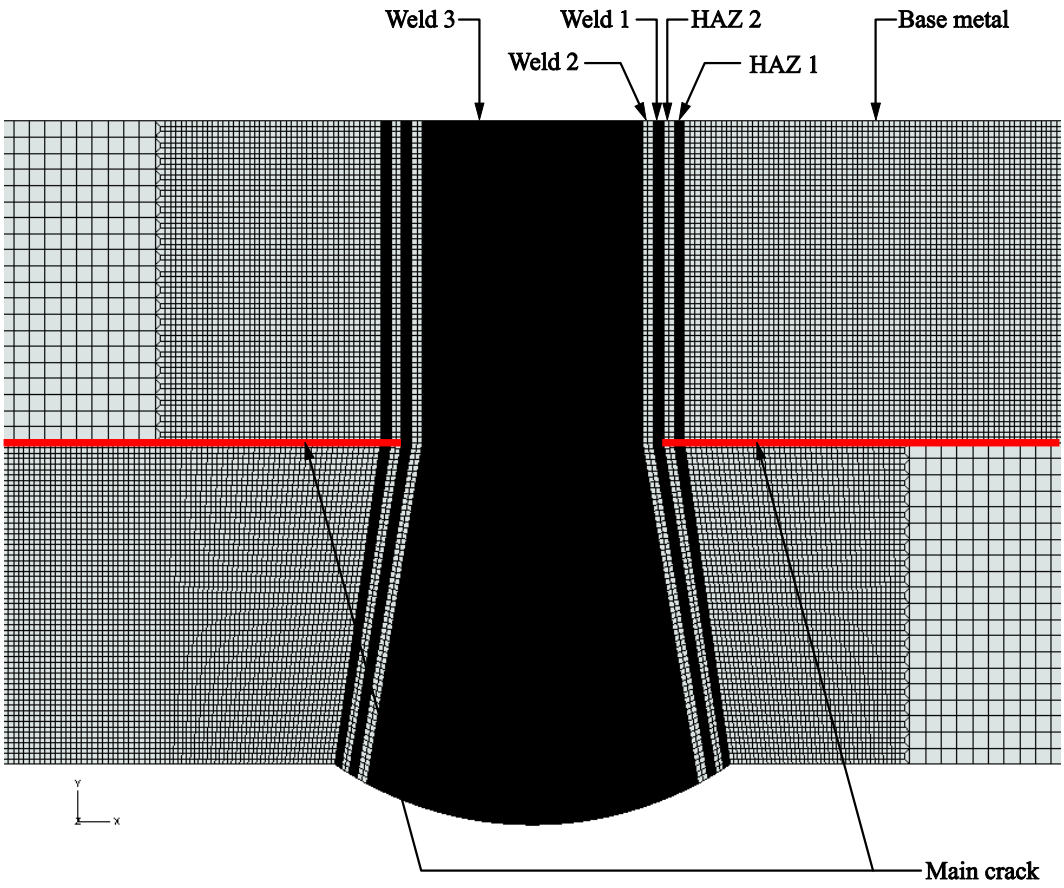

Fig. 2.14 A schematic of the 6-zone finite element model with different material sections.

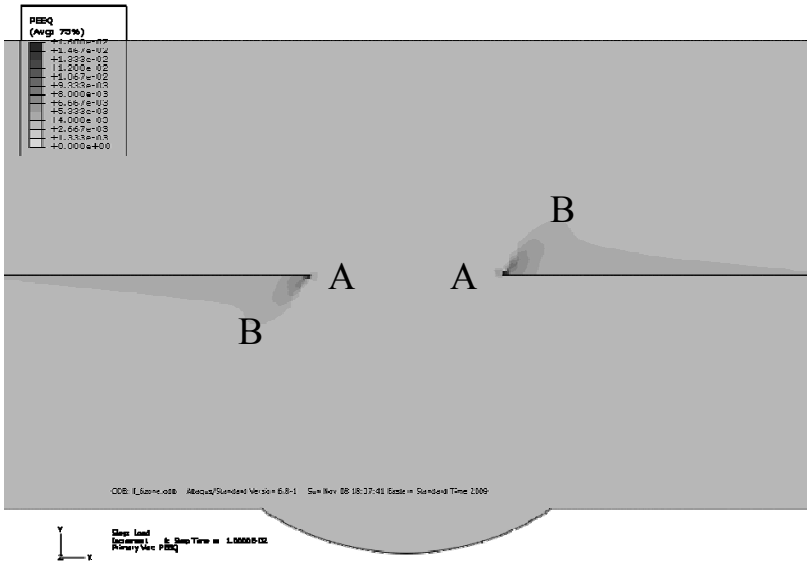

(a)

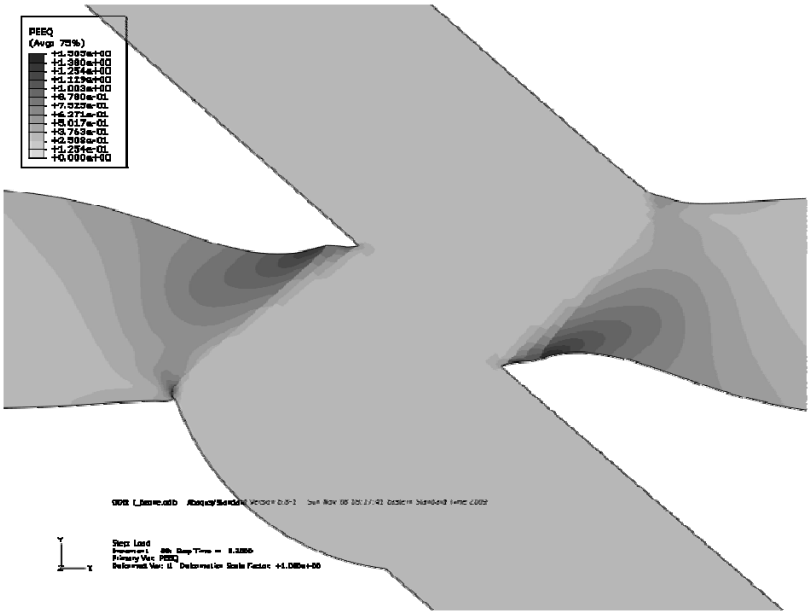

(b)

Fig. 2.15 Equivalent plastic strain distributions near a weld from the finite element analysis based on the 6-zone model at the applied displacements of (a) 0.1 mm and (b) 2.0 mm.

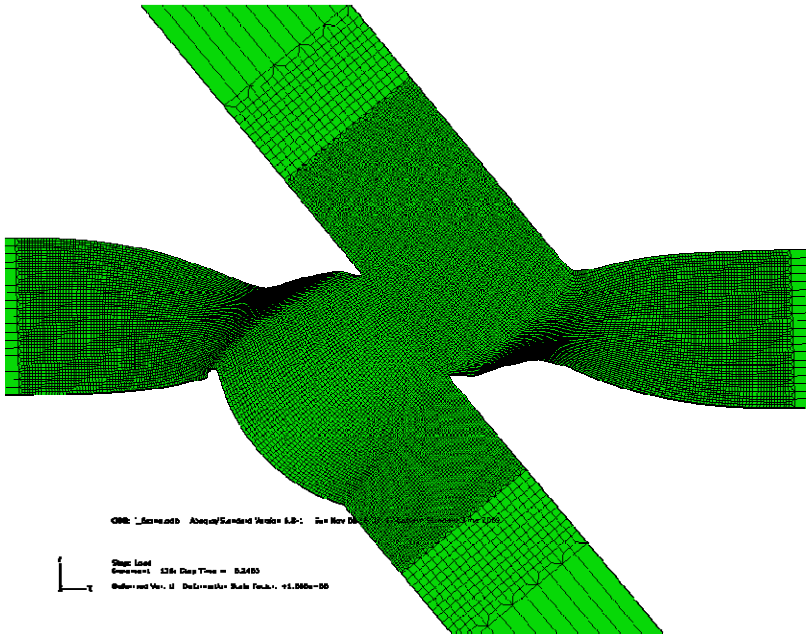

(a)

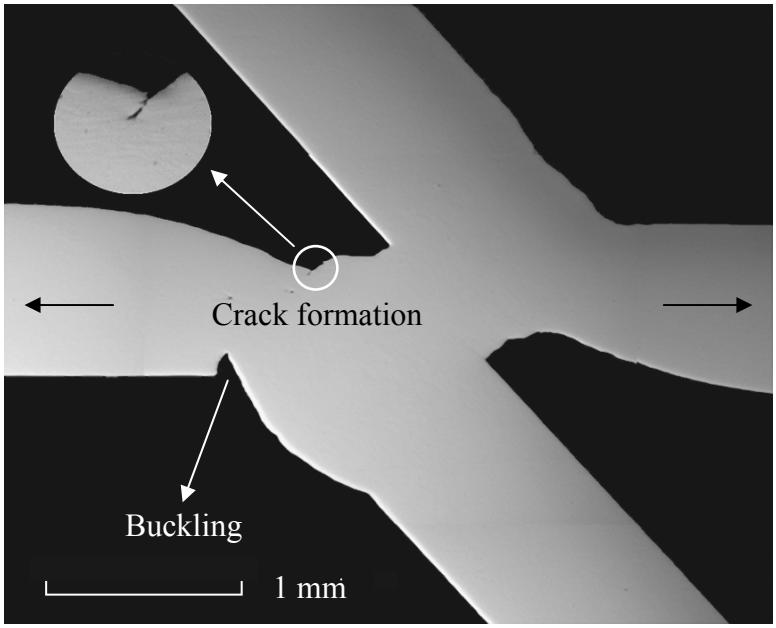

(b)

Fig. 2.16 The necking and the outer surface buckling of the lower left sheet from (a) the finite element analysis based on the 6-zone model and (b) the experiment.

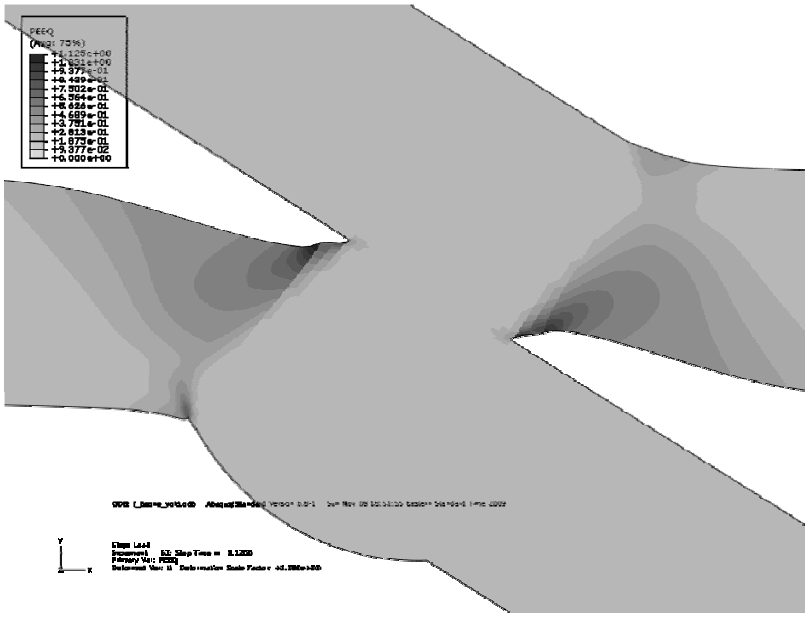

(a)

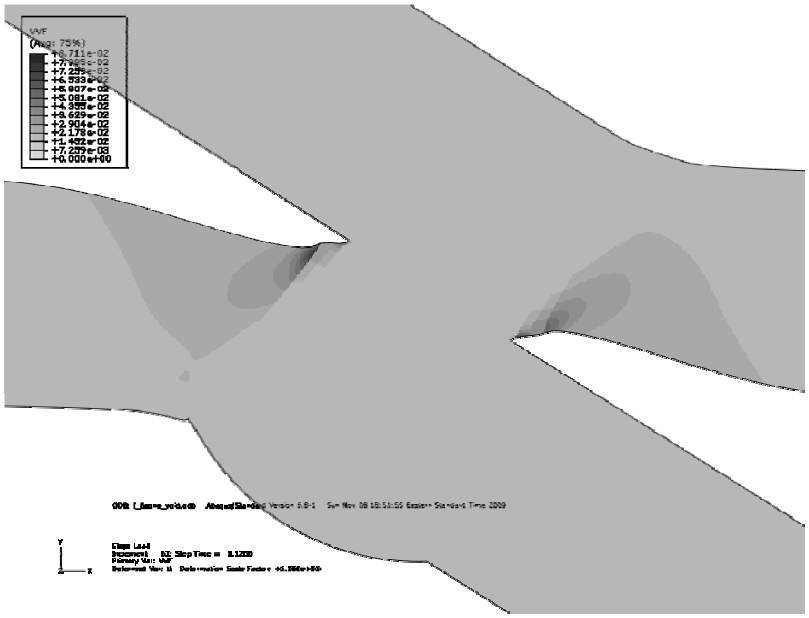

(b)

Fig. 2.17 The distributions of (a) the equivalent plastic strain and (b) the void volume fraction near a weld from the finite element analysis based on the 6-zone model at the displacement of 1.2 mm.

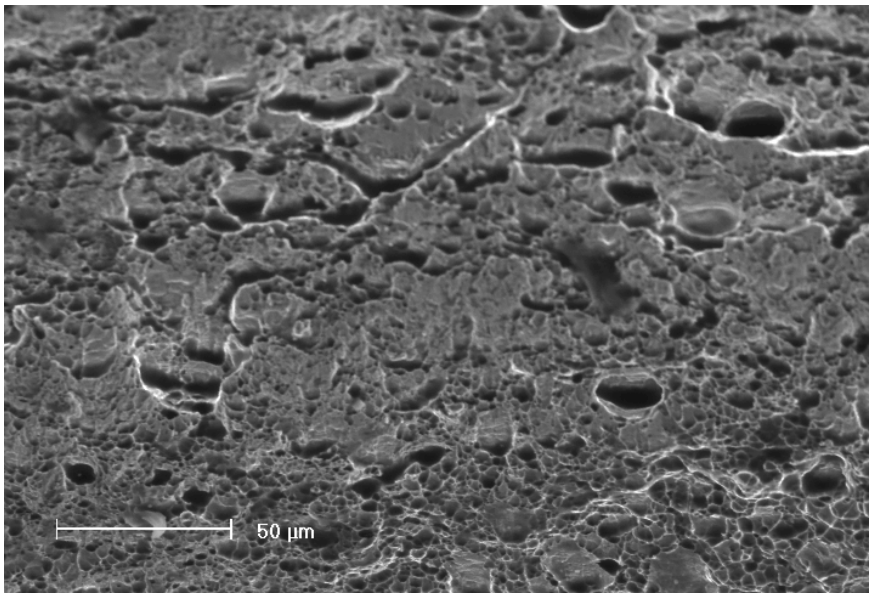

(a)

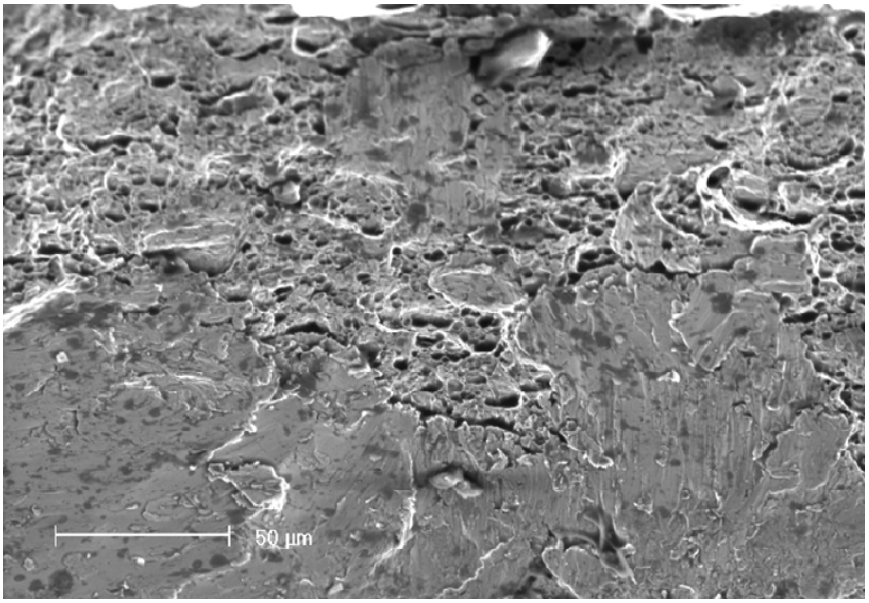

(b)

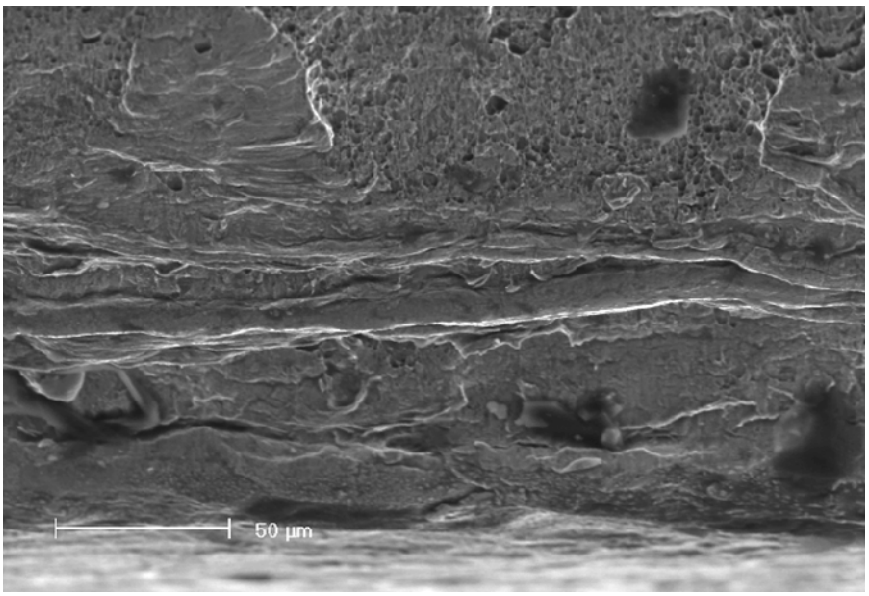

(c)

Fig. 2.18 SEM pictures of (a) the upper portion, (b) the transition region and (c) the bottom portion of the fracture surface of a failed lower left sheet.

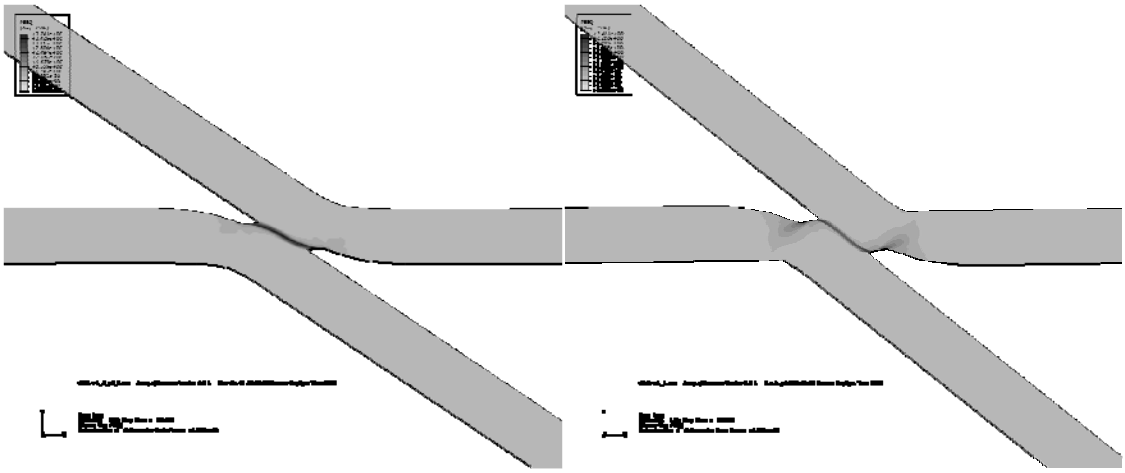

(a) (b)

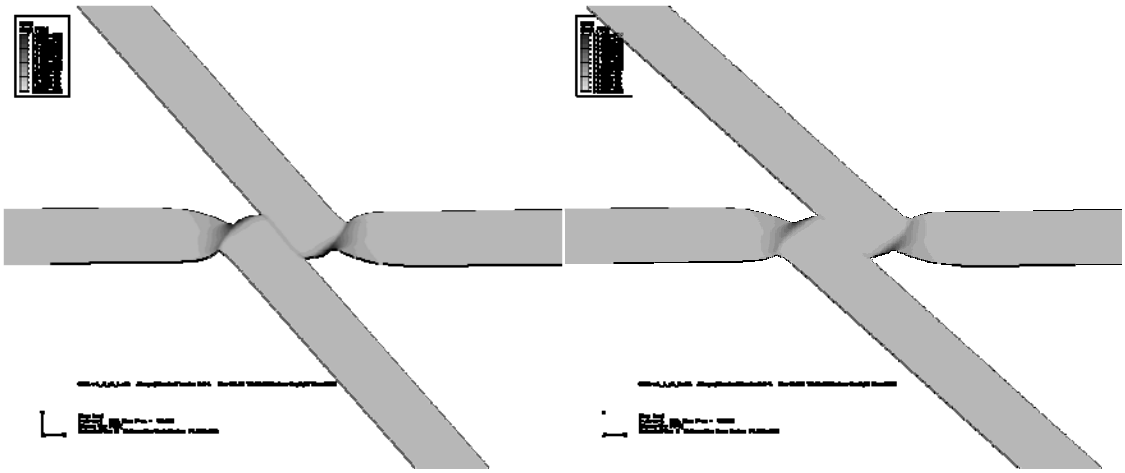

(c) (d)

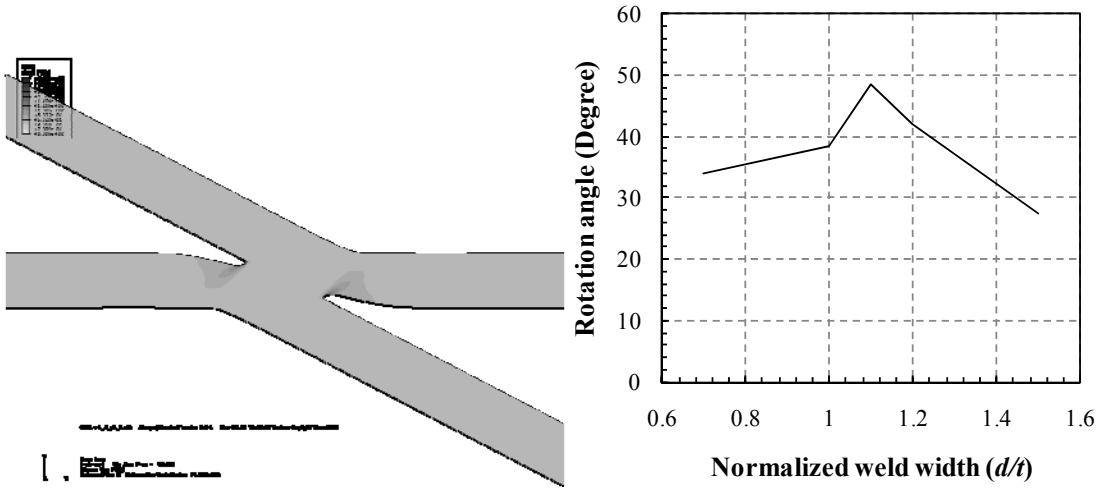

(e) (f)

Fig. 2.19 Deformed shapes and equivalent plastic strain distributions at the same applied displacement of 1.4 mm for the normalized weld width of (a) 0.7, (b) 1.0, (c) 1.1, (d) 1.2 and (e) 1.5 based on the homgeneous material model. The angles of rotation for the non-load carrying sheet as a function of normalized weld width for the five cases are shown in (f).

Chapter 3
Failure mode of ultrasonic welds in lap-shear specimens of magnesium and steel sheets

Introduction

In order to address rising concerns of fuel economy as well as environmental issues, the automotive industry is investigating ways to increase the use of lightweight materials such as magnesium or aluminum. By replacing steel in vehicles with magnesium and aluminum alloys, fuel consumption can be lowered by reducing the overall weight of the vehicle [1], [2], [3], [4]. Magnesium is 33% lighter than aluminum and 78% lighter than the traditional steel commonly used in vehicles. However, increasing use of magnesium requires overcoming technical challenges related to the joining of magnesium to steel. Joining magnesium to steel is especially challenging due to the large difference of their melting temperatures and immiscibility between magnesium and iron.

As magnesium alloys are considered for various structural components that need to attach to steel structures, the ability to reliably make durable and high-strength joints is becoming increasingly important. A complication for applying the traditional fusion welding methods comes from the fact that magnesium has a boiling temperature of 1107°C [5]. This is about 400°C lower than the melting temperatures of typical automotive sheet steels, which are in the vicinity of 1500°C. Melting magnesium alloy and steel together as might be done in resistance welding would vaporize the magnesium alloy creating unacceptable levels of porosity in the weld nuggets of resistance welds.

Due to the difficulty of the traditional fusion welding, solid state joining methods such as ultrasonic welding are poised to gain importance for joining magnesium to steel. Ultrasonic welding is considered as a solid-state bonding process that does not depend on or require melting to achieve a strong bond [6]. Other characteristics usually associated with ultrasonic welding are highly localized heating at the bond interface, relative insensitivity to modest levels of surface oxides and other contaminants, and the ability to make joints of dissimilar metals [7]. These characteristics provide the motivation for this study of using ultrasonic welding for joining magnesium to steel.

For joining similar materials by ultrasonic spot welding (USW) for automotive applications, researchers conducted studies on processing conditions of joining similar aluminum sheets, for example, see Hetrick et al. [8], Jahn et al. [9] and Wright et al. [10]. For joining dissimilar materials by USW, Watanabe et al. [11] conducted research on joining aluminum and steel sheets. Recently, Santella et al. [12] conducted research on joining magnesium to zinc-coated steel sheets by USW.

Lap-shear specimens are ideal to study the shear strength of a welded joint. The geometry of a lap joint provides pre-existing cracks or notch tips at the edges of the weld region. Lee et al. [13] and Asim et al. [14] recently conducted computational and experimental investigations on the failure mechanism and strength of laser welds in lap-shear specimens of high strength low alloy steel under quasi-static loading conditions. The lap-shear specimens were made in a dog-bone shape to avoid the failure of the specimen far away from the weld due to the necking of the specimen.

In this study, the failure mode of the ultrasonic weld in lap-shear specimens between magnesium and HSLA steel sheets under quasi-static loading conditions is investigated.

The lap-shear specimens were made in a dog bone shape in order to study the failure mode conveniently. Micrographs of the cross sections of ultrasonic welded lap joints were obtained before quasi-static tests. The results of a micro-hardness test with an ultrasonic weld of the magnesium sheet and a zinc-coated carbon steel sheet were used to assess the mechanical properties in the weld region which has varying microstructures due to the localized heat generated during the welding.

Finite element analyses were conducted to understand the effects of the weld geometry on the failure mode of ultrasonic welds in lap-shear specimens under quasi-static loading conditions. Due to the dog bone shape of the specimen, two-dimensional plane strain and plane stress finite element analyses using two-zone and multi-zone material models were carried out. The results of the finite element analyses are then compared with the experimental observations. Also, the J integral solutions for the pre-existing crack and a kinked crack with a small kink length are obtained from the finite element analyses. The J integral solutions can also be used to explain the observed failure mode of lap-shear specimens in the experiments. Finally, conclusions are made.

Experimental results

Lap-shear specimen

The lap-shear specimens used in the experiments were made by joining AZ31B-H24 magnesium alloy and HSLA steel sheets with a nominal thickness of 1.5 mm. The lap-shear specimen was made by using a 30 mm × 100 mm magnesium sheet and a 30 mm × 100 mm steel sheet with an overlap area of 30 mm × 75 mm. Prior to welding, the surfaces of the magnesium alloy sheets were buffed with non-metallic abrasive pads (Scotch-Brite™) to remove surface oxides. Both metals were cleaned with acetone

followed by isopropyl alcohol to remove lubricants and surface debris. The specimen preparation procedure and the processing conditions are explained in detail in Santella et al. [12]. An USW lap-shear specimen before being machined into a dog-bone shaped profile is shown in Fig. 3.1(a). The upper sheet is the magnesium alloy and the lower sheet is the steel.

A Sonobond CLF 2500 single-transducer, wedge-reed ultrasonic welder was used to weld the sheets into lap-shear specimens for quasi-static tests conducted in this investigation. The sonotrode tip was made from T1 steel and has a square face of 7 mm × 7 mm. The face has grooves as described by Jahn et al. [9]. A face view and a side view of the sonotrode tip are shown in Figs. 3.1(b) and 3.1(c), respectively. The only clamping during the welding was the pressure applied by the sonotrode tip. Specimens were positioned for welding so that the grooves on the sonotrode tip is parallel to the longitudinal axis of the lap-shear specimen and the primary vibration direction of the sonotrode was perpendicular to the longitudinal axis of the lap-shear specimen. Welding was made using a power of 1500 W. The pressure to the tip clamping mechanism was adjusted to make the welds under constant nominal pressure of 39 MPa.

The lap-shear specimens were then machined into a dog-bone shaped profile using a CNC milling machine. The specimen geometry in general follows the guidelines of the ANSI/AWS B4.0:2007 standard for the mechanical testing of welds. The central portion of the dog-bone shaped specimens has a reduced width. The width and length of the uniform straight part of the section with the reduced width are 8 mm and 13.5 mm, respectively. Figs. 3.2(a) and 3.2(b) show a top view and a bottom view of a lap-shear specimen after being machined into the dog-bone shaped profile. The weld zone (crack

tip to crack tip) has an average width of about 9 mm. Two doublers of 30 mm × 30 mm were used to align the fixture to avoid the initial realignment of the specimen due to the non-aligned grips under lap-shear loading conditions. Fig. 3.2(c) shows a schematic of a lap-shear specimen. As shown in the figure, the specimen has a width W, sheet thickness t and overall length L for the upper and lower sheets. The specimen has a reduced width b for the central portion, an overlap length V, a weld width d, an indentation width c and a fillet radius r for the weld zone. The dimensions of the specimens are W = 30 mm, t = 1.5 mm, L = 100 mm, b = 8 mm, V = 75 mm, d = 9 mm, c = 7 mm and r = 10 mm. Specimens with similar shapes were adopted by a number of researchers for the study of laser welded joints, for example, see, Lee et al. [13], Asim et al. [14], Anand et al. [15] and Sripichai et al. [16]. The detailed dimensions of the lap-shear specimens are listed in Table 3.1.

Weld microstructure

A USW lap-shear specimen before quasi-static testing was sectioned through the center of the weld along the loading direction of the specimen. Fig. 3.3(a) shows an optical micrograph of the cross section along the symmetry plane near the weld of the lap-shear specimen. As mentioned previously, the upper sheet is the magnesium and the lower sheet is the steel. It should be noted that the cross section in Fig. 3.3(a) has been created by cutting mostly through the ridge of the grooves created by the sonotrode tip rather than the valley. Therefore, the indentation depth appears to be shallow. During welding, the sonotrode tip indented into the upper magnesium alloy sheet and forced the magnesium under the tip to flow outward. The flash can be seen on both side of the indentation. The weld region reaches just outside of the visible indented region. On the

right side of the weld region, between the magnesium and the steel sheets, a gap and a visible Mg-Zn eutectic layer between the magnesium and steel sheets can be seen. On the left side, the Mg-Zn eutectic layer between the two sheets is quite thin and the gap between the two sheets can barely be seen. The uneven distribution of the Mg-Zn eutectic layer is possibly due to lack of constraint of the fixture and the upper sheet of the specimen [17].

Important features of the weld microstructures are shown in the micrographs in Figs. 3.3(b) and 3.3(c). The micrograph of Figs. 3.3(b) and 3.3(c) corresponds to the regions marked in Fig. 3.3(a). Fig. 3.3(b) shows the microstructure of the magnesium alloy away from the weld region. The micrograph shows a microstructure of equiaxed grains with an average size of about 5 μm. Fig. 3.3(c) shows a micrograph of the magnesium alloy near the interface directly beneath the center of the indenter tip. The magnesium alloy in this region is comprised of equiaxed grains of sizes of about 20 μm. The difference of the grain sizes is due to the grain growth under the high temperature generated during welding [12]. The grain size affects the hardness and the tensile stress-strain curve of the material as discussed later.

Quasi-static tests

The dog-bone shaped lap-shear specimens were tested under quasi-static loading conditions by using a MTS testing machine at a displacement rate of 1 mm per minute. Fig. 3.4(a) shows a lap-shear specimen just prior to failure at the applied displacement of 1.13 mm. Fig. 3.4(b) shows a failed lap-shear specimen with the upper right load carrying leg separated from the lap-shear specimen. The specimen failed at an applied displacement of 1.23 mm. During the tests, the weld region and the non-load carrying leg

rotated as the applied displacement increased. The angle of rotation continued to increase and a final value of 5° with respect to the line of loading was measured for a completely failed specimen. The rotation is the consequence of the non-uniform plastic deformation through the thickness of the load carrying sheet near the weld nugget.

Fig. 3.4(c) shows an optical micrograph of the fracture surface of the separated upper right load carrying sheet. Three distinct surfaces can be seen from the optical micrograph. The upper inclined surface was created during the welding due to the indentation of the sonotrode tip. The middle fracture surface is due to cracking from the sonotrode tip. The bottom fracture surface is due to cracking from the right pre-existing crack tip. The two cracks, each initiated and propagated from the sonotrode tip and the right pre-existing crack tip, converge and create the distinct intersection between the middle fracture surface and the bottom fracture surface as shown in Fig. 3.4(c).

Fig. 3.5 shows the load-displacement curves obtained from three quasi-static tests. The average maximum (or failure) load and the average maximum displacement obtained from three quasi-static tests are about 2,750 N and 1.23 mm, respectively.

Finite element simulations

Hardness measurement and stress-strain curve

Previous works by Lee et al. [13] and Asim et al. [14] have shown that the tensile stress-plastic strain curves of the weld region in laser-welded lap-shear specimen drastically affects the failure mode of the specimens under quasi-static loading conditions. Therefore, the variation of the tensile stress-plastic strain curves of the weld regions will be considered in this investigation.

A micro-hardness test was carried out to obtain the Vickers hardness values near the weld region for a USW of the magnesium sheet and a low carbon steel sheet specimen. An automated Vickers hardness tester at Oak Ridge National Laboratory was used to create micro hardness indentations as shown in Fig. 3.6(a). It should be noted that the low carbon steel sheet for the USW as shown in Fig. 3.6(a) is thinner than the HSLA steel sheet as shown in Fig. 3.3(a). The hardness measurements are shown as a grayscale map in Fig. 3.6(b) superposed over the cross section of the USW. A darker square represents a higher hardness value while a lighter square represents a lower hardness value. For the upper magnesium sheet, the highest hardness value measured is 78 and the lowest is 53. For the upper magnesium sheet, the far left region with relatively darker squares is assumed to be the region which is not affected by the welding. This region retains the grain microstructure and the hardness values of the base magnesium sheet as shown in Fig. 3.3(b). The region beneath the corner of the indentation have lighter squares which represents that the hardness values have decreased due to the grain growth associated with heat generation during the welding process. The variation in the hardness values along the longitudinal direction for the upper magnesium sheet can clarified by plotting the average of the four hardness measurements in the sheet thickness direction as shown in Fig. 3.6(c). The average hardness value for the base magnesium sheet region is around 70 HV. The hardness value sharply decreases near the corner of the indentation and decreases to about 64 HV beneath the indentation. Fig. 3.6(d) shows the average hardness values for the low carbon steel sheet. The highest hardness value is 107 and the lowest is 85. The transition region of the hardness values for the steel sheet is not at clear as the magnesium sheet.

Tension tests were conducted for the magnesium and steel sheets. The engineering stress-strain curves of three tensile specimens of the magnesium sheets are shown in Fig. 3.7. The tensile stress-strain curves of the magnesium sheets are fitted by an elastic power-law strain hardening relation based on the experimental tensile stress-strain curve as

$$\begin{aligned} \sigma &= E\varepsilon \quad \text{for} \quad \sigma \le \sigma_0 \\ \sigma &= K\varepsilon^n \quad \text{for} \quad \sigma > \sigma_0 \end{aligned} \tag{3.1}$$

where σ represents the tensile stress, E represents the elastic modulus, ε is the tensile strain and σ_0 is the initial yield stress. Here, K represents the strength coefficient and n represents the hardening exponent. The values of σ_0, K, n and E are determined for the magnesium sheets as 141 MPa, 254 MPa, 0.122 and 45 GPa, respectively.

Since it is difficult to determine the tensile stress-plastic strain curves for the magnesium of the weld region where the microstructure and the hardness value are different from that of the as-received magnesium sheets, the tensile stress-plastic strain curves for the magnesium of the weld region are estimated by scaling the tensile stress of the base magnesium region for a given plastic strain proportional to the corresponding hardness values of the weld region measured by the indentation tests as in [13]. For simplicity, only three tensile stress-plastic strain curves will be used for the magnesium sheet rather than scaling the tensile stress-plastic strain curves for all measured hardness values for the weld region. The magnesium regions with the hardness values higher than 71 HV will be defined as the base magnesium region. The regions with the hardness values lower than 61 HV will be defined as the low magnesium region. The regions with the hardness values between the base and low magnesium region will be defined as the

middle magnesium region. Three representative scaled stress-plastic stain curves for the base, middle and low magnesium of the weld regions are shown in Fig. 3.8.

The steel sheet will be considered to have a single tensile stress-plastic strain curve rather than multiple curves since the tensile stress-strain curve of the HSLA steel is much higher than those of the magnesium weld regions. The stress-strain curves of the HSLA steel in the weld regions should not change significantly due to the limited temperature increase during the welding.

The average values of the Vickers hardness and the scaled initial yield stresses for the base, middle and low magnesium regions as well as those for the HSLA steel are listed in Table 3.2. Fig. 3.8 also shows the tensile stresses as functions of the plastic strain for the HSLA steel. The tensile stress-plastic strain curves used in the two-zone and the multi-zone finite element models will be discussed in the next section. The tensile stress-plastic strain curves were used as the effective stress-plastic strain curves in the finite element analyses. The deformation histories of the material elements in the weld region in the lap-shear specimen obtained from the finite element analyses will be used to examine the failure mode of the ultrasonic welds that will be presented in the following section.

Finite element model

Finite element analyses based on the micrograph of the weld geometry as shown in Fig. 3.3(a) are carried out in this study to identify the influence of the weld geometry on the failure mode of the ultrasonic welds in lap-shear specimens. Two-dimensional finite element models are used to simulate the elastic-plastic behavior in the middle portion of the lap-shear specimen under plane strain conditions. Also, the two

dimensional finite element models are used to simulate the elastic-plastic behavior near the edges of the lap-shear specimen under plane stress conditions. Note that the ratio of the width to the sheet thickness is 5.2 for the narrow region of the dog-bone shaped lap-shear specimen. This ratio suggests that the majority of the crack front of the weld is possibly under plane strain loading conditions. However, the plane stress conditions near the edge of the crack front may be important and therefore both plane strain and plane stress conditions were considered in the finite element analyses.

Fig. 3.9(a) shows a schematic of the two-dimensional finite element model of a lap-shear specimen. The indentation due to the sonotrode tip is schematically shown in the figure. The Cartesian coordinate *x*-*y* system is also shown in the figure. As shown in Fig. 3.9(a), the middle plane of the left end of the model is fixed and the displacement is applied in the *x* direction at the middle plane of the right end of the model. First-order, isoparametric, quadrilateral, reduced integration, plane strain elements (CPE4R) are under plane strain conditions while plane stress elements (CPS4R) are used under plane stress conditions. The smallest element size near the crack tip is 0.0245 mm. Fig. 3.9(b) shows a close-up view of the finite element mesh near the right crack tip. For the magnesium alloy, the elastic modulus is taken as 45 GPa and the Poisson's ratio is taken as 0.3. For the steel, the elastic modulus is taken as 200 GPa and the Poisson's ratio is taken as 0.3. The Mises yield function is adopted to describe the elastic-plastic behaviors of the material elements with the previously described tensile stress-plastic strain curves used as the effective stress-plastic strain curves. The yield surface evolutions are assumed to follow the isotropic hardening rule. Computations were performed using the commercial finite element code ABAQUS v6.8 [18].

As previously mentioned, the geometry of the weld affects the failure mode significantly [13], [14]. The right crack tip and the corner of the indentation should have dominant influences on the plastic flow patterns and the failure modes. The relative position of these two locations can affect the plastic flow patterns and the failure modes of the lap-shear specimen. Therefore, four cases have been considered as shown in Figs. 3.10(a), 3.10(b), 3.10(c) and 3.10(d). The indentation due to the sonotrode tip is removed in the finite element model shown in Fig. 3.10(a) while the finite element models in Figs. 3.10(b), 3.10(c) and 3.10(d) have an indentation with a width of 7 mm. The depth of the indentation is selected as 0.625 mm for these three cases. The weld width is selected as 9 mm for the finite element models in Figs. 3.10(a) and 3.10(b). The weld widths are selected as 8 mm and 7 mm for the finite element models in 3.10(c) and 3.10(d), respectively. The right indentation corner in the 9 mm weld width model in Fig. 3.10(b) is located at an angle of 135° measured from the right crack face with the right crack tip as the origin. The right indentation corner of the 8 mm weld width model in Fig. 3.10(c) is located at an angle of 63.4° measured from the right crack face with the right crack tip as the origin. The right indentation corner in the 7 mm weld width model of Fig. 3.10(d) is located directly above the right crack tip.

The effect of the indentation on the failure mode can be determined by comparing the results of the finite element models in Figs. 3.10(a) and 3.10(b). The plastic flow patterns and crack growth propensity of the pre-existing crack tip towards the indentation corner can be examined by the three different weld width models as shown in 3.10(b), 3.10(c)and 3.10(d).

Since the bond between the Mg-Zn eutectic layer and the steel located near the right edge of the weld region appears to be weaker than the bond between the magnesium and the steel within the weld zone, the bond between the Mg-Zn eutectic layer and the steel will fail first at a lower load and the weld width effectively decreases, as suggested by the experimental observations of Franklin et al. [17]. It is assumed that under lap-shear loading conditions, a small amount of interfacial crack grows between the Mg-Zn eutectic layer and the steel first. As the crack propagates between the Mg-Zn eutectic layer and the steel, the crack tip will approach the interface between the magnesium and the steel where the bond appears to be stronger. The stronger bond disrupts the propagation of this interfacial crack. The effect of the location of the interfacial crack tip on the plastic flow patterns and the failure modes can be studied from the finite element models as shown in Figs. 3.10(b), 3.10(c) and 3.10(d).

Two types of material models were used in the finite element analyses as shown in Figs. 3.11(a), 3.11(b) and 3.11(c). The first material model is shown in Figs. 3.11(a) and 3.11(b) where a single stress-strain curve based on the base magnesium as shown in Fig. 3.8 is used for the entire magnesium sheet and a single stress-strain curve for the HSLA steel sheet is used for the entire steel sheet. This model will be referred to as the two-zone material model throughout this investigation. The second material model is shown in Fig. 3.11(c) where the three stress-strain curves for the base, middle and low magnesium as shown in Fig. 3.8 according to the hardness grayscale map of Fig. 3.6(b). This model will be referred to as the multi-zone material model throughout this investigation. The effect of the lower tensile stress-strain curves due to the change of the microstructure can be determined by using these two material property assignments.

Results of the finite element analyses

The deformed shape of the lap-shear specimen from the finite element analysis based on the 9 mm weld width, two-zone model with tool indention at the applied displacement of 1.2 mm is depicted in Figs. 3.12(a). The rotation of the non-load bearing sheets is visible. The angle of rotation of 4.5° is similar to the experimental result. Similar rotational behavior has been observed in simulations of lap-shear specimens with resistance spot welds in Lee et al [13], Radaj et al. [19] and Nielson [20].

The load-displacement curves of the lap-shear specimen obtained from the finite element analyses under plane strain and plane stress conditions based on the two-zone model with the 9 mm weld width and the tool indentation are shown in Fig. 3.12(b). The load-displacement curve of an actual lap-shear specimen should be lower than load-displacement curve under plane strain conditions but higher than that under plane stress conditions. The experimental load-displacement curve seems to fit between the load-displacement curves under plane strain and plane stress conditions.

The load-displacement curves of the lap-shear specimen from the finite element analyses based on the two-zone models with the 9 mm, 8 mm and 7 mm weld width and the tool indentation are shown in Fig. 3.12(c) to compare with the experimental result. The load-displacement curves of the three models seems to match well at small displacements. The load-displacement curve is slightly lower for a smaller weld width at large displacements.

Fig. 3.13 shows the equivalent plastic strain distributions near the right crack tip at the displacement of 0.3 mm under plane strain conditions for the two-zone model with the 9 mm weld width and without the tool indentation. Figs. 3.14(a), 3.14(b) and 3.14(c)

show the equivalent plastic strain distributions near the right crack tip at the displacement of 0.3 mm under plane strain conditions for the two-zone model with the 9 mm, 8 mm and 7 mm weld widths and the tool indentation, respectively. Figs. 3.15(a), 3.15(b) and 3.15(c) show the equivalent plastic strain distributions near the right crack tip at the displacement of 0.3 mm under plane strain conditions for the multi-zone model with the 9 mm, 8 mm and 7 mm weld widths and the tool indentation, respectively.

The plastic zone sizes near the crack tip are large in two directions due to the mixed mode loading conditions and the constraint conditions imposed by the loading and geometry of the lap-shear specimen for all models as shown in Figs. 3.13, 3.14 and 3.15. The plastic zones in these two directions are marked as A and B in Figs. 3.13, 3.14 and 3.15. Note that for elastic perfectly plastic materials, centered fan sectors can result in large sizes of plastic zones in these directions [21]. At the relatively small displacement of 0.3 mm, plastic zone B is larger compared to plastic zone A.

As the applied displacement increases, both plastic zones in the A and B directions near the right crack tip develop. Fig. 3.16 shows the equivalent plastic strain distributions near the right crack tip at the displacement of 1 mm under plane strain conditions for the two-zone model with the 9mm weld width and without the tool indentation. Both plastic zones develop at the larger applied displacement but fail to link with the plastic deformation on the upper surface due to a lack of a plastic flow initiation site on the upper surface of the magnesium sheet at this displacement.

The absence of a dominant plastic deformation mode as shown in Fig. 3.16 does not necessary lead to the conclusion that the lap-shear specimen will not fail under the applied displacement. The focus of this study is the effect of the indentation on the

plastic flow patterns. The model without the indentation serves its purpose to show that the presence of the indentation accelerates the development of a dominant plastic deformation mode. With the indentation as shown in Figs. 3.17 and 3.18, the plastic zones link up with the indentation corner which acts as a plastic flow initiation site, and develop into a dominant plastic deformation mode.

Figs. 3.17(a), 3.17(b) and 3.17(c) show the equivalent plastic strain distributions near the right crack tip at the displacement of 1 mm under plane strain condition for the two-zone model with the 9 mm, 8 mm and 7 mm weld widths and the indentation, respectively. In Fig. 3.17(a), the right indentation corner is located in the direction of plastic zone A from the right crack tip. The plastic zone A from the right crack tip links up with the plastic zone of the indentation corner and develops into a dominant plastic shear deformation mode. In Fig. 3.17(b), plastic flow patterns similar to the plastic zones A and B near the right crack tip develop from the corner of the indentation as the displacement increases. One of the plastic zones from the indentation corner and the plastic zone B from the right crack tip link up with each other. The plastic zones from the indentation corner and the crack tip create a distinctive plastic flow pattern which resembles the fracture surfaces of the failed specimen as shown in Fig. 3.4(c). Fig. 3.17(c) shows the plastic flow pattern for the 7 mm weld width model. As shown in the figure, the plastic zone from the indentation corner and the plastic zone from the right crack tip do not link as those in Fig. 3.17(b). One possible reason that the two plastic zones do not link up is that the plastic zone from the indentation corner grows to the opposite surface of the magnesium sheet to accommodate the applied displacement. There is no need to link with the plastic zoned from the crack tip to accommodate the applied displacement.

Finally, as shown in Figs. 17(b) and 17(c), the crack faces make contact due to the large scale yielding of the magnesium sheet.

Figs. 3.18(a), 3.18(b) and 3.18(c) show the equivalent plastic strain distributions near the right crack tip at the displacement of 1 mm under plane strain conditions for the multi-zone model with the 9 mm, 8 mm and 7 mm weld widths and the indentation, respectively. As can be seen, the plastic flow patterns are similar to those of the corresponding two-zone models. Therefore, it seems that the variation of the material stress-strain curves due to the variation of the hardness values has no significant effects on the failure mode of the welds.

J integral solutions for pre-existing and kinked cracks

In this section, the *J* integral solutions for the pre-existing crack tip and a kinked crack with a small kink length obtained from the finite element analyses based on the multi-zone material model with the previously mentioned three weld widths are used to explain the failure mode observed in the experiment. Fig. 3.19 shows a schematic of a crack and an arbitrary contour Γ surrounding the crack tip. As shown in the figure, a Cartesian coordinate system is centered at the crack tip. The *J* integral is defined as [22]

$$J = \int_{\Gamma} \left(W n_x - T_i \frac{\partial u_i}{\partial x} \right) ds, \left(i = x, y, z \right) \tag{3.2}$$

where Γ represents a counterclockwise contour enclosing the crack tip from the lower crack face to the upper crack face, *ds* represents the differential arc length of the contour Γ, n_x represents the *x* component of the unit outward normal **n** to the differential arc length *ds*, $T_i \left(= \sigma_{ij} n_j \right)$ represent the components of the traction vector **T** on the

differential arc length ds, and u_i represent the components of the displacement vector **u**. In the above equation, the strain energy density W is defined as

$$W = \int_0^{\varepsilon_{ij}} \sigma_{ij} d\varepsilon_{ij}, \quad (i, j = x, y, z) \tag{3.3}$$

The J integral is path independent for a crack in a homogenous non-linear elastic material. For elastic-plastic power-law strain hardening materials under proportional loading conditions, the J integral can be used to represent the singularity amplitude of the crack-tip stress and strain fields.

Fig. 3.20 shows a close-up view of the finite element model near the right pre-existing crack tip for the multi-zone model with the 7 mm indentation and 9 mm weld width. A total of nine contours were assigned in the finite element model to obtain the J integral solutions. These contours are shown as thick lines surrounding the right pre-existing crack tip in Fig. 3.20. The area above the pre-existing crack is low magnesium alloy region with one stress-strain curve and the area below is the steel region. Since, the top half of the contours are within a homogeneous low magnesium alloy region and the bottom half are within the steel region, the J integral should be path independent and represent the fracture parameter of the crack tip under nearly proportional loading conditions. The J integral, instead of the local crack tip parameters such as the crack tip opening displacement (CTOD) or crack tip opening angle (CTOA), is selected here for the fracture parameter because the J integral is a macroscopic continuum path independent fracture parameter whereas the local CTOD or CTOA is mesh dependent from finite element analyses.

The J integral contours are numbered 1 to 9 where contour 9 is farthest away from the crack tip. The J integral solutions from the finite element analyses of the 9 mm weld

width model of contours 5 to 9 for the right pre-existing crack tip are plotted as functions of the applied load in Fig. 3.21. It should be noted that the *J* integral solutions from the finite element analysis are higher for the right pre-existing crack tip as compared to those for the left pre-existing crack tip due to most of the deformation occurring in the stronger steel for the left crack tip. Therefore, only the *J* integral solution for the right pre-existing crack tip is considered in this study since the failure will be initiated from the right pre-existing crack tip. The maximum variation of the *J* integral solutions for contours 5 to 9 is less than 1% for a given load.

A kinked crack model is also created as shown in Fig. 3.22(a). The kinked crack extend from the pre-existing crack along the interface in the in the vertical direction. Other kink angle can be selected. However, the general trend of the J integral solution obtained here should be representative of kinked cracks with different kink angles. The length of the kinked crack, a is 0.125 mm, which gives the ratio of the kink length to the sheet thickness of $a/t = 0.083$. A close-up view of the finite element model near the right kinked crack tip for the 7 mm indentation length model is shown in Fig. 3.22(b). A total of six contours were assigned in the finite element model to obtain the *J* integral solutions in order to prevent the contours from passing through the steel region. These contours are shown as thick lines surrounding the kinked crack tip as shown in Fig. 3.22(b).

The *J* integral solutions for the 3 contours farthest away from the kinked crack tip are path independent. Fig. 3.23 shows the *J* integral solutions for the contours farthest from the crack tip as a function of the normalized applied load for the pre-existing crack tip with three weld widths and the kinked crack with the 9 mm weld width from the finite element analyses. Fig. 3.23 can be used to understand the failure mode of the ultrasonic

welds in lap-shear specimens. As shown in the figure, the kinked crack has a significantly larger *J* integral value than the three pre-existing cracks at a given load. At the failed load of 2,750 N, the crack growth driving force, the J integral, to grow the crack along the interface is quite small when compared with that for the kinked crack with the kink angle of 90°. Since at the failure load, significant plastic deformation occurs in the magnesium sheet, the large value of J integral solution for the kinked crack represent a much larger driving force to justify that the crack should kink out of the interface. Kinking of a crack out of an interface was investigated by He and Hutchinson [23] based in the linear elastic model.

Discussions

The Mg-Eutectic layer visible at the right edge of the weld zone between the magnesium and steel sheet is shown in Fig. 3.3(a). The bonding strength between the Mg-Zn eutectic layer and the steel appears to be weaker than the bonding strength between the magnesium and steel sheets as suggested by Franklin et al.

As the applied displacement increases during a quasi-static test of the USW lap-shear specimen, the bond between the Mg-Zn eutectic layer and the steel fails first. Once the crack propagates through the entire bond length of the Mg-Zn eutectic layer and the steel and reaches the strong bond between the magnesium and steel sheets, the crack kings out from the interface. The weld then fails along the paths that follow the plastic flow patterns similar to Figs. 3.17(b) and 3.17(c). One failure path following the plastic flow pattern shown in Fig. 3.17(b) is shown in Fig. 3.4(c).

The variation of the material properties was shown to affect the failure mode of lap-shear specimens as in Lee et al. [13]. However, a comparison of the equivalent plastic strain patterns between Figs. 3.17(b) and 3.18(b) shows that the variation of material properties seems to have minimal effects on the failure mode of the lap-shear specimen. This is possibly due to the relatively smaller variation in the initial yield stresses of the base, mid and low magnesium. The change in the initial yield stress of the base and the weld zone due to laser welding for HSLA steel is about 45% [13]. However, the change in the initial yield stress due to the ultrasonic weld process is about 8%. Therefore, the variation of the material properties due to welding has minimal effects in the plastic flow patterns and most likely on the failure modes.

Although lap-shear specimens are used to investigate the shear strength of the weld under shear dominant loading conditions, the load carrying sheets near the weld are subjected to dominant tensile deformation. The rotation of the weld zone is affected by the normalized weld width (d/t) [13]. The 7 mm weld width USW lap-shear model has a ratio of the weld width to the sheet thickness of 4.7. It has been shown that the critical weld width to thickness ratio for the maximum rotation of the weld zone is around 1.1 with the rotation angle decreasing with increasing ratio of the weld width to the sheet thickness. Therefore, the load carrying sheet near the weld lap-shear specimen is subjected to dominant tensile deformation. Note that Lin et al. [24] recognized the fact that the large plastic deformation near a spot weld in a lap-shear sheet specimen gives dominant tensile deformation mode at the critical locations near the weld.

Conclusions

In this investigation, the experiments for ultrasonic welds in dog-bone shaped lap-shear specimens of magnesium and steel sheets under quasi-static loading conditions are reviewed first. The micrograph of the fracture surface of a failed lap-shear specimen shows two distinct intersecting surfaces which were initiated from the pre-existing crack tip and from the indentation corner created due to the sonotrode tip and. Two-dimensional plane strain and plane stress finite element analyses were then carried out to understand the plastic flow patterns and the failure modes of ultrasonic welds in lap-shear specimens under quasi-static loading conditions.

The results of finite element analyses based on the weld model with and without indentation suggest that the plastic flow initiation site from the indentation corner, in addition to the pre-existing crack tip, is mainly responsible for dominant plastic flow patterns to occur. Finite element analyses for models with and without indentation and with different weld widths were developed with two-zone and multi-zone material schemes. The results of the finite element analyses show that the weld indentation corner can trigger the unique fracture surface shown in Fig. 3.4(c). The plastic flow pattern from the results of the finite element analyses closely matches the fracture surface profile form experimental observations. Additionally, finite element analyses based on the multi-zone material models with different weld widths were conducted to obtain the J integral solutions for the pre-existing crack and a kinked crack with a small kink length. The result of the finite element analyses are used to explain the crack kinking out of the interface.

It should be emphasized that the conclusions of this investigation are applicable to the ultrasonic welds in lap-shear specimens under quasi-static loading conditions. Finally,

the results of this investigation for ultrasonic welds, the research work of Lin et al. [24] for resistance spot welds, the research work of Amodeo et al. [25] for gas metal arc welds and the research work of Lee et al. [13] and Asim et al. [14] indicate that the failure mode of the welds in automotive structures should be examined carefully and the necking/shear failure mode needs to be considered for development of failure or separation criteria for welds under more complex loading conditions for crash simulations.

References

[1] Gaines L, Cunena R, Stodolsky F, Wu S. Analysis of the potential for new automotive uses of wrought magnesium. ANL/ESD-35, Argonne National Laboratory 1996.

[2] Hakamada M, Furuta T, Chino Y, Chen Y, Kusuda H, Mabuchi M. Life cycle inventory study on magnesium alloy substitution in vehicles. Energy 2007; 32: 1352-60.

[3] Carpenter JA, Jackman J, Li N, Osborne RJ, Powell BR, Sklad P. Automotive Mg research and development in North America. Materials Science Forum 2007; 546: 11-24.

[4] Kulekci MK. Magnesium and its alloys applications in automotive industry. Int J Advanced Manufacturing Technology 2008; 39: 851-65.

[5] Metals Handbook, Volume 2, 10th Edition, Properties and Selection: Nonferrous Alloys and Special-Purpose Materials, ASM International, 1990.

[6] Neppiras EA. Ultrasonic welding of metals. Ultrasonics 1965; 3: 128-35.

[7] Doumanidis C, Gao Y. Mechanical modeling of ultrasonic welding. Welding Journal 2004; 83: 140-6.

[8] Hetrick E, Jahn R, Reatherford L, Skogsmo J, Ward SM, Wilkosz D, Devine J, Graff K, Gehrin R. Ultrasonic spot welding: A new tool for aluminum joining. Welding Journal 2005; 84: 26-30.

[9] Jahn R, Cooper R, Wilkosz D. The effect of anvil geometry and welding energy on microstructures in ultrasonic spot welds of AA6111-T4. Metallurgical and Materials Transactions: A 2007; 38A: 570-83.

[10] Wright NW, Robson JD, Prangnell PB. Effects of thickness combinations on joint properties and process windows in ultrasonic metal welding. SAE Technical Paper No. 2009-01-0027. Warrendale (PA): Society of Automotive Engineers; 2009.

[11] Watanabe T, Sakuyama H, Yanagisawa A. Ultrasonic welding between mild steel sheet and Al–Mg alloy sheet. J Material Processing Tech 2009; 209: 5475-80.

[12] Santella M, Franklin T, Pan J, Pan TY, Brown E. Ultrasonic spot welding of AZ31B to galvanized mild steel. SAE Technical Paper No. 2010-01-0975. Warrendale (PA): Society of Automotive Engineers; 2010.

[13] Lee J, Asim K, Pan J. Modeling of failure mode of laser welds in lap-shear specimens of HSLA steel sheets. Eng Fract Mech 2011; 78: 374-96.

[14] Asim K, Lee J, Pan J. Failure mode of laser welds in lap-shear specimens of high strength low alloy (HSLA) steel sheets. submitted for publication.

[15] Anand D, Chen DL, Bhole SD, Andreychuk P, Boudreau G. Fatigue behavior of tailor (laser)-welded blanks for automotive applications. Mater Sci Eng: A 2006; 420: 199-207.

[16] Sripichai K, Asim K, Jo WH, Pan J, Li M. Fatigue behavior of laser welds in lap-shear specimens of high strength low alloy (HSLA) steels. SAE Technical Paper No. 2009-01-0028. Warrendale (PA): Society of Automotive Engineers; 2009.

[17] Franklin TJ, Pan J, Santella M, Pan TY. Fatigue Behavior of Dissimilar Ultrasonic Spot Welds in Lap-Shear Specimens of Magnesium and Steel Sheets. SAE Technical Paper No. 2011-01-0475. Warrendale (PA): Society of Automotive Engineers; 2011.

[18] ABAQUS v6.7 User Manual. Providence, RI: SIMULIA; 2007.

[19] Radaj D, Zheng Z, Möhrmann W. Local stress parameters at the weld spot of various specimens. Eng Fract Mech 1990; 37: 933-51.

[20] Nielson KL. 3D modelling of plug failure in resistance spot welded shear-lab specimens (DP600-steel). Int J Fract 2008; 153: 125-39.

[21] Dong P, Pan J. Plane-strain mixed-mode near-tip fields in elastic perfectly plastic solids under small-scale yielding conditions. Int J Fract 1990; 45: 243-62.

[22] Rice JR. A path independent integral and the approximate analysis of strain concentration by notches and cracks. J App. Mech. 1968; 35: 379–86.

[23] He MY, Hutchinson JW. Kinking of a crack out of an interface. J of Applied Mechanics 1989; 56: 270-8.

[24] Lin PC, Lin SH, Pan J. Modeling of failure near spot welds in lap-shear specimens based on a plane stress rigid inclusion analysis. Eng Fract Mech 2006; 73: 2229-49.

[25] Amodeo CA, Lee J, Pan J. presented at the SAE 2010 World Congress, Detroit, Michigan, April 13-15, 2010; manuscript to be submitted for publication in 2011.

Table 3.1 Dimensions of the lap-shear specimen.

Width of the grip section (W)	30.0 mm
Sheet thickness (t)	1.50 mm
Length of each leg (L)	100.0 mm
Width of the central portion (b)	8.0 mm
Overlap length (V)	75.0 mm
Weld width (d)	9.0 mm
Indentation width (c)	7.0 mm
Fillet radius (r)	10.0 mm
Length of doubler (s)	30.0 mm

Table 3.2 The hardness values from indentation tests and the scaled initial yield stresses for the base, middle, low magnesium alloy and steel.

	Base Mg	Middle Mg	Low Mg	Steel
Vickers hardness	70	67	64	98
Yield stress σ_0 (MPa)	141	135	129	363

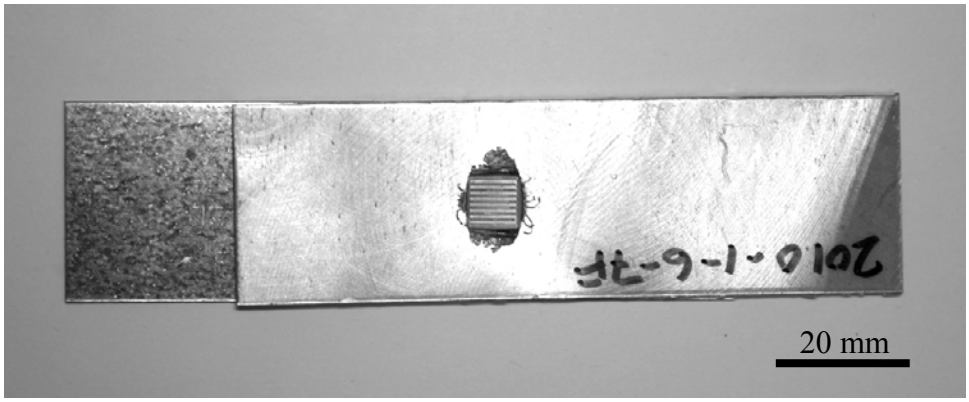

(a)

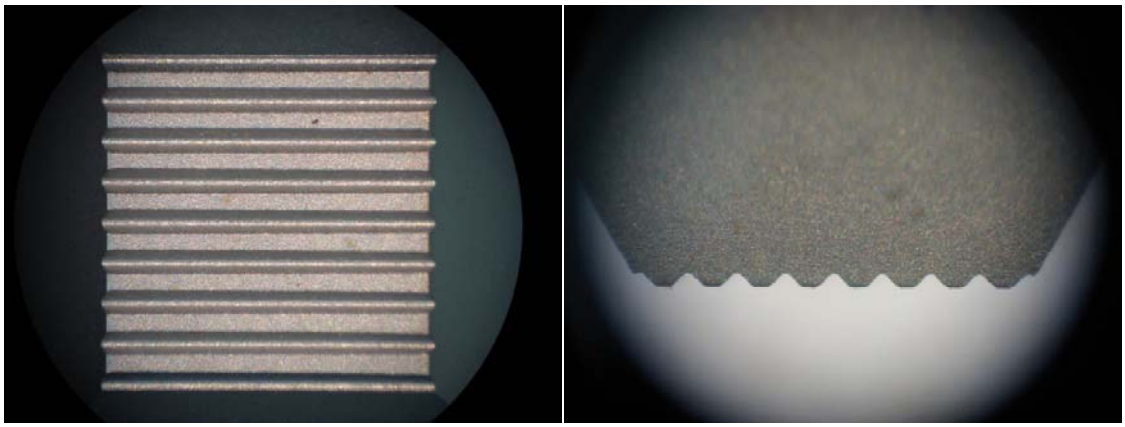

(b) (c)

Fig. 3.1 (a) A top view of an ultrasonic welded lap-shear specimen prior to being machined into a dog-bone shaped specimen. (b) A face view and (c) a side view of the sonotrode tip used in the ultrasonic welding.

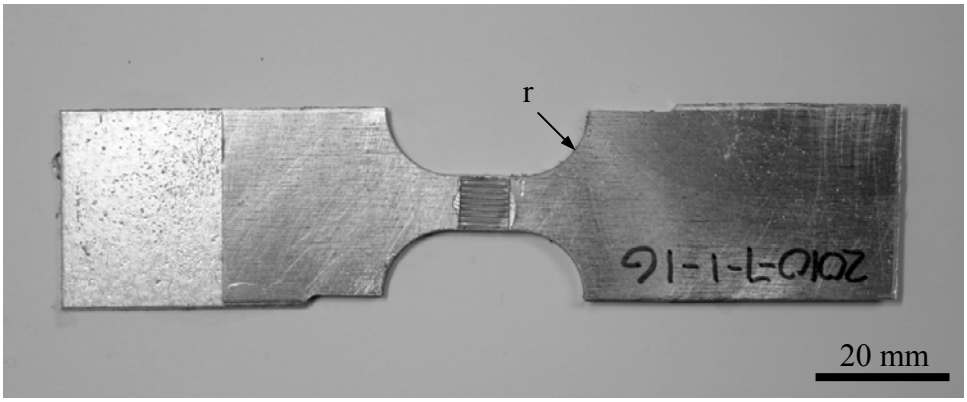

(a)

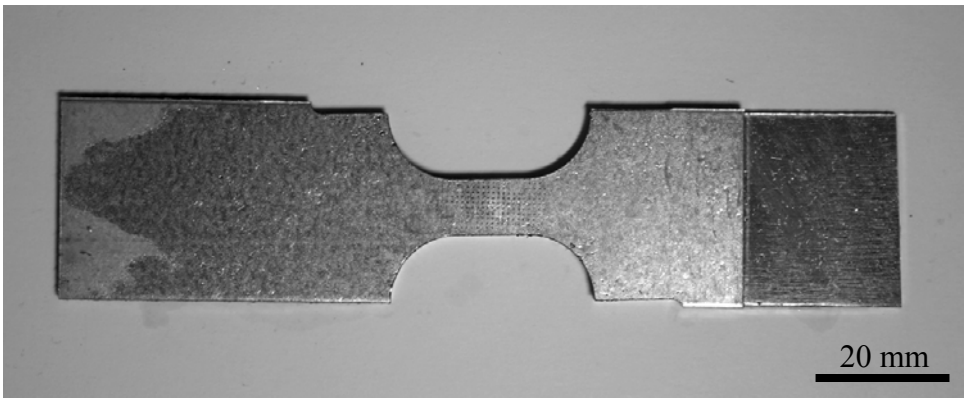

(b)

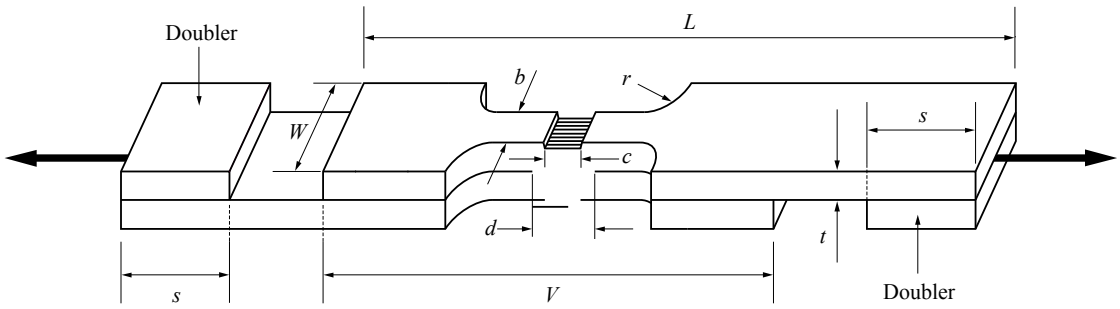

(c)

Fig. 3.2 (a) A top view and (b) a bottom view of an ultrasonic welded lap-shear specimen and (c) a schematic of a lap-shear specimen with the loading direction shown as the bold arrows.

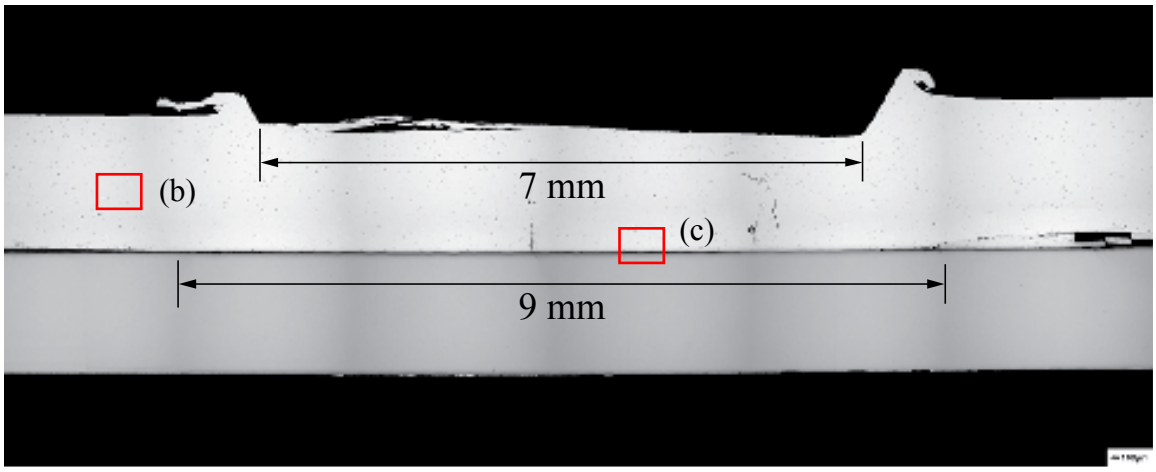

(a)

(b)

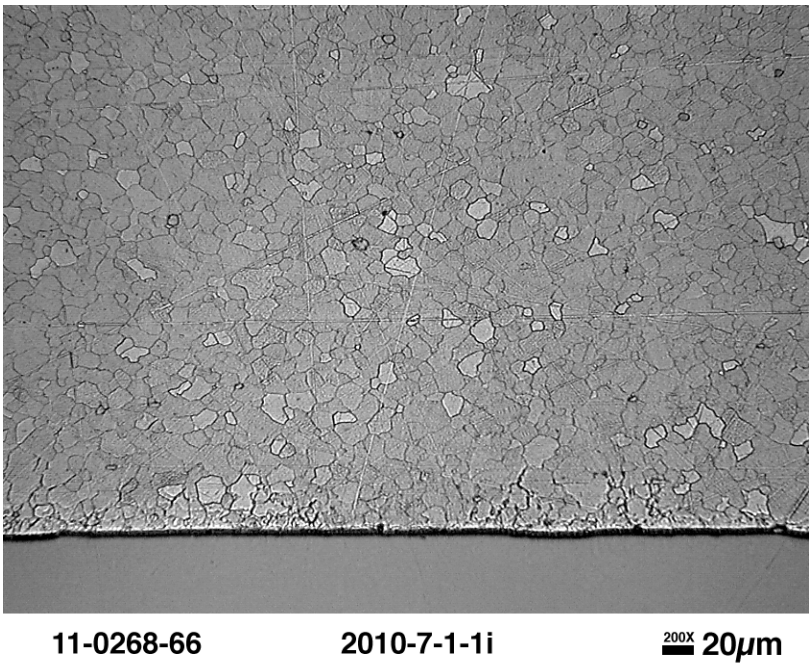

(c)

Fig. 3.3 (a) An optical micrograph of the cross section of an ultrasonic welded joint. Close-up views of (b) the area away from the weld region and (c) the area directly beneath the weld tip as marked in (a).

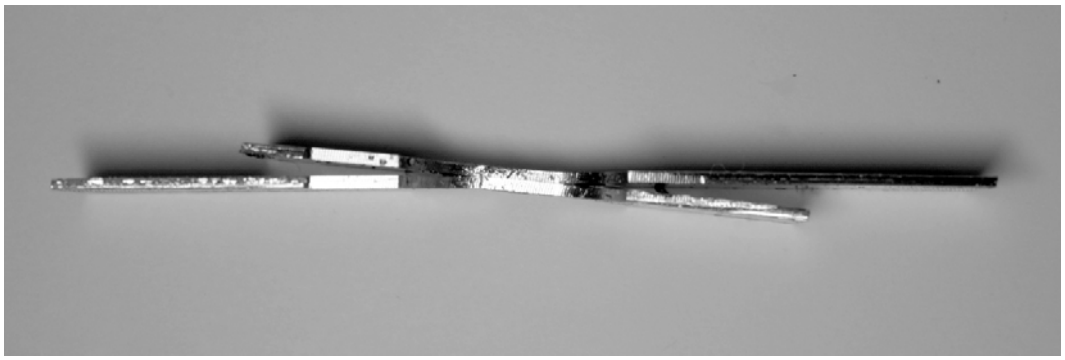

(a)

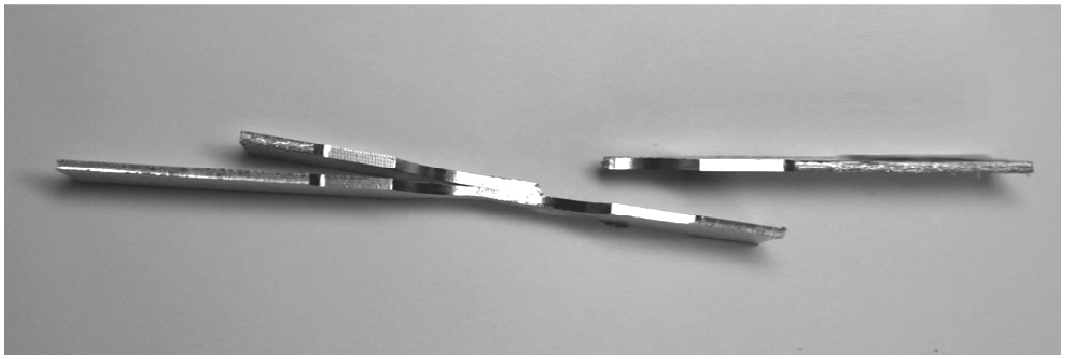

(b)

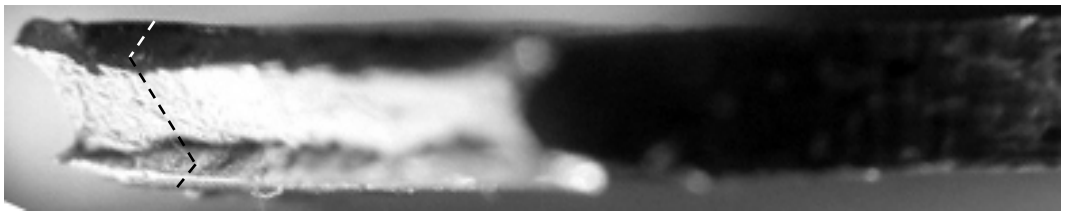

(c)

Fig. 3.4 Side views of specimens at the applied displacements of (a) 1.13 mm prior to failure and (b) 1.23 mm with the right upper sheet separated from the lap-shear specimen. (c) An optical micrograph of the fracture surface from the separated upper right sheet.

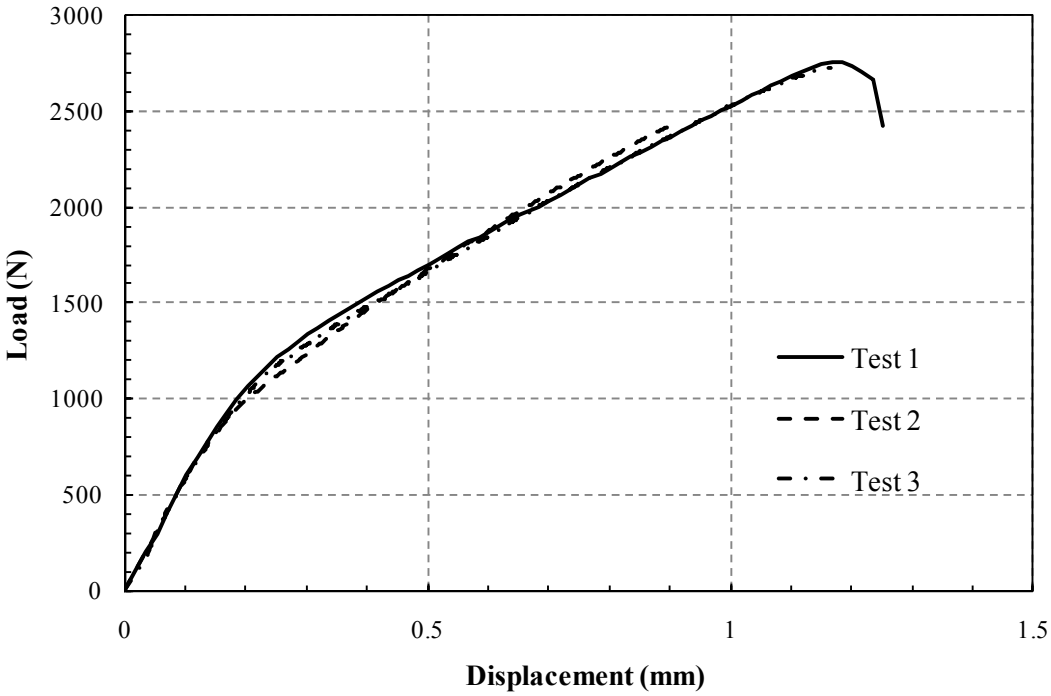

Fig. 3.5 The load-displacement curves from quasi-static tests of three lap-shear specimens.

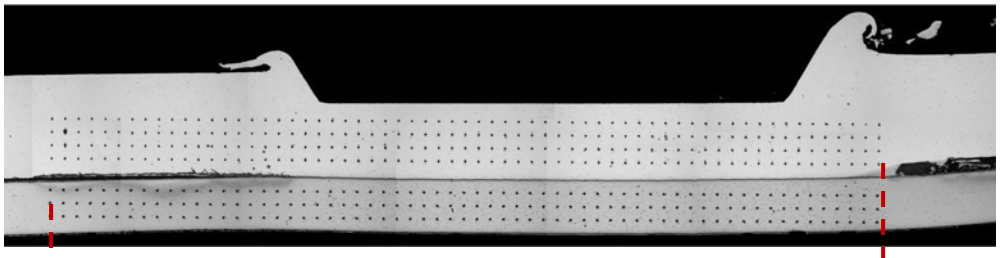

(a)

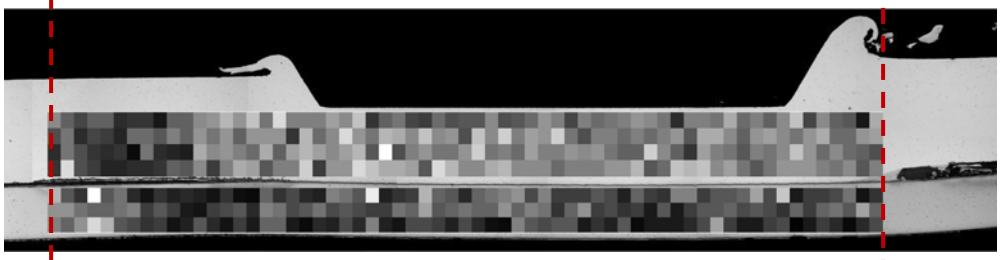

(b)

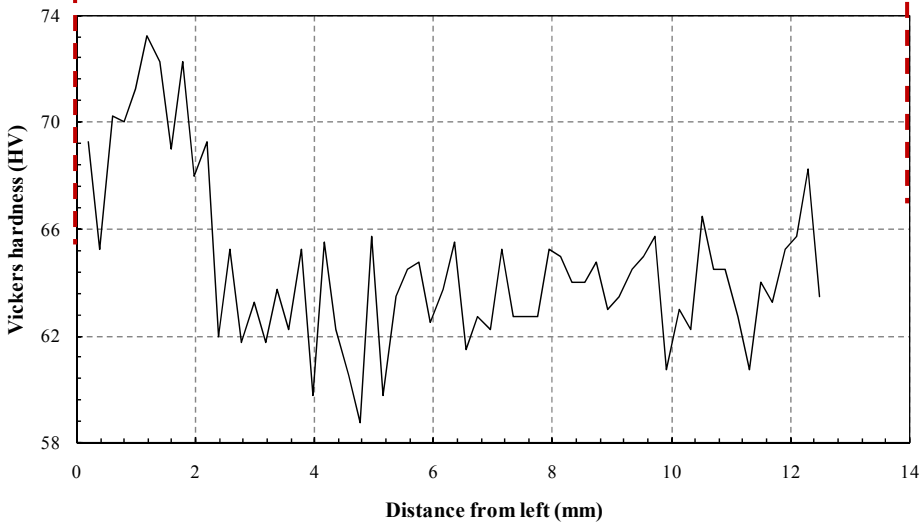
74
70
66
62
58
Vickers hardness (HV)
0
2
4
6
8
10
12
14
Distance from left (mm)

(c)

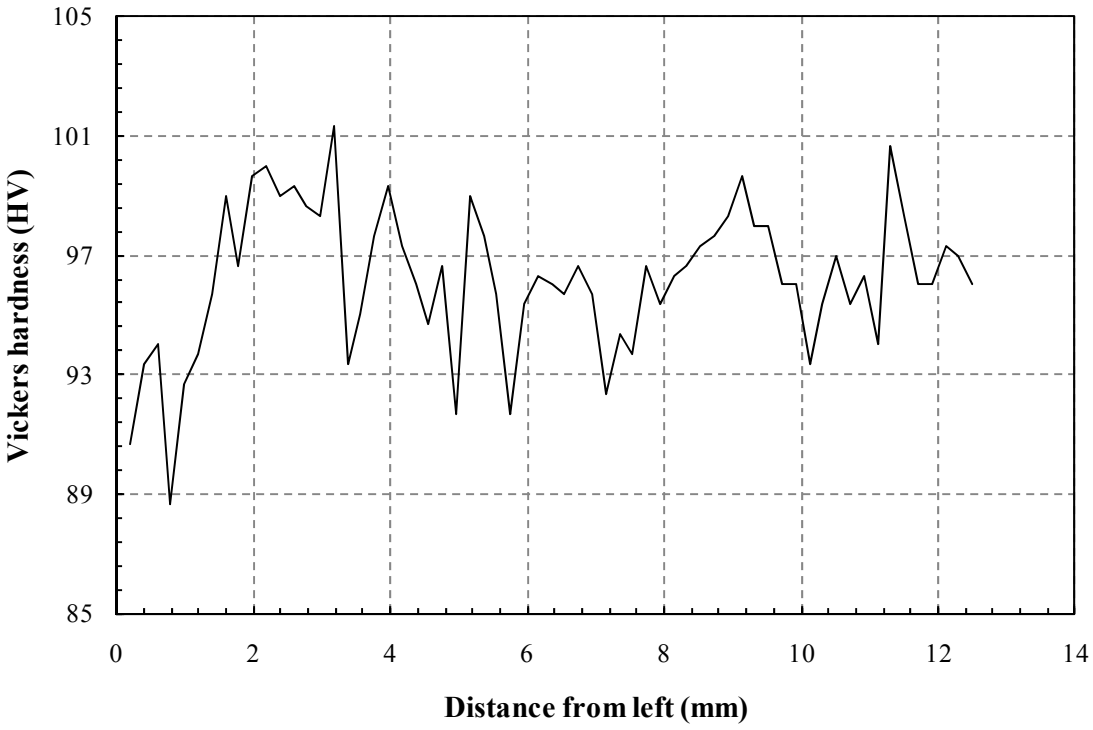

(d)

Fig. 3.6 (a) A cross-section view of an ultrasonic welded joint with micro hardness indentations on the surface. (b) The cross-section overlapped with a grayscale color map depicting the Vickers hardness values. Darker squares represent higher hardness values. The thickness-wise average values of the hardness values across the weld for (c) the magnesium and (d) the steel sheets.

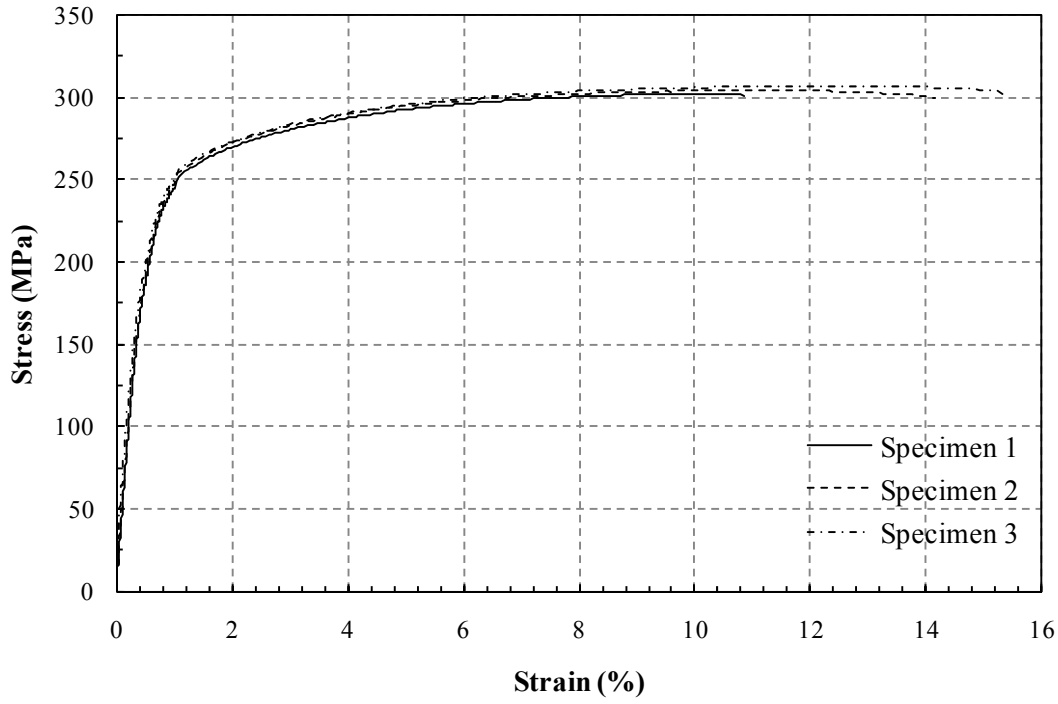

Fig. 3.7 The engineering stress-strain curves for the AZ31B magnesium sheets from three tensile specimens.

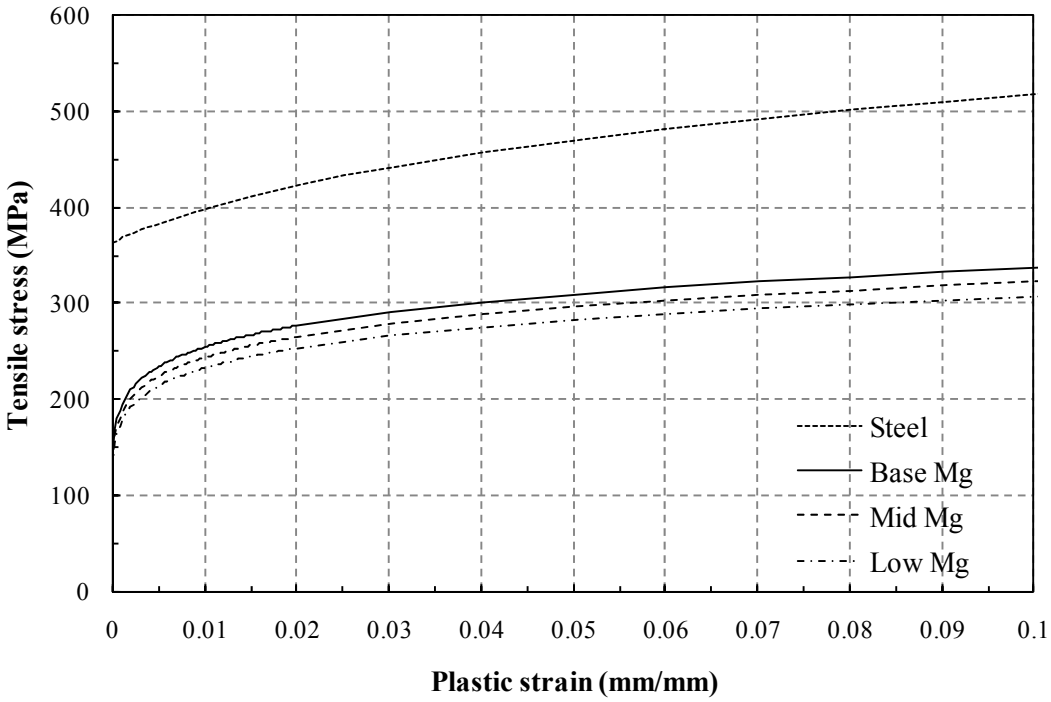

Fig. 3.8 The tensile stresses as functions of the plastic strain for the, base, middle, low magnesium alloy and the steel used in the multi-zone finite element analyses.

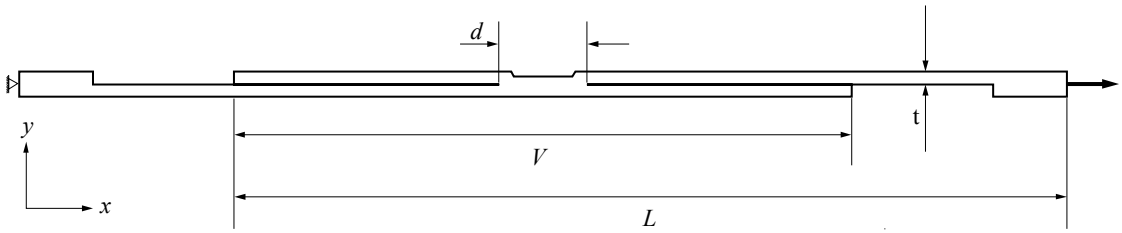

(a)

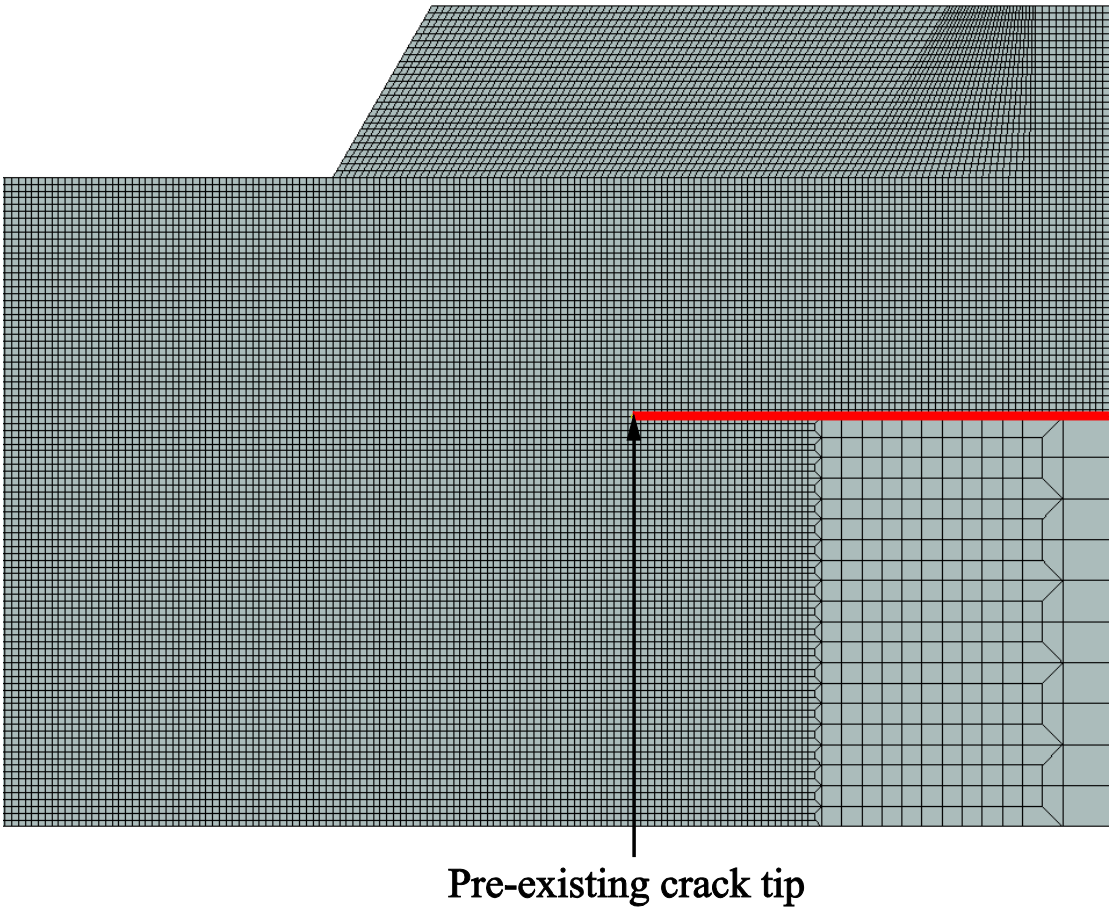

(b)

Fig. 3.9 (a) A schematic of a two-dimensional finite element model of a lap-shear specimen showing the boundary conditions and (b) a close-up view of the finite element mesh near the right pre-existing crack tip.

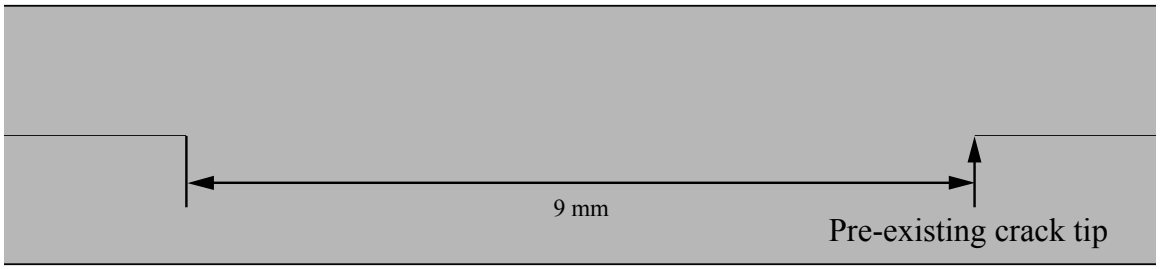
9 mm
Pre-existing crack tip

(a)

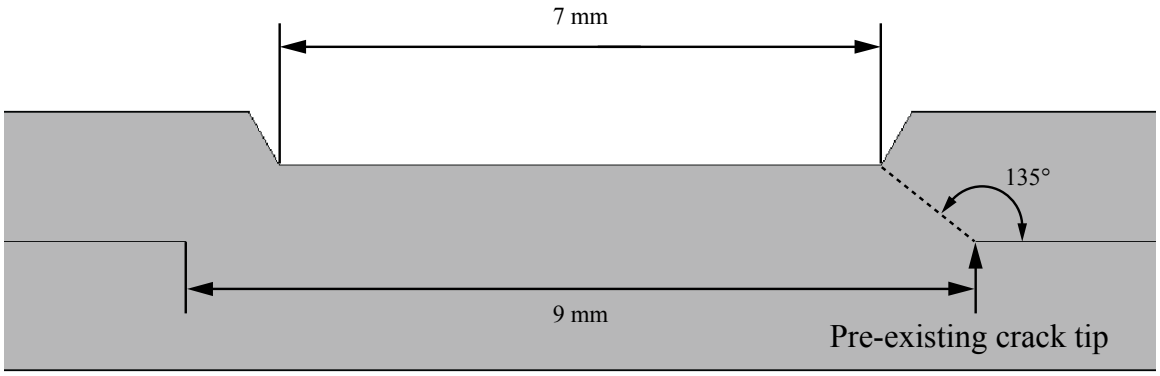
7 mm
135°
9 mm
Pre-existing crack tip

(b)

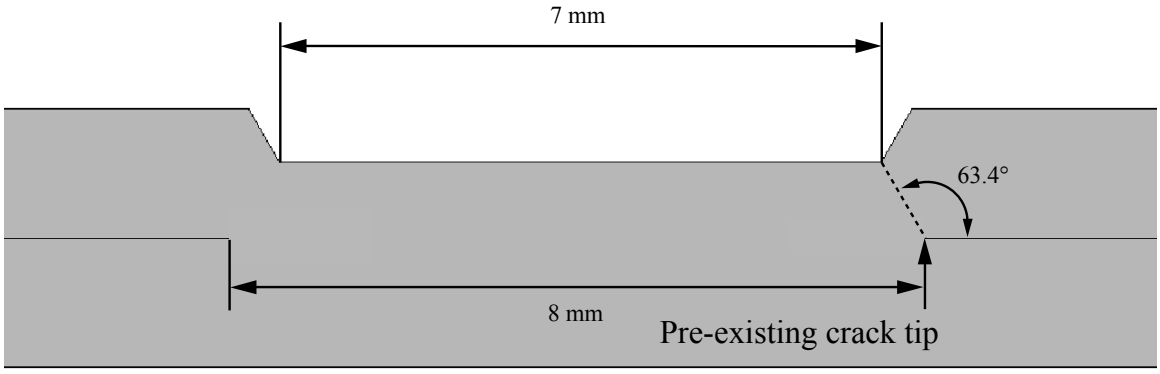
7 mm
63.4°
8 mm
Pre-existing crack tip

(c)

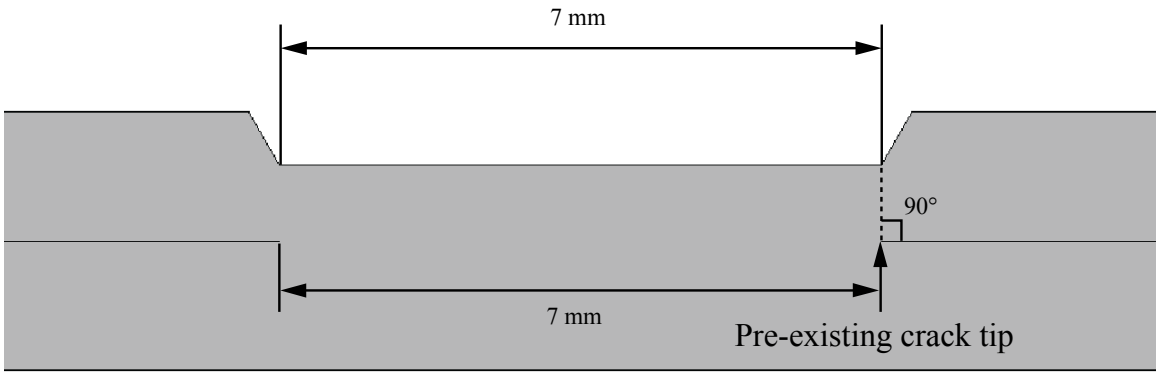

(d)

Fig. 3.10 (a) The finite element model for the lap-shear specimen without indentation. The finite element models with the indentation width of 7 mm and the weld widths of (b) 9 mm, (c) 8 mm and (d) 7 mm.

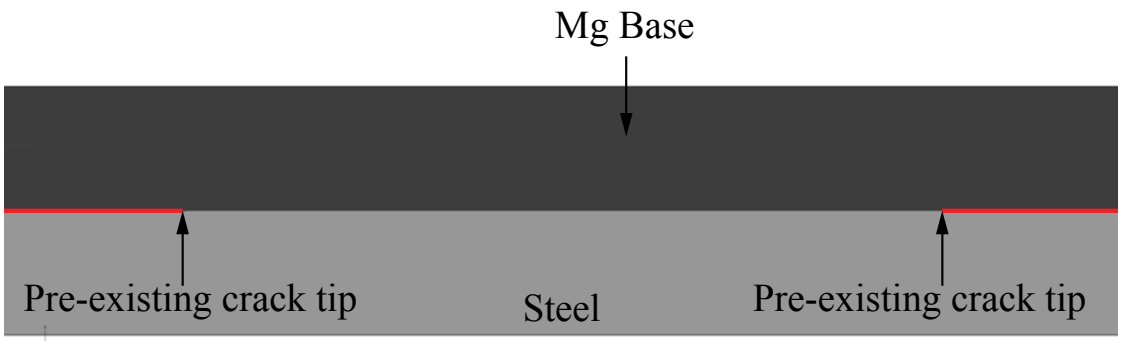

(a)

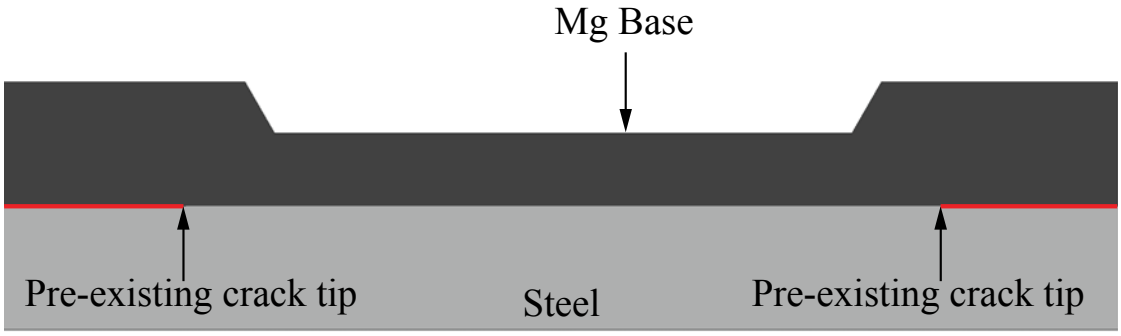

(b)

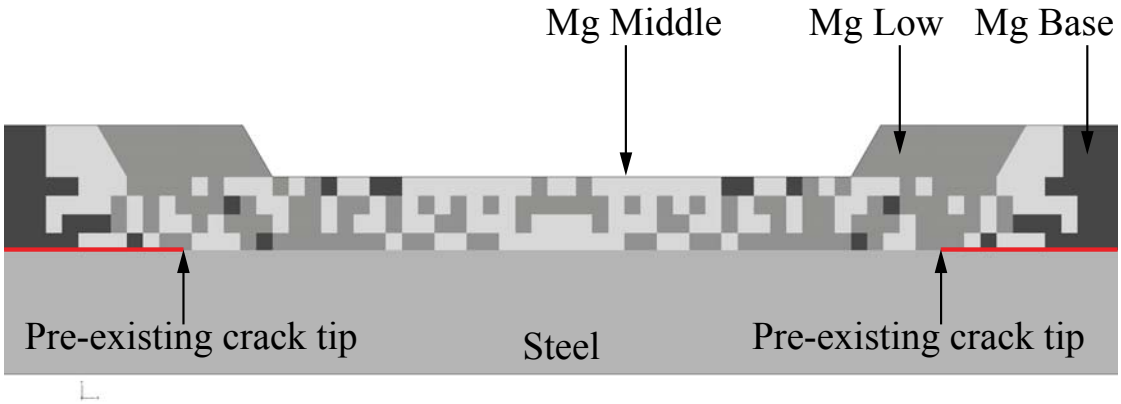

(c)

Fig. 3.11 Schematics of (a) the two-zone model without the indentation, (b) the two-zone model with the indentation and (c) the multi-zone model with the indentation.

(a)

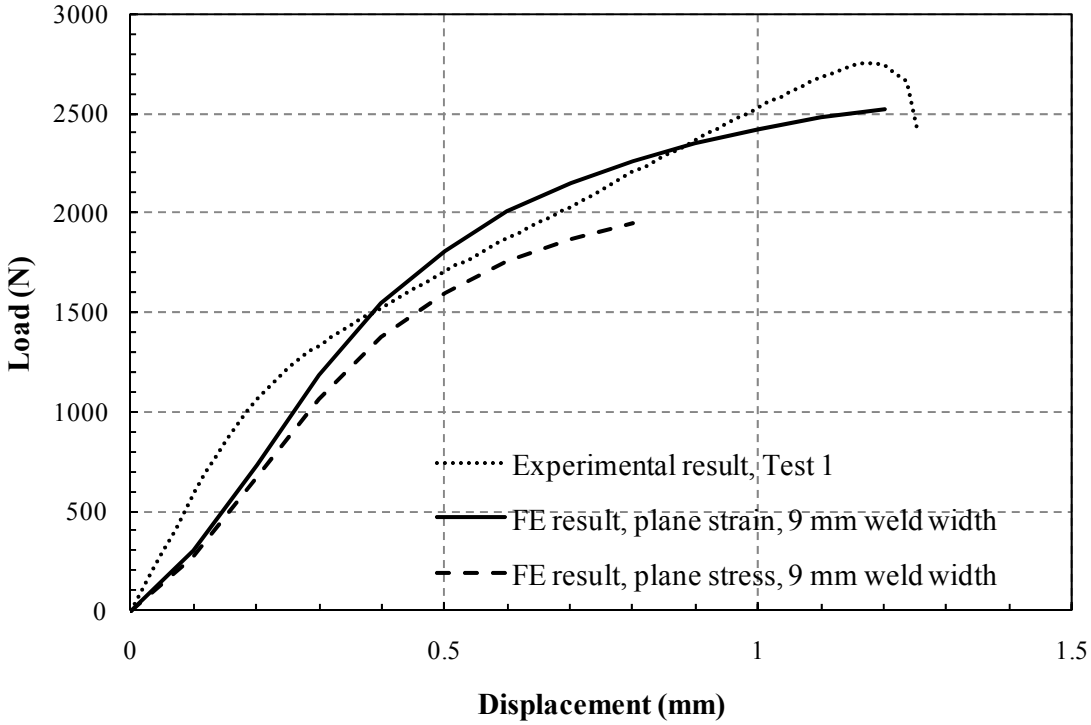
3000
2500
2000
1500
1000
500
0
Load (N)
0
0.5
1
1.5
Displacement (mm)
Experimental result, Test 1
FE result, plane strain, 9 mm weld width
FE result, plane stress, 9 mm weld width

(b)

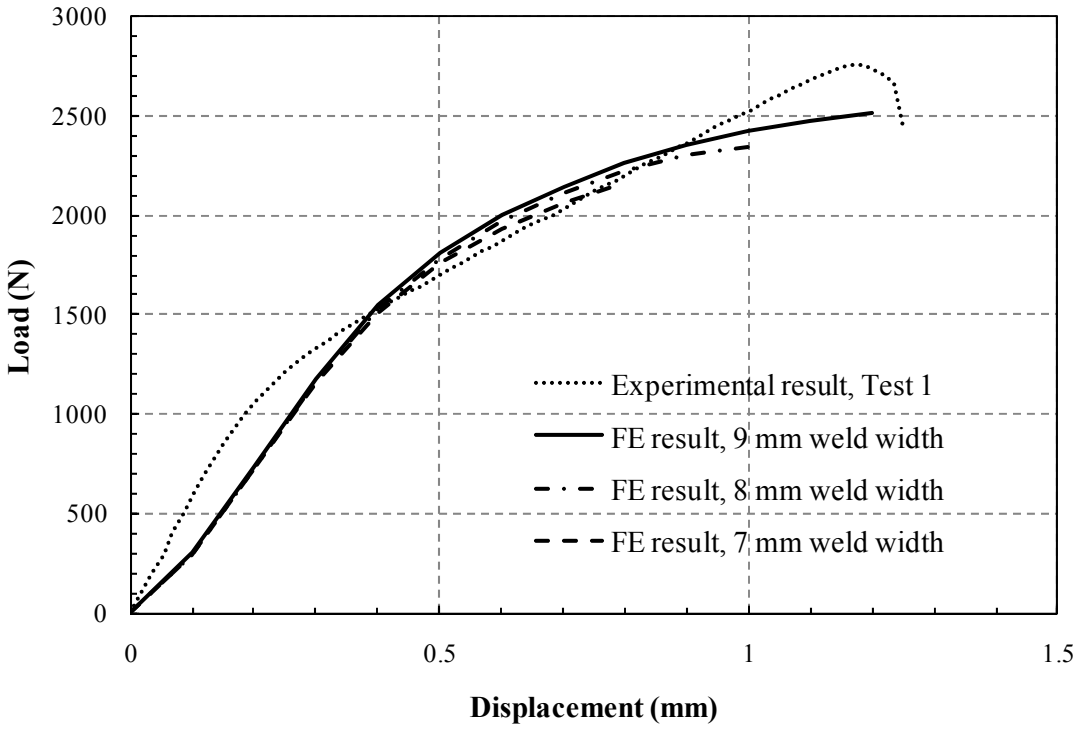

(c)

Fig. 3.12 (a) The deformed shape of the two-zone model with the 9 mm weld width. (b) The load-displacement curves obtained from the finite element analyses based on the two-zone model with the 9 mm weld width under plane strain and plane stress conditions and the experimental results. (c) The load-displacement curves obtained from the finite element analyses based on the two-zone model with the 9 mm, 8 mm and 7 mm weld widths and the experimental results.

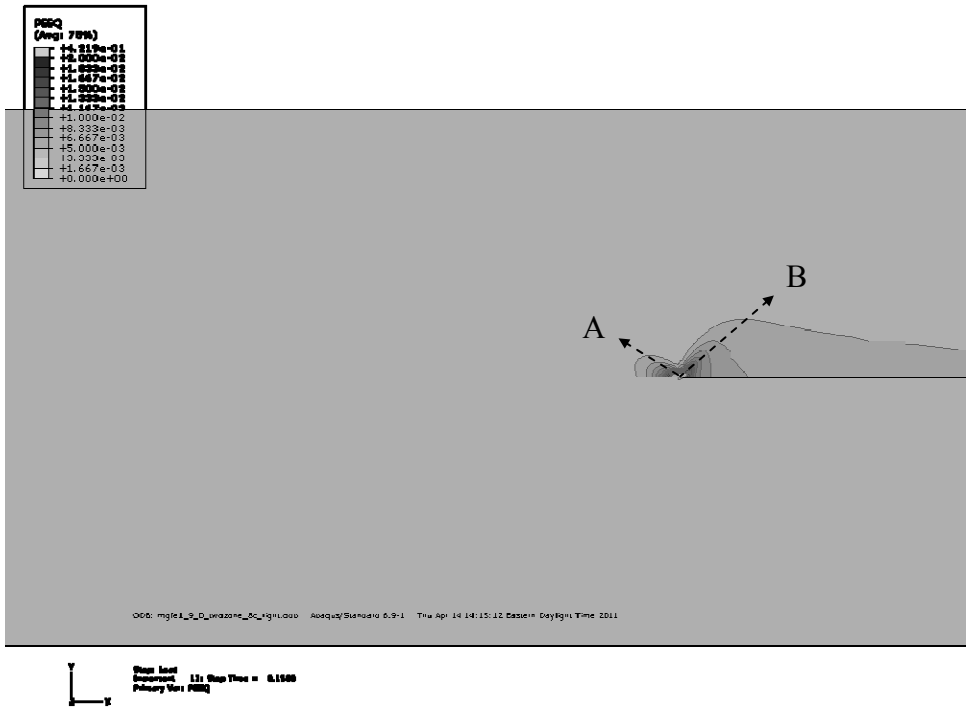

Fig. 3.13 Equivalent plastic strain distributions near the right pre-existing crack tip from the two-zone model with the 9 mm weld width and without the indentation at the applied displacement of 0.3 mm.

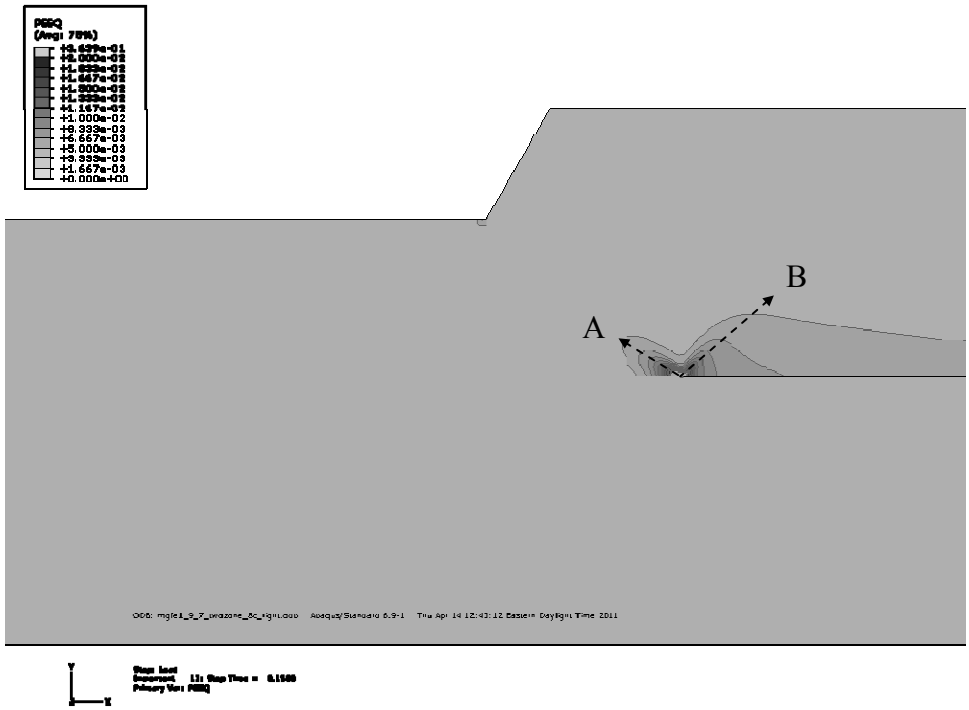
PEEQ
(Avg: 75%)
+1.000e-02
+9.333e-03
+8.667e-03
+8.000e-03
+7.333e-03
+6.667e-03
+6.000e-03
+5.333e-03
+4.667e-03
+4.000e-03
+3.333e-03
+2.667e-03
+2.000e-03
+1.333e-03
+6.667e-04
+0.000e+00
A
B

(a)

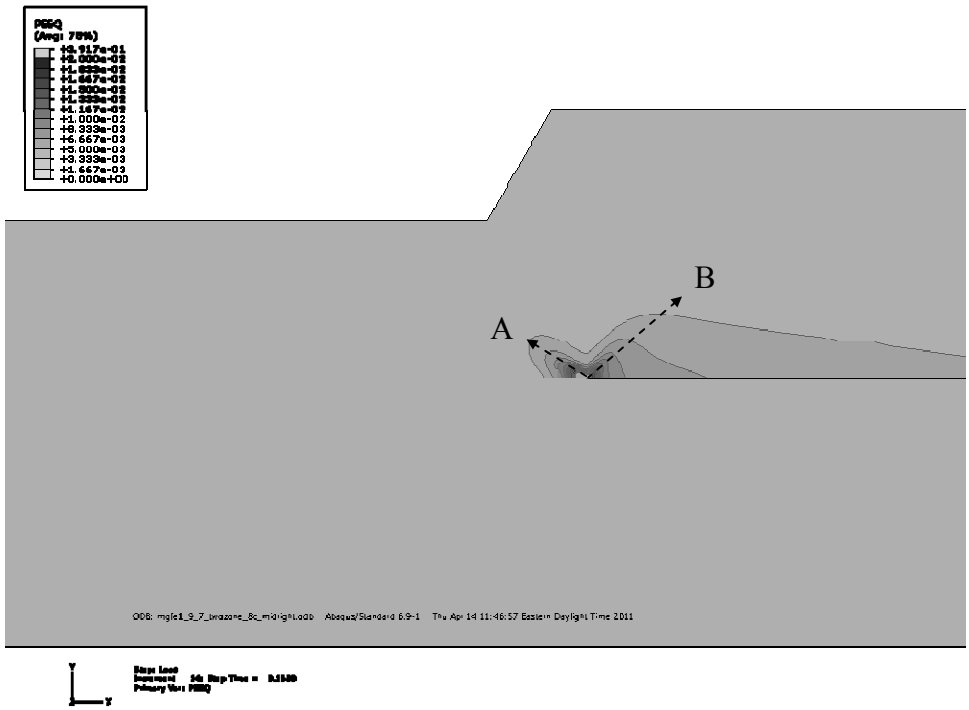
PEEQ
(Avg: 75%)
+1.000e-02
+9.333e-03
+8.667e-03
+8.000e-03
+7.333e-03
+6.667e-03
+6.000e-03
+5.333e-03
+4.667e-03
+4.000e-03
+3.333e-03
+2.667e-03
+2.000e-03
+1.333e-03
+6.667e-04
+0.000e+00
A
B

(b)

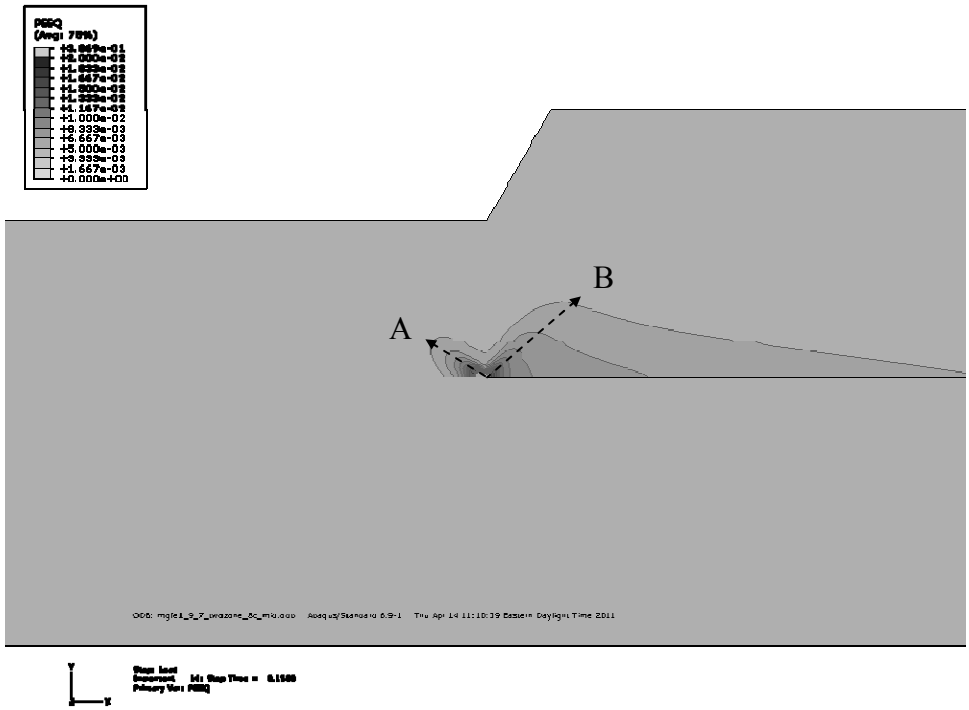

(c)

Fig. 3.14 Equivalent plastic strain distributions near the right pre-existing crack tip from the two-zone model with the weld widths of (a) 9 mm, (b) 8 mm and (c) 7 mm. The applied displacement is 0.3 mm for all cases.

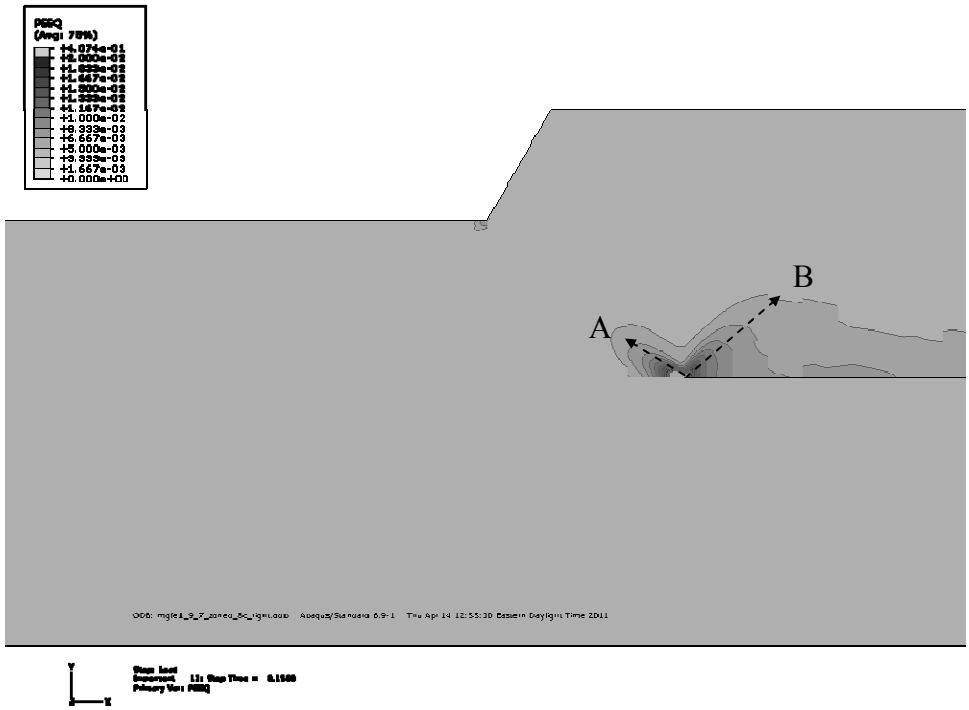
PEEQ
(Avg: 75%)
+1.074e-01
+1.000e-02
+9.333e-03
+8.667e-03
+8.000e-03
+7.333e-03
+6.667e-03
+6.000e-03
+5.333e-03
+4.667e-03
+4.000e-03
+3.333e-03
+2.667e-03
+2.000e-03
+1.333e-03
+6.667e-04
+0.000e+00
A
B

(a)

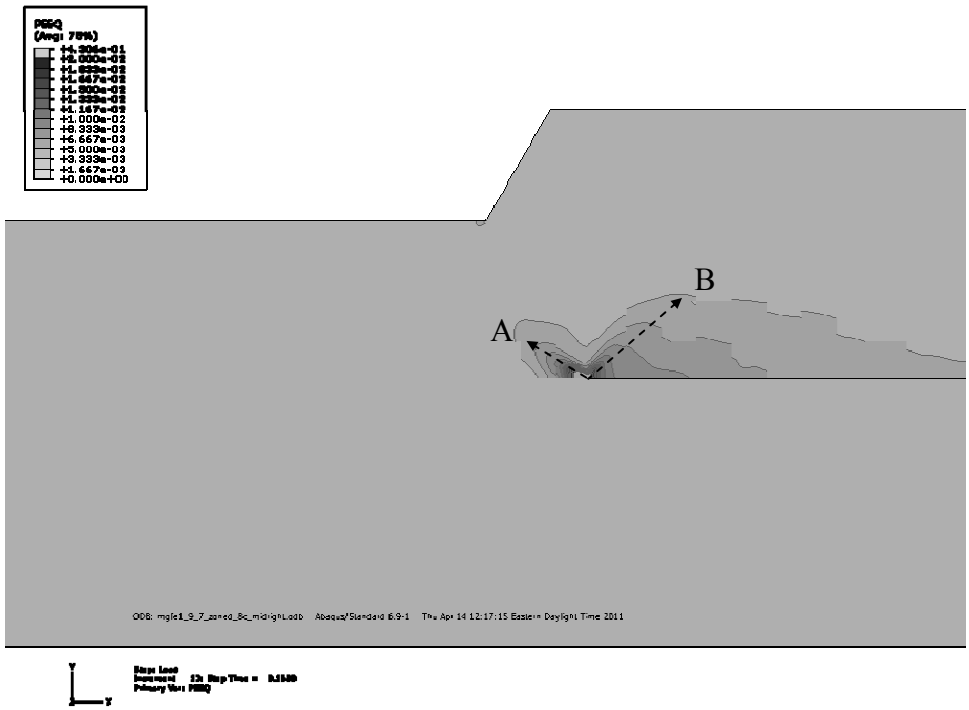
PEEQ
(Avg: 75%)
+1.304e-01
+1.000e-02
+9.333e-03
+8.667e-03
+8.000e-03
+7.333e-03
+6.667e-03
+6.000e-03
+5.333e-03
+4.667e-03
+4.000e-03
+3.333e-03
+2.667e-03
+2.000e-03
+1.333e-03
+6.667e-04
+0.000e+00
A
B

(b)

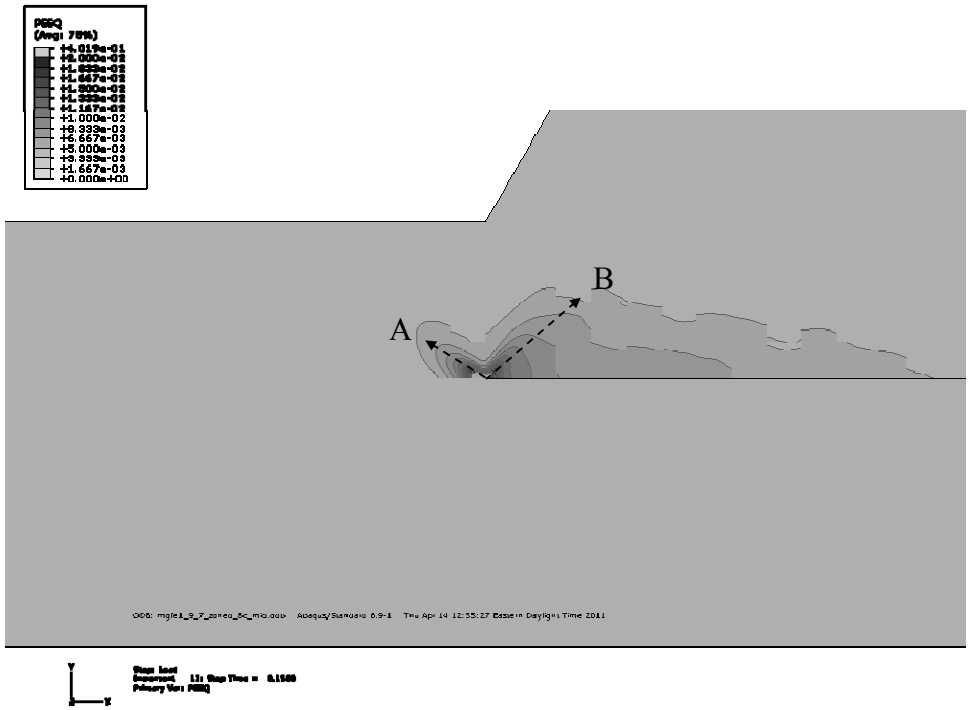

(c)

Fig. 3.15 Equivalent plastic strain distributions near the right pre-existing crack tip from the multi-zone model with the weld widths of (a) 9 mm, (b) 8 mm and (c) 7 mm. The applied displacement is 0.3 mm for all cases.

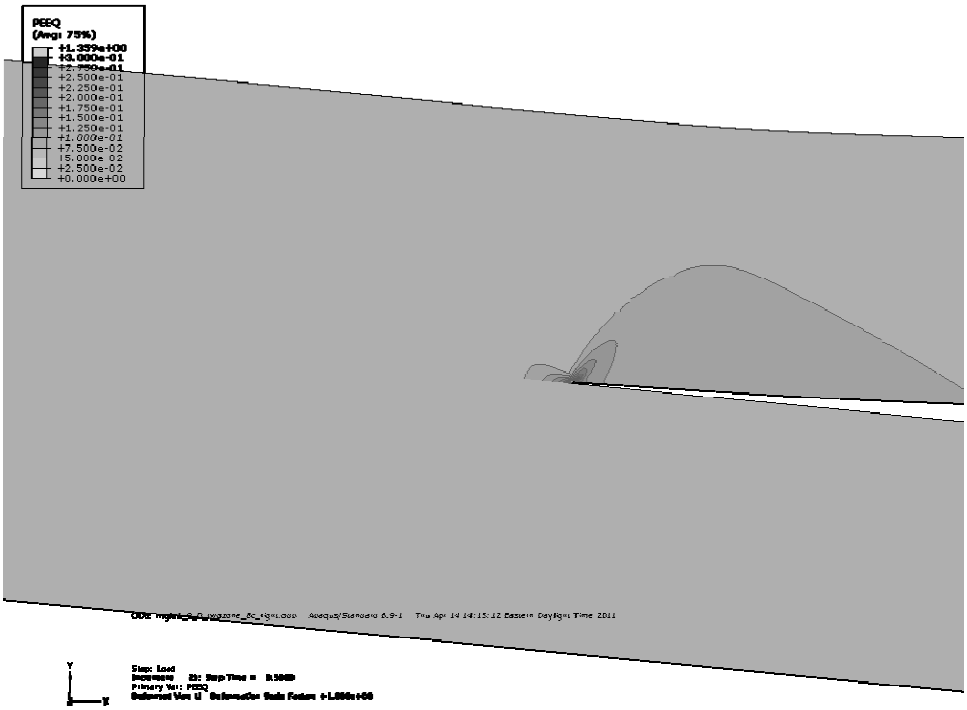

Fig. 3.16 Equivalent plastic strain distributions near the right pre-existing crack tip from the two-zone model without the indentation at the applied displacement of 1 mm.

(a)

(b)

(c)

Fig. 3.17 Equivalent plastic strain distributions near the right pre-existing crack tip from the two-zone model with the weld widths of (a) 9 mm, (b) 8 mm and (c) 7 mm. The applied displacement is 1 mm for all cases.

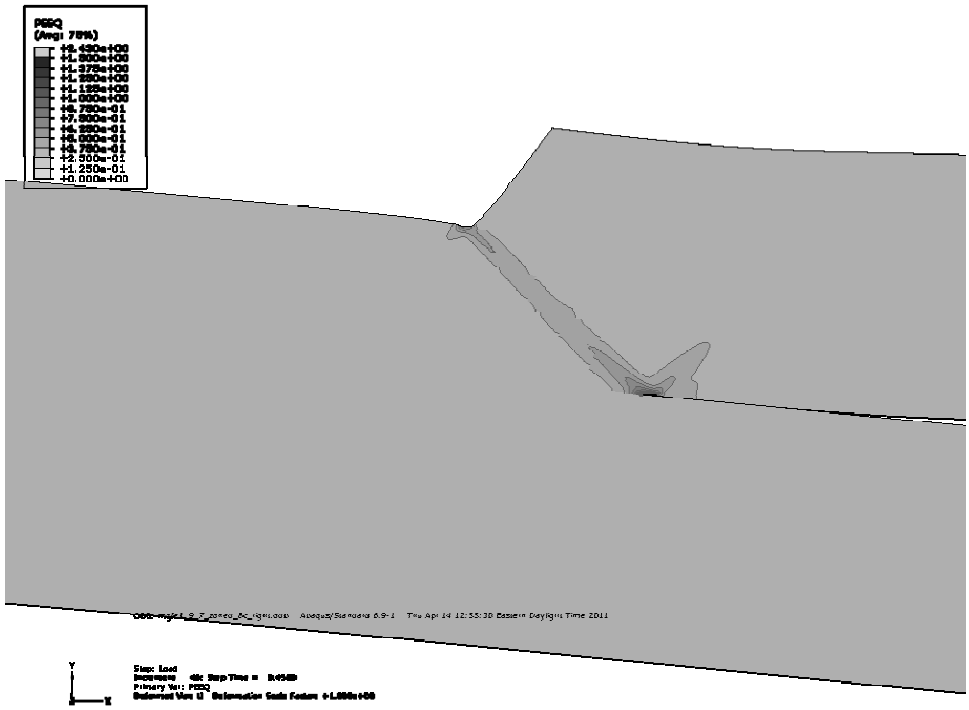

(a)

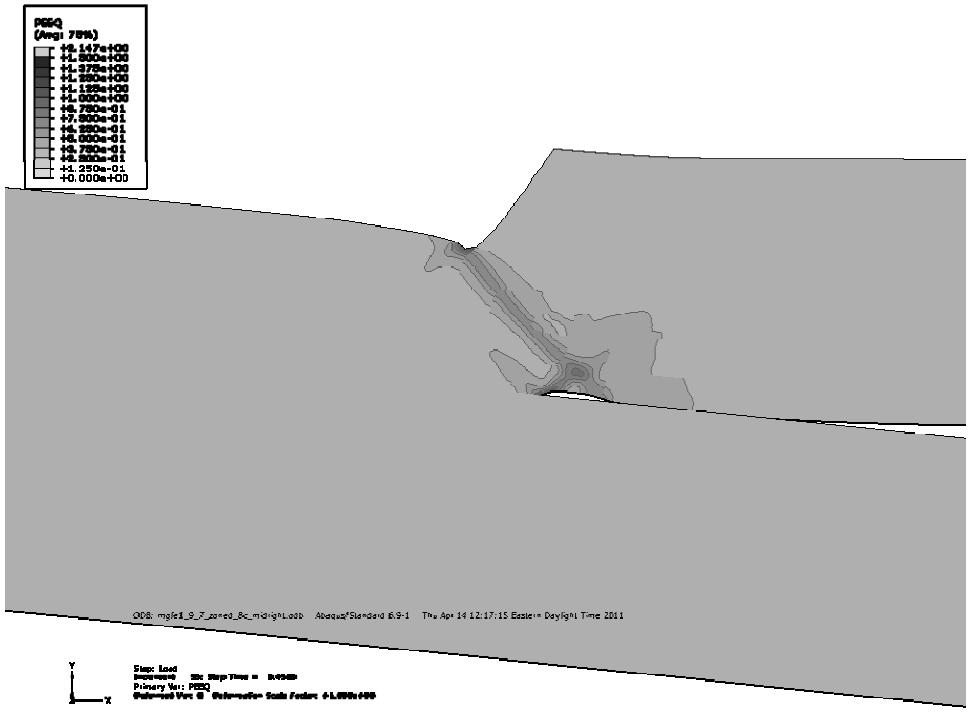

(b)

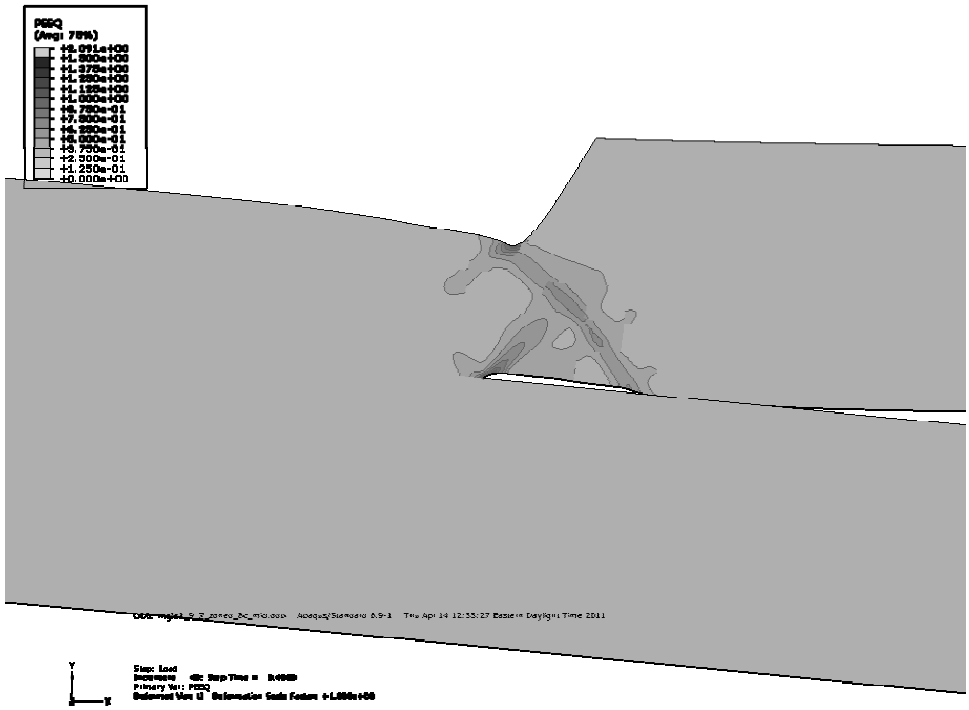

(c)

Fig. 3.18 Equivalent plastic strain distributions near the right pre-existing crack tip from the multi-zone model with the weld widths of (a) 9 mm, (b) 8 mm and (c) 7 mm. The applied displacement is 1 mm for all cases.

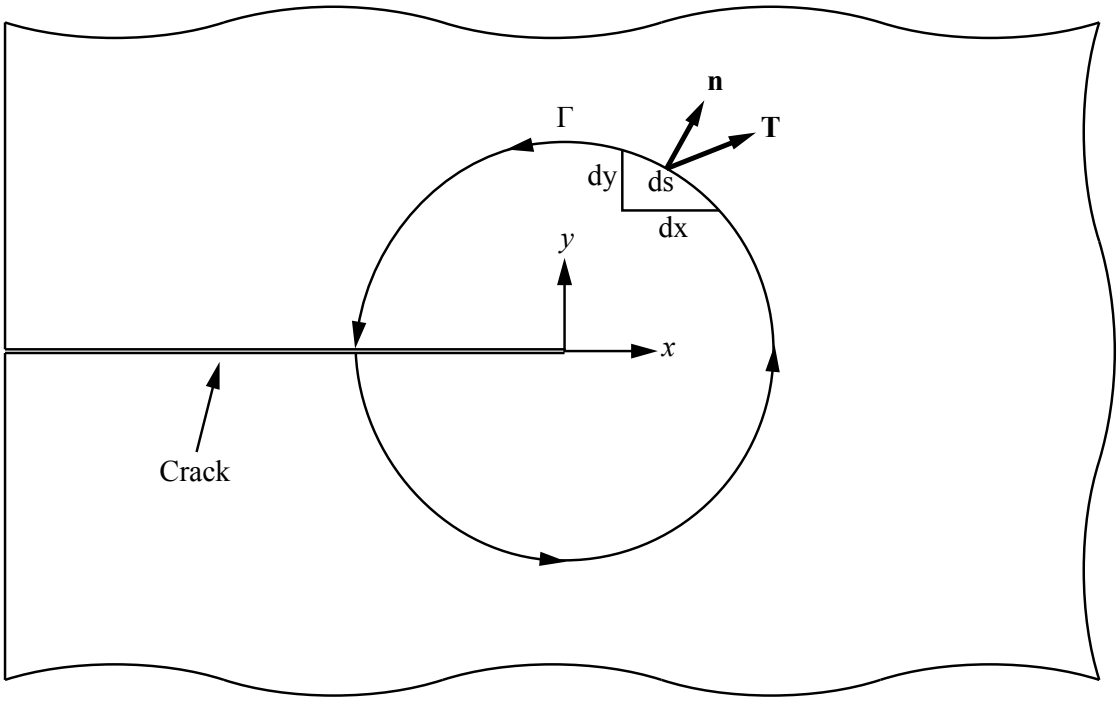

Fig. 3.19 A schematic of a crack and an arbitrary contour Γ surrounding the crack tip.

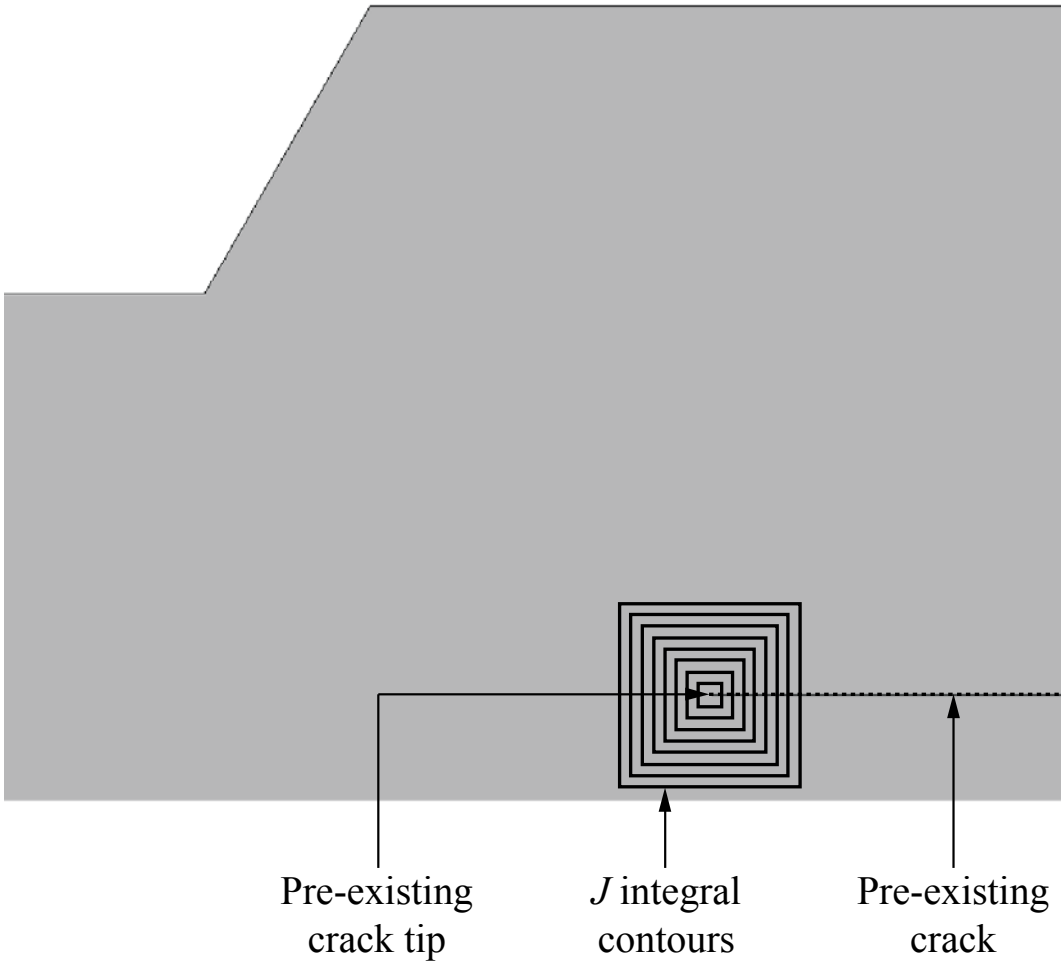

Fig. 3.20 A close-up view of the two-zone finite element model near the right pre-existing crack tip along with the *J* integral contours.

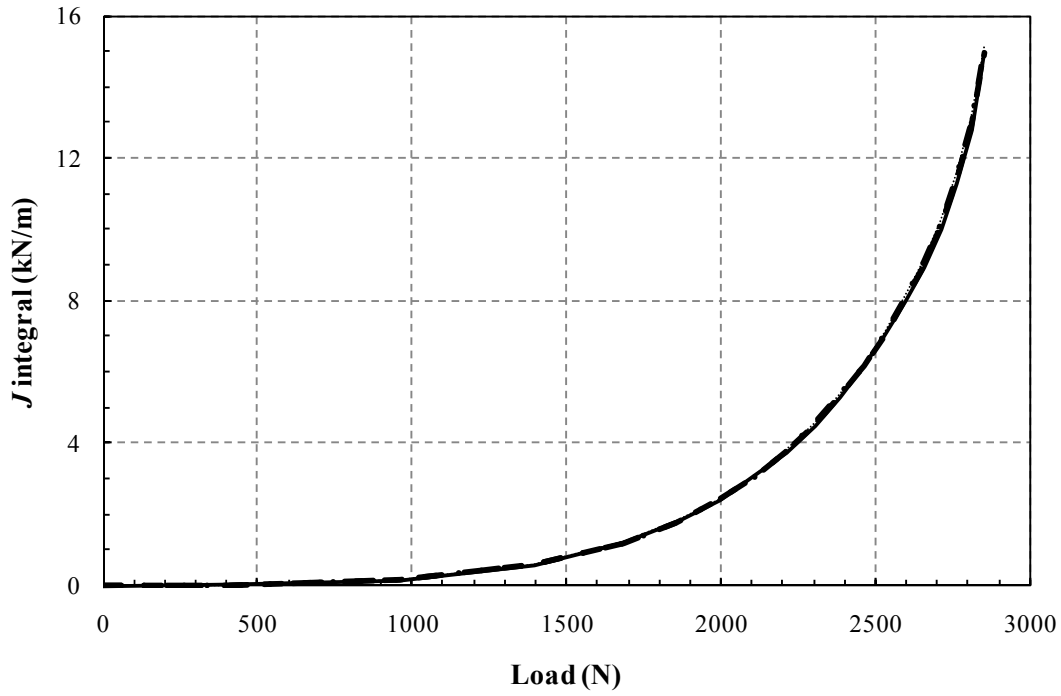

Fig. 3.21 The *J* integral solutions for contours 5 to 9 for the right pre-existing crack tip as functions of the load from the finite element analysis for the two-zone model with the 9 mm weld width.

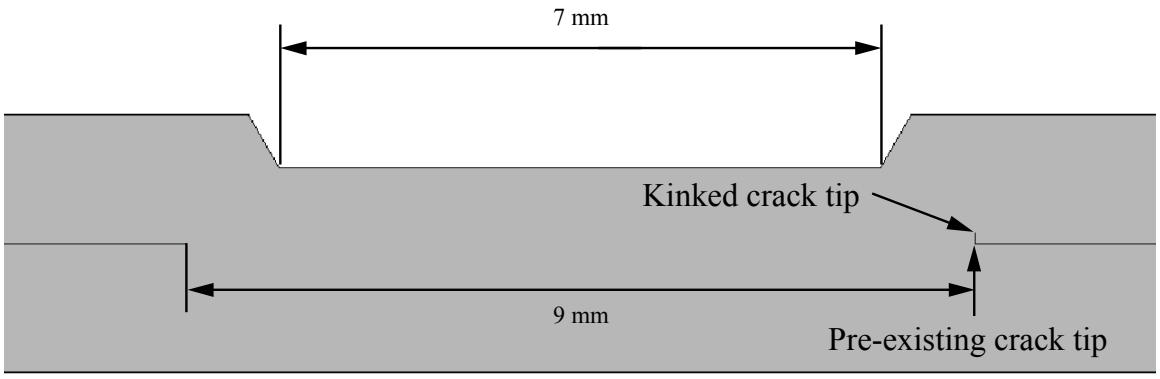

(a)

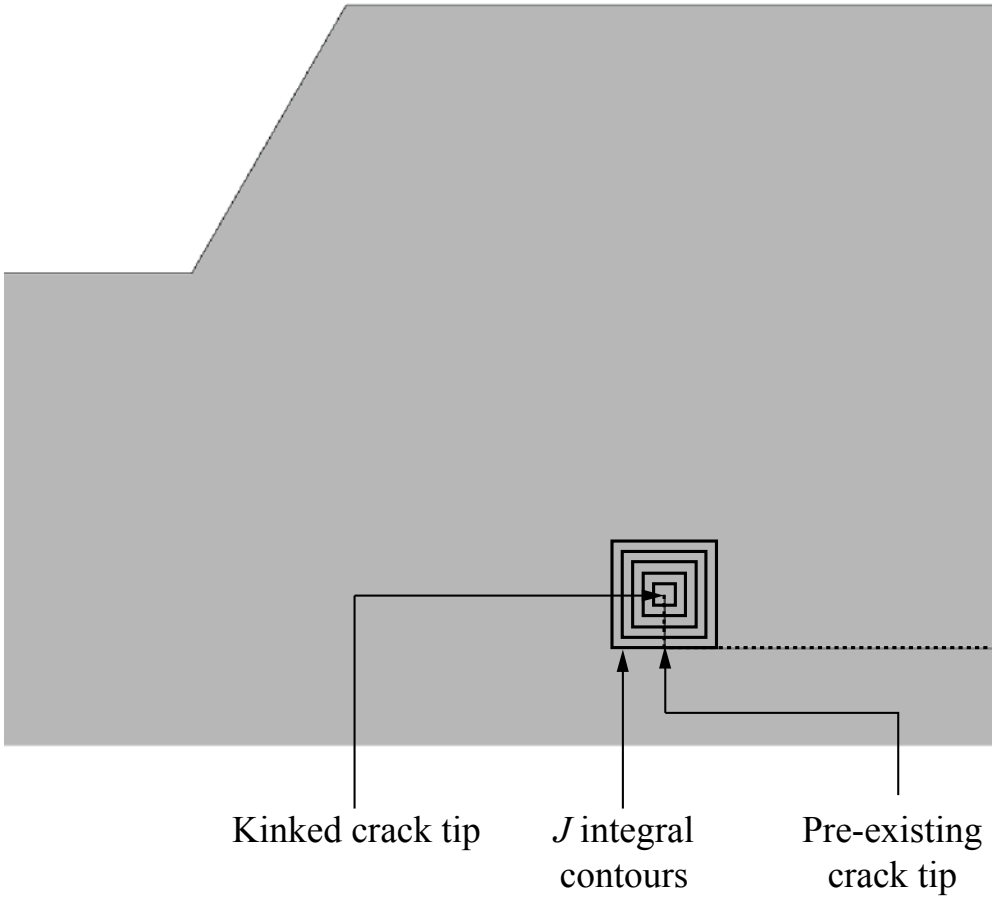

(b)

Fig. 3.22 (a) A finite element model near the weld region showing a kinked crack and (b) a close-up view of the finite element model near the kinked crack tip and the *J* integral contours for the kinked crack.

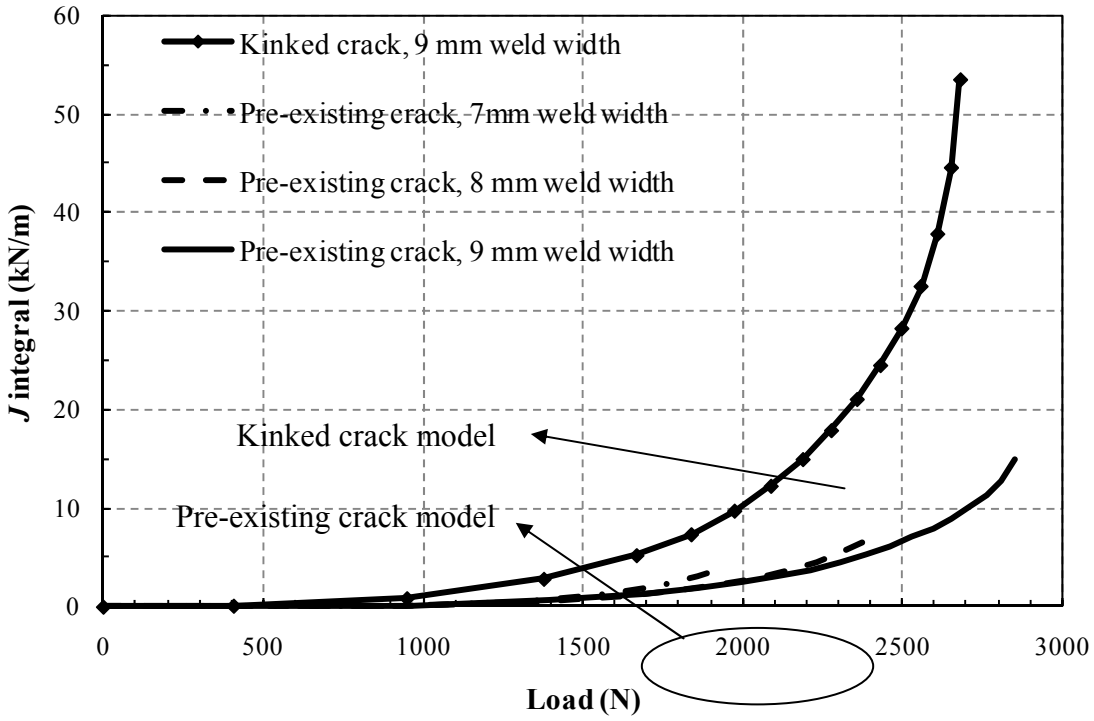

Fig. 3.23 The *J* integral solutions from the finite element analyses of the contour farthest from the crack tip as functions of the load of the 9 mm, 8 mm and 7 mm weld width, two-zone models and the 9 mm weld width two-zone kinked crack model.

Chapter 4
A closed-form analytical solution for calculation of loads and contact pressures for roller and ball bearings

Introduction

Bearings are essential components in machines and vehicles allowing relative motions of components with minimal friction. The fatigue lives of the bearings in machines and vehicles are expected to outlast the lives of the machines and vehicles themselves. However, large cyclic service loads will tend to shorten the lives of the bearings. For use in vehicles, bearings should be designed to withstand both the constant load due to the vehicle weight and the service loads caused by the operation of vehicles. The stresses under the raceway from these loads and in the ball or cylindrical rollers should be designed within the elastic range of the material.

A bearing should be designed such that the mechanical stresses due to contact and deformation are under some design limits, given that the bearing is maintained under well lubricated conditions. Therefore, the mechanical stresses within the bearing components should be well studied during the design and selection process to maximize the fatigue life of a bearing.

In order to test the structural durability and the failure lives of bearings such as those in vehicles, the bearings are usually put in a test equipment and rotated while external loads are applied. The Society of Automotive Engineers has a standardized test for automotive biaxial wheel tests which is well documented by Nurkala and Wallace [1].

However, extensive testing time on the test equipment is necessary to duplicate the failure modes of bearings under actual operational conditions [2]. An accelerated test was suggested in order to reduce the required testing time, but investigations such as those by Grubisic and Fischer [3] have shown that the fatigue damage characteristics will be changed such that the failure mode will not be representative of that from the actual usage of vehicles. Finite element analyses may be considered as a reasonable alternative but has their limitations. Solving multiple and simultaneous contact problems using finite element analyses, as is the case for the bearing analysis, require a tremendous amount of pre-processing time and computing power which again creates time and cost issues.

In order to overcome these time and cost related issues, an analytical solution is proposed here to estimate the loads exerted by the rolling elements on the raceway in a bearing. Stribeck [4] proposed an equation to find the maximum load on a rolling element based on experimental observations. Goodelle et al. [5] developed a method to record the static load distribution for radial as well as thrust rolling elements. Harris [6] developed methods to obtain the load distribution based on radial and thrust integrals. De Paula et al. [7] presented a software package that can be used to calculate the stresses based on the Hertz contact theory and the fatigue lives of bearings for industry use.

Once the load distribution or the loads exerted by rolling elements are obtained, the contact pressures and the subsurface contact stresses can be obtained analytically from solutions by McEwen [8] or Sackfield and Hills [9]. The subsurface stresses can be combined with the existing multiaxial fatigue theories and the critical plane approach such as those by Findley [10] or Socie [11] or standardized bearing life calculation

relationships such as those by Lundberg and Palmgren [12], Ioannides and Harris [13] and Lösche [14].

The proposed analytical solution which is based on the previous well known analytical solutions by Hertz [8] and Persson [15] is efficient since it is a closed-form solution which does not require trial-and-error iterations. By using the proposed analytical solution, the same bearing evaluation procedure which requires significant CPU time by the corresponding finite element analysis can be accomplished quickly and then a preliminary assessment of a given bearing design can be provided. Also, certain geometric parameters such as the inner and outer raceway diameters, the size/number of the rolling elements and the applied load can be adjusted to decide which design combination gives the optimum fatigue life before initiating costly experiments or computations.

In this investigation, the elastic contact theory by Hertz for cylindrical contact is first reviewed. The analytical work by Persson for conforming contact is also reviewed. Based on the solutions by Hertz and Persson, an analytical load distribution solution is proposed to calculate the distribution of the loads of the rolling elements in bearings. Two-dimensional and three-dimensional finite element analyses were conducted to validate the accuracy of the proposed analytical solution. The limitations of the analytical solution are also discussed. Finally, conclusions are made.

Closed-form contact solutions of Hertz and Persson

Hertz solution for non-conforming contact

The solution for the contact between elastic cylindrical bodies was derived by Hertz [8]. As shown in Fig. 4.1(a), a long cylinder with the radius *R* is pressed onto a flat surface by a load per unit length, *P*. The Cartesian X, Y and Z coordinates are shown in the figure. The cylinder makes contact with the flat surface over a long strip of area with a width of 2*a* parallel to the Y axis. Here, *a* is defined as the half contact width. Due to the contact, an elliptical contact pressure profile *p*(*x*) is created on the flat surface along the long strip of area.

For the cylinder pressed in contact with the flat surface by a load per unit length *P* as in Fig. 4.1(a), the contact pressure profile *p*(*x*) can be expressed as

$$p(x) = \frac{2P}{\pi a^2}\left(a^2 - x^2\right)^{1/2}, \; -a \le x \le a \tag{4.1}$$

where x denotes a location within the contact area. Fig. 4.1(b) shows the normalized contact pressure $p(x)/p_{\max}$ as a function of the normalized distance from the symmetry plane of contact, x/a. The relationship between the load per unit length P and the half contact width a is given by

$$a = \sqrt{\frac{4PR}{\pi E^*}} \tag{4.2}$$

where E^* is the equivalent elastic modulus defined as

$$\frac{1}{E^*} = \frac{1-\nu_1^2}{E_1} + \frac{1-\nu_2^2}{E_2}. \tag{4.3}$$

Here, E_1, ν_1, E_2 and ν_2 are the elastic moduli and the Poisson's ratios for the cylinder and the flat surface, respectively. When two elastic cylinders in contact with each other

as shown in Fig. 4.1(c), the contact pressure profile $p(x)$ and the half contact width a still follow Eqns. (4.1) and (4.2), respectively. However, R becomes the relative radius of curvature defined by the radii of curvature of the two contacting bodies as

$$\frac{1}{R} = \frac{1}{R_1} + \frac{1}{R_2}. \tag{4.4}$$

For the cylinder and flat surface problem, R is equal to R_1 as the radius of curvature of the flat surface, R_2 becomes infinity. The maximum contact pressure can be found by substituting $x = 0$ into Eq. (4.1) and combining with Eq. (4.2) as

$$p_{\max} = \sqrt{\frac{PE^*}{\pi R}}. \tag{4.5}$$

Eq. (4.5) can be rearranged in terms of the maximum contact pressure such that,

$$P = p_{\max}^2 \frac{\pi R}{E^*}. \tag{4.6}$$

Persson solution for conforming contact

A short description of the solution of Persson [15] is provided in this section. Two elastic bodies are in contact with a concentrated force Q applied to the center of the circular inner body as shown in Fig. 4.2. The inner body is a cylinder with a radius of R_{in}. The outer body is assumed to be an infinite body with a circular hole with a radius of R_{out}. The two body establish contact over an angle of ψ. The stress becomes zero at infinity for the outer body. Since the difference in the radius ($\Delta R = R_{out} - R_{in}$) is small, the assumption of small contact area of Hertz is no longer valid. The contact pressure $p(y)$ is obtained by Persson [15] as

$$\frac{R_{out}p(y)}{Q}=\frac{2}{\pi\sqrt{d^2+1}}\frac{\sqrt{d^2-y^2}}{1+y^2}+\frac{1}{2\pi d^2(1+d^2)}\ln\frac{\sqrt{d^2+1}+\sqrt{d^2-y^2}}{\sqrt{d^2+1}-\sqrt{d^2-y^2}} \tag{4.7}$$

where d is defined by the subtended angle ψ as

$$d=\tan\frac{\psi}{2} \tag{4.8}$$

and y is the angular position of a point on the contact surface such that

$$y=\tan\frac{\theta}{2},\ -d\le y\le d\ . \tag{4.9}$$

The relation of d, ΔR and Q is given by

$$\frac{E\Delta R}{Q}=\frac{2}{\pi}\frac{1-d^2}{d^2}-\frac{I_6}{\pi^2 d^2(1+d^2)} \tag{4.10}$$

where the I_6 defined by

$$I_6=\int_{-d}^{d}\frac{\ln\dfrac{\sqrt{d^2+1}+\sqrt{d^2-t^2}}{\sqrt{d^2+1}-\sqrt{d^2-t^2}}}{1+t^2}dt\ . \tag{4.11}$$

Closed-form load distribution solutions

The proposed load distribution function for bearings is based on the assumption that the profile of the maximum contact pressures of a group of multiple rollers in contact with an opposing surface is the same as the continuous contact pressure profile created by the corresponding continuous body in contact with the opposing surface. Consider the two two-dimensional contact problems as shown in Figs. 4.3(a) and 4.3(b). In both cases, the outer body is infinite with a circular hole. In Fig. 4.3(a), an inner pin is placed concentric to the hole. Multiple cylindrical rolling elements, which are spaced at a

constant angular interval, are placed between the gap of the hole and the inner pin. In Fig. 4.3(b), the inner pin and the equally spaced cylindrical rolling elements are replaced by a single lumped cylinder. The diametral clearances for both cases in Figs. 4.3(a) and 4.3(b) are zero for this analysis. All bodies are assumed to be elastic. The polar coordinate system is also shown in the figures.

A load is applied to the center of the inner pin and the lumped cylinder as in Figs. 4.3(c) and 4.3(d). The multiple rolling elements and the lumped cylinder come in contact with the outer body. If the magnitude of the applied load is such that the stresses due to contact are within the elastic range and yield does not occur, each rolling element positioned in the lower half of the outer body will create an elliptic contact pressure profile as shown in Fig. 4.3(c) as described in Eq. (4.1) since the contact width is much smaller than the relative radius of contact. Note that only the contact pressure profiles on the outer body are depicted in Fig. 4.3(c). The overall contact pressure profile on the outer body will be a discrete with regions of zero pressure between the pressure profiles of the rolling elements. Also, the elliptic contact pressure profiles will have different maximum pressures for the rolling elements. The elliptic contact pressure profile for the i-th rolling element has a maximum contact pressure $p_{\max,i}$. The rolling element which is located closest to the line of loading, which is at or near $\theta = 0°$ will have the largest maximum contact pressure $p_{\max}$ among the maximum contact pressures of all rolling elements. The largest maximum contact pressure is expressed as

$$p_{\max} = \max\left\{p_{\max,i},\ 1 \le i \le n\right\} \tag{4.12}$$

where n is the number of rolling elements.

It should be noted that the multiple rolling element contact is statically indeterminate and cannot be solved solely by considering the force equilibrium alone since the total applied load is not distributed equally among the cylinders in contact. Therefore, additional information is required to find the loads exerted by each rolling element on the outer body.

When the load is applied to the center of the lumped cylinder as in Fig. 4.3(d), a contact pressure profile, $p(\theta)$, will be created on the outer body as shown in Fig. 4.3(d). This contact pressure profile is smooth and continuous compared to the discrete contact pressure profile from the multiple rolling elements as shown in Fig. 4.3(c). The maximum contact pressure due to the lumped cylinder will be much smaller than the largest maximum contact pressure due to the multiple rolling element contact because of the increase in the contact area such that

$$p_{\max} > \max\{p(\theta)\}. \tag{4.13}$$

Now consider the limiting case such that the gap between the outer body and the inner pin decreases to zero, the diameter of the roller elements also decreases to zero, and the number of the rolling elements increases to infinity. The limiting case represents the lumped cylinder case as shown in Fig. 4.3(d). The discrete pressure profile of the limiting case will also approach to that of the lumped cylinder case as shown in Fig. 4.3(d). With this in mind, it is assumed that the ratio between the maximum contact pressures of two different rolling elements in Fig. 4.3(c) is equal to the ratio between the contact pressures due to the lumped cylinder at the corresponding angular location as in Fig. 4.3(d) such that

$$\frac{p_{\max,i}}{p_{\max,j}} = \frac{p(\theta_i)}{p(\theta_j)},\ 1 \le i \le n,\ 1 \le j \le n \tag{4.14}$$

where $p(\theta_i)$ denotes the contact pressure due to the lumped cylinder at the corresponding location of the *i*-th rolling element. In this case, the ratios, rather than the actual values, between the maximum contact pressures from the multiple rolling elements case can be found once the contact pressure profile due to the lumped cylinder is given. Based on this assumption, a closed-form load distribution solution can be derived in the following and then validated by the corresponding finite element analyses based on the typical geometries of wheel roller bearings and cam follower roller bearings.

An idealized two-dimensional cylindrical roller bearing is shown in Fig. 4.4(a). For the idealized roller bearings, there is no interference between the bodies and the bearing is prismatic and infinitely long. The cylindrical roller bearing has an outer cylinder, an inner cylinder and cylindrical rolling elements. The outer cylinder is stationary. The outer surface of the outer cylinder is fixed and the inner cylinder is rotating. All axial motion in the Y axis direction is prohibited. A vertical load P_{total} is applied to the center of the inner cylinder in the z axis direction. The rolling elements in the lower half of the bearing will have contact forces with the inner and outer raceways. These rolling elements will each create a contact pressure profile on the surfaces of the inner and outer raceway as in Fig. 4.4(b). Again, only the contact pressure profiles on the outer raceway are depicted in Fig. 4.4(b). It has been shown that the stationary outer raceway experiences a comparably harsher stress state than the inner raceway. Therefore, only the contact pressure on the stationary outer raceway will be investigated. Each and every contact pressure profile created by the rolling elements on the surface of the outer

raceway will follow the Hertz theory in Eq. (4.1) as the contact area is small compared to the relative radius of curvature. Also, the magnitude of the applied load is low such that the stresses in the bearing components are in the elastic range.

As discussed earlier, the rolling elements as well as the inner cylinder are again replaced by a single lumped cylinder having the same radius as that of the inner surface of the outer cylinder as shown in Fig. 4.5(a). The contact pressure profile that the replaced cylinder creates on the outer raceway, $p(\theta)$, is smooth and continuous as in Fig. 4.5(a). This contact pressure profile can be analytically obtained by using the Persson solution in Eqns. (4.7) to (4.11).

For non-conforming contact, i.e. the contact between a rolling element and the raceway, the size of the contact area is dependent on the magnitude of the applied load as shown in Eq. (4.2). However, assuming that there is no interference between the outer cylinder and the lumped cylinder, the Persson solution in Eq. (4.10) indicates that the size of the contact area is independent of the applied load. This leads to the most important part of the assumption for the proposed solution conclusion that the contact pressure profiles in Fig. 4.5(a) created by an applied load will be self-similar regardless of the magnitude of the applied load. Therefore, a normalized contact pressure function $\bar{p}(\theta)$ can be obtained by the Persson solution as

$$\bar{p}(\theta) = \frac{p(\theta)}{\max\{p(\theta)\}}. \tag{4.15}$$

This normalized contact pressure function $\bar{p}(\theta)$ is shown in Fig. 4.5(b). The contact angle measured from the vertical symmetry plane spans from -91.7° to +91.7°.

The contact angle is a constant value for the zero-interference condition. The number of rollers in contact, *n*, is equal to the number of rolling elements within this contact angle.

The normalized contact pressure function $\bar{p}(\theta)$ can be used to obtain the normalized maximum contact pressures of the rolling elements. The ratio between the maximum contact pressure of the *i*-th rolling element, $p_{\max i}$, and the largest maximum contact pressure $p_{\max}\left(=\max\left\{p_{\max i},\ 1\le i\le n\right\}\right)$ can be estimated by

$$\frac{p_{\max,i}}{p_{\max}}=\bar{p}(\theta_i),\ 1\le i\le n \tag{4.16}$$

where θ_i is the angular location of the *i*-th rolling element. The load exerted by the *i*-th rolling element, P_i, which is shown in Fig. 4.6 can be obtained by Eq. (4.6) in terms of the maximum contact pressure of the *i*-th rolling element as

$$P_i=\frac{\pi R}{E^*}p_{\max,i}^2,\ 1\le i\le n. \tag{4.17}$$

As referring to Fig. 4.6, the sum of the vertical components of the loads exerted by the rolling elements should be equal to the total applied load P_{total} due to the force equilibrium such that

$$\sum_{i=1}^{n}\left(P_i\cos\theta_i\right)=P_{total} \tag{4.18}$$

Combining Eqns. (4.16), (4.17) and (4.18) gives the following expression for the load exerted by the *i*-th rolling element on the outer raceway in terms of the total applied load as

$$P_i=\frac{\bar{p}^2(\theta_i)}{\sum_{j=1}^{n}\bar{p}^2(\theta_j)\cos\theta_j}P_{total},\ 1\le i\le n. \tag{4.19}$$

By using Eq. (4.19), the load exerted by the *i*-th rolling element on the outer raceway can be obtained by the number of rolling elements, n , the angular location of the rolling elements θ_i, and the normalized contact pressure function $\bar{p}(\theta)$.

Validation of the closed-form solution

Two-dimensional finite element analyses were carried out to validate the analytical load distribution function. The contact pressures from the finite element analyses are compared to the contact pressures of the analytical solution. Two-dimensional plane strain finite element models were developed to obtain the loads between the rolling elements and the outer raceway in the middle portion of a cylindrical roller bearing. A representative finite element model is shown in Fig. 4.7(a). The Cartesian X-Y coordinates are also shown in the figure. Fig. 4.7(a) shows the three essential parts of the finite element model; an inner cylinder, the rolling elements and the outer cylinder. Second-order, isoparametric, plane strain, quadrilateral, reduced integration elements (CPE8R) are used in the models. The minimum element size is 10.0 $x10^{-3}$ mm. The outer surface of the outer cylinder is constrained in both X and Y directions. The central region of the inner cylinder is constrained in the X direction to prohibit undesirable horizontal motion. A uniformly distributed vertical load in the negative Y direction is applied to the central region of the inner cylinder. The bold arrow in Fig. 4.7(a) shows the direction of the applied load. Fig. 4.7(b) shows a close-up view of the mesh refinement near the contact region boxed in Fig. 4.7(a). The elastic modulus *E* is 200 GPa and the Poisson's ratio *v* is 0.3 for all material elements in the finite element model. The steels used for manufacturing bearing components usually have high yield

stresses of more than 1200 MPa. For a given design load 60 N, stresses on the contact surface and in the subsurface area near the contact are within the elastic range. Computations were performed using the commercial finite element software Abaqus v6.8 [16].

The maximum contact pressures between the rolling elements and raceway obtained from the finite element analysis are compared to the contact pressures calculated using the analytical solution. Since the analytical solution method gives the loads exerted by the rollers as shown in Fig. 4.6 instead of the maximum contact pressures from the rollers as shown in Fig. 4.4(b). Therefore, Eqns. (4.5) and (4.6) are used to calculate the maximum contact pressures for the *i*-th rolling element, $p_{\max,i}$, from the load exerted by the *i*-th rolling element, P_i.

The maximum contact pressures of the rolling elements obtained from the two-dimensional finite element analysis and the analytical solution are listed in Table 4.1 and shown in Fig. 4.8. Table 4.1 also shows the details of using Eq. (4.19) based on the analytical solution to obtain the loads exerted by the rolling elements in contact. The first row of Table 4.1 shows the angular locations of the rolling elements in contact. The 0° is defined as where the load line intersects the outer raceway. The second row of Table 4.1 show the values from the normalized contact pressure function, $\overline{p}(\theta_i)$, for the corresponding angular locations in the first row based on the Persson solution as shown in Fig. 4.5(b). The third and fourth rows show the necessary values needed for Eq. (4.19). The fifth row shows the values of the load P_i exerted by the rolling elements. These

values are substituted into Eq. (4.5) to calculate the values of the maximum contact pressure $p_{\max i}$ for each rolling element which are shown in the sixth row.

The seventh row shows the values of the maximum contact pressures for the rolling elements in contact obtained from the two-dimensional finite element analysis. The errors of the maximum contact pressures calculated from the analytical solution compared to those of the two-dimensional finite element analysis for the rolling elements are shown in the last row. As listed in the table, the largest error occurs at the rolling elements located at ±50° and is about 6%. Also, the error between the highest possible maximum contact pressure rolling elements located at ±10°, which causes the largest subsurface stresses, is less than 3%.

The maximum contact pressures from the two-dimensional finite element analysis and the analytical solution are shown in Fig. 4.8(a). As shown in the figure, the analytical solution gives the maximum contact pressures which are close to the maximum contact pressures obtained from the finite element analysis. Fig. 4.8(b) shows the normalized maximum contact pressures from the two-dimensional finite element analysis and the analytical solution. The pressures are normalized by the maximum pressures of the rolling element with the largest load. Note that the eight contact pressure profiles shown as vertical lines from the finite element analysis in Fig. 4.8 actually are elliptical curves defined in Eq. (4.1).

It should be noted that the discrete nature of using finite element analysis to simulate elastic or elastic-plastic contact problems usually give the maximum contact pressure from the simulations with an error of a few percents when compared to the analytical Hertz solutions [17]. For this particular simulation, there are at least 18 finite

elements in contact for the given load. The contact pressure profiles for the roller at θ=10° from the finite element analysis and the Hertz solution are shown in Fig. 4.8(c). As shown in the figure, the contact pressure solutions from the finite element analysis and the Hertz solution are compared well with each others.

As shown in Fig. 4.7, the outer cylinder appears to have the thickness in the same order of the roller diameter. The outer cylinder appears not to represent an infinite body as required by the assumption for derivation of the Persson solution used to derive the analytic load distribution solution. However, by considering the small contact length for the given design load, the cylinder is still large enough to represent an infinite outer cylinder. Note that the geometric parameters of the bearing investigated here are representative of the cam follower roller bearings and wheel bearings. The analytical solution appears to work well. As the diameter of the rollers becomes smaller and the number of the rollers increases, the approximate solution should be more applicable as discussed earlier for the limiting case.

Fatigue life estimation

The loads exerted by the rolling elements obtained by the analytical solution in Eq. (4.19) have been validated for a typical bearing design in the previous section. However, the loads given by Eq. (4.19) may not be the most important consideration during bearing design or selection processes. Rather, the fatigue lives of the subsurface material due to the contact stresses induced by the loads through the contact of the rolling elements is a better measure of the performance of a given bearing. The process of estimating the fatigue life of a given bearing is summarized in this section. This process has been used

as the basis for a bearing fatigue life estimation software. The software has been successfully implemented into the bearing selection procedure at Chrysler LLC.

The subsurface stresses along the symmetry plane directly under a Hertz contact pressure profile having a maximum pressure of p_0 is given by

$$\sigma_x = -\frac{p_0}{a}\left\{\frac{a^2+2z^2}{\sqrt{a^2+z^2}} - 2z\right\} \tag{4.20}$$

$$\sigma_z = -p_0 \frac{a}{\sqrt{a^2+z^2}} \tag{4.21}$$

$$\sigma_y = \nu\left(\sigma_x + \sigma_z\right). \tag{4.22}$$

The maximum contact pressure can be obtained by using Eq. (4.5) with the load exerted by the rolling elements from Eq. (4.19). Here, a is the half contact width and z is the subsurface depth. The maximum shear stress occurs directly under the roller in the subsurface at a depth of $z = 0.78a$ and is given by

$$\tau_{\max} = 0.3p_0. \tag{4.23}$$

Also, the Mises stress as a function of the principal stresses is given by

$$\sigma_{mises} = \frac{1}{\sqrt{2}}\sqrt{\left(\sigma_x - \sigma_y\right)^2 + \left(\sigma_y - \sigma_z\right)^2 + \left(\sigma_z - \sigma_x\right)^2}\,. \tag{4.24}$$

Substituting Eqns. (4.20), (4.21) and (4.22) into Eq. (4.24) will given the Mises stress as a function of the maximum contact pressure, the half contact width and the subsurface depth. The maximum Mises stress occurs in the subsurface at a depth of $z = 0.7a$ and is given by

$$\left(\sigma_{mises}\right)_{\max} = 0.28p_0. \tag{4.25}$$

The maximum shear stress obtained in Eq. (4.23) can be used with the bearing life predictions by Lundberg and Palmgren [12], Ioannides and Harris [13] and Lösche [14]. Here, a simplified fatigue life estimation method is proposed with the use of Goodman relation to find the equivalent stress amplitude for fully reversed loading. The equivalent stress amplitude is combined with the stress-life curve of the material to estimate the number of cycles to failure.

The simplified fatigue life estimation is based on the assumption that the total applied load on the bearing is constant. The simplified fatigue life estimation is also based on the assumption that the initial load and the interference load are not considered. By assuming a constant value for the total applied load, the loads exerted by the rolling elements on the outer raceway as well as the maximum contact pressures due to these loads will remain constants. Also, the maximum value of the Mises stress and the location of the maximum Mises stress remain the same. Therefore, a material element located in the subsurface of the outer raceway at a depth of $z = 0.7a$ experiences a cyclic stress state ranging from zero to the maximum Mises stress. The mean stress σ_m and the stress amplitude σ_a is given by

$$\sigma_m = \frac{1}{2}\sigma_{mises} \tag{4.26}$$

$$\sigma_a = \frac{1}{2}\sigma_{mises} \tag{4.27}$$

Therefore, the equivalent stress amplitude for fully reversed loading, S_n, is

$$S_n = \left\{ \frac{1-\sigma_m / S_u}{\sigma_a} \right\}^{-1} . \tag{4.28}$$

where S_u is the ultimate stress of the bearing material. Once, the equivalent stress amplitude is obtained, the fatigue life of a bearing can be estimated from the stress-life curve of the bearing material as

$$N_f = \left(\frac{S_n}{A} \right)^{1/B} \tag{4.29}$$

Here, N_f is the number of cycles to failure and A and B are material constant which are obtained with standardized fatigue testing procedures. At the initial design stage, the simple life estimation method based on the Goodman relation and the Mises stress can be used. Life estimations based on multiaxial fatigue theories and the critical plane approach can be used at the later stages of bearing design.

Discussions

The normalized contact pressure function $\overline{p}(\theta)$ for the zero interference model is critical to accurately calculate the loads exerted by the rolling elements and the maximum contact pressures created by these loads. Alternate candidates for the normalized contact pressure profile for the zero interference model can be a higher order polynomial functions or an elliptic function. However, it has been determined that the alternate candidates did not achieve the accuracy of the original Persson solution by comparing the maximum contact pressures of the rolling elements as in the previous section.

The Persson solution is derived based on an assumption that the outer raceway should be an infinite body without any constraints such that the stress due to contact vanishes at infinity. However, in reality, bearings have geometric restrictions and finite outer cylinder dimensions. Therefore, the bearing models discussed in this chapter does

not satisfy the original infinite outer body assumption. The thickness of the outer cylinder has a length usually larger that the radius of the rolling elements. However, due to the small contact lengths of the rolling elements compared to the radius of the rolling elements, the analytical solution based on the Persson solution fits well to the finite element results.

The analytical solution is applicable in situations where the outer cylinder is fixed. Bearings used in cam systems, such as the cam follower roller bearings, do not have any constraints on the outer surface of the outer cylinder except for the area of contact with the cam. Since the outer cylinder does not have geometric constraints, the outer ring is able to deform under the load applied to the cam follower roller bearing by the cam. The applied load causes the outer cylinder to become lopsided which results in decrease of the number of rolling elements in contact. The contact pressures between the rolling elements and the raceway surface on the outer cylinder can no longer be estimated by the normalized contact pressure function, $\bar{p}(\theta)$ as discussed in this chapter.

For spherical roller bearings, a similar derivation can be used to estimate the loads exerted by the rolling elements on the outer raceway such that

$$P_i = \frac{\alpha^3(\theta_i)}{\sum_{j=1}^{n} \alpha^3(\theta_j)\cos\theta_j} P_{total}, \quad 1 \le i \le n. \tag{4.30}$$

A three-dimensional finite element analysis has been conducted to validate the applicability of Eq. (4.30). A finite element model which is based on a double row angular contact generation 3 automobile wheel bearing is shown in Figs. 4.9(a) and 4.9(b). Due to the limited computing resources, the mesh is crude with relatively large element size near the contact region. The maximum contact pressures from the three-dimensional

finite element analysis and the analytical solution from Eq. (4.30) are shown in Fig. 4.10(a). Fig. 4.10(b) shows the normalized maximum contact pressures from the two-dimensional finite element analysis and the analytical solution. The pressures are normalized by the maximum pressures of the rolling element with the largest load. As shown in Figs. 4.10(a) and 4.10(b), the analytical solution gives a reasonable estimation of the loads for the rolling elements.

Conclusion

In this chapter, an analytical load distribution solution to calculate the loads exerted by the rolling elements in cylindrical bearings without interference is proposed based on the analytical solutions of Hertz and Persson. The analytical solution is based on the assumption that the profiles of the maximum contact pressure between the multiple rolling elements and the opposing surface is the same as the contact pressure profile between the continuous body and the opposing surface. This assumption combined with the force equilibrium condition forms the basis to derive the analytical solution. With the normalized load distribution solution, the only input required to obtain the loads exerted by the rolling elements is the total applied load.

Two-dimensional finite element analyses were conducted to validate the analytical solution. The maximum contact pressures from the rolling elements that are in contact with the outer raceway obtained from the two-dimensional finite element analysis are compared with the contact pressures calculated from the analytical solution. A comparison shows that the maximum error for the rolling elements having the largest maximum contact pressure is less than 3%.

A simplified method to estimate the fatigue of the bearing is also summarized. The method is based on the load exerted by the rolling element and the closed-form solution to calculate the subsurface Mises stress. The Mises stress is then combined with the Goodman relation and the stress-life relation of the bearing material to estimate the number of cycle to failure under constant amplitude loading conditions.

Based on the analytical solution, a software has been developed to estimate the fatigue life of a given bearing. The proposed method will not be able to eliminate the experimental or computational validation process of the bearing but will be able to provide a quick assessment of the fatigue life of a given bearing. Engineers can implement the software in the design and selection process of automotive wheel bearings in order to reduce cost and time by being able to have a guideline of fatigue properties of bearing candidates.

References

[1] Nurkala LD, Wallace RS. Development of the SAE biaxial wheel test load file. SAE Technical paper No. 2004-01-1578. Society of Automotive Engineers, Warrendale, PA; 2004.

[2] Hoeprich MR, Rolling element bearing fatigue damage propagation. J Tribology 1992; 114: 328-33.

[3] Grubisic V, Fischer G. Methodology for effective design evaluation and durability approval of car suspension components. SAE Technical paper No. 970094. Society of Automotive Engineers, Warrendale, PA; 1997.

[4] Jacobson B. The Stribeck memorial lecture. Tribology Int. 2002; 36: 781-9.

[5] Goodelle RA, Derner WJ, Root LE. Determination of static load distributions from elastic contacts in rolling element bearings. Tribology Transactions 1971; 14: 275-91.

[6] Harris, T. Rolling bearing analysis. 4th ed. John Wiley & Sons Inc. New York 2001.

[7] De Paula FN, Cavalcanti D, Cavalca KL, Arima G, Development of software applying the Hertz contact theory to commercial rolling bearings. SAE Technical paper No. 2005-01-4031. Society of Automotive Engineers, Warrendale, PA; 2005.

[8] Johnson KL, Contact mechanics 2003; ISBN 0 521 34796 3. 9th ed. Cambridge University Press, UK 2003.

[9] Sackfield A, Hills DA. Some useful results in the classical Hertz contact problem. The Journal of Strain Analysis for Engineering Design 1983; 18: 101-5.

[10] Findley WN. A theory for the effect of mean stress of fatigue of metals under combined torsioin and axial load or bending. J Eng for Industry 1959; 81:301-6.

[11] Socie DF. Critical plane approaches for multiaxial fatigue damage assessment. Advances in Multiaxial Fatigue (ASTM STP 1191) 1993. American Society of Testing and Materials, Philadelphia, PA, 7-36.

[12] Zaretsky EV. A. Palmgren revisited - A basis for bearing life prediction. NASA Technical Memorandum 107440.

[13] Ioannides E, Harris TA. A new fatigue life model for rolling bearings. J Tribology 1985; 107: 367-78.

[14] Lösche T. New aspects in the realistic prediction of the fatigue life of rolling bearings. Wear 1989; 134: 357-75.

[15] Persson A. On the stress distribution of cylindrical elastic bodies in contact. PhD dissertation, Chalmers Tekniska Högskola; 1964.

[16] ABAQUS v6.8 User Manual. Providence, RI: SIMULIA; 2008.

[17] Ali MY, Pan J. to be submitted for publication.

Table 4.1 Maximum contact pressure obtained from the approximate solution and the two-dimensional finite element analysis.

θ_i (degrees)	-70	-50	-30	-10	10	30	50	70
$\bar{p}(\theta_i)$	0.526	0.779	0.925	0.992	0.992	0.925	0.779	0.526
$\bar{p}^2(\theta_i)$	0.276	0.607	0.855	0.984	0.984	0.855	0.607	0.276
$\bar{p}^2(\theta_i)\cos\theta_i$	0.094	0.390	0.741	0.969	0.969	0.741	0.390	0.094
p_i (N/m) (solution)	1.89	4.15	5.85	6.73	6.73	5.85	4.15	1.89
$p_{\max,i}$ (MPa) (solution)	105.4	156.2	185.5	198.9	198.9	185.5	156.2	105.4
$p_{\max,i}$ (MPa) (FEM)	110.1	165.9	194.5	204.6	204.6	194.5	165.9	110.1
Error (%)	4.27	5.85	4.63	2.79	2.79	4.63	5.85	4.27

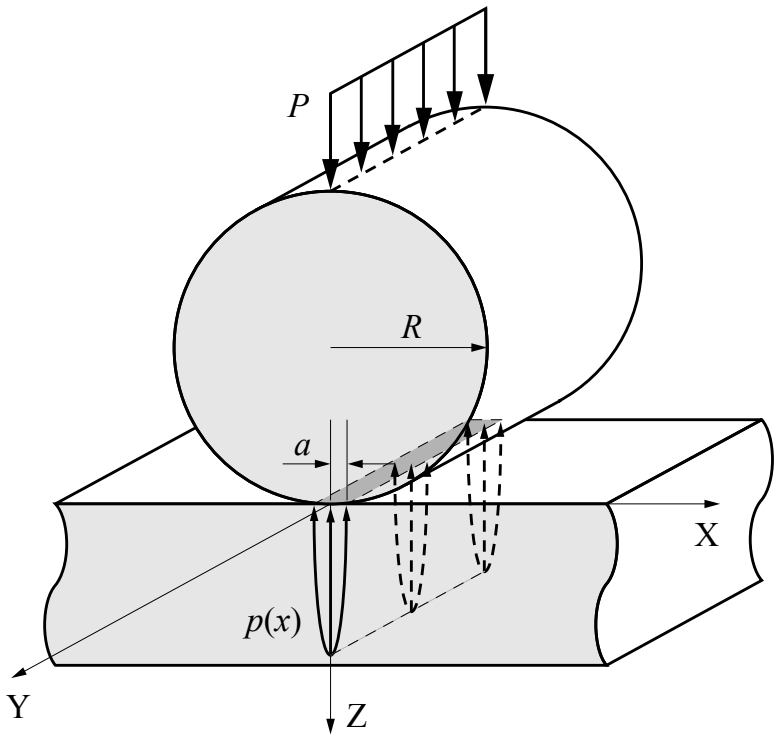
P
R
a
X
p(x)
Y
Z

(a)

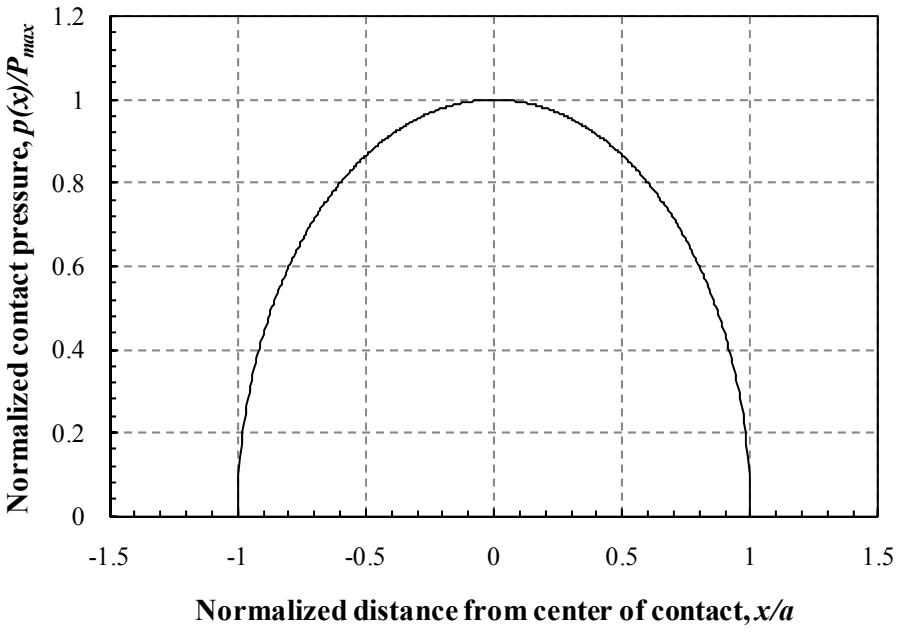
1.2
1
0.8
0.6
0.4
0.2
0
Normalized contact pressure, p(x)/P_max
-1.5
-1
-0.5
0
0.5
1
1.5
Normalized distance from center of contact, x/a

(b)

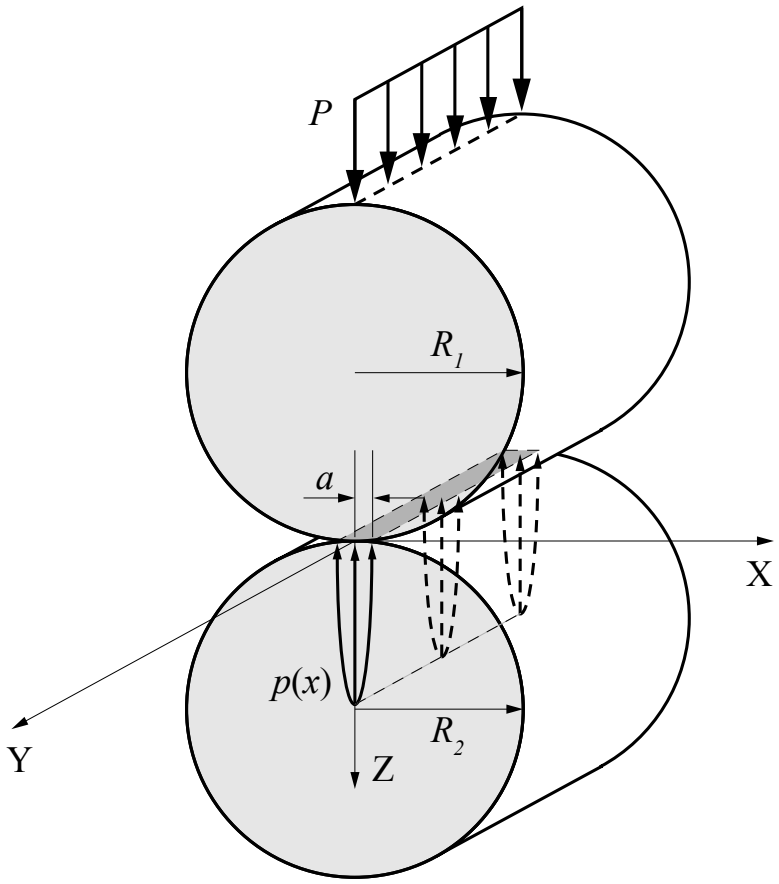

(c)

Fig. 4.1 (a) Contact between a cylinder and a flat surface due to a load per unit length. (b) The normalized elliptical contact pressure profile between a cylinder and a flat surface. (c) Contact between two cylinders due to a load per unit length.

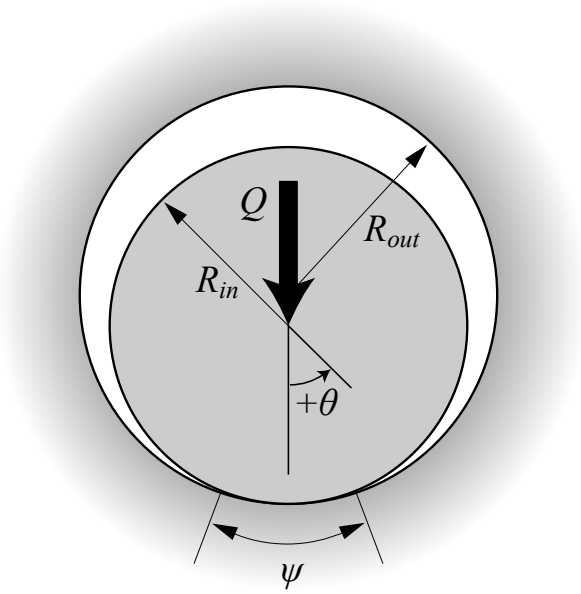

Fig. 4.2 Contact between an inner cylinder and an infinite outer body.

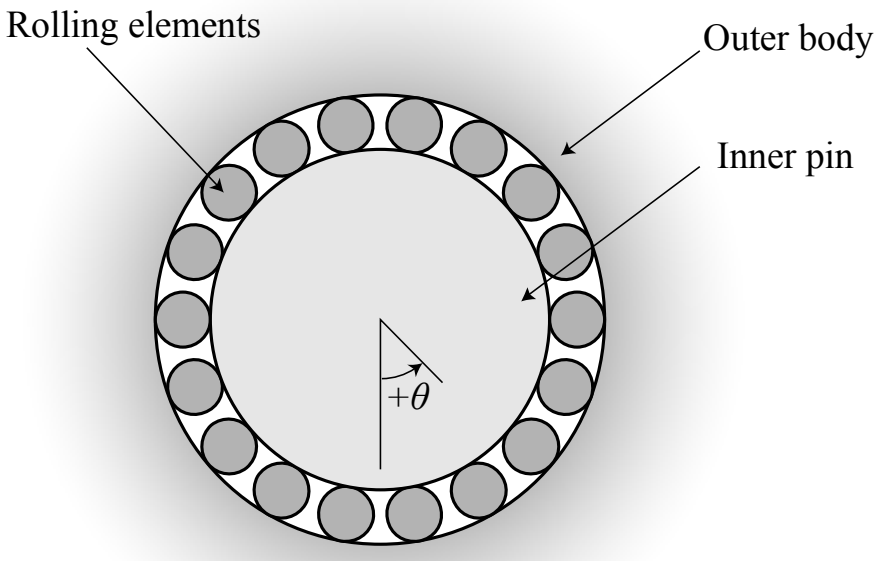
Rolling elements
Outer body
Inner pin
+θ

(a)

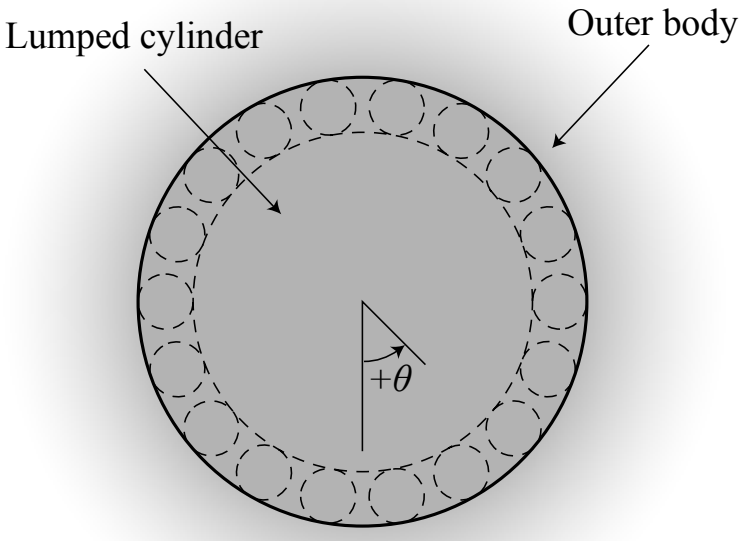
Lumped cylinder
Outer body
+θ

(b)

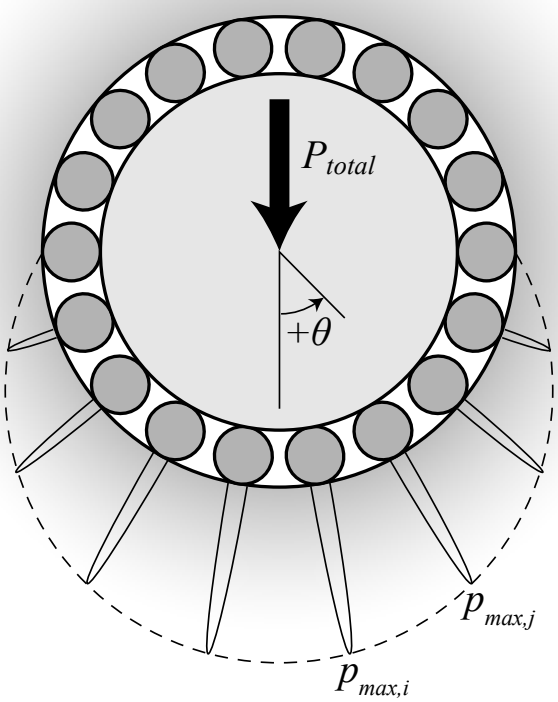

(c)

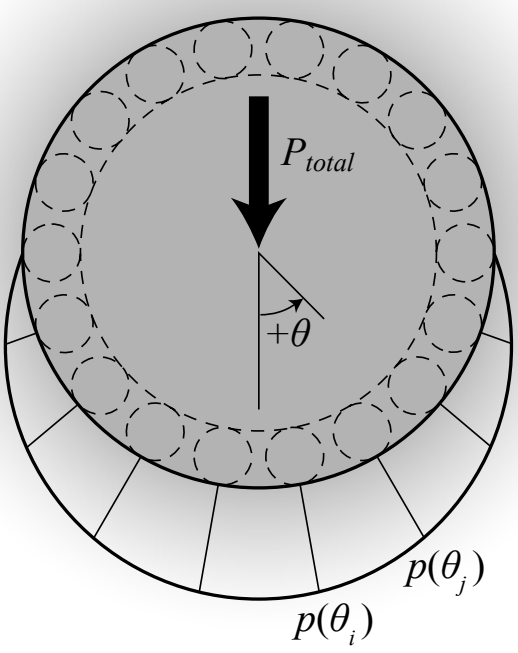

(d)

Fig. 4.3. (a) Contact to the outer cylinder due to multiple rolling elements. (b) Contact to the outer cylinder due to a single smooth and continuous cylinder. (c) Contact pressure profiles due to multiple cylinders. (d) Contact pressure profile due to a single smooth and continuous cylinder.

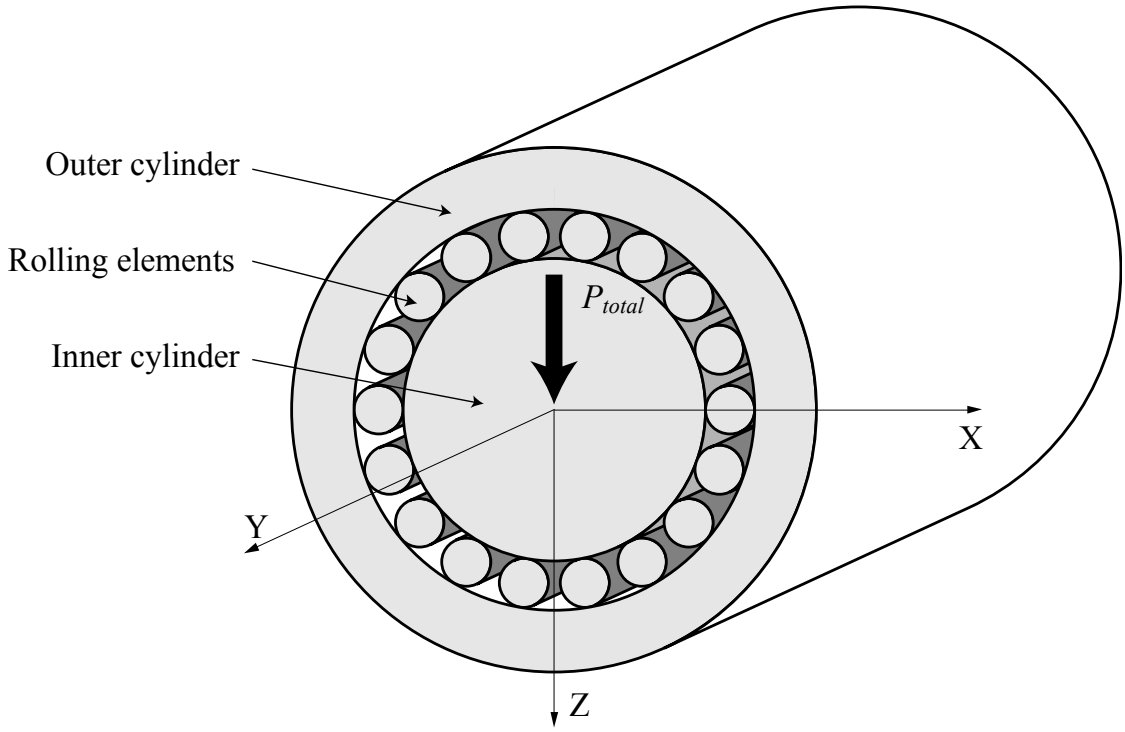

(a)

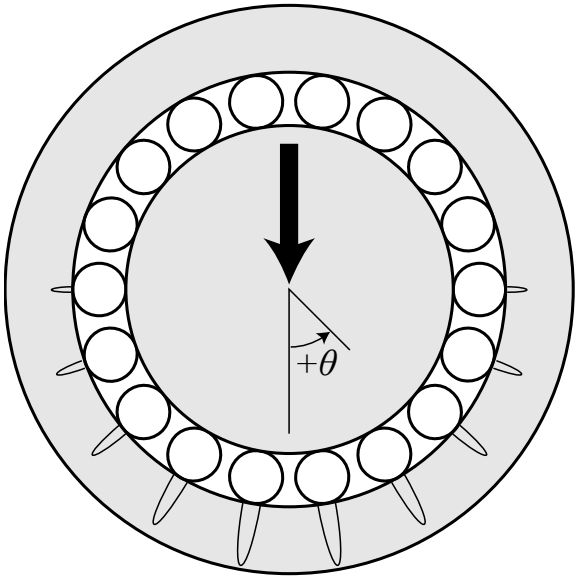

(b)

Fig. 4.4. (a) An idealized cylindrical roller bearing under a load and (b) the contact pressure profiles on the outer raceway due to the load.

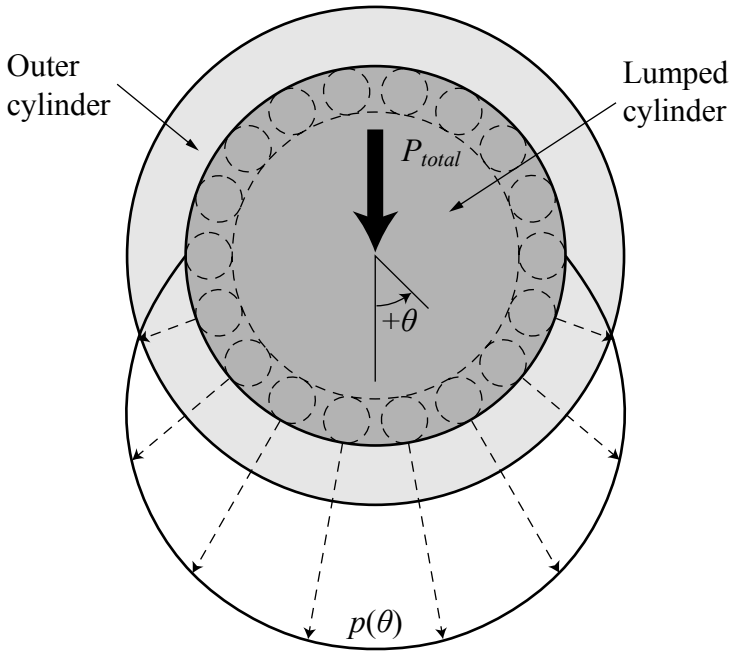

(a)

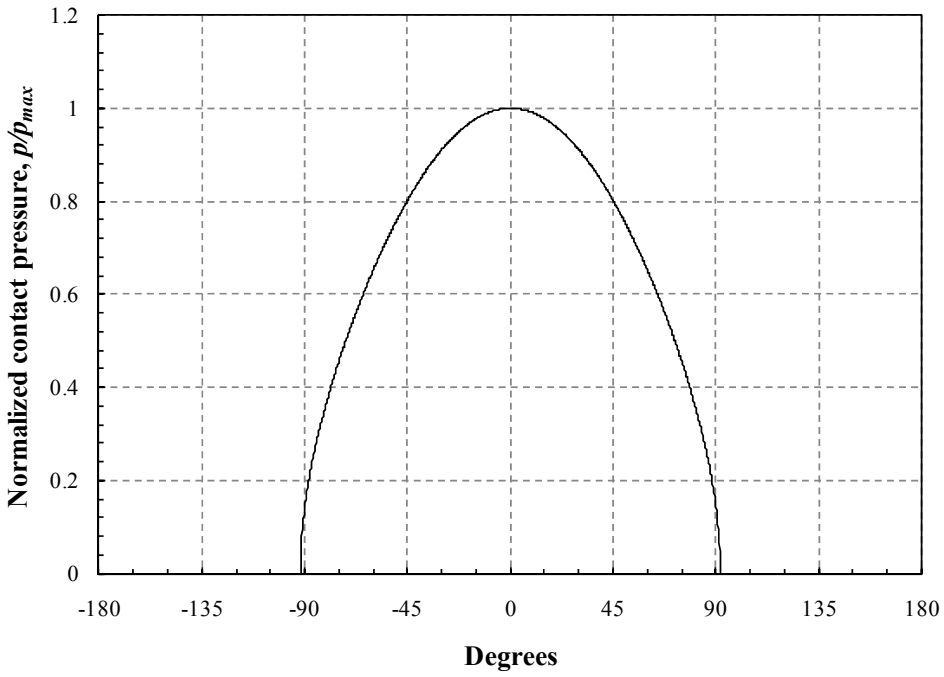

(b)

Fig. 4.5. (a) Contact pressure profile for a conforming contact. (b) The normalized contact pressure function due to the conforming contact.

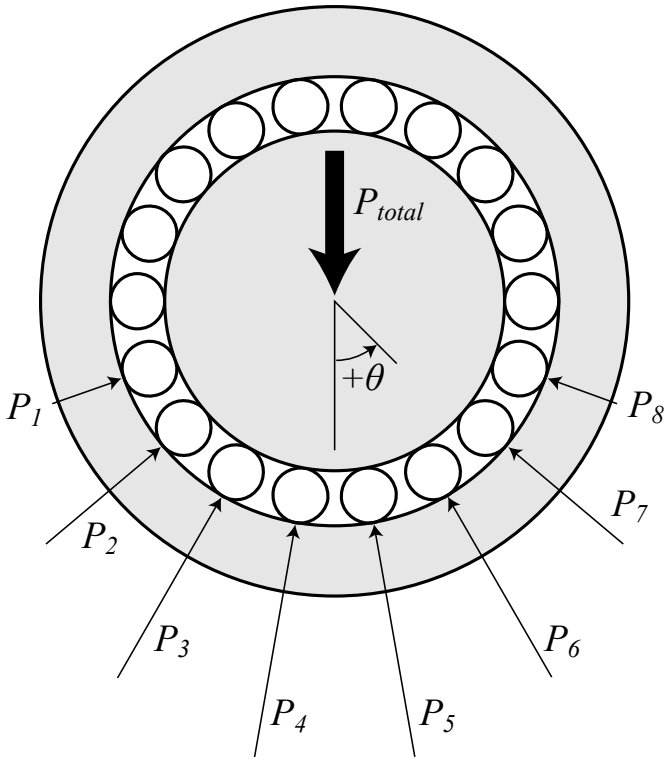

Fig. 4.6. The loads exerted by the rolling elements on the outer raceway.

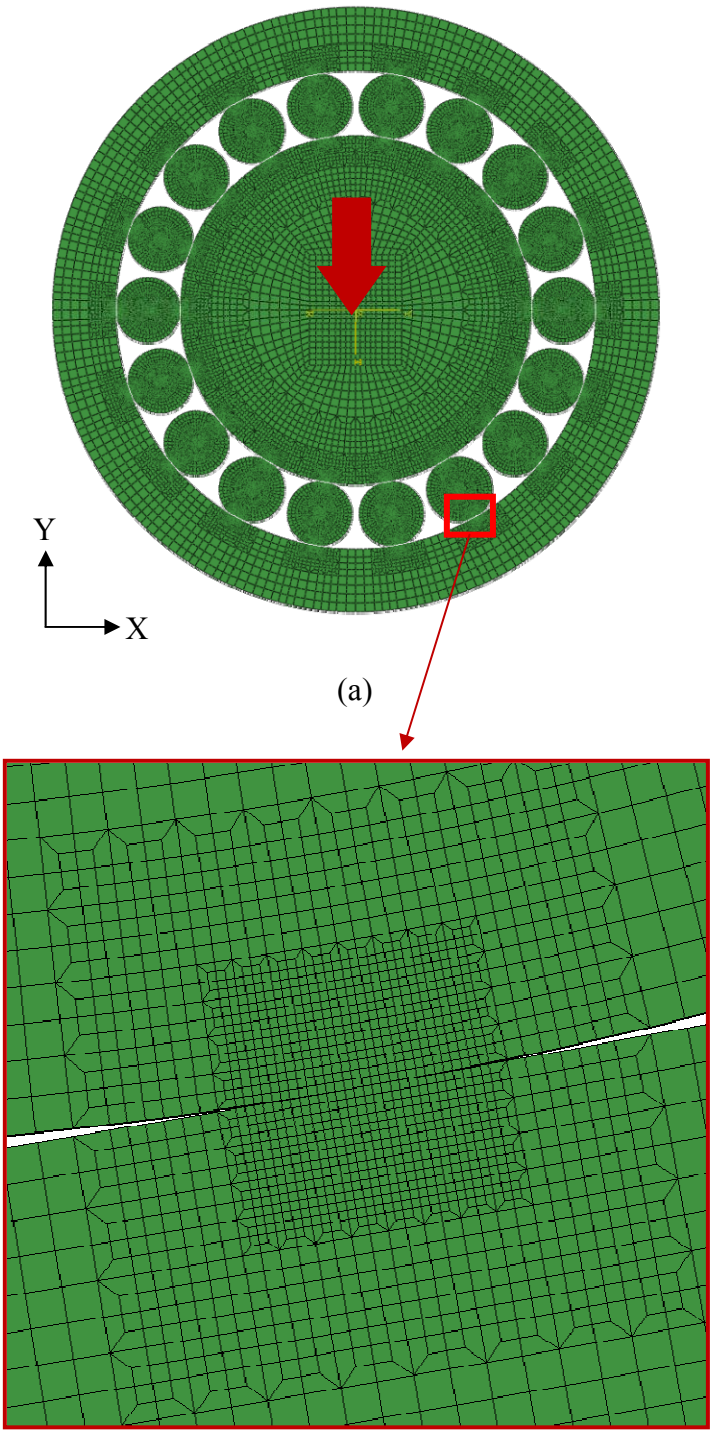

Fig. 4.7. (a) A two-dimensional finite element model. The bold arrow indicates the applied load. (b) A close-up view of the mesh refinement near the contact region of a roller and the outer raceway.

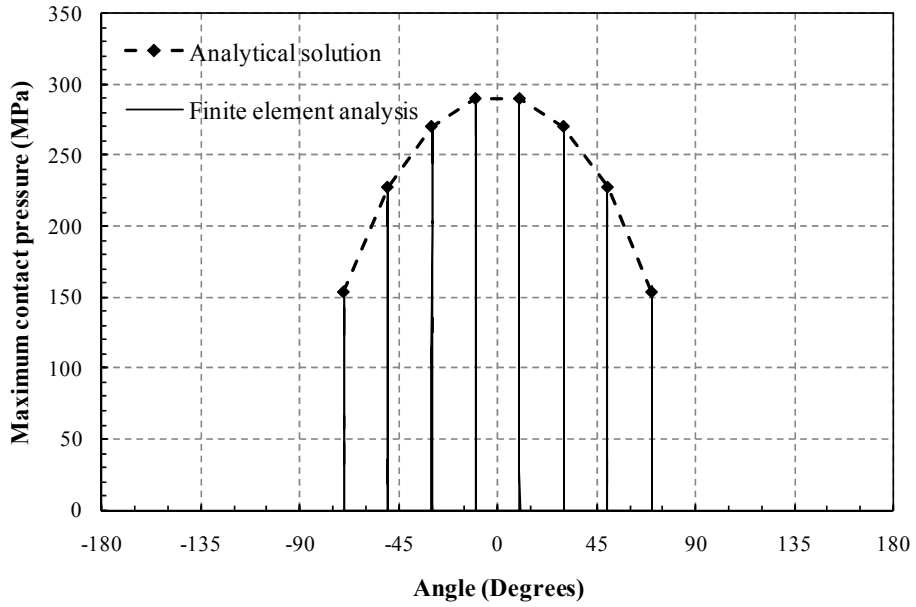
Analytical solution
Finite element analysis
Maximum contact pressure (MPa)
350
300
250
200
150
100
50
0
-180
-135
-90
-45
0
45
90
135
180
Angle (Degrees)

(a)

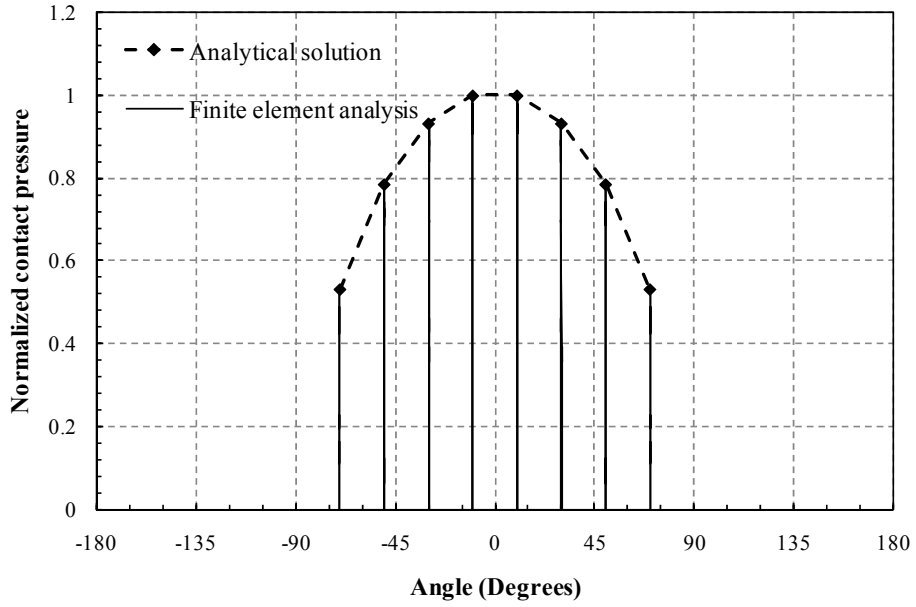
Analytical solution
Finite element analysis
Normalized contact pressure
1.2
1
0.8
0.6
0.4
0.2
0
-180
-135
-90
-45
0
45
90
135
180
Angle (Degrees)

(b)

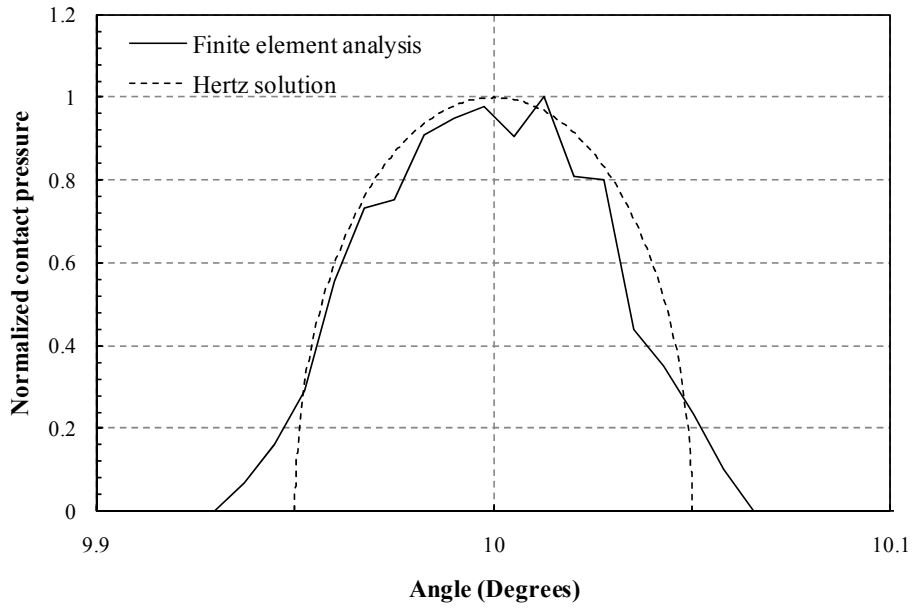

(c)

Fig. 4.8. (a) The maximum contact pressures obtained from the analytical solution and the two-dimensional finite element analysis. (b) The normalized contact pressures obtained from the analytical solution and the two-dimensional finite element analysis. (c) The contact pressure profiles for the rolling element at $\theta=10°$ from the finite element analysis and the Hertz solution.

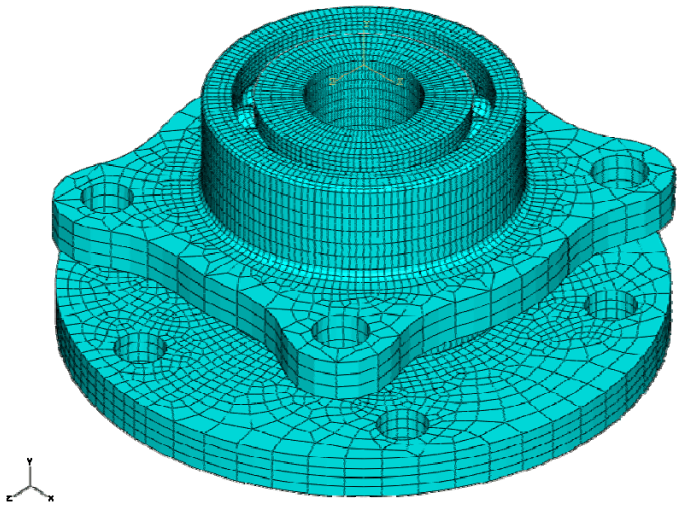

(a)

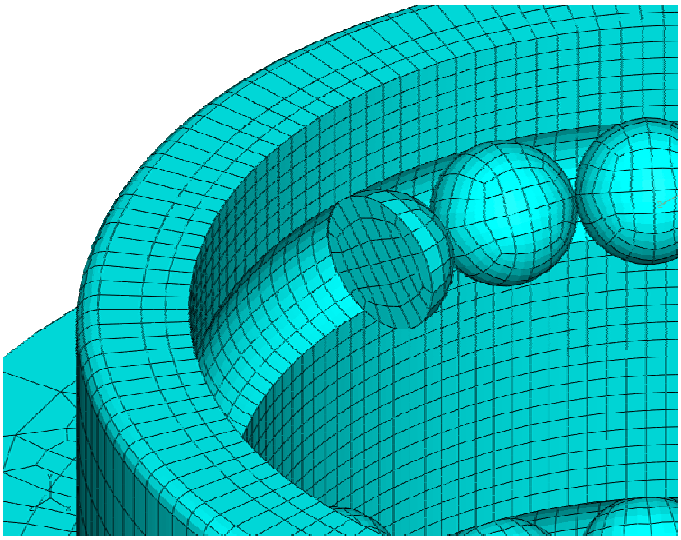

(b)

Fig. 4.9. (a) A three-dimensional finite element model based on the Gen3 automobile wheel bearing. (b) A close-up and cut-away view of the rolling elements and the outer raceway in the three-dimensional model.

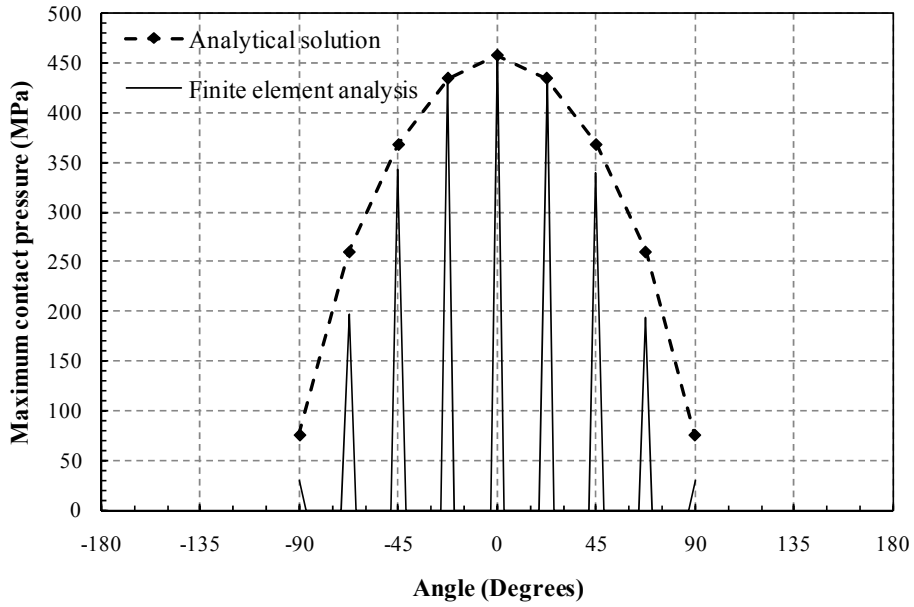

(a)

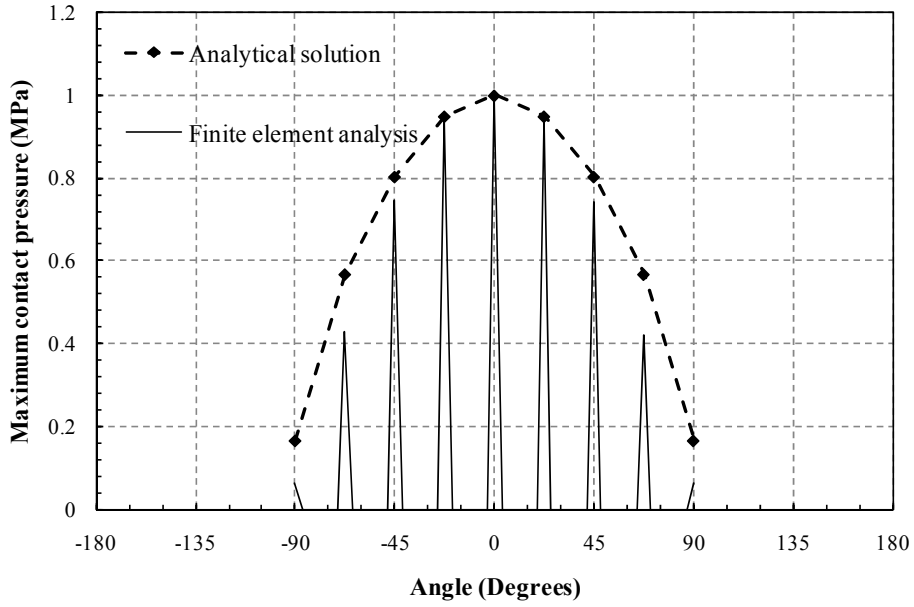

(b)

Fig. 4.10. (a) The maximum contact pressures obtained from the analytical solution and the three-dimensional finite element analysis. (b) The normalized contact pressures obtained from the analytical solution and the three-dimensional finite element analysis.

Chapter 5
Geometric Effects on Contact Pressure Distribution and Fatigue Lives of Cam Follower Roller Bearings

Introduction

Cam followers are an essential component of internal combustion engines and are required to control air and fuel flow into the combustion chambers. Previously and even in the current applications, cam followers with sliding contact have been and are still being used due to its simplicity. The fatigue lives and wears of cam followers with sliding contact have been investigated [1], [2], [3]. However, due to the requirements for high performance engines [4], [5], engineers have sought design changes which demand valvetrains with higher speed and acceleration and thus more force applied to the cam follower system. Since an increase in the normal force directly results in the increase of frictional force, the current trend is to use cam roller followers instead of cam followers with sliding contact to lower the frictional coefficient and thus minimize frictional forces. Cam roller followers are expected to soon replace most cam followers with sliding contact [6]. The advantages of using cam roller followers instead of cam followers with sliding contact also includes less wear and energy loss [7]. However, there are also disadvantages of cam roller followers due to the increase in contact stress, complex functional requirements and manufacturing processes [6].

Studies have been conducted on the fatigue lives of cam roller followers both experimentally and analytically. Gecim [8] investigated the lubrication characteristics

between the cam and cam roller follower, and derived a fatigue life equation. Lee et al. [9] developed a method to calculate the normal force and contact stress between a cam and a cam roller follower. Krepulat et al. [10] obtained the contact pressure between a cam and a cam roller follower with use of finite element analyses. Hua et al. [11] conducted an investigation on the contact fatigue of the cam surface using a multi-scale system analysis. Cheng et al. [12] have identified through experiments that the failure mode of cam roller follower bearings is subsurface crack initiation and propagation. It should be noted that, an exhaustive review by Sadeghi et al. [13] on rolling contact fatigue can provide insight on the fatigue life assessment of cam roller follower bearings.

A simple solution to increase the fatigue lives of bearings in general appears to utilize rollers with larger diameters. A larger roller will increase the contact area and allow the applied load to spread out. The maximum contact pressure is inversely proportional to the square of the radius of curvature. Consequently, the contact pressures and the subsurface stresses are reduced. However, for cam roller follower bearings, there exists is a trade-off between the increase in the roller diameter and the decrease in the outer ring thickness. A larger roller must be accompanied by a decrease of the outer ring thickness or the inner pin diameter due to the geometric restriction of the bearings. The outer ring thickness directly affects the compliance and the amount of deformation of the outer ring under a given load. The effect of this increase of compliance has not been investigated previously.

In this chapter, finite element analyses were conducted to understand the effects of the diameter and the number of rolling elements on the contact pressure distribution, maximum subsurface Mises stress and fatigue lives of the cam roller follower bearing.

Two groups of cam roller follower bearing models having different diameters and numbers of rolling elements are investigated using two-dimensional plane strain finite element analyses. Based on the results of the finite element analyses, the fatigue lives of the cam roller follower bearings of theses bearing models are estimated and compared. Finally, conclusions are made.

Finite element analyses

A schematic of a cam and a cam follower roller bearing is shown in Fig. 5.1(a). In this investigation, finite element models were developed for the cam follower roller bearings. As shown in the figure, the roller bearing has a outer ring, inner pin and rolling elements. Finite element analyses were carried out to identify the influence of the bearing geometry on the contact pressure distribution, maximum subsurface Mises stress and fatigue lives of the cam roller follower bearing. The major design parameters investigated in the finite element analyses are the diameter and number of rolling elements and the thickness of the outer ring.

Main simplifications

Several assumptions were made to simplify the finite element model. Needle rollers in cam roller follower bearings have a large ratio of length to diameter of about 10. Therefore, the plane strain assumption will give good approximation near the middle portion of the contact area where most fatigue failures are initiated. By using this assumption, the edge effect of the rollers on the contact surface is ignored [10].

Also, a concentrated force will be used to simulate the load applied to the cam follower roller bearing by the cam. In fact, a finite contact area exists between the two elastically deformable bodies. The cam will apply a distributed force to the cam follower over this contact area. However, for simplicity, the distributed force on this finite contact area will be replaced with a single concentrated resultant force applied to a single node. Finite element model of the roller bearing model 18-1 as discussed later with a concentrated load and a distributed load applied to the roller bearings were developed. The results of the finite element analyses for the subsurface Mises stresses are plotted as a function of the normalized depth by the thickness of the outer ring as shown in Fig. 5.14 for the critical contact region of the outer ring under the largest contact force from the rolling element. As shown in the figure, the Mises stress distributions are quite close to each other and the error is quite small near the contact surface. Therefore, the use of a concentrated force on the roller bearing is a feasible yet simple method to obtain the stresses near the critical contact region which is far away from the location of the applied force.

Another assumption is the use of a constant load. The cam follower is under a variable loading condition during normal operation. However, the load applied to the cam roller follower bearing model is assumed to be at a constant maximum load. The resulting contact pressures and subsurface stresses of the critical contact region will represent those of the cam roller follower bearing experienced at the constant maximum load of the cam and cam follower. This assumption can underestimate the fatigue lives of the cam roller follower bearings. However, a comparison between different models can

be nonetheless obtained to find the optimal geometry which gives the longest fatigue life for the given condition.

Roller bearing models

Two groups of roller bearing models mainly have been used for the analyses. The first group has 18 rolling elements (denoted as the 18 roller model group) while the second group has 15 rolling elements (denoted as the 15 roller model group) with comparatively larger diameters of rolling elements than those of the 18 roller models. Each group has three models. The six models have been labeled as 18-1, 18-2, 18-3, 15-1, 15-2, and 15-3 with increasing diameters of rolling elements. In order to continue to increase the diameter of the rolling elements beyond model 18-3, the number of rolling elements must be reduced from 18 to 15 to avoid overlap of the rolling elements. The transition from model 18-3 to model 15-1 represents this process of reducing the number of rolling elements for increasing the diameter of the rolling elements.

Roller bearing models in both 18 and 15 groups have the same inner pin diameter (d_i) of 9 mm and outer diameter (D_o) of 17.8 mm. Here, the subscript i refers to the inner pin whereas the subscript o refers to the outer ring. Note that the outer diameter for the cam follower (D_o) is not a variable parameter and cannot be changed without a redesign of the cam system. The dimensions of the roller models shown schematically in Figs. 5.1(b) and 5.1(c). The location of the roller is shown as a function of θ as shown in Figs. 5.1(b) and 5.1(c). The rolling element diameter is smallest for model 18-1 and largest for model 15-3 as listed in Tables 5.1(a) and 5.1(b). The subscripts *18* and *15* refer to the 18-roller and the 15-roller model groups, respectively. Note the angle θ and

the numbering (only shown from 1 to 3) of the rolling elements are defined in Figs. 5.1(b) and 5.1(c). The values of the inner pin diameter d_i, outer ring diameter D_o, outer diameter and the relative radius of curvature R (explained later) are also listed in Tables 5.1(a) and 5.1(b).

Finite element models

Finite element analyses of the cam roller follower bearings based on the dimensions given in Tables 5.1(a) and 5.1(b) were carried out to obtain the contact pressures as well as the subsurface stresses on the inner surface of the outer ring and the surface of the inner pin. Two-dimensional plane strain finite element models are used to simulate the middle portion of the cam roller follower bearings. Figs. 5.2(a) and 5.2(b) show the finite element model for models 18-1 and 15-1, respectively. The Cartesian coordinate X-Y system is also shown in the figures. Second-order, isoparametric, plane strain, quadrilateral, reduced integration elements (CPE8R) are used in the models.

The refined finite element mesh near the contact surface between the inner pin and the 1st rolling element is shown in Fig. 5.3. A mesh sensitivity study was conducted in order to compare the maximum Mises stress and the contact pressure to those of the elastic Hertz solution [14]. The minimum element size is 1.54×10^{-3} mm for the given load. The elastic modulus *E* is taken as 200 GPa and the Poisson's ratio *v* is taken as 0.3 for the outer ring, inner pin, and rolling elements. Computations were performed using the commercial finite element software Abaqus v6.8 [15].

The outer surface of an actual cam roller follower bearing is free of contact except for the area of contact with the cam. Therefore, in the finite element analyses, the outer

surface of the outer ring is absent of constraints. For the cam contact region, a concentrated force is applied to simulate the distributed load between the cam and the cam follower as discussed earlier. The magnitude of the concentrated force is 4200 N which represents a typical maximum load produced between the cam and the cam follower during a normal valvetrain operation. Constraints for the displacements in all in-plane directions have been applied to a central region of the inner pin. The rolling elements have no constraints except for the spring elements attached to the rolling elements, which prohibit the rigid body motion. The spring constants for the spring elements are small that they do not affect the computational results of the stresses.

Rotation of the outer ring and revolution of the rolling elements

During the operation of the cam roller follower bearing, the outer ring rotates while following the cam. The rotation of the outer ring, in turn, causes the cylindrical rolling elements to rotate about their longitudinal axes and simultaneously revolve around the inner pin. A schematic defining rotation and revolution of a rolling element and the outer ring is shown in Fig. 5.4. Assuming pure rolling condition between the outer ring, inner pin and the roller elements, the relationship between the rotation angular velocity of the outer ring, ω_o, and the revolution angular velocity of the rolling elements, ω_C, can be found to be

$$\omega_o = \left(\frac{d_i + d_o}{d_o} \right) \omega_C . \tag{5.1}$$

From Eq. (5.1), it can be seen that the outer ring will always rotate at a higher angular velocity than the revolution of the rolling elements. This phenomenon is shown

sequentially in Figs. 5.5(a) to 5.5(d). The shaded roller element, the outer and inner ring reference lines are initially positioned at $\theta = 180°$. At this initial state, the outer and inner ring reference lines are located vertically. The material elements on the outer and inner ring reference lines will experience the largest possible subsurface stress at the initial positions. As the cam follower roller bearing begins to follow the cam, the rotation of the outer ring will cause the rolling elements to rotate and revolve around the inner pin under pure rolling conditions.

As shown in the figure, the reference line of the inner ring almost experience three high stress loading history due to nearly three rolling elements passing through the vertical load application line, whereas the reference line of the outer ring already moves away from the high stress region near the vertical load application line.

This can be used to explain the observations that the failure in cam roller follower bearings occurs in the stationary inner pin [12]. The material elements located along the reference line at $\theta = 180°$ of the inner pin cannot escape from the high cyclic stresses caused by all rolling elements passing through $\theta = 180°$ whereas the material elements along the reference line of the outer ring can escape the high stress region by moving away from the load application line.

Results of finite element analyses

Stress history due to rotation and revolution

The stress histories for two material elements of interest were obtained from the finite element methods for the 18-1 model. The first material element of interest is located in the inner pin and the second in the outer ring as shown in Fig. 5.6. These two

material elements of interest are located at the subsurfaces of their respective components at a fixed depth below the contact surfaces where the maximum Mises stresses due to contact are likely to occur. As mentioned in the previous section, the material element of interest in the inner pin is stationary while the material element of interest in the outer ring rotates during the operation of the cam follower. The material element of interest in the inner pin is located on the reference line which is located at $\theta = 180°$. The material element of interest in the outer ring is located on the reference line which is initially located at $\theta = 180°$.

In order to investigate the stress histories experienced by the two material elements of interest during the operation of the cam follower while taking into account the previously mentioned revolution and rotation, finite element analyses were conducted for every 1° of revolution of the rolling elements from 0° to 10°. Finite element analyses were also conducted by using a smaller increment of rotation of 0.1° to mimic the continuous rotation. The stress history obtained by using the rotational increment of 1° was shown to capture all the major stress peaks that influence the fatigue lives by comparing with that by using the rotational increment of 0.1°. Figs 5.7(a) to 5.7(d) show the representative Mises stress distributions at the revolution of the 0°, 4°, 7° and 10° of the rolling elements. Based on these 11 stress solutions, spanning every 1° from 0° to 10°, the stress solution for a full rotation of the outer ring and revolution of the rolling elements can be obtained by use of symmetry.

The arrows in Figs. 5.7(a) to 5.7(d) indicate the approximate locations of the two material elements of interest. As mentioned earlier, the material element of interest is the inner pin remains stationary while the material element of interest on the outer pin rotates

at a higher angular velocity than that of the revolution of the rolling elements. At 0° rotation and revolution as in Fig. 5.7(a), both material elements of interest are located at θ = 180° and are under the highest possible stress at this position. In Fig. 5.7(b), the rolling elements have begun its departure by revolving 4° while the material element on the outer ring has rotated about 6°. The material element of interest on the outer ring will not encounter a stress peak due to contact until about a rotation of 45°.

Based on the results of the finite element analyses obtained with consideration of the rotation of the outer ring and the revolution of the rolling elements, the stress histories for the material elements of interest are plotted in Figs. 5.8(a) and 5.8(b). Fig. 5.8(a) shows the stress history for the material element of interest located in the inner pin while Fig. 5.8(b) shows the stress history for the material element located in the outer ring of the 18-1 model. Note that Figs. 5.8(a) and 5.8(b) show the stress histories that the two materials elements experience during the same time period as the outer ring rotates two full cycles (720°) for both material elements initially located at θ = 180°. From Eq. (5.1), the rolling elements only revolve about 413° while the outer ring rotates 720° for the dimensions given for the 18-1 model. The stationary material element in the inner pin experiences a cyclic stress history with constant stress amplitude and mean stress with a peak at every 20° of revolution of the rolling elements. During the same time period, the material element in the outer ring experiences a stress cycle which is drastically different than the stress history that material element in the inner pin experiences. The stress history for the material element in the outer ring contains much fewer high stress peaks since the material element moves away from the high stress region near the load application line as the outer ring rotates. Also shown in Fig. 5.8(b) is the smooth low

stress curve with peaks, for example, at 180° and 540° of 40 MPa caused by the deformation of the outer ring. Based on this observation, it is evident that the inner pin will fail earlier than the outer ring.

Effect of the radius of curvature

Figs. 5.9(a), 5.10 and 5.11 show the contact pressure, percentage of the load carried by the 1st rolling element, and the maximum subsurface Mises stress in the inner pin under the 1st rolling element from the three 18 roller models and the three 15 roller models as a function of the relative radius of curvature. The relative radius of curvature, R is defined as

$$\frac{1}{R} = \frac{1}{d_r/2} + \frac{1}{d_i/2} \tag{5.2}$$

where d_r is the diameter of the rolling elements and d_i is the diameter of the inner pin. Note that a larger relative radius of curvature represents a larger rolling element diameter since the diameter of the inner pin is maintained to be constant.

Fig. 5.9(a) shows the maximum contact pressure between the 1st rolling element and the inner pin as a function of the relative radius of curvature when the 1st rolling element is located at θ = 180°. In general, the use of a larger rolling element will decrease the contact pressure due to the increase in the contact area based on the elastic Hertz solution. This is true for the 18 roller model group because the maximum contact pressure decreases from model 18-1 to 18-3. However, the maximum contact pressures for all three models in the 15 roller model group are larger than the maximum contact pressures in the 18 roller model group even though the smallest rolling element in the 15 roller model group is larger than the largest rolling element in the 18 roller model group.

Also, the maximum contact pressure within the 15 roller model group does not decrease with the increase of the relative radius of curvature. The 15-2 model has the smallest maximum contact pressure among the three 15 roller models. The apparent deviation from the expectation that the contact pressure should decrease with the use of larger rolling elements can be explained by calculating the percentage of the total load carried by the 1st rolling element. Figs. 5.9(b) and 5.9(c) show the contact pressure on the raceway of the inner pin between model 18-1 and model 15-3. Five contact pressure peaks can be seen in Fig. 5.9(b) while that number reduces to three in Fig. 5.9(c). This indicates that the while the total applied load is distributed among five rolling elements in model 18-1, the same total applied load is distributed among only three rolling elements.

Fig. 5.10 shows the percentage of the total load carried by the 1st rolling element as a function of the relative radius of curvature when the 1st rolling element is located at $\theta = 180°$. The load carried by the 1st rolling element can be calculated by

$$P_1 = \frac{\pi R}{E^*} p_{1,\max}{}^2 \tag{5.3}$$

where P_1 is the load carried by the 1st rolling element, $p_{1,\max}$ is the maximum contact pressure for the 1st rolling element as presented in Fig. 5.9. E^* is the equivalent elastic modulus given by

$$\frac{1}{E^*} = 2\left(\frac{1-\nu^2}{E}\right). \tag{5.4}$$

Substituting the values of the maximum contact pressure in Fig. 5.9 to Eq. (5.3) gives the load carried by the 1st rolling element for each model. The percentage of the total load carried by the 1st rolling element is simply

$$\%\ \text{of total load carried by 1st rolling element} = \frac{P_1}{P} \times 100 \tag{5.5}$$

where P is the total applied load. As can be seen in Fig. 5.10, the percentage of the total load carried by the 1st rolling element increases with the increase in the relative radius of curvature. Therefore, the 1st rolling element tends to carry more load with an increase in the diameter of the rolling elements. The increase of the percentage is due to the increase of compliance in the outer ring. As the diameter of the rolling element increases, the outer ring must become thinner since the diameter of the inner pin (d_i) and the outer diameter of the outer ring (D_o) must remain constant. The ring becomes increasingly compliant as the outer ring becomes thinner. Within the 18 roller model group, the increases in the relative radius of curvature are 6.2% from models 18-1 to 18-2 and 5.6% from models 18-2 to 18-3. Similarly, the increases in the percentage of the total load carried by the 1st rolling element are 3.9% from models 18-1 to 18-2 and 4% from models 18-2 to 18-3. Based on the elastic Hertz solution [14], the contact pressure is given by

$$p_0 = \sqrt{\frac{P_1 E^*}{\pi R}}\,. \tag{5.6}$$

If the increase in the relative radius of curvature R in the denominator is larger than the increase of the applied load P_1 in the numerator, the contact pressure p_0 should decrease. However, from models 18-3 to 15-1, the increase of the relative curvature is 8% while the increase of the percentage of the total load carried by the 1st rolling element is 21%. Therefore, the contact pressure of the 15-1 model is larger than that of the 18-3 model. Also, the increases of the relative radius of curvature within the 15 roller model

group are 6.3% and 5.7% while the increases of the percentage of the total load carried by the 1st rolling element are 5.4% and 5.8%. Therefore, the contact pressure does not decrease as the rolling element diameter increases within the 15 roller model group. The benefit expected from the use of rolling elements with larger diameters cannot be achieved due to the larger load that the 1st rolling element has to carry.

For bearings with a constrained outer raceway unlike the cam follower roller bearings, the % of total load carried by the 1st rolling element is a constant value which can be determined by the number of rolling elements and does not depend on the geometry. For the 18 roller models, the % of total load carried by the first 1st rolling element is 27% based on the formula by Stribeck [4] and 23% based on the solution by Lee and Pan [17]. For the 15 roller models, the % of total load carried by the first 1st rolling element is 33% based on the formula by Stribeck [4] and 28% based on the solution by Lee and Pan [17].

Fig. 5.11 shows the maximum subsurface Mises stress in the inner pin as a function of the relative radius of curvature. Since the total load carried by the 1st rolling element also increases by using larger rolling elements, the contact stress and, consequently, the maximum subsurface Mises stresses of the 15 roller models are higher than those of the 18 roller models.

Fatigue analysis of the inner pin

The algorithm to calculate fatigue lives of the cam follower components is presented in Fig. 5.12. When the load histories, material properties and geometric information of the components are available, finite element models can be developed and

the stress histories at the critical locations of the component can be obtained from the computations. Applying the rainflow counting method gives the closed hysteresis loops for the stress history. The fatigue damage of the closed stress loop resulting from the rainflow counting is calculated for the cam follower loads using Goodman's relation and Miner's linear damage rule. The fatigue life of the cam follower in terms of the load events is the inverse of the accumulative fatigue damage of each revolution. Rainflow counting is not necessary for the material elements of the inner pin since the material element is subject to constant amplitude cyclic loading conditions.

Goodman relation and damage accumulation

For each model, the equivalent fully reversed stress S_n under the given Mises stress amplitude σ_a and the mean stress σ_m can be calculated using the Goodman relation as

$$\frac{\sigma_a}{S_n} + \frac{\sigma_m}{S_u} = 1 \tag{5.7}$$

where S_u is the tensile strength. The fatigue properties for the inner pin are based on the experimental study by Smith et al. [18] for AISI 52100 steel. The *S*-*N* relation of the AISI 52100 steel which is shown in Fig. 5.13 has been curve fitted to follow the power law relation as

$$S_n = 2372 N_f^{-0.093} \tag{5.8}$$

where N_f is the number of cycles to failure. Using Miner's rule, the accumulated damage of the inner pin at the depth where the Mises stress is maximum can be calculated by

$$D = \sum \frac{1}{N_f}. \tag{5.9}$$

Fatigue life estimation of the inner pin

Based on the stress history the finite element model 18-1 in Fig. 5.8(a), σ_a is 633 MPa and σ_m is also 633 MPa. Using S_u of 2013 MPa with Eq. (5.7), the completely reversed stress S_n is calculated to be 924 MPa. The life to failure corresponding to this completely reversed stress is 25,147 cycles based on the $S - N_f$ relationship of Eq. (5.8). The damage per cycle is thus 1/25147. Since the inner pin experiences a peak in the stress history every 20° of revolution of the rolling elements which corresponds to 34.7° of rotation of the outer ring, the material element of interest will fail after 2500 rotations of the outer ring. This number of rotations is an unrealistic low number due to the assumption that the cam roller follower bearing model is under the constant maximum load during the engine operations. However, the rotation to failure can be compared between the models to find the geometry which gives the largest cycles to failure. Fatigue life estimations for all six roller models are shown in Tables 5.2(a) and 5.2(b). As listed in the tables, the fatigue life increases within both groups with increasing relative radius of curvature. However, the 15 roller models, even with the larger rolling elements, have fatigue lives which are shorter than those of the 18 roller models.

Conclusion

The contact pressures, maximum subsurface Mises stresses, and fatigue lives of cam roller follower bearings with different diameters and numbers of rolling elements have been obtained and compared based on the results of the finite element analyses.

A kinematic analysis under pure rolling conditions indicates that the material elements in the inner pin experiences higher stresses compared to the material elements in the outer ring.

The results of the finite element analyses indicate that the contact pressure and maximum subsurface Mises stress generally decrease with an increase in the rolling element diameter. However, reducing the number of rolling elements and decreasing the outer ring thickness to accommodate larger rollers may not be beneficial to the contact pressure and maximum subsurface Mises stress due to the increase of the outer ring compliance.

Once the maximum subsurface Mises stresses are obtained through finite element analyses, the fatigue lives are estimated. The fatigue lives of the 15 roller models are determined to be shorter than those of the 18 roller models. The increased compliance of the outer ring for the 15 roller models causes a significant deformation of the outer ring and the applied load is carried by a fewer number of rolling elements. Consequently, the fatigue lives of the inner pin decrease. The 15 roller models have rollers with larger diameters compared to the 18 roller models. However, due to the increase of the percentage of the total load carried by the 1st rolling element originating from the increase of the outer ring compliance, the contact pressures and the maximum subsurface Mises stresses are higher for the 15 roller models. It is recommended that a parametric study based on the finite element analyses should be conducted to obtain the optimum

geometry which gives the lowest contact pressure and maximum subsurface Mises stress which results in the longest fatigue life of cam follower roller bearings.

References

[1] Hugnell A, Andersson S. Simulating follower wear in a cam-follower contact. Wear 1994; 179: 101-7.

[2] Hugnell A, Björklund S, Andersson S. Simulation of the mild wear in a cam-follower contact with follower rotation. Wear 1996; 199: 202-10.

[3] Nayak N, Lakshminarayanan PA, Gajendra Babu MK, Dani AD. Predictions of cam follower wear in diesel engines. Wear 2006; 260: 181-92

[4] Falkowski A, McElwee M, Bonne M. Design and development of the DaimlerChrysler 5.7L HEMI engine multi-displacement cylinder deactivation system. SAE Technical Paper No. 2004-01-2106. Warrendale (PA): Society of Automotive Engineers; 2004.

[5] Hendriksma N, Kunz T, Greene C. Design and development of a 2-step rocker arm. SAE Technical Paper No. 2007-01-1285. Warrendale (PA): Society of Automotive Engineers; 2007.

[6] Korte V, Glas T, Lettmann M, Krepulat W, Steinmetz C. Cam roller follower design for heavy duty diesel engines. SAE Technical Paper No. 2000-01-0525. Warrendale (PA): Society of Automotive Engineers; 2000.

[7] Staron JT, Willermet PA. An analysis of valve train in terms of lubrication principles. SAE Technical Paper No. 830165. Warrendale (PA): Society of Automotive Engineers; 1983.

[8] Gecim BA. Lubrication and fatigue analysis of a cam and roller follower. Tribological design of machine elements 1989. 91-100.

[9] Lee JM, Patterson DJ, Morrison KM, Schwartz GB. Friction measurement in the valve train with a roller follower. SAE Technical Paper No. 940589. Warrendale (PA): Society of Automotive Engineers; 1994.

[10] Krepulat W, Dusik M, Korte V. Advanced calculation method of the contact stress in roller follower valve train systems. SAE Technical Paper No. 2002-01-0852. Warrendale (PA): Society of Automotive Engineers; 2002.

[11] Hua DY, Farhang K, Seitzman LE. A multi-scale system analysis and verification for improved contact fatigue life cycle of a cam-roller system. J Tribology 2007; 129: 321-5.

[12] Cheng W, Cheng HS, Yasuda Y. Wear and life prediction of cam roller follower. SAE Technical Paper No. 940822. Warrendale (PA): Society of Automotive Engineers; 1994.

[13] Sadeghi F, Jlalahmadi B, Slack TS, Raje N, Arakere NK. A review of rolling contact fatigue. J Tribology 2009; 131: 041403 1-15

[14] Johnson KL, Contact Mechanics, Cambridge University Press, 2003, 99-104

[15] ABAQUS v6.8 User Manual. Providence, RI: SIMULIA; 2007.

[16] Jacobson B. The Stribeck memorial lecture. Tribology Int. 2002; 36: 781-9.

[17] Lee JW, Pan J. A closed-form analytical solution for calculation of loads and contact pressures for roller and ball bearings. To be published.

[18] Smith RW, Hirschberg MH, Manson SS. Fatigue behavior of materials under strain cycling in low and intermediate life range. NASA Technical Note D-1574; 1963, 51-2

Table 5.1 Dimensions for (a) the 18-roller and (b) 15-roller models (mm).

(a)

	18-1	18-2	18-3
Inner pin diameter, d_i	9	9	9
Inner diameter of outer ring, d_o	12.174	12.408	12.639
Outer diameter, D_o	17.8	17.8	17.8
Rolling element diameter, d_r	1.587	1.704	1.82
Relative radius of curvature	0.675	0.716	0.757

(b)

	15-1	15-2	15-3
Inner pin diameter, d_i	9	9	9
Inner diameter of outer ring, d_o	13	13.312	13.624
Outer diameter, D_o	17.8	17.8	17.8
Rolling element diameter, d_r	2	2.156	2.312
Relative radius of curvature	0.818	0.870	0.920

Table 5.2 Fatigue lives of the inner pin for (a) the 18-roller and (b) 15-roller model.

(a)

	18-1	18-2	18-3
Peak stress (MPa)	1267	1243	1222
Minimum stress (MPa)	0	0	0
S_u (MPa)	2013	2013	2013
σ_m (MPa)	633.5	621.5	611
σ_a (MPa)	633.5	621.5	611
S_n (MPa)	924	899	877
N_f	25147	33904	44149

(b)

	15-1	15-2	18-3
Peak stress (MPa)	1342	1334	1331
Minimum stress (MPa)	0	0	0
S_u (MPa)	2013	2013	2013
σ_m (MPa)	671	667	665.5
σ_a (MPa)	671	667	665.5
S_n (MPa)	1007	998	994
N_f	10075	11093	11502

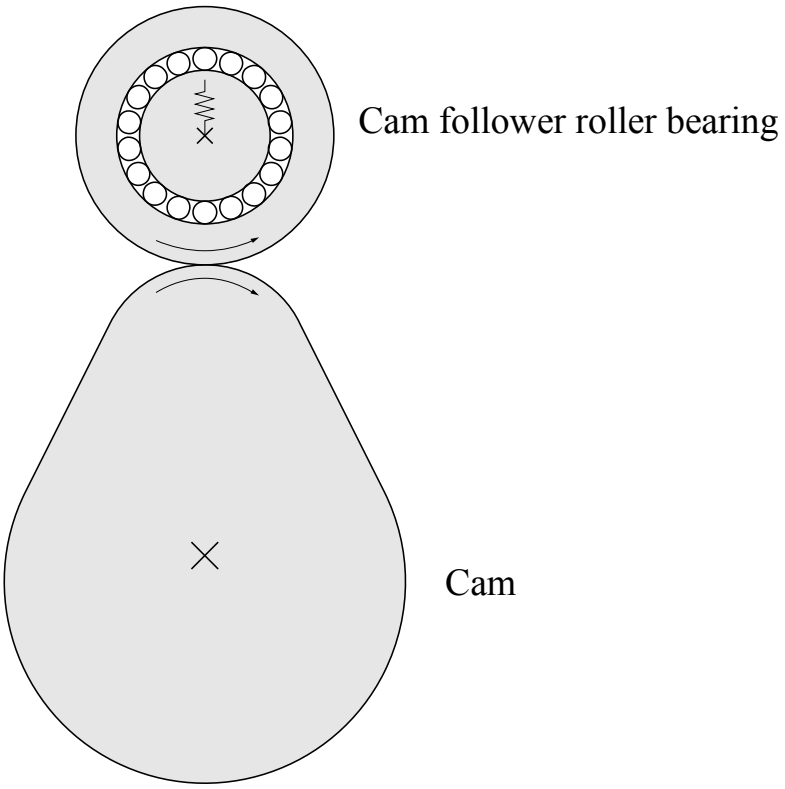
Cam follower roller bearing
Cam

(a)

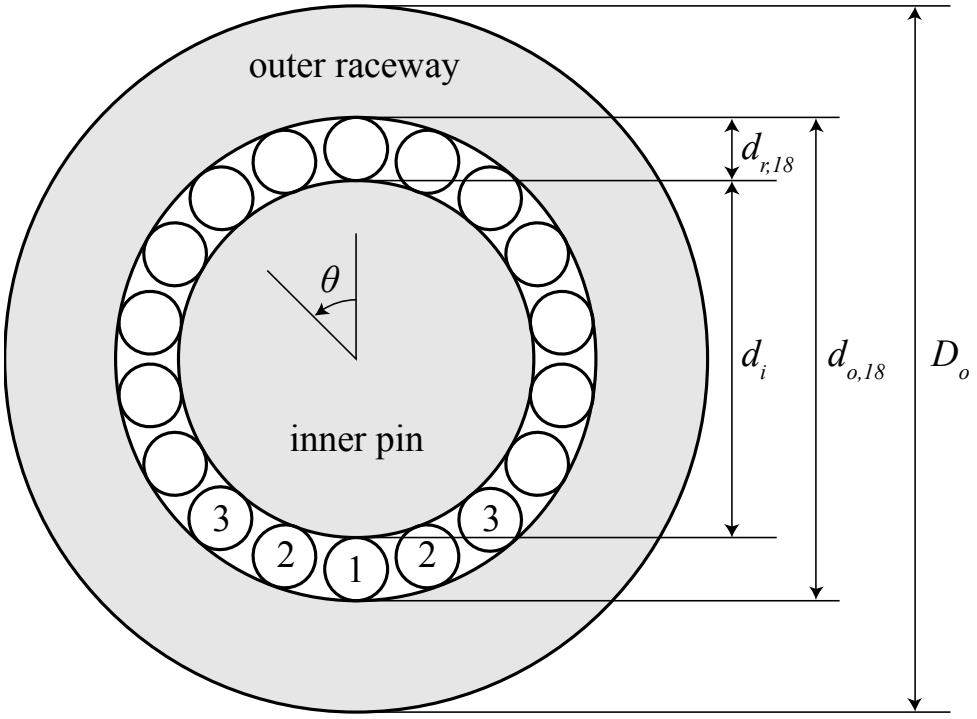
outer raceway
$d_{r,18}$
θ
d_i
$d_{o,18}$
D_o
inner pin
3
2
1
2
3

(b)

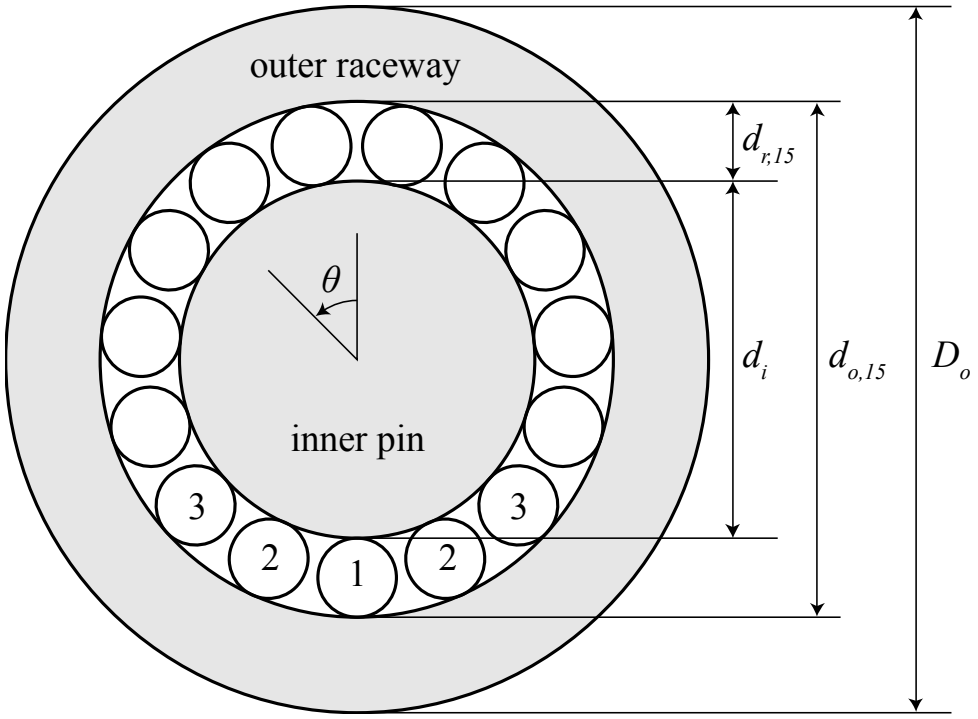

(c)

Fig. 5.1 Schematics of (a) the cam and the cam roller follower bearings and (b) 18-1 of the 18 roller models and (c) 15-1 of the 15 roller models.

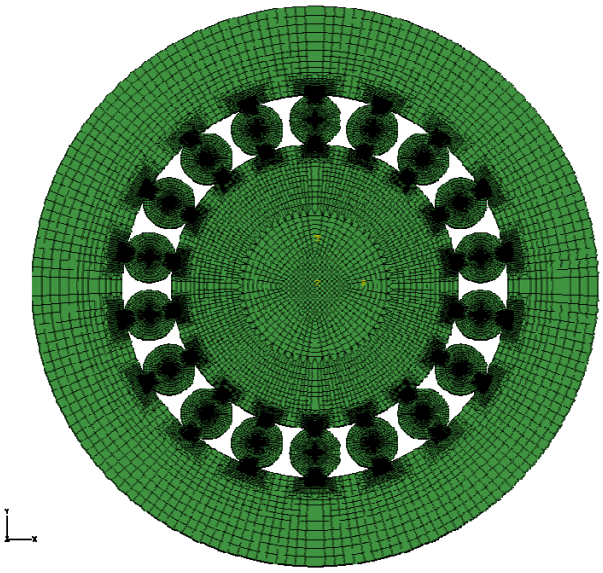

(a)

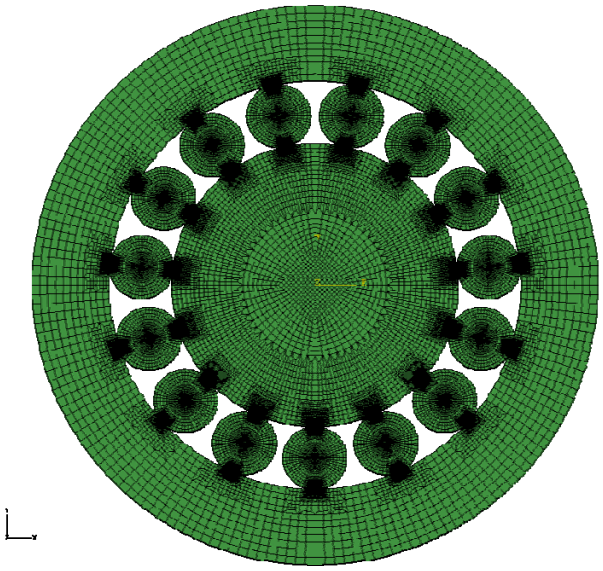

(b)

Fig. 5.2 Finite element models for (a) 18-1 of the 18 roller models and (b) 15-1 of the 15 roller models.

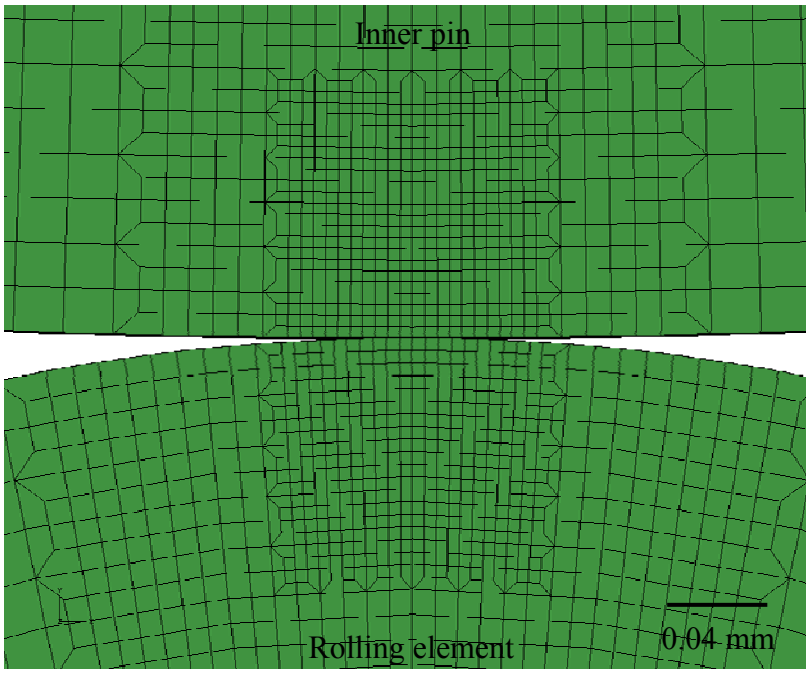

Fig. 5.3 A close-up view of the finite element mesh near the contact surfaces between the inner pin and the 1st rolling element.

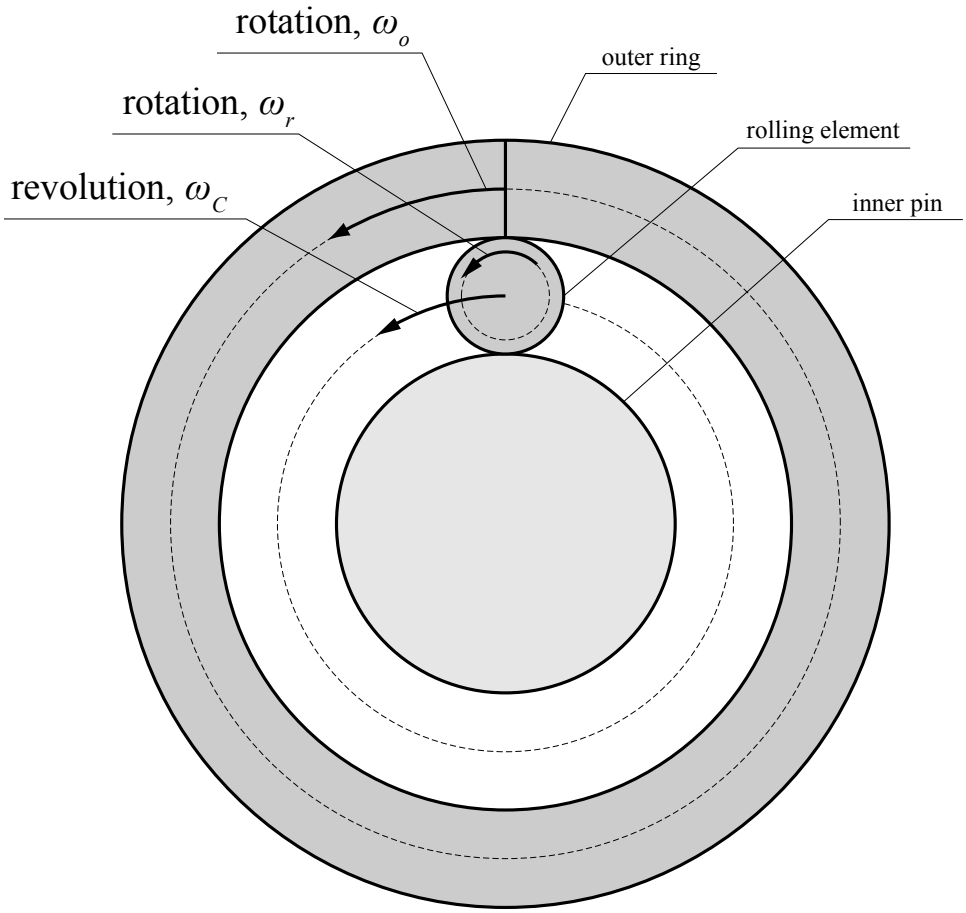

Fig. 5.4 A schematic showing the definition of revolution and rotation of the rolling element and the rotation of the outer ring.

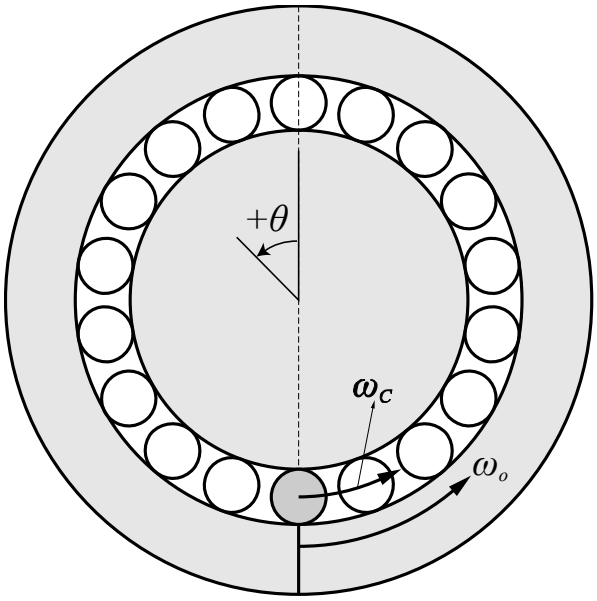

(a)

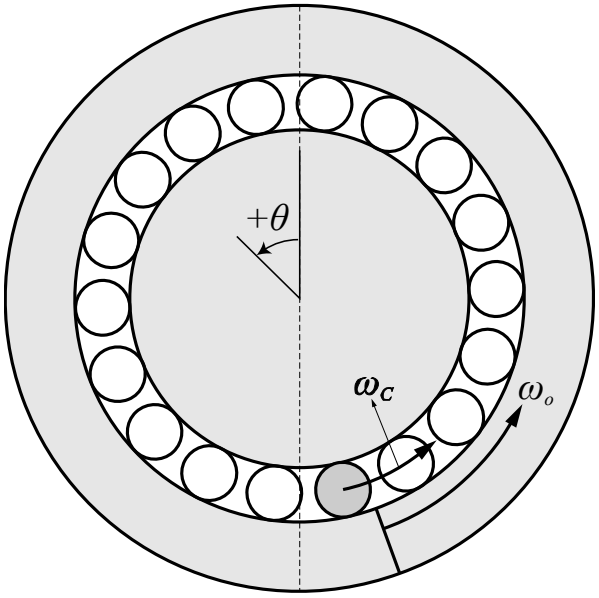

(b)

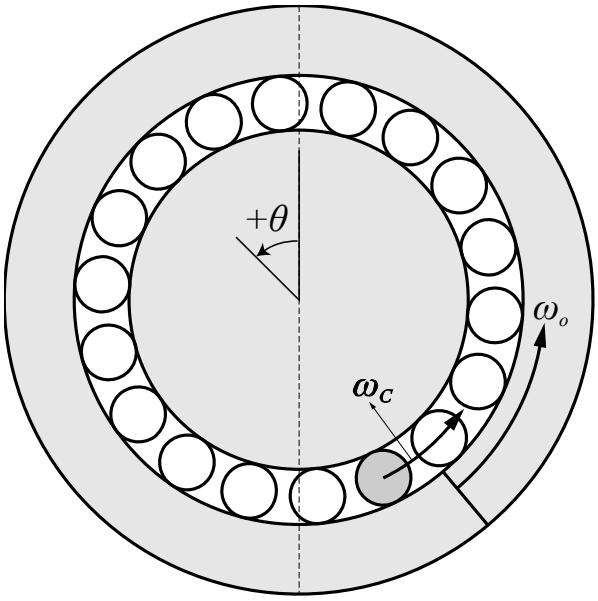

(c)

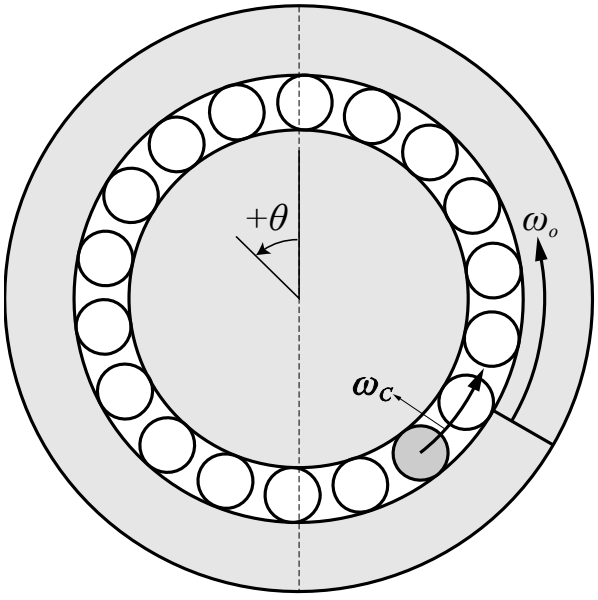

(d)

Fig. 5.5 A sequential schematic of the rotation of the outer ring and the revolution of a rolling element with the outer ring rotation of (a) 0°, (b) 20°, (c) 40° and (d) 60°.

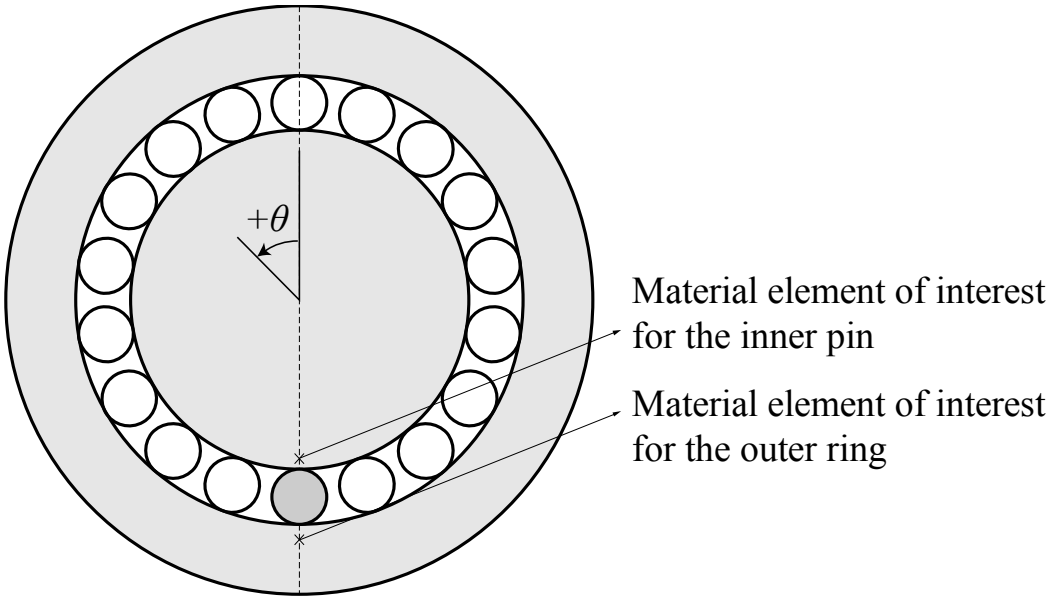

Fig. 5.6 Approximate locations for the material elements of interest in the inner pin and the outer ring.

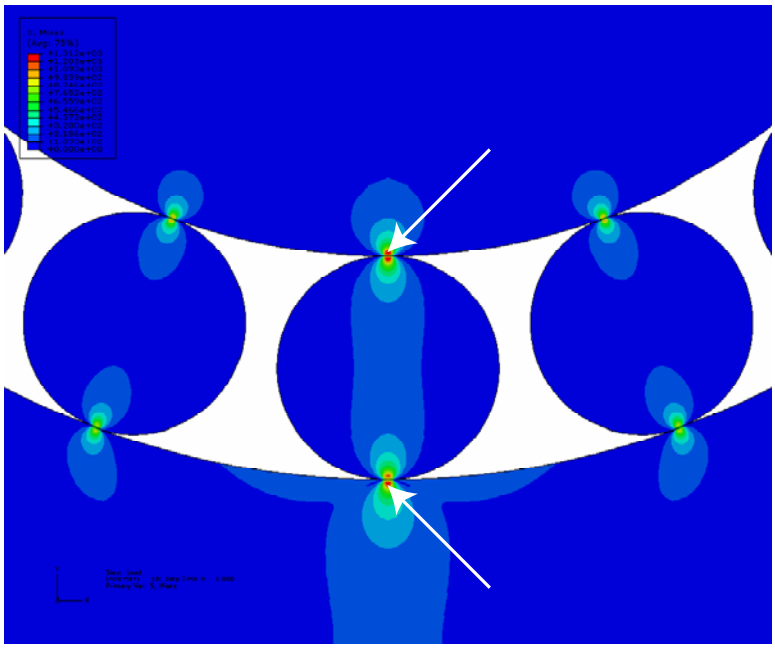

(a)

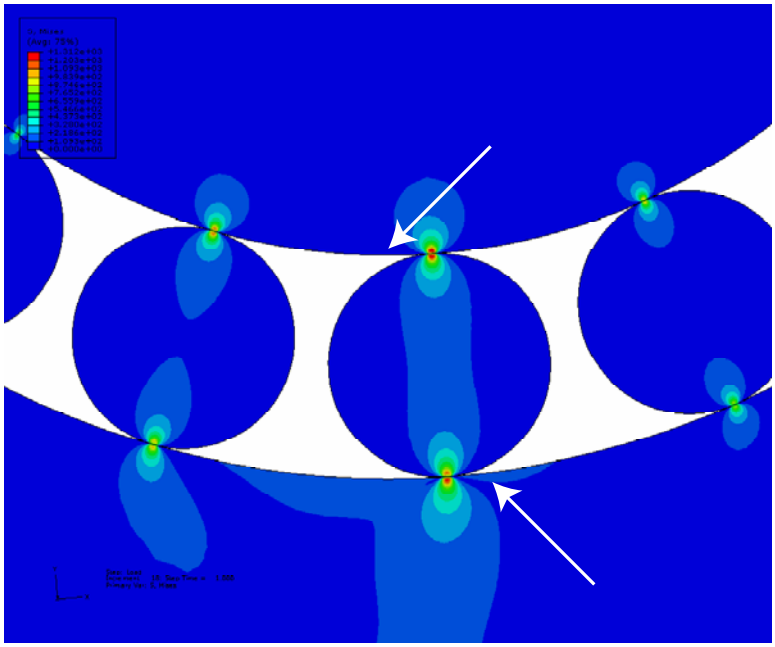

(b)

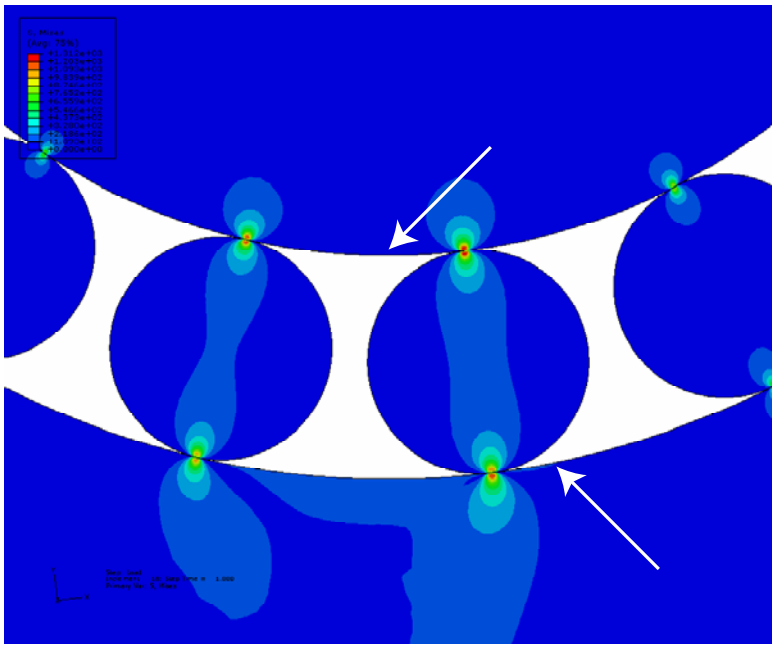

(c)

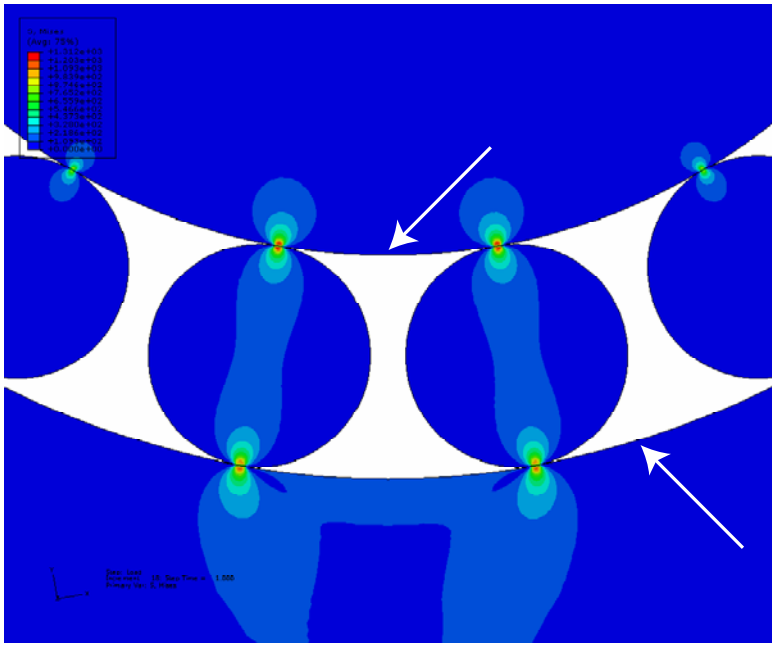

(d)

Fig. 5.7 The Mises stress distributions from finite element analyses for the revolution angle of (a) 0°, (b) 4°, (c) 7° and (d) 10° for the rolling elements. The arrows indicate the approximate locations of the material elements of interest.

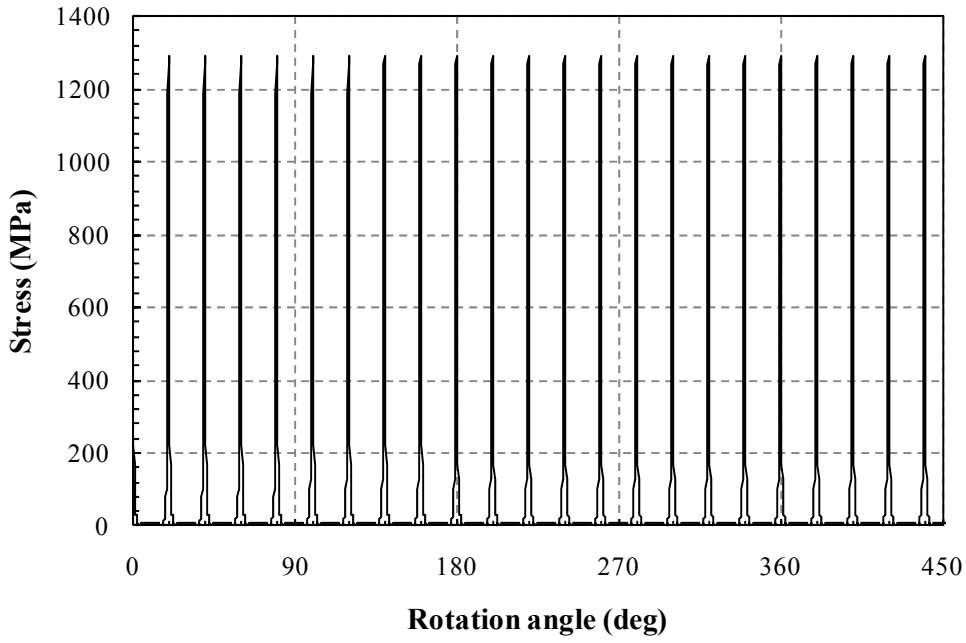

(a)

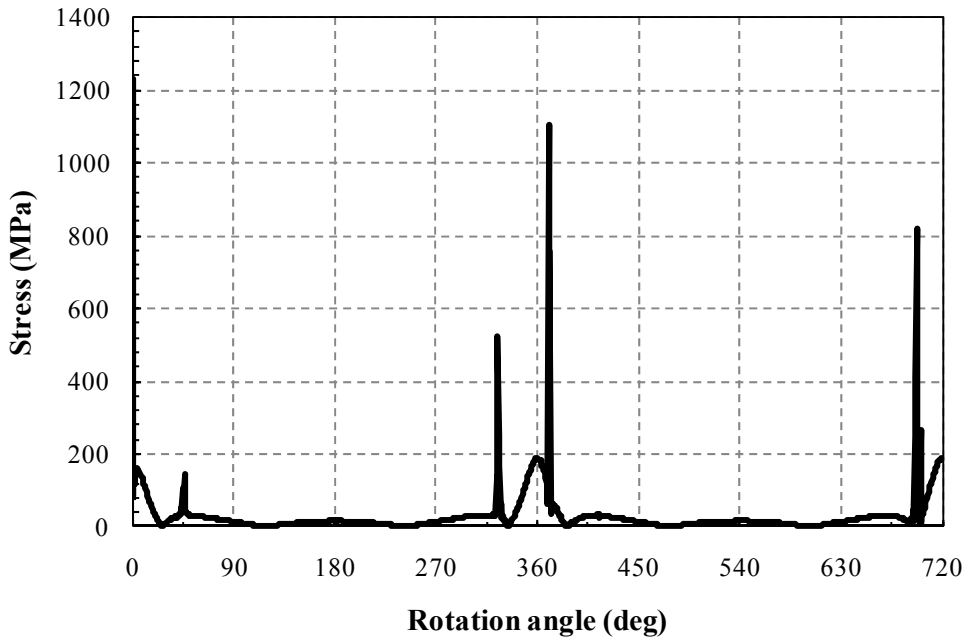

(b)

Fig. 5.8 The Mises stress histories for the 18-1 model for the material elements of interest in (a) the inner pin and (b) the outer ring.

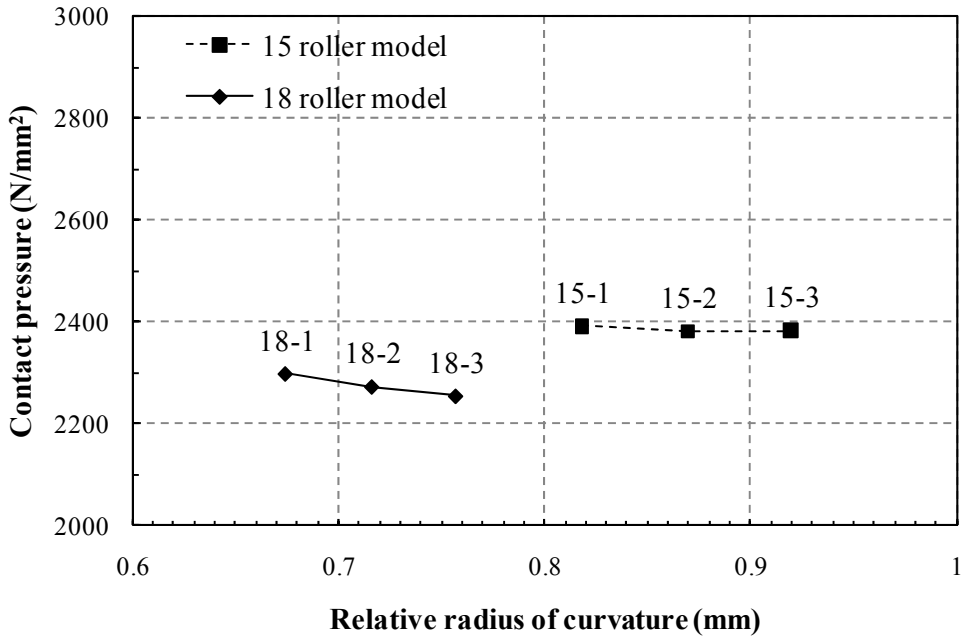
15 roller model
18 roller model
Contact pressure (N/mm²)
3000
2800
2600
2400
2200
2000
15-1
15-2
15-3
18-1
18-2
18-3
0.6
0.7
0.8
0.9
1
Relative radius of curvature (mm)

(a)

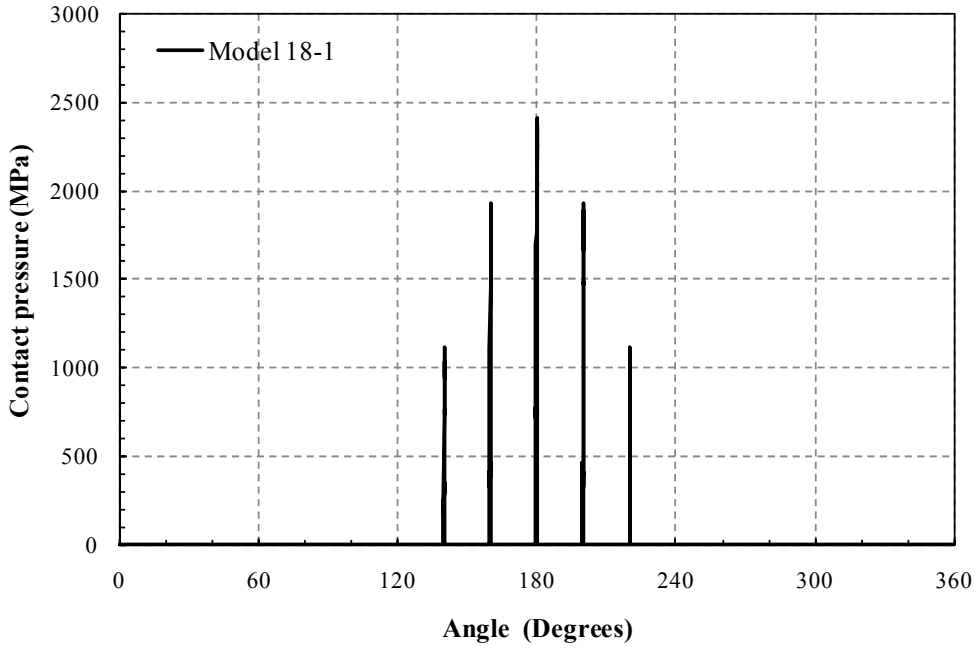
Model 18-1
Contact pressure (MPa)
3000
2500
2000
1500
1000
500
0
0
60
120
180
240
300
360
Angle (Degrees)

(b)

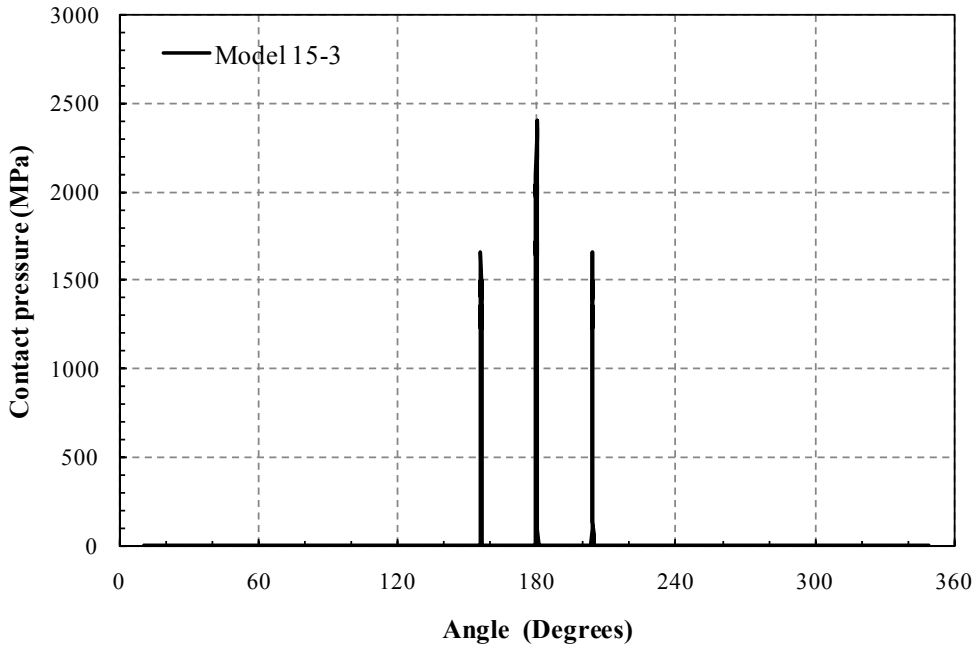

(c)

Fig. 5.9 (a) The maximum contact pressure between the 1st rolling element and inner pin as a function of the relative radius of curvature. The contact pressure distributions on the inner pin due to the rolling elements for (b) model 18-1 and (c) model 15-3.

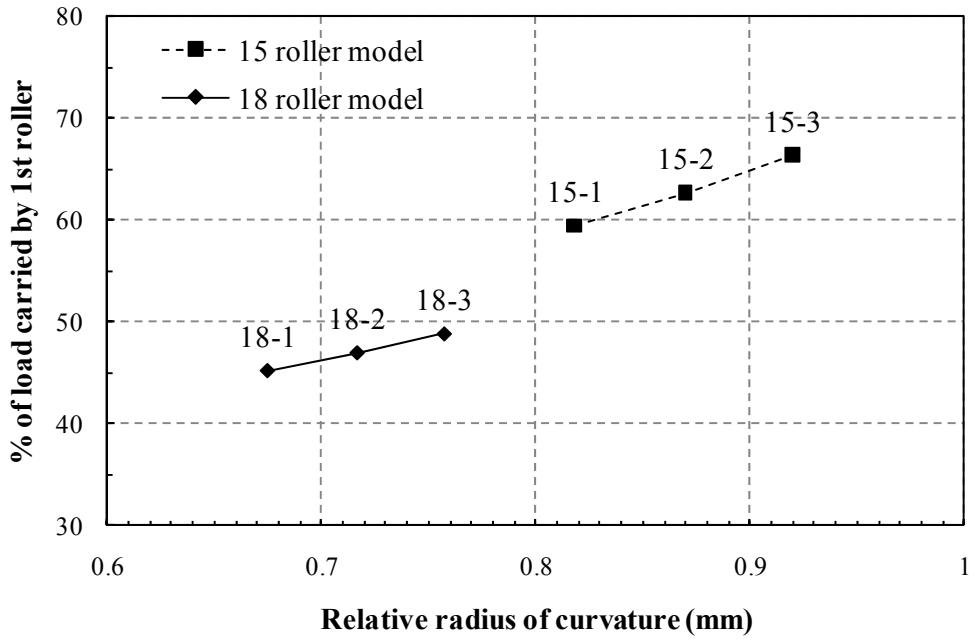

Fig. 5.10 The percentage of the total load carried by the 1st rolling element as a function of the relative radius of curvature.

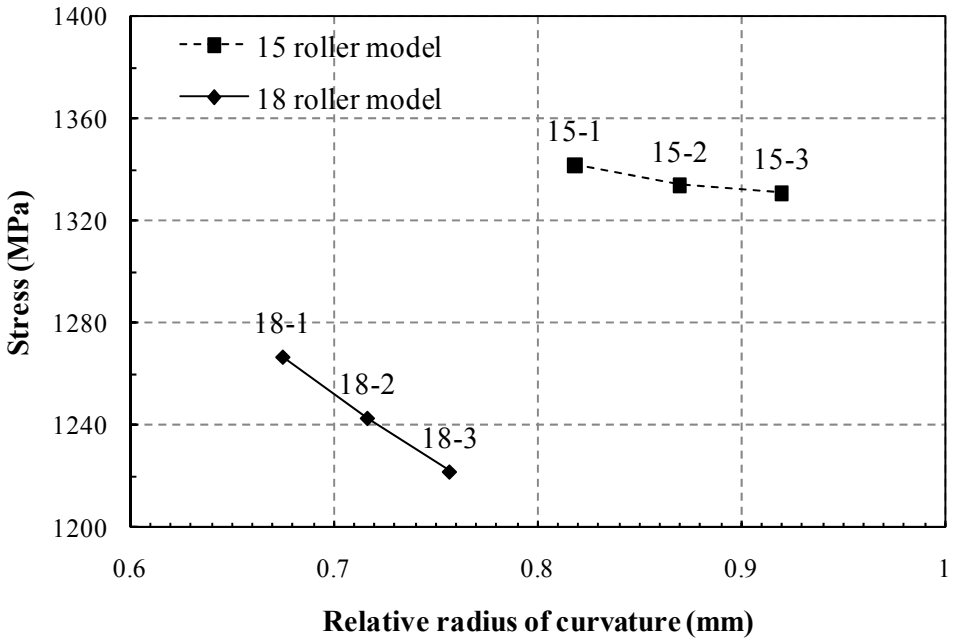

Fig. 5.11 The maximum subsurface Mises stress under the 1st rolling element in the inner pin as a function of the relative radius of curvature.

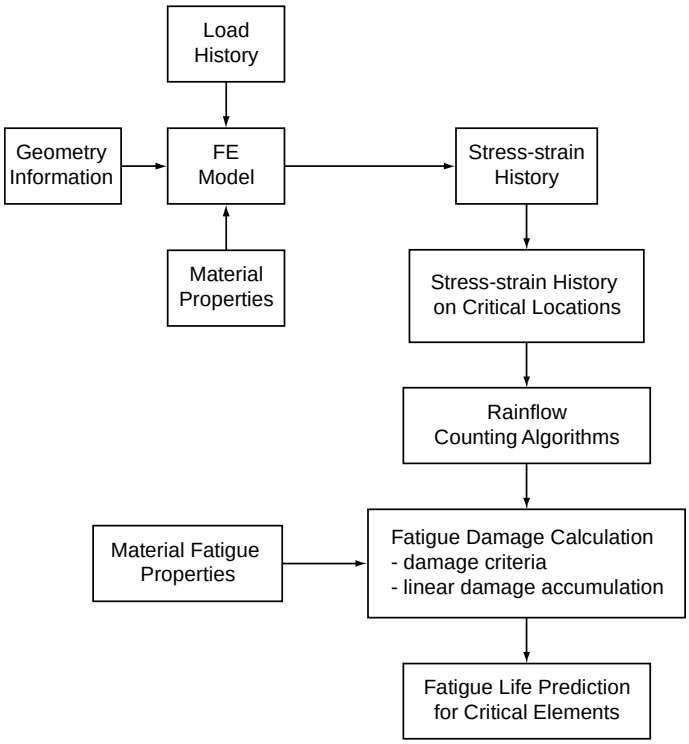

Fig. 5.12 An algorithm for fatigue analysis of structural components.

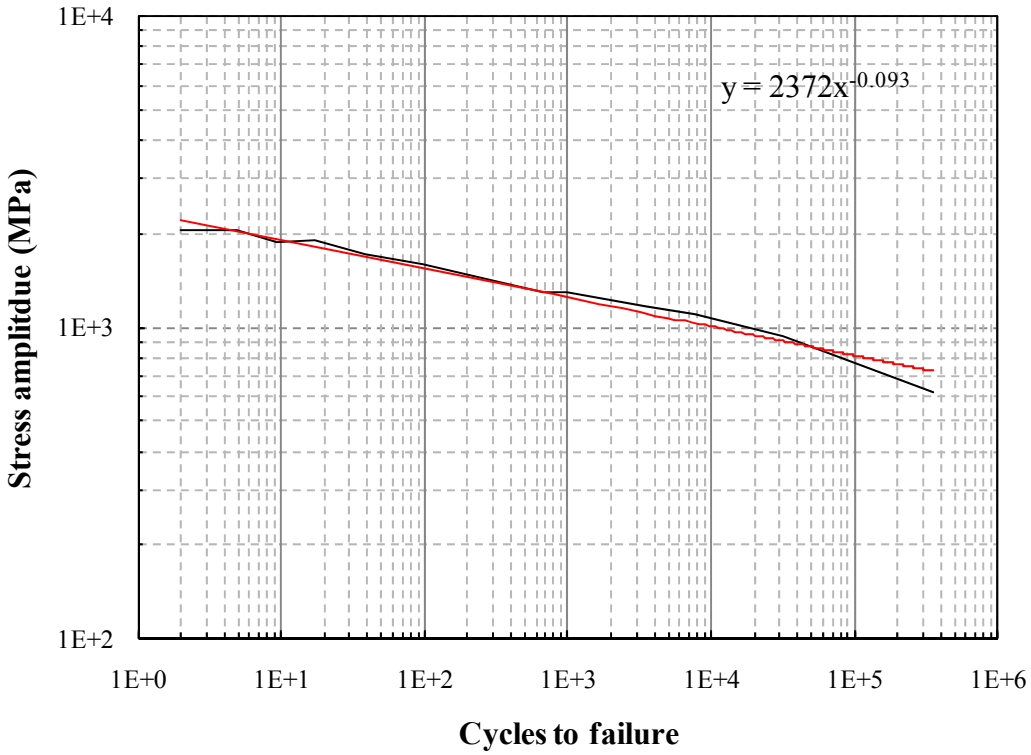

Fig. 5.13 The stress vs. cycles to failure curve for AISI 52100.

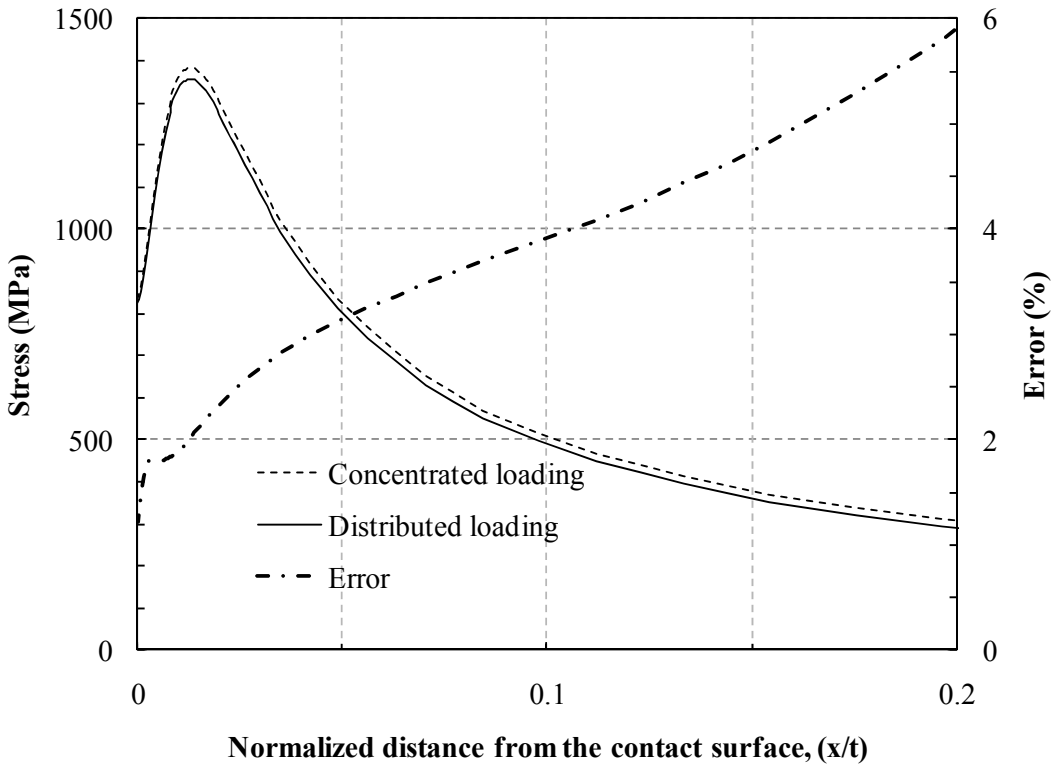

Fig. 5.14 The subsurface Mises stress distributions in the outer ring under a concentrated load and a distributed load.

Chapter 6
A closed-form solution for calculation of load and contact pressure in cylindrical roller bearings with consideration of interference fit of rollers

Introduction

Wheel bearings are an essential component of vehicles and contribute significantly to the overall performance of vehicles by allowing the wheels to rotate with minimal friction. Wheel bearings also have to withstand the weight of the vehicle and the dynamic loading caused by acceleration, deceleration and directional changes of vehicles. The expected lives of automotive bearings are set to outlast the expected lives of vehicles. However, the constant loading on the bearings due to the weight of a vehicle combined with the large cyclic external loads due to the operation of the vehicle will tend to shorten the lives of the bearings. If a failure occurs in a wheel bearing, the bearing must be replaced. The replacement results in a warranty issue for the automaker and a maintenance cost issue for the vehicle owner. Therefore, the bearing should remain in a near perfect condition from the time of installation to the retirement of the vehicle.

To ensure that the bearing life outlasts the vehicle life, certain mechanical and environmental conditions should be maintained. The bearing should be designed to withstand both the constant load due to the vehicle weight as well as the cyclic loads caused by the operation of the vehicle. The mechanical stresses caused by these loads within the bearing along the raceway and in the balls or the rollers should be within the elastic range of the materials. Also, the seals should prevent the lubricant from leaking

out while at the same time preventing dirt and moisture from coming inside. The bearing components should be well lubricated and the lubricants contaminant-free. If the bearing is maintained in a well lubricated condition, the cyclic stresses caused by the normal operation may ultimately cause the bearing components to fail by fatigue. Therefore, the mechanical stresses within the bearing components should be well studied during the design process to maximize the fatigue life of a bearing.

Once bearings are manufactured based on the design processes, the bearings are usually put into a test equipment and rotated while external loads are applied to test the failure lives of the bearings [1], [2]. These external loadings are programmed to represent the actual customer vehicle usage. However, an extensive testing time is necessary to duplicate the failure modes of bearings installed in vehicles [3]. An accelerated test might be suggested in order to reduce the required testing time but previous investigations [4], [5] showed that the fatigue damage characteristics will be changed such that the failure mode will not be representative of those from actual customer usage. In addition to the time related issues, there is also cost issue due to the fact that the laboratory test equipments are expensive to operate continuously. Also, the process becomes inefficient due to the long testing time compared to the demand for short vehicle development schedule. Finite element analyses may be proposed as a reasonable alternative but have their own limitations. Solving multiple simultaneous contact problems using finite element analyses, as is the case for the wheel bearing analysis, require a tremendous amount of computing power which again creates time and cost related issues.

In order to overcome these issues, a closed-form solution is proposed to calculate the loads exerted by the rolling elements in a bearing with consideration of interference fit under a radial load. Similar approach was proposed in the industry [6]. Once the loads exerted by the rolling elements are obtained, the contact pressures, the subsurface contact stresses and the fatigue lives of roller bearings can be obtained analytically. The proposed solution to obtain the loads exerted by the rolling elements is a closed-form solution which has been derived based on the previous well known analytical solutions by Hertz [8] and Persson [8] and the approximate closed-form interference load of the rolling element from finite analyses for a given set of geometric parameters for bearings. The proposed solution requires a minimal amount of effort, cost and time while still maintaining a reliable accuracy and does not require finite element analyses or trial-and-error iterations.

By using the proposed solution, the bearing design process to obtain the contact pressures and contact forces of the rolling elements can be accomplished analytically with a closed-form equation and it gives engineers a preliminary assessment of a given bearing design without long pre-processing time and significant CPU time of the corresponding finite element analysis. Also, certain geometric parameters such as the inner and outer raceway diameters, the size/number of the rolling elements and the applied load can be adjusted to decide which design combination gives the optimum fatigue life for the wheel bearing before initiating costly experiments or computations.

In this investigation, the elastic contact theory by Hertz for cylindrical contact is first reviewed. The solution by Persson for conforming contact with interference is also reviewed. Based on the solutions of Hertz and Persson, a closed-form solution to

calculate the loads exerted by the rolling elements on the outer raceway is proposed. Two-dimensional finite element analyses were conducted to validate the applicability of the closed-form solution. The limitations for the closed-form solution are also discussed. Finally, conclusions are made.

Theoretical background

Hertz solution for non-conforming contact

The solution for the contact between elastic cylindrical bodies was derived by Hertz [8]. As shown in Fig. 6.1(a), a long cylinder with the radius *R* is pressed onto a flat surface by a load per unit length, *P*. The Cartesian X, Y and Z coordinates are shown in the figure. The cylinder makes contact with the flat surface over a long strip of area with a width of 2*a* parallel to the Y axis. Here, *a* is defined as the half contact width. Due to the contact, an elliptical contact pressure profile $p(x)$ is created on the flat surface along the long strip of area.

For the cylinder pressed in contact with the flat surface by a load per unit length *P* as in Fig. 6.1(a), the contact pressure profile $p(x)$ can be expressed as

$$p(x) = \frac{2P}{\pi a^2}\left(a^2 - x^2\right)^{1/2}, \quad -a \le x \le a \tag{6.1}$$

where x denotes a location within the contact area. Fig. 6.1(b) shows the normalized contact pressure $p(x)/p_{\max}$ as a function of the normalized distance from the symmetry plane of contact, x/a. The relationship between the load per unit length P and the half contact width a is given by

$$a = \sqrt{\frac{4PR}{\pi E^*}} \tag{6.2}$$

where E^* is the equivalent elastic modulus defined as

$$\frac{1}{E^*} = \frac{1-\nu_1^2}{E_1} + \frac{1-\nu_2^2}{E_2}. \tag{6.3}$$

Here, E_1, ν_1, E_2 and ν_2 are the elastic moduli and the Poisson's ratios for the cylinder and the flat surface, respectively. When two elastic cylinders in contact with each other as shown in Fig. 6.1(c), the contact pressure profile $p(x)$ and the half contact width a still follow Eqns. (6.1) and (6.2). However, R becomes the relative radius of curvature defined by the radii of curvature of the two contacting bodies as

$$\frac{1}{R} = \frac{1}{R_1} + \frac{1}{R_2}. \tag{6.4}$$

For the cylinder and flat surface problem, R is equal to R_1 as the radius of curvature of the flat surface, R_2 becomes infinity. The maximum contact pressure can be found by substituting $x = 0$ into Eq. (6.1) and combining with Eq. (6.2) as

$$p_{\max} = \sqrt{\frac{PE^*}{\pi R}}. \tag{6.5}$$

Eq. (6.5) can be rearranged in terms of the maximum contact pressure such that,

$$P = p_{\max}^2 \frac{\pi R}{E^*}. \tag{6.6}$$

Persson solution for non-conforming contact with interference

A short description of the solution of Persson [8] with consideration of interference is provided in this section. Two elastic bodies are in contact with a

concentrated force Q applied to the center of the circular inner body as shown in Fig. 6.2(a). The inner body is a cylinder with a radius of R_{in}. The outer body is assumed to be an infinite body with a circular hole with a radius of R_{out}. The stress becomes zero at infinity for the outer body. The two body establish contact over an angle of ψ. Fig. 6.2(b) shows the interference case where R_{in} is larger than R_{out}. Since the difference in the radius ($\Delta R = R_{out} - R_{in}$) is negative for the interference condition, the small contact area assumption of Eq. (6.1) is no longer valid. For a given ΔR which is negative, the pressure $p(\theta)$ is constant which is expressed as

$$p(\theta) = -\frac{E^* \Delta R}{2R_{out}} \tag{6.7}$$

where E^* is the equivalent elastic modulus in Eq. (6.4). The top left figure in Fig. 6.2(c) schematically shows that the pressure distribution is uniform along the circumference when the magnitude of Q is zero. As the force Q increases, the contact pressure is given by

$$p(\theta) = -\frac{E^* \Delta R}{2R_{out}} + \frac{Q}{\pi R_{out}} \cos\theta . \tag{6.8}$$

Note that the contact angle is 360° when Eq. (6.8) is applicable. As indicated in Eq. (6.8), when Q increases to a critical value $Q_{separation}$, the condition

$$p(\theta = \pi) = 0 \tag{6.9}$$

can be satisfied. Here, the critical $Q_{separation}$ is expressed as

$$Q_{separation} = -\frac{\pi E^* \Delta R}{2} . \tag{6.10}$$

When Q is less than or equal to $Q_{separation}$, the pressure distributions are schematically shown in the top right and the bottom left figures in Fig. 6.2(c). When Q is larger than $Q_{separation}$ as shown in the bottom right figure in Fig. 6.2(c), the pressure distribution can be obtained numerical from the solution provided by Persson [8]. Here, $Q_{separation}$ can be thought of the separation load when the contact pressure between the inner and outer surfaces at $\theta=\pm\pi$ becomes zero. As Q increases, the contact angle decreases from 360°. When Q approaches to infinity, the contact angle approaches to 169.83°.

The loads exerted by the rolling elements

Now, an idealized cylindrical roller bearing is considered as shown in Fig. 6.3. For the idealized roller bearings, the rolling elements, outer and inner cylinders are prismatic and infinitely long in the axial direction. The outer cylinder is stationary to represent the constraint condition of wheel bearings. The outer surface of the outer cylinder is fixed in the X, Y and Z directions and the inner cylinder is free to rotate with respect to the Y axis. All axial motion in the Y axis direction is prohibited. A vertical load P_{total} is applied to the center of the inner cylinder in the Z axis direction. The bearing model shown in Fig. 6.3 has 18 rolling elements. However, the number of rolling elements can vary as long as a reasonable number of rolling elements are present to sustain the function of the bearing. It can be shown that the outer raceway experiences a comparably harsher stress state then the inner raceway. Therefore, only the contact pressures on the stationary outer raceway are investigated. The magnitude of the applied load is low such that the stresses in the bearing components remain in the elastic range.

Interference load

Interference between the rolling elements and raceways are introduced either intentionally in order to minimize rolling element play or due the press-fit of the bearings to a shaft or housing [9], [10]. That is, the diametral clearance of the rolling elements becomes negative. This is to ensure that all rolling elements maintain contact with the both raceways during normal operation. The interference Δd is defined as

$$\Delta d = d_o - d_i - 2d_r \tag{6.11}$$

where d_o is the outer raceway diameter, d_i is the inner raceway diameter and d_r is the rolling element diameter as shown in Fig. 6.4.

Due to the interference Δd, the rolling elements create elliptical contact pressures profiles on the inner and outer raceway as in Fig. 6.5. Note that only the contact pressures on the outer raceway are depicted in Fig. 6.5. The contact pressure profiles due to interference have the same maximum values and can be considered as identical under the idealized condition. This maximum contact pressure exerted on the outer raceway by the rolling elements due to the interference prior to the application of an external load will be defined as the interference pressure $p_{interference}$.

The interference pressure can be estimated analytically by using the solutions listed in Johnson [8]. First, the compression of the diameter of a rolling element, $\delta_{cylinder}$, is given by

$$\delta_{cylinder} = \frac{F}{\pi E^*}\left\{\ln\left(\frac{4R_i}{a_i}\right) + \ln\left(\frac{4R_o}{a_o}\right) - 1\right\}. \tag{6.12}$$

Here, F is the load created between the rolling element and the raceways due to the interference. Also, R_i and R_o are the relative radii of curvature between the rolling elements and the inner and the outer raceways, respectively, and a_i and a_o are the half contact width between the rolling elements and the inner and the outer raceways, respectively. It should be noted that a_i and a_o are functions of F.

Based on the Hertz solution of a cylinder on a half-space, the compressions of the inner and outer raceways, δ_{inner} and δ_{outer}, can be estimated by

$$\delta_{inner} = \frac{F}{2\pi E^*}\left\{2\ln\left(\frac{2r_i}{a_i}\right) - \frac{\nu}{1-\nu}\right\} \tag{6.13}$$

and

$$\delta_{outer} = \frac{F}{2\pi E^*}\left\{2\ln\left(\frac{2T}{a_o}\right) - \frac{\nu}{1-\nu}\right\} \tag{6.14}$$

where r_i is the radius of the inner cylinder and T is the radial thickness of the outer cylinder. The sum of these compressions should be equal to the interference such that

$$\frac{\Delta d}{2} = \delta_{cylinder} + \delta_{inner} + \delta_{outer} = f\left(F\right). \tag{6.15}$$

The load between the rolling element and the raceways due to the interference, F, can be found by inverting Eq. (6.15). This load can be used with Eq. (6.5) to find the interference pressure. However, due to the complexity of Eqns. (6.12), (6.13) and (6.14), the load created between the rolling element and the raceway can only be computed numerically. Also, Eqns. (6.13) and (6.14) has been derived based on the solution for a cylinder indenting on a half-space. Therefore, the relatively small values of the radius of the inner cylinder and the thickness of the outer cylinder tend to give estimations of the

interference pressures that are as much as twice of those obtained from finite element analyses.

Therefore, the interference pressure will be obtained from the first term of Eq. (6.8) with a geometric function κ to take into account the effects of the bearing geometries of interest as

$$p_{interference} = \kappa\left(-\frac{E^*\Delta d}{4(d_o/2)}\right). \tag{6.16}$$

Here, κ is expressed as a function of the relative radius of curvature and the interference normalized by the diameter of the outer raceway as

$$\kappa = \kappa_1 + \kappa_2 \frac{2R_o}{d_o} + \kappa_3 \frac{\Delta d}{d_o} \tag{6.17}$$

where

$$\kappa_1 = 164.3 \tag{6.18}$$

$$\kappa_2 = -175.9 \tag{6.19}$$

$$\kappa_3 = -31969.2\,. \tag{6.20}$$

for the bearings with a given ranges of d_i, d_o and d_r investigated here.

The load exerted on the outer raceway by the rolling elements due to the interference prior to the application of an external load will be defined as the interference load $P_{interference}$ as shown in Fig. 6.6(a). The magnitudes of the interference loads for all rolling elements are equal under the idealized symmetry conditions since the rolling elements are assumed to be uniformly spaced along the circumference. The sum of the interference loads must be zero in order to satisfy the self force equilibrium conditions.

The interference load $P_{interference}$ can be obtained by substituting Eq. (6.16) into Eq. (6.6) as

$$P_{interference} = p_{interference}^2 \frac{\pi R_o}{E^*}. \tag{6.21}$$

When the geometries of roller bearings are significantly different from the geometries of the bearing models considered in this study, Eq. (6.15) may be used for estimation of the interference load of rolling elements cautiously to avoid time consuming finite element analyses. It should be noted that when the inner cylinder radius and outer cylinder thickness are much larger than the contact length, the estimations from Eq. (6.15) should be more accurate.

Separation load

A downwards vertical load P_{total} is applied at the center of the inner cylinder as shown in Fig. 6.6(b). The horizontal sum of the loads exerted by the rolling elements on the outer raceway remains zero because the total applied load does not have a horizontal component. The vertical sum of the loads exerted by the rolling elements on the outer raceway should be of equal and opposite to the total applied load in order to satisfy the force equilibrium condition. The loads exerted by the rolling elements on the lower half of the outer raceway will increase while the loads exerted by the rolling elements on the upper half of the outer raceway will decrease as the total applied load is increased as shown in Fig. 6.6(b). As the total applied load is increased to a certain value, the load exerted by the rolling elements on or near the outer raceway at $\theta = \pm 180°$ will become zero as schematically shown in Fig. 6.6(c). This phenomenon will be defined as the

separation as the zero load between the rolling element and the outer raceway at $\theta = \pm 180°$. The separation indicates that the two bodies are not in a full 360° contact. The magnitude of the total applied load at which separation occurs will be defined as the separation load $P_{separation}$. The separation load can be found based on the following observations. First, the vertical sum of the loads exerted by the rolling elements on the outer raceway should equal the total applied load such that

$$\sum_{i=1}^{n}\left(P_i \cos\theta_i\right) = P_{total} \tag{6.22}$$

where P_i is the load exerted on the outer raceway by the *i*-th rolling element, θ_i is the angular location of the *i*-th rolling element, and n is the number of the rolling elements. The loads exerted by the rolling elements on the outer raceway are assumed in the form similar to the solution by Persson as in Eq. (6.8) as

$$P_i = A\cos\theta_i + B\ ,\ 1 \le i \le n \tag{6.23}$$

where A and B are constants to be determined. Finally, the average of the magnitudes of the loads exerted by the rolling elements on the outer raceway is equal to the interference load such that

$$\frac{\sum_{i=1}^{n} P_i}{n} = P_{interference}\ . \tag{6.24}$$

The constant A can be found by substituting Eq. (6.23) into Eq. (6.22) as

$$A = P_{total}\frac{2}{n}. \tag{6.25}$$

When Eq. (25) is substituted back into Eqns. (6.23) and (6.24) with $P_{total} = 0$, the constant B can be identified to be

$$B = P_{interference}. \tag{6.26}$$

Then, the separation load can be found by the definition such that

$$P_i\left(\theta_i = \pm\pi\right) = 0 \tag{6.27}$$

which gives

$$-A + B = -P_{separation}\frac{2}{n} + P_{interference} = 0 \tag{6.28}$$

Therefore, the total applied load at which separation occurs is found to be

$$P_{separation} = \frac{n}{2}P_{interference} = \frac{n}{2}\left(\kappa\frac{E^*\Delta d}{4\left(d_o/2\right)}\right)^2\frac{\pi R}{E^*}. \tag{6.29}$$

Loads exerted by rolling elements on the outer raceway

The load exerted by the *i*-th rolling element on the outer raceway is found by substituting the constants in Eqns. (6.16), (6.25) and (6.26) into Eq. (6.23) as

$$P_i = P_{total}\frac{2}{n}\cos\theta_i + \left(\kappa\frac{E^*\Delta d}{4\left(d_o/2\right)}\right)^2\frac{\pi R}{E^*},\ 1 \le i \le n \tag{6.30}$$

when

$$P_{total} \le P_{separation}. \tag{6.31}$$

The largest possible load exerted by a rolling element on the outer raceway can be obtained by setting $\theta_i = 0$ in Eq. (6.30) as

$$P_{\max} = P_{total}\frac{2}{n} + \left(\kappa\frac{E^*\Delta d}{4\left(d_o/2\right)}\right)^2\frac{\pi R}{E^*}. \tag{6.32}$$

When P_{total} is larger than $P_{separation}$, a similar procedure can be used to find the load P_i of the rolling elements. However, since the number of the rolling elements in contact

depends on the P_{total} and the geometric parameters such as d_i, d_o and d_r, the solution will be quite complex and is not in the closed-form as presented in this section.

Validation of the closed-form solution

Two-dimensional finite element analyses were carried out to validate the applicability of the closed-form solution to calculate the loads exerted by the rolling elements on the outer raceway. Since the finite element analyses give the contact pressures rather than the loads exerted by the rolling element on the outer raceway, the load exerted by the *i*-th rolling element calculated from Eq. (6.30) will be converted to the maximum contact pressure by the *i*-th rolling element by using Eq. (6.5) as

$$p_{\max,i} = \sqrt{\frac{E^*}{\pi R_o} P_i} \,. \tag{6.33}$$

Two-dimensional plane strain finite element models were developed to simulate the middle portion of the idealized cylindrical roller bearing. Two representative finite element models based on the geometries of typical wheel bearings and cam follower roller bearings are shown in Figs. 6.7(a) and 6.8(a). The finite element model in Fig. 6.7(a) has 18 rolling elements while the model in Fig. 6.8(a) has 15 rolling elements. The X-Y Cartesian coordinates are shown in the figures. Figs. 6.7(a) and 6.8(a) show the three components in the finite element model; an outer cylinder, an inner cylinder and the rolling elements. Second-order, isoparametric, plane strain, quadrilateral, reduced integration elements (CPE8R) are used in the models. The minimum element size is 10.0 x10^{-3} mm. Figs. 6.7(b) and 6.8(b) show close-up views of the mesh refinement near the contact regions boxed in Figs. 6.7(a) and 6.8(a), respectively. The elastic modulus *E* is

200 GPa and the Poisson's ratio v is 0.3 for all material elements in the finite element models. The steel used for manufacturing bearing components usually have a high yield stress of more than 1200 MPa. For the load range investigated here, the stresses on the contact surface and in the subsurface near the contact regions are within the elastic range.

Finite element models with different magnitudes of interference, relative radius of curvature and outer raceway diameter have been used to validate the applicability of the closed-form solution. The dimensions for the models used in the finite element analyses are shown in Table 6.1. Table 6.1 shows the values for the outer raceway diameter, the inner raceway diameter, the rolling element diameter, the relative radius of curvature, the thickness of the outer cylinder, the interference, the number of rolling elements and the separation load for eight finite element models.

The finite element analyses were conducted in two separate steps. Figs. 6.9(a) and 6.9(b) show the boundary conditions for the finite element analyses for the first and second steps, respectively. The Cartesian and polar coordinate systems are also shown. The interference pressure is calculated in the first step and the vertical load is applied in the second step. The outer surface of the outer cylinder is constrained in all X and Y directions during both steps. Also, the horizontal motion in the X direction of the central region of the inner cylinder is constrained during both steps. For the first step, the rolling elements are constrained in the tangential direction in the polar coordinate system. For the second step, the tangential constraints of the rolling elements and the vertical constraint of the central regions of the inner cylinder are removed. Uniformly distributed vertical loads are applied to a group of nodes in the central portion of the inner cylinder.

The arrows in Fig. 6.9(b) show the direction of the applied load. Computations were performed using the commercial finite element software Abaqus v6.8 [11].

Fig. 6.10(a) show the contact pressure profile from the finite element analysis for model 1 from the first step (the total applied load is zero). The contact pressure shown in Fig. 6.10(a) is therefore the interference pressure. As expected, 18 almost equally distributed contact pressure profiles with the almost same maximum contact pressure are shown in Fig. 6.10(a). Each contact pressure profile in general follows Eq. (6.1). One contact pressure profile is shown in Fig. 6.10(b).

Figs. 6.11, 6.12 and 6.13 show the contact pressures obtained from the finite element analyses and the closed-form solution in Eq. (6.33) for models 1, 5 and 8 from the second step. The contact pressures from the finite element analyses are shown in solid lines while the contact pressures obtained from the closed-form solution are shown in dashed lines. It should be noted that the results from the other models show similar results as shown in Figs. 6.11, 6.12 and 6.13 and therefore are not shown here.

Figs. 6.11(a), 6.11(b) and 6.11(c) show the contact pressures obtained from the finite element analysis and the closed-form solution for model 1. The estimated separation load for model 1 is 562 N/mm. The ratios of the total applied load to the separation load are 0, 0.47 and 0.93 for Figs. 6.11(a), 6.11(b) and 6.11(c), respectively.

Figs. 6.12(a), 6.12(b) and 6.12(c) show the contact pressures obtained from the finite element analysis and the closed-form solution for model 5. The estimated separation load for model 5 is 982 N/mm. The ratios of the total applied load to the separation load are 0, 0.50 and 0.96 for Figs. 6.12(a), 6.12(b) and 6.12(c), respectively.

Figs. 6.13(a), 6.13(b) and 6.13(c) show the contact pressures obtained from the finite element analysis and the closed-form solution for model 8. The estimated separation load for model 8 is 288 N/mm. The ratios of the total applied load to the separation load are 0, 0.43 and 0.81 for Figs. 6.13(a), 6.13(b) and 6.13(c), respectively.

Fig. 6.14 shows the error of the maximum contact pressures obtained from the closed-form solution at $\theta = \pm 10°$ when compared with those from the finite element analyses as a function of the ratio of the total applied load to the separation load. The contact pressures at $\theta = \pm 10°$ are selected for comparison since the rolling element at this locations experienced the largest pressure and load from the finite element analyses. As can be seen, the error is below 1% for the given total applied load range. The fluctuations seem to have negligible meaning and the error does not increase nor decrease with the increase of the total applied load when below the separation load.

Discussion

The loads exerted by the rolling elements on the outer raceway given by Eq. (6.30) may not be directly used during bearing design and selection processes. Rather, bearing life or rating life is used by most manufacturers as an estimate for the life for a given bearing. However, the load values calculated from Eq. (6.30) can be combined with the stress solutions in [12] and [13] to obtain the subsurface stresses of the raceway as in Lee et al. [14]. The subsurface stresses can then be combined with the existing fatigue theories, for example, see [15] and [16]. The fatigue life obtained from this process can be used to compare design changes of the geometry and the number of rolling elements or the applied load for the bearings of interest.

Based on the validation, the loads obtained from Eqns. (6.30) and (6.33) are in good agreement with the finite element results for the given geometries of bearings and the total applied load. However, Eqns. (6.30) and (6.33) have an upper limit set by the separation load in Eq. (6.31). When the total load is larger than the separation load, the contact angle is less than 360 ° or the number of the rolling elements in contact is less than the total number of the rolling elements. Fig. 6.15 shows the normalized load exerted by the rolling element located at $\theta = \pm 10°$ obtained from the finite element analysis for model 1 and from the closed-form solution in Eq. (6.30) as a function of the normalized total load. The loads are normalized by the separation load as shown in the figure.

As the ratio of the total applied load to the separation load exceeds 1, the result of the finite element analysis becomes higher than that from the closed-form solution. Therefore, Eqns. (6.30) and (6.33) should be used when the total applied load is less than the separation load. When the total applied load exceeds the separation load, the overall contact angle is no longer 360° and the assumption of Eq. (6.23) is no longer valid. Persson has obtained the solution for the non-conforming contact of cylinders and thus a further study should be conducted to find the corresponding solutions applicable to a bearing model when the total applied load is larger than the separation load.

The separation load can also be used as a design limit for the applied load for bearing operation. Separation of the rolling elements and the raceways is not beneficial toward the overall fatigue life of the bearing since the equivalent stress amplitude for fully reversed loading increases as the mean stress decreases when a fatigue theory based

on the Goodman relation and the Mises stress amplitude as the equivalent stress amplitude is adopted.

Additional considerations for using Eq. (6.30) should be listed. First, the proposed method is based on the force equilibrium condition under static loading conditions and does not consider rolling of the rolling elements. Rolling contact fatigue has been studied by numerous researchers [17], [18], [19] and is shown to have different results compared to cyclic standing contact fatigue conditions in terms of subsurface stress distributions, crack location and fatigue lives [20].

The closed-form solution is derived on the assumption that the outer and inner cylinders and the rolling elements have the same material properties with the same elastic moduli when the outer and inner cylinders and the rolling elements have different elastic moduli and may even show plastic and shakedowns behaviors [21], [22]. The subsurface stresses must be evaluated such that they do not meet the yield condition prior to the use of Eq. (6.30). Different elastic moduli and Poisson's ratios between the outer or inner cylinders and the rolling elements can be taken into account by using Eq. (6.4) to obtain the equivalent elastic modulus of the contact solution.

Conclusion

In this chapter, a closed-form solution to calculate the loads exerted by the rolling elements in cylindrical roller bearings with consideration of interference fit of rollers is proposed in this chapter. The non-conforming Hertz solution and the conforming Persson solution are first briefly reviewed. The interference loads by the rolling elements due to the interference are derived and then approximated for a given set of geometric

parameters of bearings. With the solution for the interference load, the loads exerted by the rolling elements on the outer raceway are obtained when the total load is less than the separation load where a rolling element possibly start to lose contact with the cylinders. These loads of the rolling elements can be calculated by a closed-form equation with the total applied load, the number of rolling elements, the angular locations of the rolling elements, the equivalent elastic modulus, the interference, the outer raceway diameter and the thickness of the outer cylinder as the input parameters. Two-dimensional finite element analyses were conducted to verify the applicability of the closed-form solution. Finite element models with different diameters of the outer and inner cylinders, diameters of the rolling element, number of rolling elements, and the thickness of the outer cylinder were considered for the validation. The results of the finite element analyses show that the maximum contact pressures of the rolling elements obtained from the closed-form solution are within 1% of those of the finite element analyses when the total load is less than the separation load.

References

[1] Nurkala LD, Wallace RS. Development of the SAE biaxial wheel test load file. SAE Technical paper No. 2004-01-1578. Society of Automotive Engineers, Warrendale, PA; 2004.

[2] Fischer G, Zinke R. Validation of wheel bearing systems in biaxial wheel/hub test facilities. SAE Technical paper No. 2005-01-1827. Society of Automotive Engineers, Warrendale, PA; 2005.

[3] Schlicht H, Schreiber E, Zwirlein O. Fatigue and failure mechanism of bearings. Fatigue of Engineering Materials and Structures 1986; 1: 85-90.

[4] Hoeprich MR, Rolling element bearing fatigue damage propagation. J Tribology 1992; 114: 328-33

[5] Grubisic V, Fischer G. Methodology for effective design evaluation and durability approval of car suspension components. SAE Technical paper No. 970094. Society of Automotive Engineers, Warrendale, PA; 994.

[6] De Paula FN, Cavalcanti D, Cavalca KL, Arima G, Development of software applying the Hertz contact theory to commercial rolling bearings. SAE Technical paper No. 2005-01-4031. Society of Automotive Engineers, Warrendale, PA; 2005.

[7] Johnson KL, Contact mechanics 2003; ISBN 0 521 34796 3. 9th ed. Cambridge University Press, UK 2003.

[8] Persson A, On the stress distribution of cylindrical elastic bodies in contact. Doctoral dissertation, Chalmers Tekniska Högskola; 1964.

[9] Ricci MC. Internal loading distribution in statically loaded ball bearings, subjected to a combined radial and thrust load, including the effects of temperature and fit. World Academy of Science, Engineering and Technology 2009; 57: 290-8

[10] Oswald FB, Zaretsky EV, Poplawski JV. Interference-fit life factors for roller bearings. NASA Technical memorandum TM-2009-215285, Cleveland, OH, 2009.

[11] ABAQUS v6.8 User Manual. Providence, RI: SIMULIA; 2008.

[12] McEwen E. Stresses in elastic cylinders in contact along a generatrix. Philosophical Magazine 1949; 40: 454-9

[13] Sackfield A, Hills DA. Some useful results in the classical Hertz contact problem. The Journal of Strain Analysis for Engineering Design 1983; 18: 101-5.

[14] Lee J, Pan J. A closed-form analytical solution for calculation of loads and contact pressures for roller and ball bearing. to be submitted for publication.

[15] Socie DF. Critical plane approaches for multiaxial fatigue damage assessment. Advances in Multiaxial Fatigue (ASTM STP 1191) 1993. American Society of Testing and Materials, Philadelphia, PA, 7-36.

[16] Findley WN. A theory for the effect of mean stress of fatigue of metals under combined torsioin and axial load or bending. J Eng for Industry 1959; 81:301-6.

[17] Ringsberg JW. Life prediction of rolling contact fatigue crack initiation. Int J Fatigue 2001; 23: 575-86.

[18] Bhargava V, Hahn GT, Rubin CA. Rolling contact deformation and microstructural changes in high strength bearing steel. Wear 1989; 133: 65-71

[19] Yu M, Moran B, Keer LM. A direct analysis of two dimensional elastic plastic rolling contact. J Tribology 1993; 115: 227-36

[20] Dahlberg J, Alfredsson B. Standing contact fatigue with a cylindrical indenter. Fatigue & Fracture of Engineering Materials & Structures 2005; 28: 599-613

[21] Kulkarni SM, Hahn GT, Rubin CA, Bhargava V. Elastoplastic finite element analysis of three dimensional pure rolling contact at the shakedown limit. J Applied Mech 1990; 57: 57-65

[22] Kral ER, Komvopoulos K, Bogy DB. Elastic plastic finite element analysis of repeated indentation of a half space by a rigid sphere. J Applied Mech 1993; 60: 829-841

Table 6.1 Dimensions, number of rolling elements and the separation load for the finite element models used for verification. All length dimensions in mm.

Model	Outer raceway diameter d_o	Inner raceway diameter d_i	Rolling element diameter d_r	Relative radius of curvature R	Outer cylinder thickness T	Inter-ference Δd	Number of rolling elements n	Separ-ation load $P_{separation}$
1	76	55.4	10.3	5.95	10.3	-4.12×10^{-3}	18	562
2	38	27.7	5.15	2.98	5.15	-2.06×10^{-3}	18	281
3	57	41.6	7.72	4.47	7.72	-3.09×10^{-3}	18	425
4	76	57.5	9.27	5.28	9.27	-4.12×10^{-3}	18	546
5	76	55.4	10.3	5.95	10.3	-6.90×10^{-3}	18	982
6	76	55.4	10.3	5.95	10.3	-3.89×10^{-3}	18	529
7	76	55.4	10.3	5.95	10.3	-3.68×10^{-3}	15	431
8	50.7	36.9	6.87	3.97	6.87	-2.47×10^{-3}	15	288

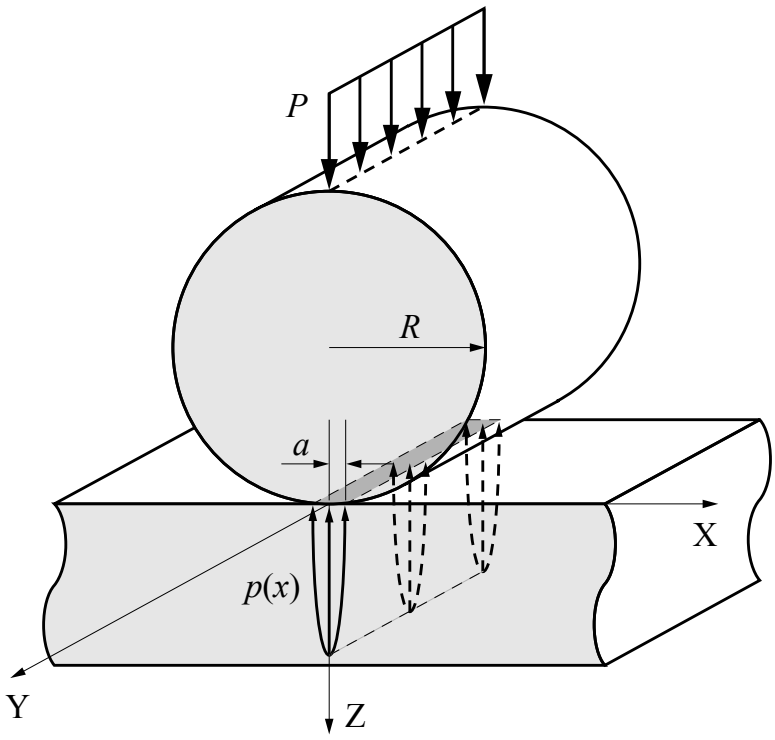

(a)

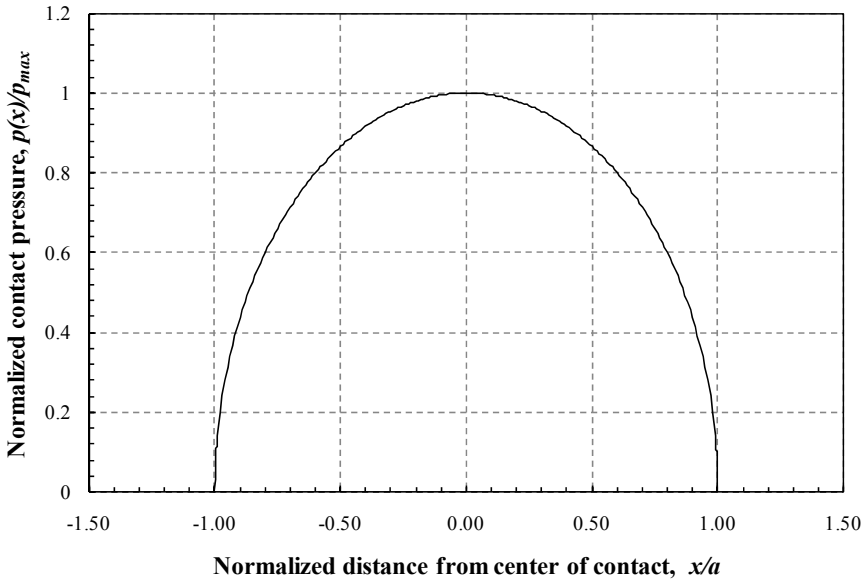

(b)

Fig. 6.1 (a) Contact between a long cylinder with radius of R and a flat surface due to a load per unit length, P. (b) The normalized elliptical contact pressure profile between the cylinder and the flat surface as a function of the normalized distance from the symmetry plane.

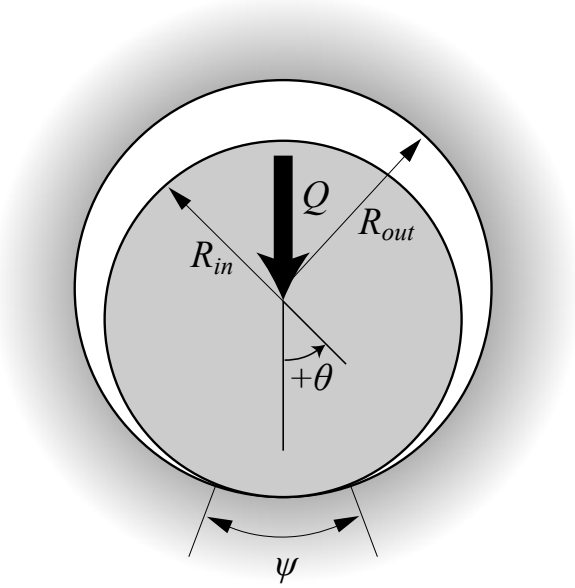

(a)

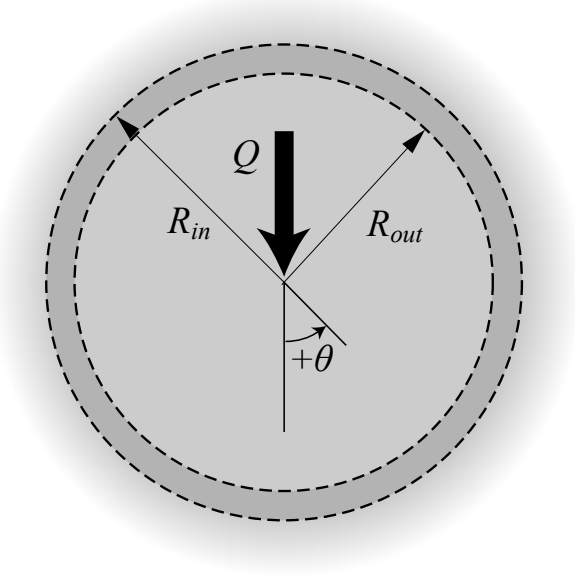

(b)

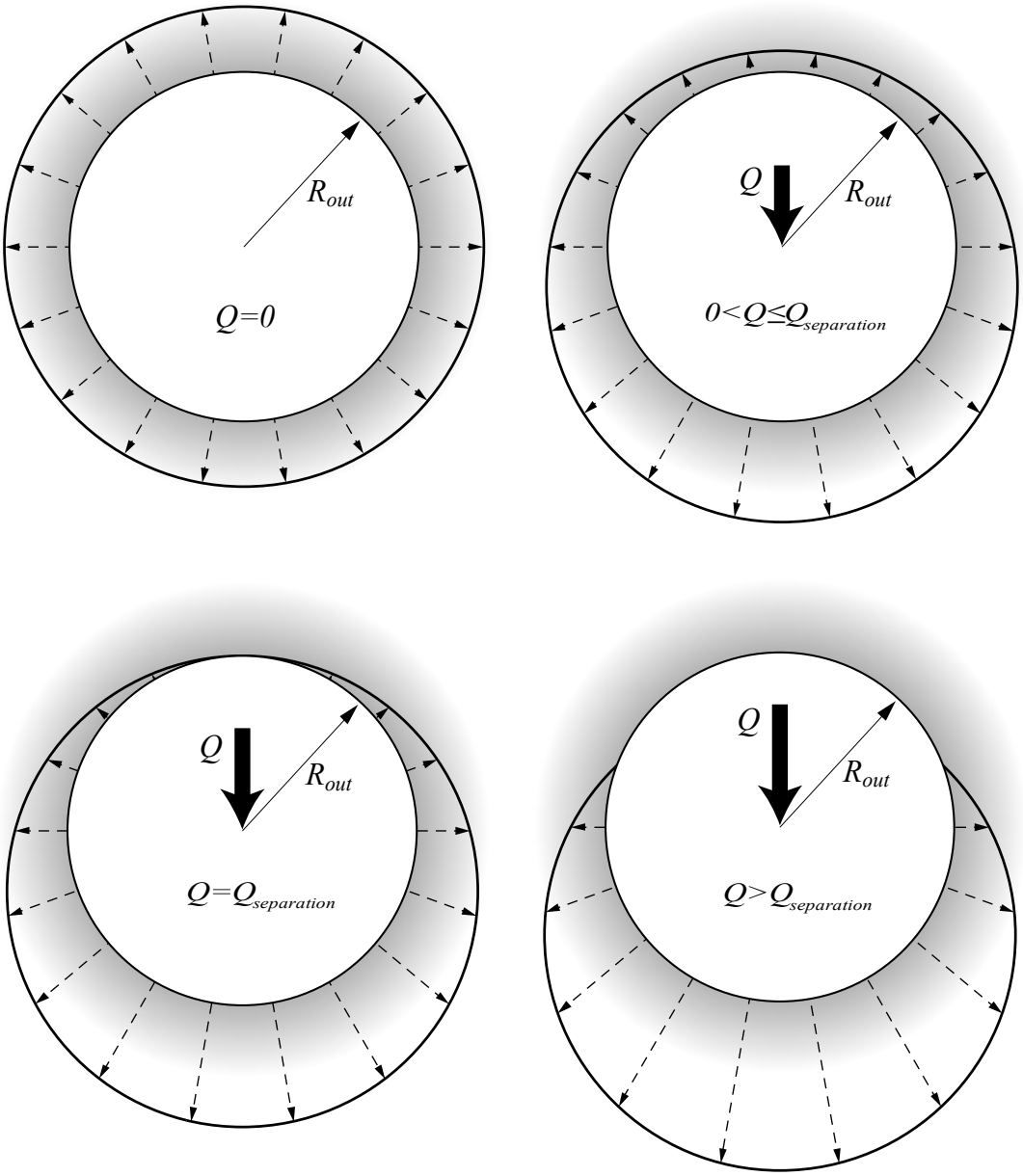

(c)

Fig. 6.2 Contact between an inner cylinder and an infinite outer body where (a) R_{in} is smaller than R_{out} and (b) R_{in} is larger than R_{out}. (c) The change in contact pressure distribution on the surface of the outer body with increasing applied load Q.

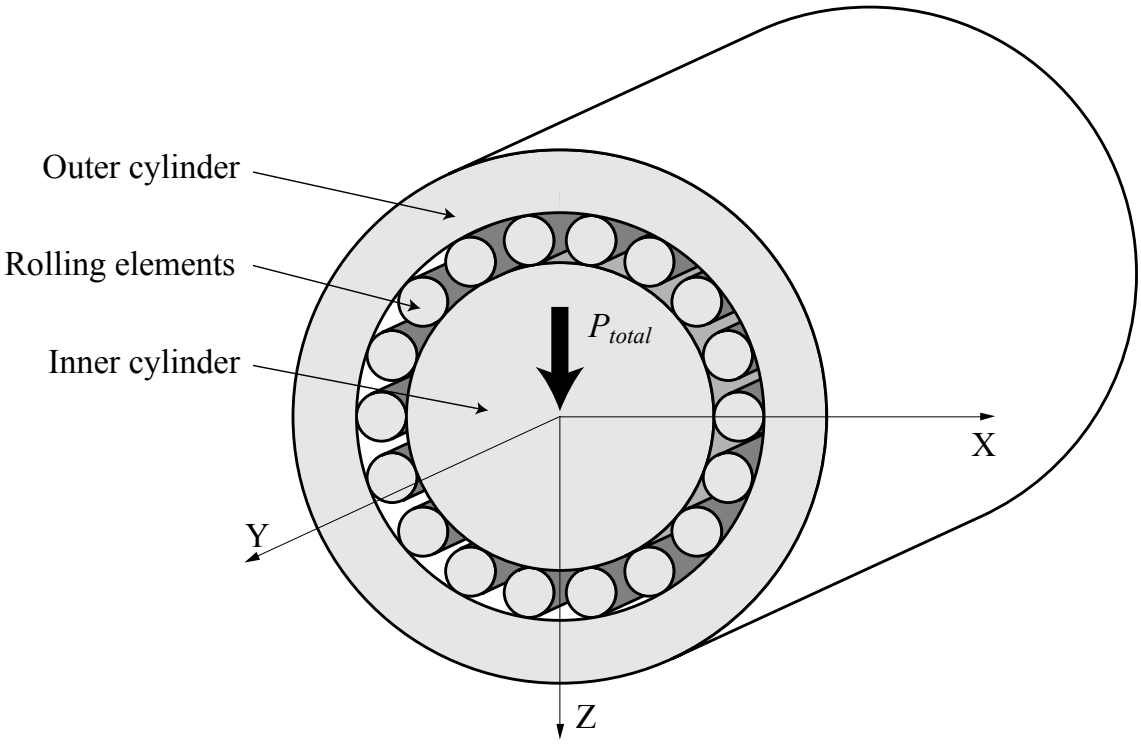

Fig. 6.3 A schematic of an idealized cylindrical roller bearing with an outer cylinder, inner cylinder and rolling elements with a load of P_{total} applied to the inner cylinder.

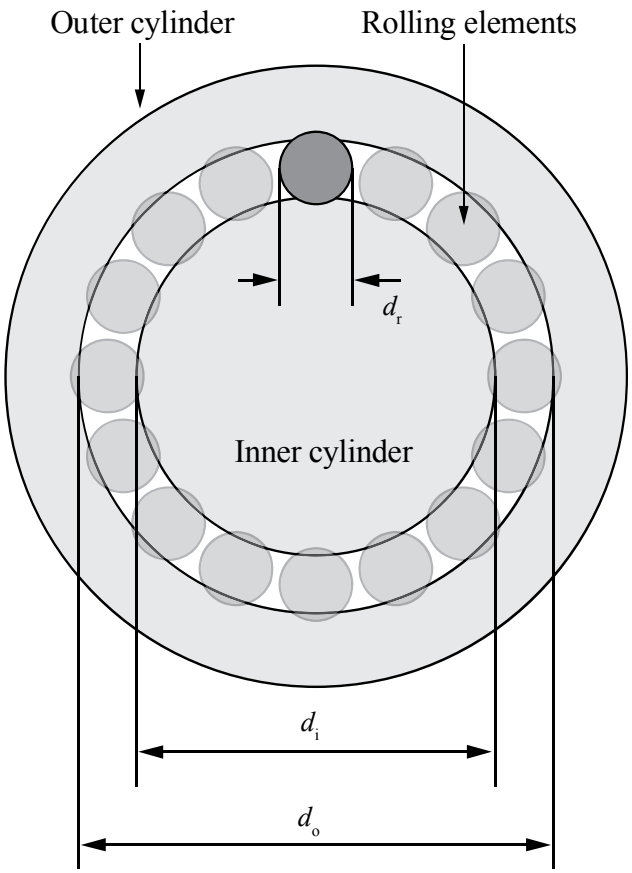

Fig. 6.4 The axial view of an idealized cylindrical roller bearing with interference.

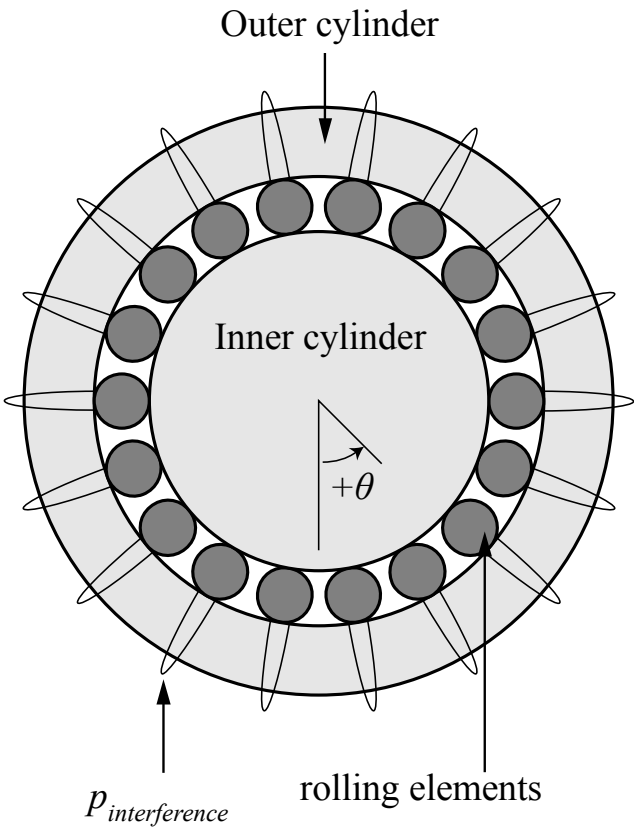

Fig. 6.5 The contact pressures exerted on the outer raceway by the rolling elements due to the interference.

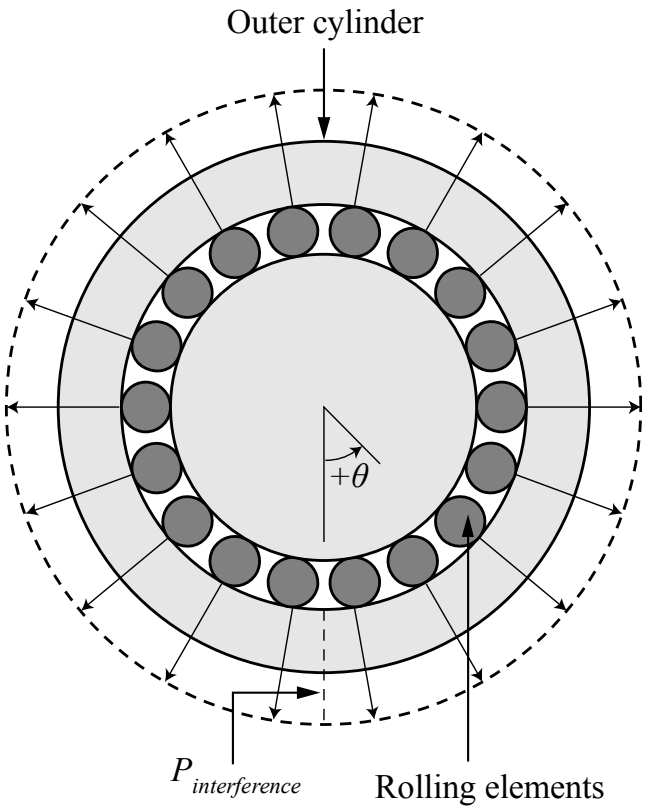
Outer cylinder
$+\theta$
$P_{interference}$
Rolling elements

(a)

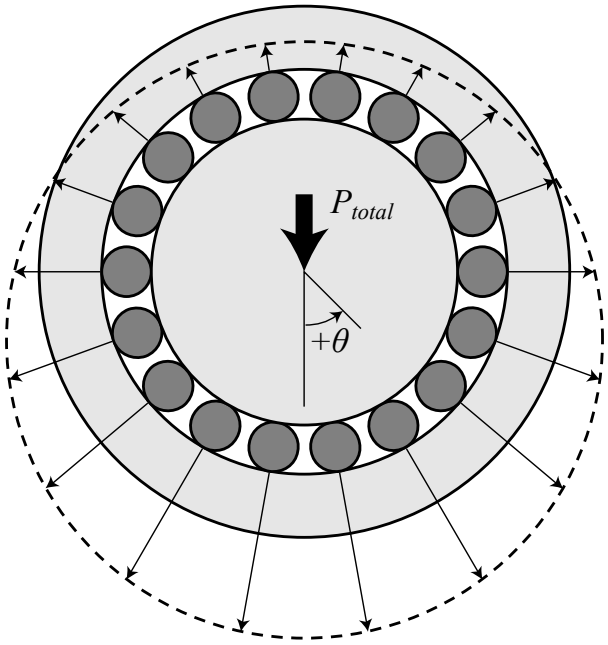
P_{total}
$+\theta$

(b)

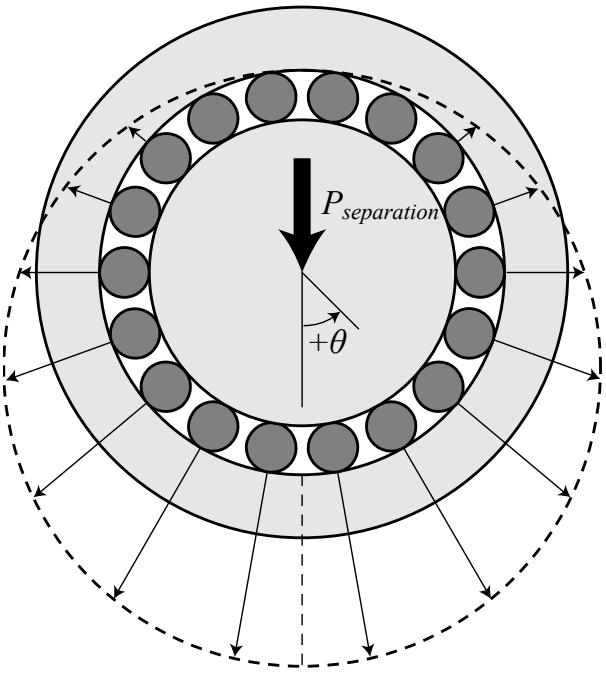

(c)

Fig. 6.6 The loads exerted by the rolling elements on the outer raceway due to the interference under (a) no applied load, (b) an applied load smaller than the separation load and (c) an applied load equal to the separation load.

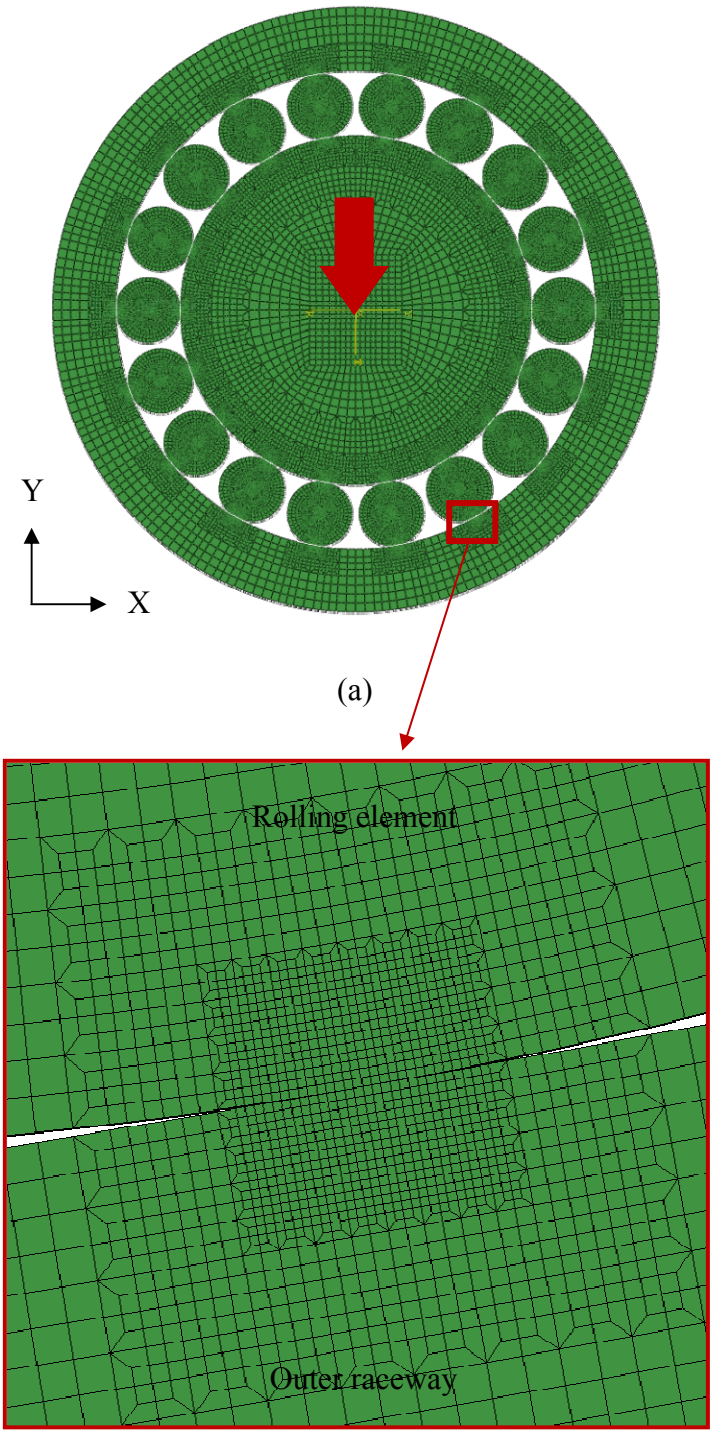

Fig. 6.7 (a) A 18 roller finite element model used in the two-dimensional finite element analysis. The large arrow indicates the direction and the location of the applied load. (b) A close-up view showing the mesh refinement near a contact region.

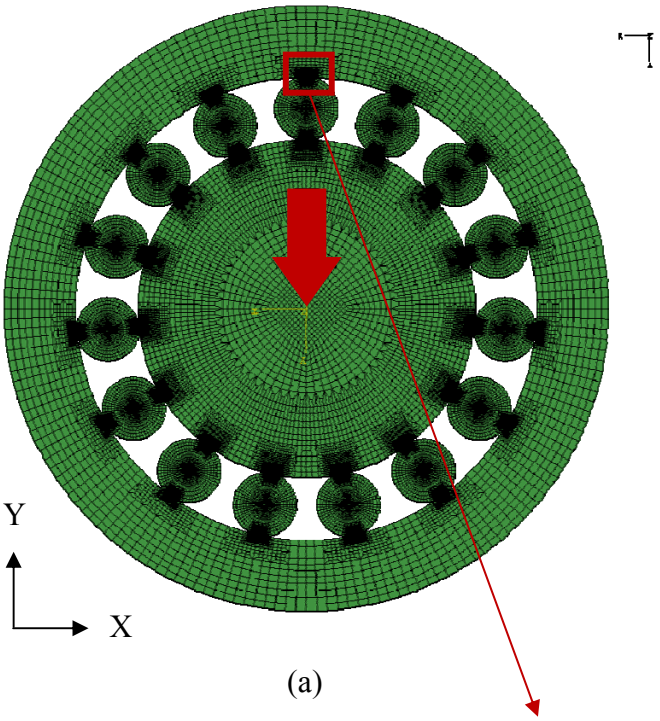

(a)

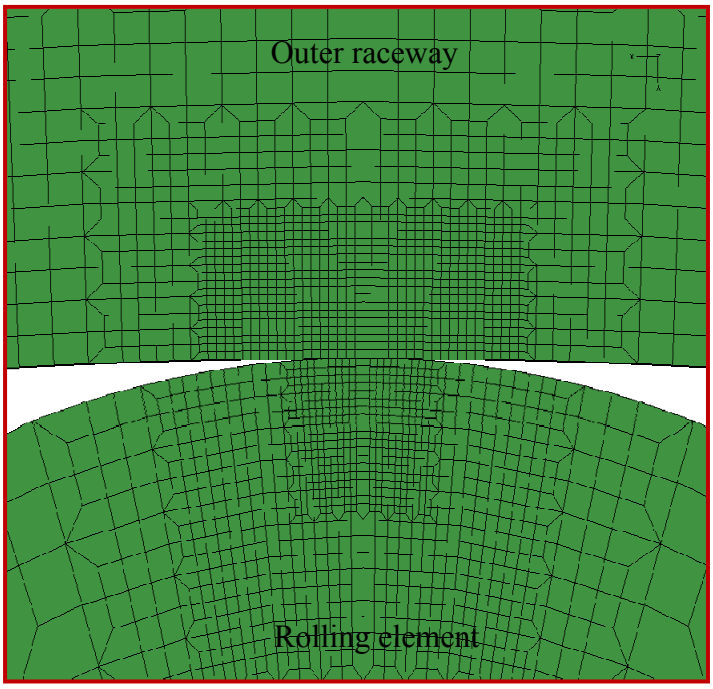

(b)

Fig. 6.8 (a) A 15 roller finite element model used in the two-dimensional finite element analysis. The large arrow indicates the direction and the location of the applied load. (b) A close-up view showing the mesh refinement near a contact region.

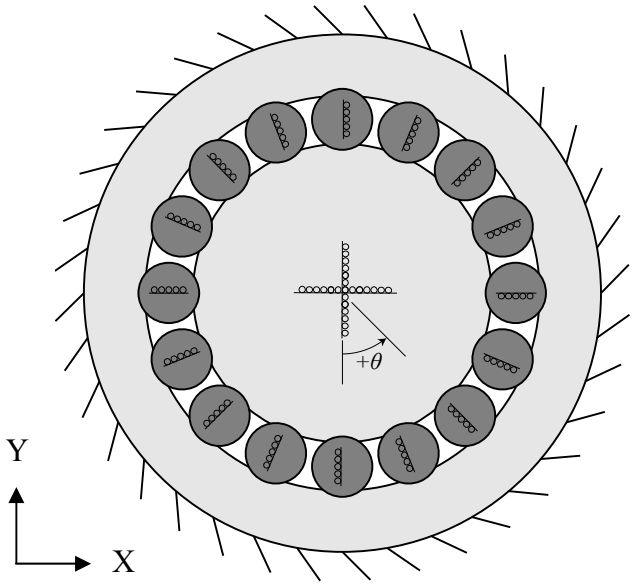

(a)

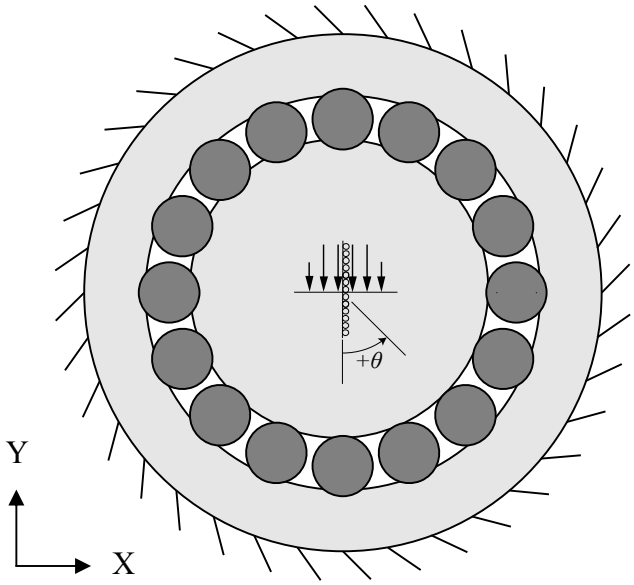

(b)

Fig. 6.9 Boundary conditions in the finite element models for (a) the first step when the interference is introduced and (b) the second step when the vertical load is applied.

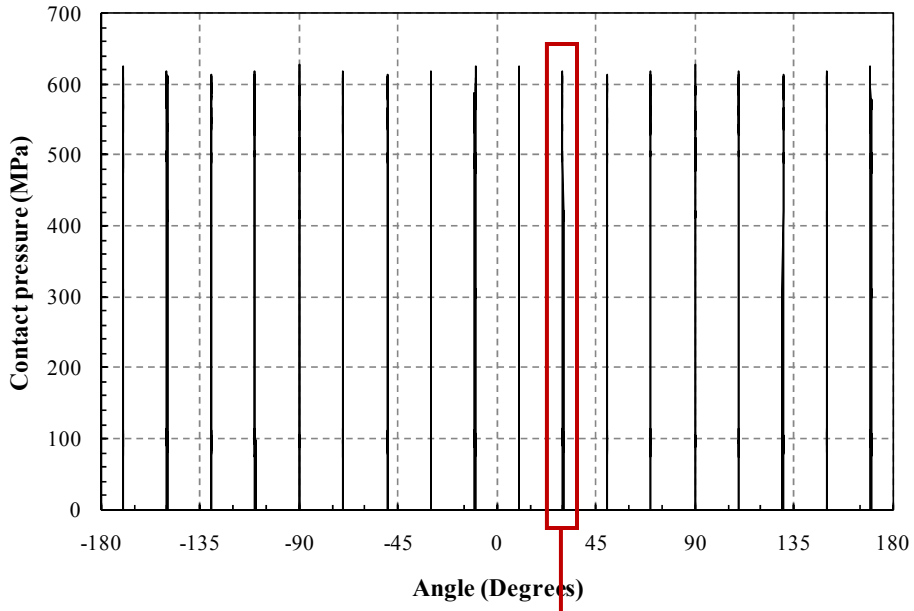

(a)

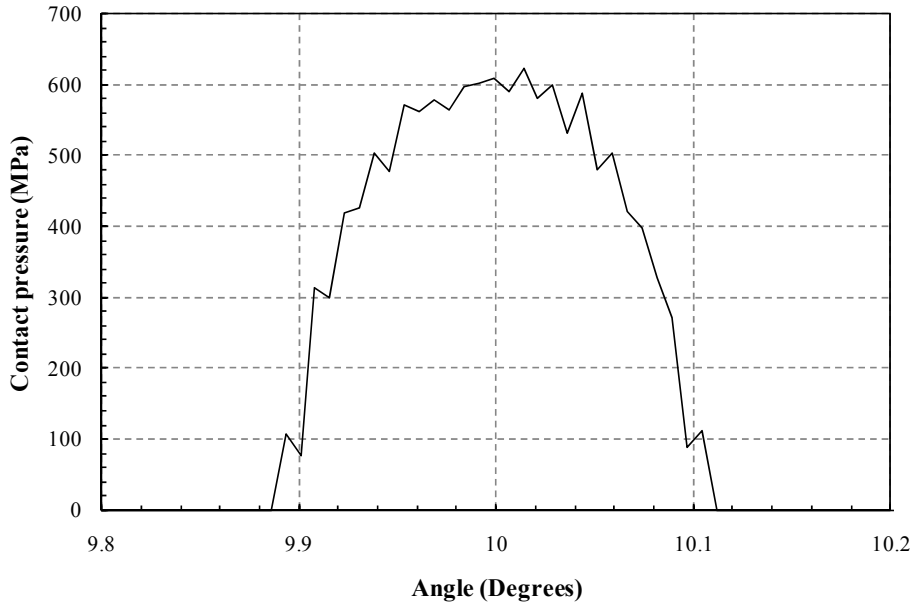

(b)

Fig. 6.10 The results of the contact pressures exerted by the rolling elements on the outer raceway due to the interference from the finite element analysis of model 1 for (a) all 18 rolling elements and (b) a single rolling element.

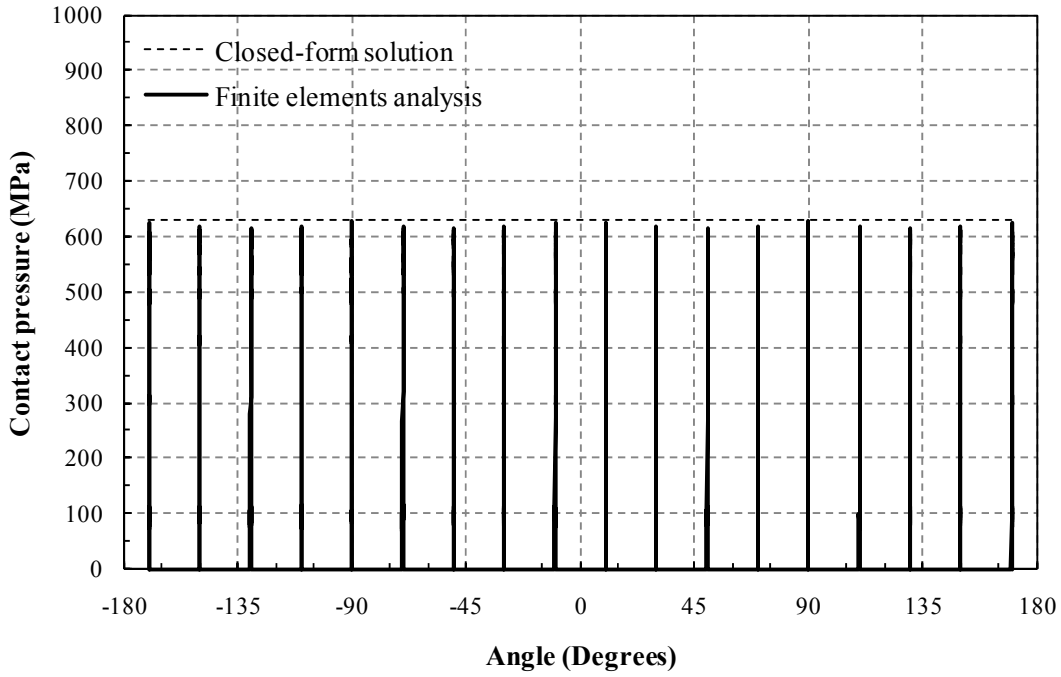
Closed-form solution
Finite elements analysis
Contact pressure (MPa)
1000
900
800
700
600
500
400
300
200
100
0
-180
-135
-90
-45
0
45
90
135
180
Angle (Degrees)

(a)

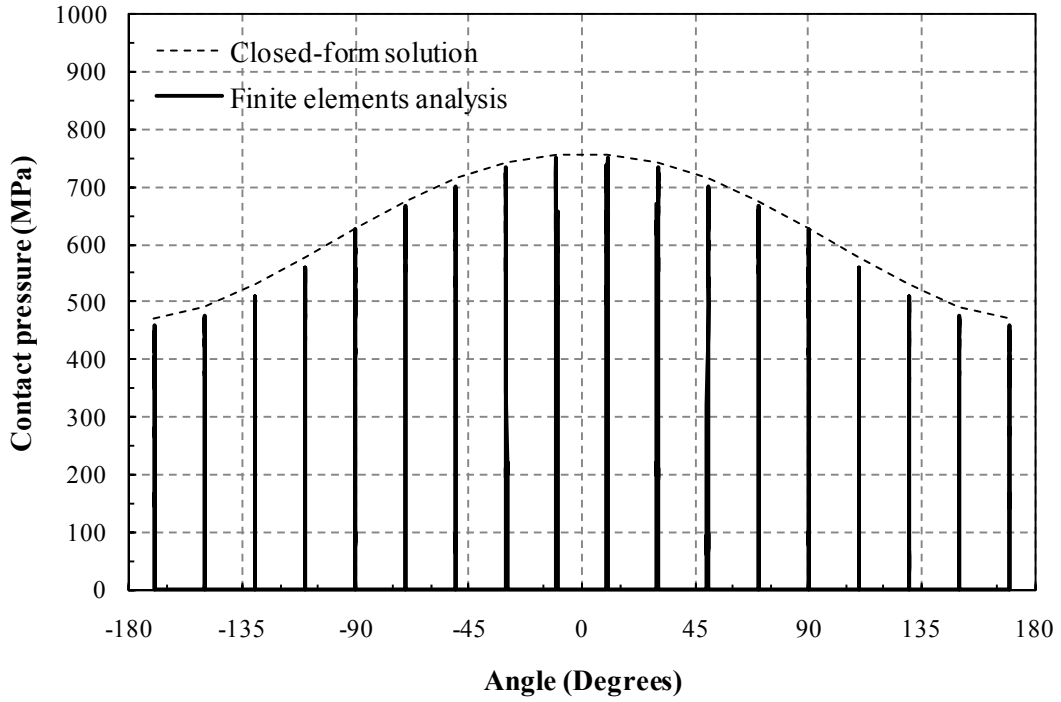
Closed-form solution
Finite elements analysis
Contact pressure (MPa)
1000
900
800
700
600
500
400
300
200
100
0
-180
-135
-90
-45
0
45
90
135
180
Angle (Degrees)

(b)

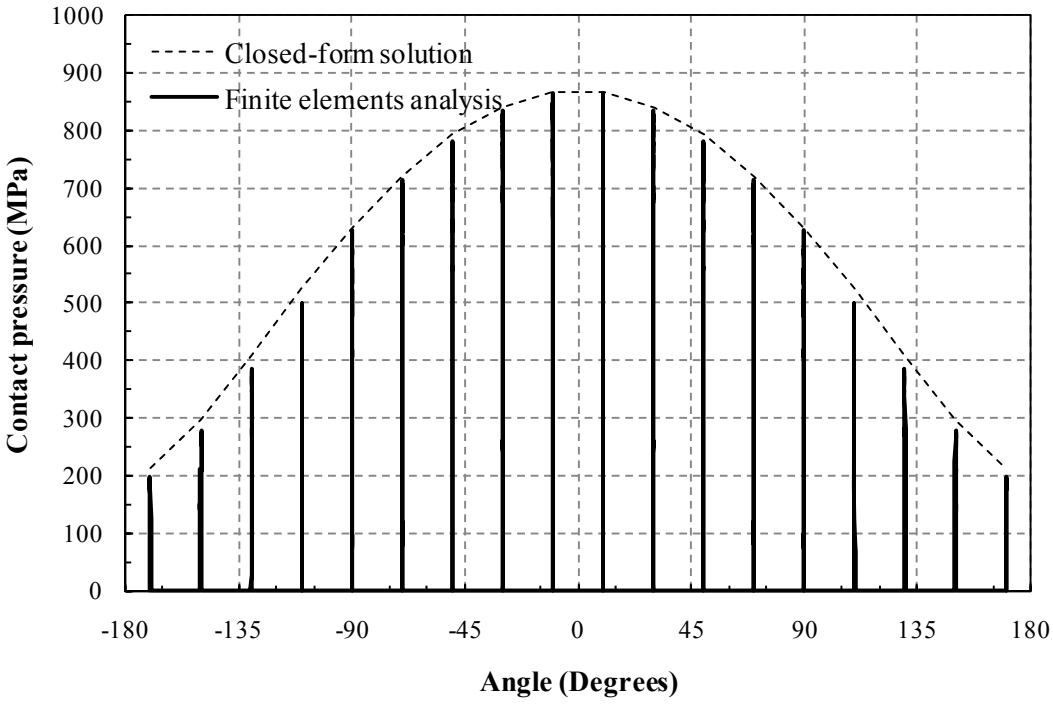

(c)

Fig. 6.11 The contact pressures from the finite element analysis and the closed-form solution for model 1 for the ratio $P_{total}/P_{separation}$ of (a) 0, (b) 0.47 and (c) 0.93.

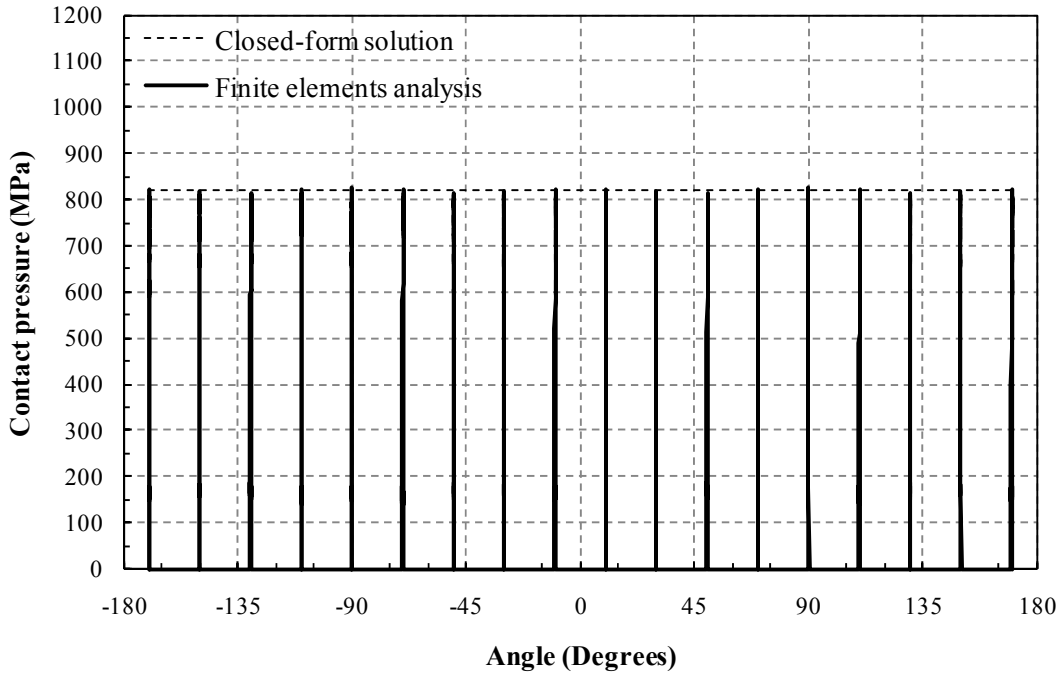
Closed-form solution
Finite elements analysis
Contact pressure (MPa)
Angle (Degrees)
1200
1100
1000
900
800
700
600
500
400
300
200
100
0
-180
-135
-90
-45
0
45
90
135
180

(a)

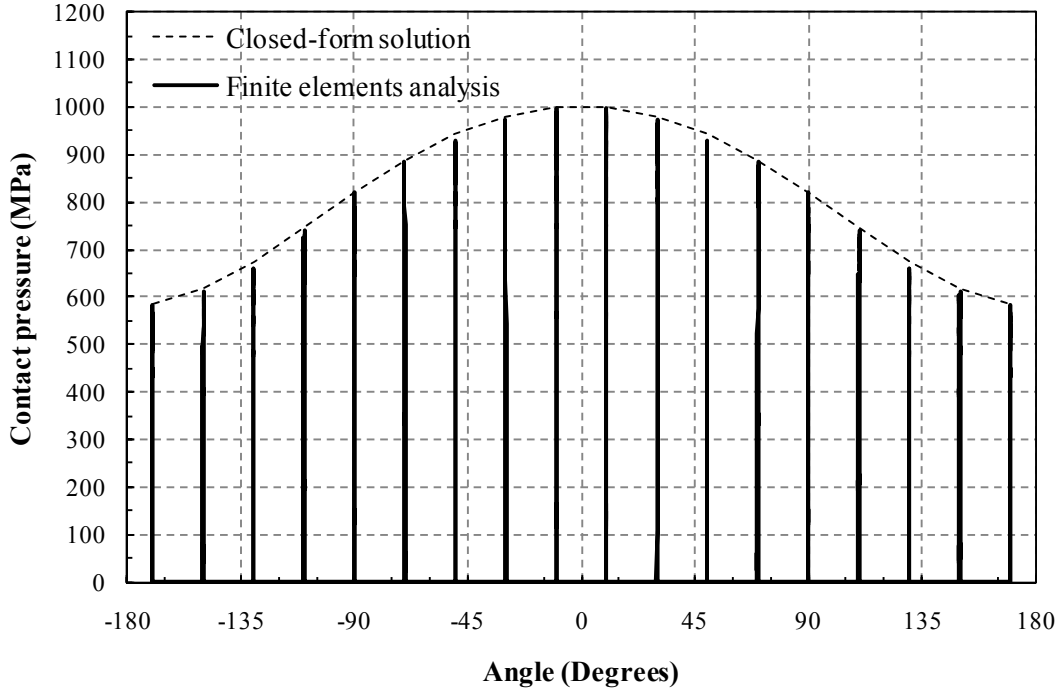
Closed-form solution
Finite elements analysis
Contact pressure (MPa)
Angle (Degrees)
1200
1100
1000
900
800
700
600
500
400
300
200
100
0
-180
-135
-90
-45
0
45
90
135
180

(b)

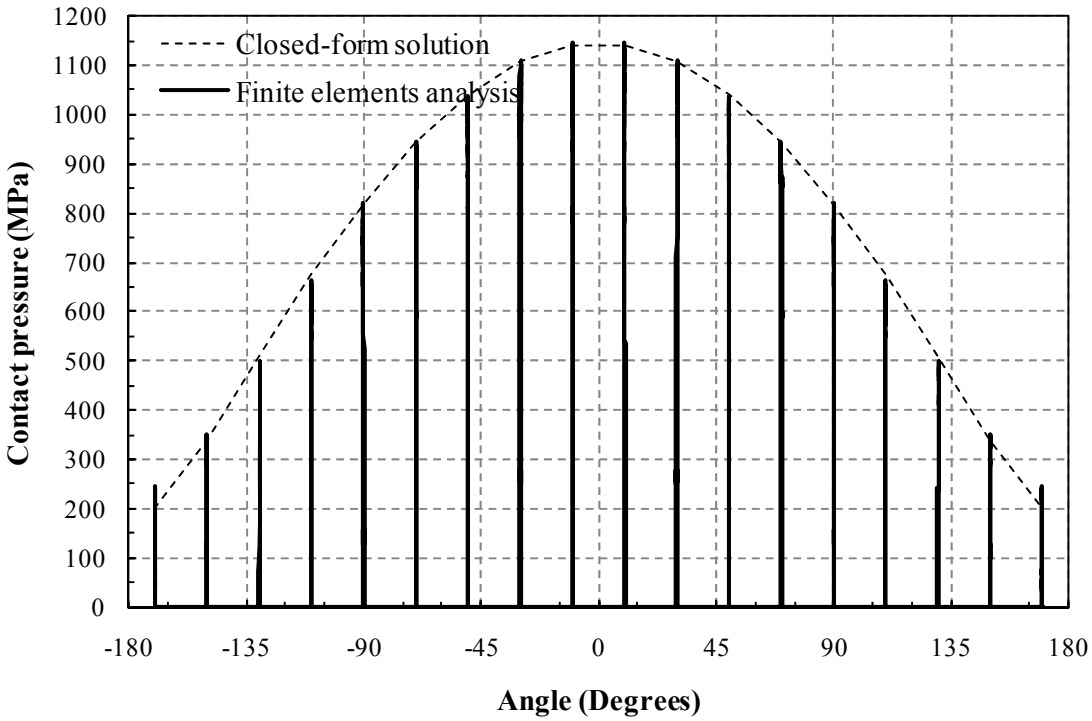

(c)

Fig. 6.12 The contact pressures from the finite element analysis and the closed-form solution for model 5 for the ratio $P_{total}/P_{separation}$ of (a) 0, (b) 0.5 and (c) 0.96.

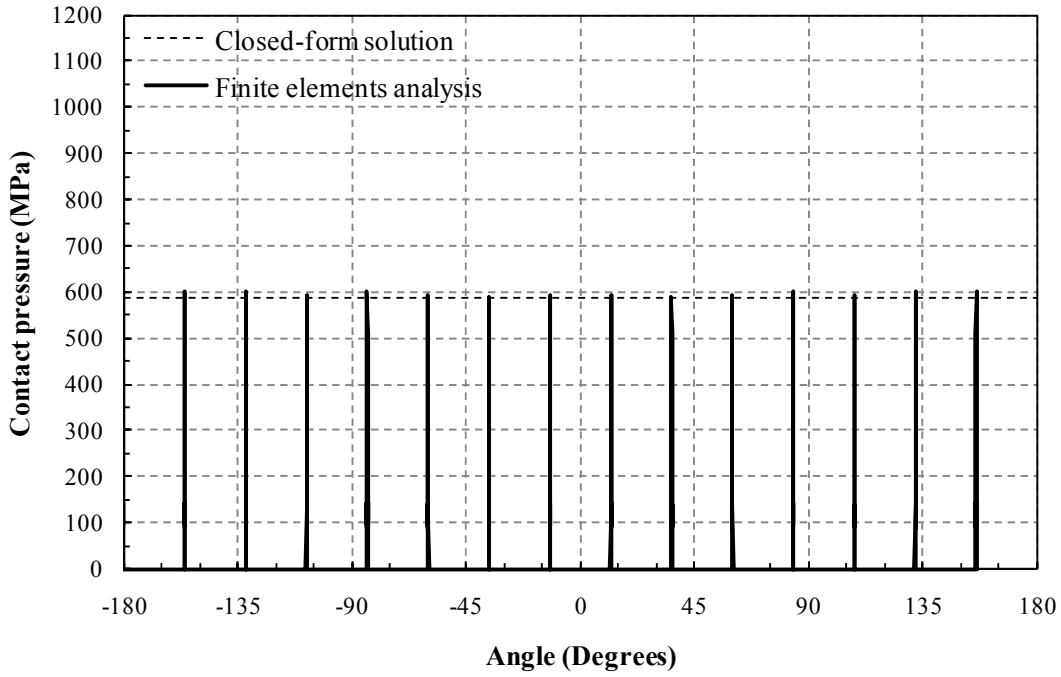
Closed-form solution
Finite elements analysis
Contact pressure (MPa)
1200
1100
1000
900
800
700
600
500
400
300
200
100
0
-180
-135
-90
-45
0
45
90
135
180
Angle (Degrees)

(a)

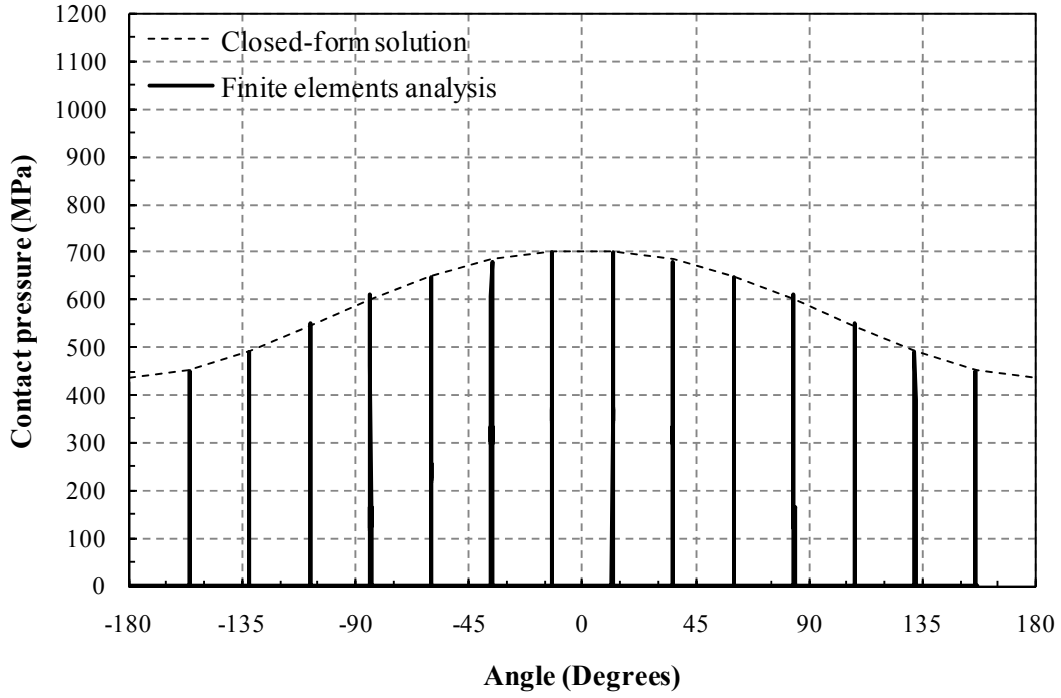
Closed-form solution
Finite elements analysis
Contact pressure (MPa)
1200
1100
1000
900
800
700
600
500
400
300
200
100
0
-180
-135
-90
-45
0
45
90
135
180
Angle (Degrees)

(b)

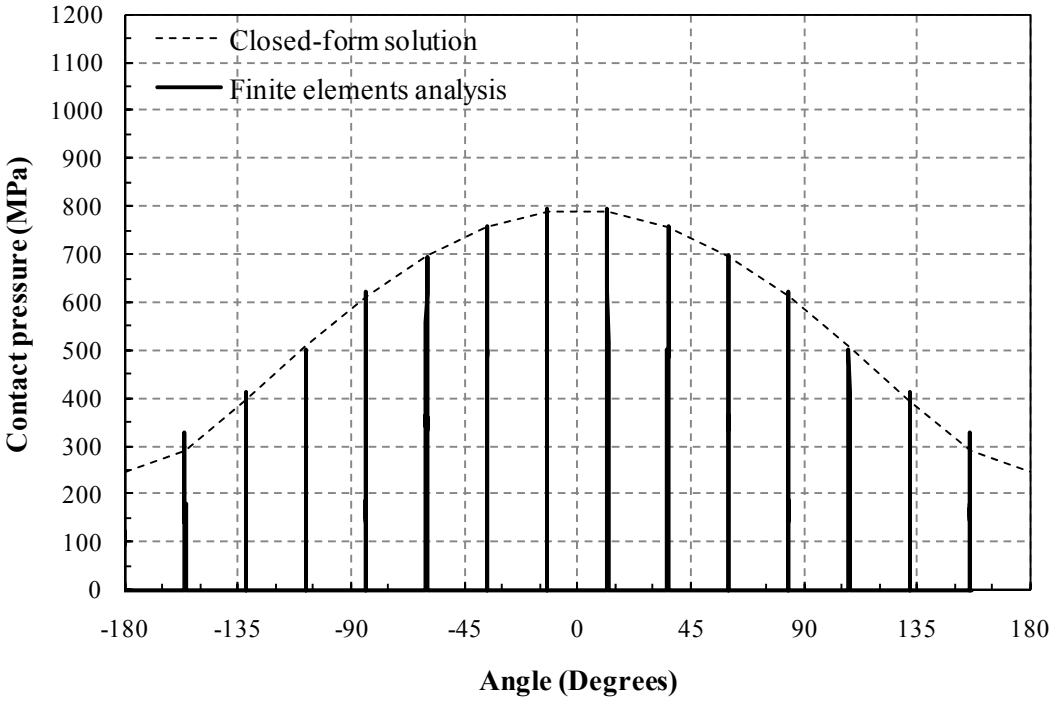

(c)

Fig. 6.13 The contact pressures from the finite element analysis and the closed-form solution for model 8 for the ratio $P_{total}/P_{separation}$ of (a) 0, (b) 0.43 and (c) 0.81.

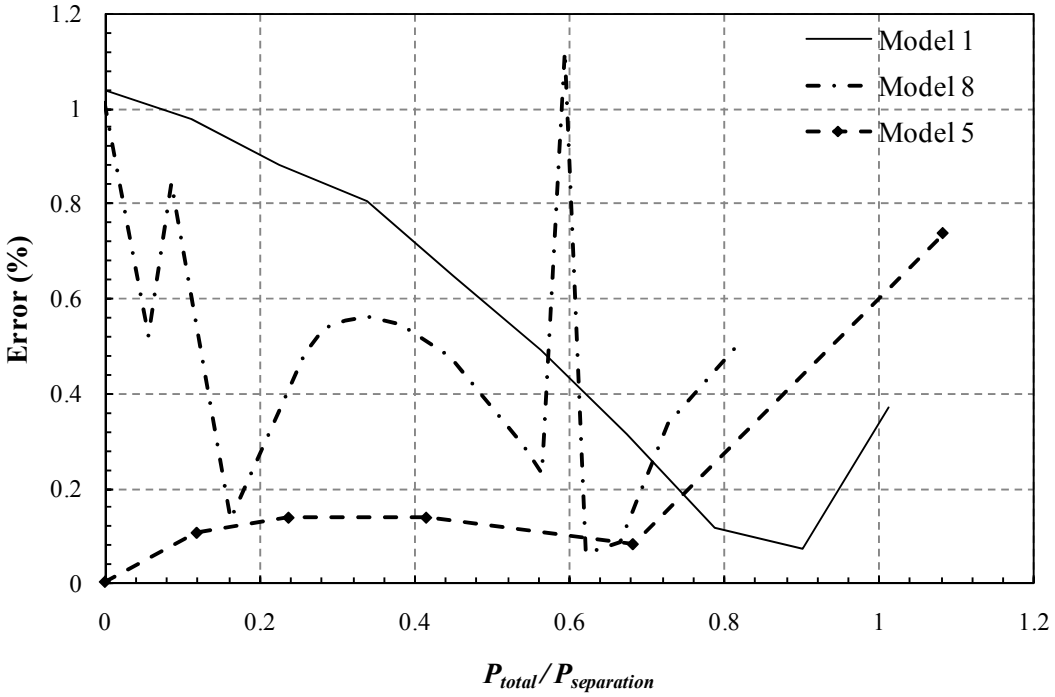

Fig. 6.14 The errors of the maximum contact pressures at $\theta = \pm 10°$ obtained from the closed-form solution when compared with those from the finite element analyses as a function of the ratio of the total applied load to the separation load.

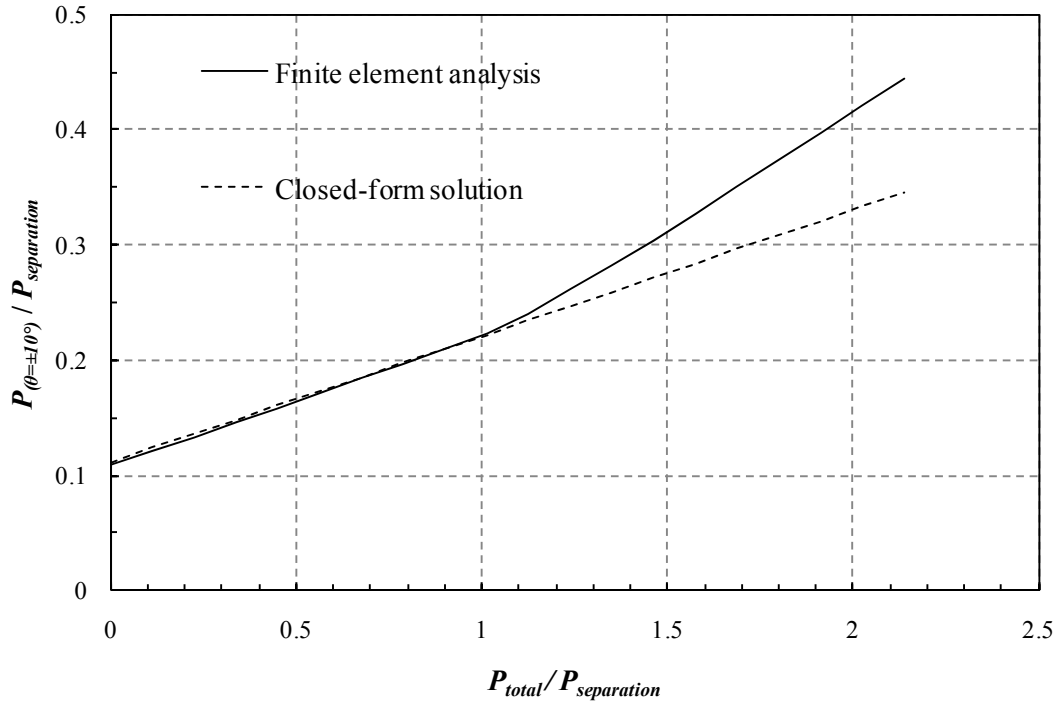

Fig. 6.15 The normalized load exerted by the rolling elements at $\theta = \pm 10°$ on the outer raceway from the finite element analysis for model 1 and the closed-form solution as a function of the normalized total applied load.

Chapter 7
Conclusions

In chapter 2, the experiments for laser welds in lap-shear specimens under quasi-static loading conditions are briefly reviewed first. The experimental results showed that the laser welds failed in a ductile necking/shear failure mode and the ductile failure was initiated at a distance away from the crack tip near the boundary of the base metal and heat affected zone. Two-dimensional plane strain finite element analyses were then carried out to understand the failure mode of laser welds in lap-shear specimens under quasi-static loading conditions. The results of the reference finite element analysis based on the homogeneous material model suggest a possible middle surface shear failure mode in the weld, which does not match with the experimental results. Therefore, the multi-zone models are developed to take into account the higher hardness values and the higher stress-strain curves of the heat affected and weld zones. The results of the finite element analyses based on the multi-zone non-homogeneous material models show that the higher effective stress-plastic strain curves of the weld and heat affected zones and the geometry of the weld protrusion can result in the necking/shear failure mode in the load carrying sheet. The results of the finite element analyses closely match with the experimental observations. Although lap-shear specimens are used to investigate the strength of the weld under shear dominant loading conditions, the load carrying sheets near the weld are subjected to dominant tensile deformation due to large plastic deformation.

A two-dimensional plane strain finite element analysis of the lap-shear specimen with consideration of void nucleation and growth was also conducted. Initially, the material elements located near the two crack tips exhibit a high rate of void nucleation and growth. As the applied displacement increases, the plastic strains of the material elements of the base metal near the heat affected zone begin to exceed the plastic strains of the material elements near the crack tips due to the higher stress-strain behavior of the material elements in the heat affected zone. The location of the large void volume fraction gradually shifts from the material elements near the two crack tips to the material elements in the base metal near the heat affected zone. With the absence of the round protrusion, the void volume fraction is thought to be equal in the base metal regions for both the lower left and the upper right load carrying sheets due to symmetry. However, the round protrusion imposes additional geometric constraint to the lower left sheet and thus the computational results show that the void volume fractions are larger for the material elements on the base metal side of the boundary of the base metal and the heat affected zone. The location of the material elements with the larger void volume fraction matches well with that of the crack formation as observed in the experiment. With the adoption of the Gurson yield function, the location of the initiation of ductile fracture can be clearly correlated with the experimental observation. It should be emphasized that the conclusions of this investigation are applicable to the laser welds in lap-shear specimens under quasi-static loading conditions.

In chapter 3, the experiments for ultrasonic welds in dog-bone shaped lap-shear specimens of magnesium and steel sheets under quasi-static loading conditions are reviewed first. The micrograph of the fracture surface of a failed lap-shear specimen

shows two distinct intersecting surfaces which were initiated from the pre-existing crack tip and from the indentation corner created due to the sonotrode tip and. Two-dimensional plane strain and plane stress finite element analyses were then carried out to understand the plastic flow patterns and the failure modes of ultrasonic welds in lap-shear specimens under quasi-static loading conditions.

The results of finite element analyses based on the weld model with and without indentation suggest that the plastic flow initiation site from the indentation corner, in addition to the pre-existing crack tip, is mainly responsible for dominant plastic flow patterns to occur. Finite element analyses for models with and without indentation and with different weld widths were developed with two-zone and multi-zone material schemes. The results of the finite element analyses show that the weld indentation corner can trigger the unique fracture surface shown in Fig. 3.4(c). The plastic flow pattern from the results of the finite element analyses closely matches the fracture surface profile form experimental observations. Additionally, finite element analyses based on the multi-zone material models with different weld widths were conducted to obtain the J integral solutions for the pre-existing crack and a kinked crack with a small kink length. The result of the finite element analyses are used to explain the crack kinking out of the interface. It should be emphasized that the conclusions of this investigation are applicable to the ultrasonic welds in lap-shear specimens under quasi-static loading conditions.

In chapter 4, an analytical load distribution solution to calculate the loads exerted by the rolling elements in cylindrical bearings without interference is proposed based on the analytical solutions by Hertz and Persson. The analytical solution is based on the

assumption that the profiles of the maximum contact pressure between the multiple rolling elements and the opposing surface is the same as the contact pressure profile between the continuous body and the opposing surface. This assumption combined with the force equilibrium condition forms the basis to derive the analytical solution. With the normalized load distribution solution, the only input required to obtain the loads exerted by the rolling elements is the total applied load.

Two-dimensional finite element analyses were conducted to validate the analytical solution. The maximum contact pressures from the rolling elements that are in contact with the outer raceway obtained from the two-dimensional finite element analysis are compared with the contact pressures calculated from the analytical solution. A comparison shows that the maximum error for the rolling elements having the largest maximum contact pressure is less than 3%.

A simplified method to estimate the fatigue of the bearing is also summarized. The method is based on the load exerted by the rolling element and the closed-form solution to calculate the subsurface Mises stress. The Mises stress is then combined with the Goodman relation and the stress-life relation of the bearing material to estimate the number of cycle to failure under constant amplitude loading conditions. Based on the analytical solution, a software has been developed to estimate the fatigue life of a given bearing. The proposed method will not be able to eliminate the experimental or computational validation process of the bearing but will be able to provide a quick assessment of the fatigue life of a given bearing. Engineers can implement the software in the design and selection process of automotive wheel bearings in order to reduce cost and time by being able to have a guideline of fatigue properties of bearing candidates.

In chapter 5, the contact pressures, maximum subsurface Mises stresses, and fatigue lives of cam roller follower bearings with different diameters and numbers of rolling elements have been obtained and compared based on the results of the finite element analyses. A kinematic analysis under pure rolling conditions indicates that the material elements in the inner pin experiences higher stresses compared to the material elements in the outer ring. The results of the finite element analyses indicate that the contact pressure and maximum subsurface Mises stress generally decrease with an increase in the rolling element diameter. However, reducing the number of rolling elements and decreasing the outer ring thickness to accommodate larger rollers may not be beneficial to the contact pressure and maximum subsurface Mises stress due to the increase of the outer ring compliance.

Once the maximum subsurface Mises stresses are obtained through finite element analyses, the fatigue lives are estimated. The fatigue lives of the 15 roller models are determined to be shorter than those of the 18 roller models. The increased compliance of the outer ring for the 15 roller models causes a significant deformation of the outer ring and the applied load is carried by a fewer number of rolling elements. Consequently, the fatigue lives of the inner pin decrease. The 15 roller models have rollers with larger diameters compared to the 18 roller models. However, due to the increase of the percentage of the total load carried by the 1st rolling element originating from the increase of the outer ring compliance, the contact pressures and the maximum subsurface Mises stresses are higher for the 15 roller models. It is recommended that a parametric study based on the finite element analyses should be conducted to obtain the optimum

geometry which gives the lowest contact pressure and maximum subsurface Mises stress which results in the longest fatigue life of cam follower roller bearings.

In chapter 6, a closed-form solution to calculate the loads exerted by the rolling elements in cylindrical roller bearings with consideration of interference fit of rollers is proposed in this chapter. The non-conforming Hertz solution and the conforming Persson solution are first briefly reviewed. The interference loads by the rolling elements due to the interference are derived and then approximated for a given set of geometric parameters of bearings. With the solution for the interference load, the loads exerted by the rolling elements on the outer raceway are obtained when the total load is less than the separation load where a rolling element possibly start to lose contact with the cylinders. These loads of the rolling elements can be calculated by a closed-form equation with the total applied load, the number of rolling elements, the angular locations of the rolling elements, the equivalent elastic modulus, the interference, the outer raceway diameter and the thickness of the outer cylinder as the input parameters. Two-dimensional finite element analyses were conducted to verify the applicability of the closed-form solution. Finite element models with different diameters of the outer and inner cylinders, diameters of the rolling element, number of rolling elements, and the thickness of the outer cylinder were considered for the validation. The results of the finite element analyses show that the maximum contact pressures of the rolling elements obtained from the closed-form solution are within 1% of those of the finite element analyses when the total load is less than the separation load.